IntechOpen

# Advancements in Energy Storage Technologies

*Edited by Xiangping Chen and Wenping Cao*

# ADVANCEMENTS IN ENERGY STORAGE TECHNOLOGIES

Edited by **Xiangping Chen**
and **Wenping Cao**

**Advancements in Energy Storage Technologies**
http://dx.doi.org/10.5772/intechopen.68717
Edited by Xiangping Chen and Wenping Cao

**Contributors**

Adio Miliozzi, Raffaele Liberatore, Daniele Nicolini, Elisabetta Veca, Manila Chieruzzi, Tomaso Crescenzi, Luigi Torre, Youngil Kim, Robert J. Harrington, Rached Dhaouadi, Kamyar Khosravi, Yoichi Hori, Sang Jae Kim, Ananthakumar Ramadoss, Balasubramaniam Saravanakumar, Amjad Anvari-Moghaddam, Jeremy Dulout, Corinne Alonso, Bruno Jammes, Josep M. Guerrero, Uroš Stritih, Dragan Stevanovic, Alessandro Serpi, Mario Porru, Alfonso Damiano



**Notice**



First published in London, United Kingdom, 2018 by IntechOpen
eBook (PDF) Published by IntechOpen, 2019
IntechOpen is the global imprint of INTECHOPEN LIMITED, registered in England and Wales, registration number: 11086078, The Shard, 25th floor, 32 London Bridge Street
London, SE19SG – United Kingdom
Printed in Croatia

British Library Cataloguing-in-Publication Data
A catalogue record for this book is available from the British Library

Additional hard and PDF copies can be obtained from orders@intechopen.com

Advancements in Energy Storage Technologies
Edited by Xiangping Chen and Wenping Cao

p. cm.

Print ISBN 978-1-78923-054-3

Online ISBN 978-1-78923-055-0

eBook (PDF) ISBN 978-1-83881-346-8

# Meet the editors

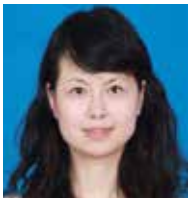

Dr Xiangping Chen received her PhD degree in Electronic and Electrical Engineering from Newcastle University, Newcastle upon Tyne, UK, in 2013. She is currently an associate professor in Guizhou University, China. Her research interests are renewable energy with energy storage, energy management and energy efficiency improvement.

Dr Wenping Cao received his BEng degree in electrical engineering from Beijing Jiaotong University, Beijing, China, in 1991, and his PhD degree in electrical machines and drives from the University of Nottingham, Nottingham, UK, in 2004. He is currently a chair professor of Electrical Power Engineering in Aston University, Birmingham, UK. His research interests include fault analysis and condition monitoring of electrical energy systems.

# Contents

# Preface

Energy storage is becoming increasingly important for renewables, smart grids, electrified propulsion and smart buildings. Collectively, these will help establish a low-carbon economy worldwide, and the related technologies are evolving rapidly. This book is aimed at informing the audience of the latest technological developments in energy storage derived from research community and industrial R&D. The topic covers multi-energy storage forms (batteries, supercapacitors, solar, thermal energy storage, etc.). The book is also concerned with the associated control technologies and economic models of these energy storage systems.

The book is organised into three sections: "Thermal Energy Storage", "Electrical Energy Storage" and "Integration of Energy Storage into Applications". The reader will be exposed to these broad topics in technical depth, including system architecture, modelling, trial tests, energy management and control, implementation and integration with systems, such as wind turbine, smart grids and smart buildings. The editors are grateful to all contributing authors and especially to the Publishing Process Manager, Ms. Dajana Pemac, for her support throughout the process.

**Dr. Xiangping Chen**
Guizhou University, Guiyang, P.R. China

**Prof. Wenping Cao**
Aston University, Birmingham, UK

Section 1

# Thermal Energy Storage

Chapter 1

# Heat Exchange Analysis on Latent Heat Thermal Energy Storage Systems Using Molten Salts and Nanoparticles as Phase Change Materials

Adio Miliozzi, Raffaele Liberatore, Daniele Nicolini,
Manila Chieruzzi, Elisabetta Veca,
Tommaso Crescenzi and Luigi Torre

Additional information is available at the end of the chapter

http://dx.doi.org/10.5772/intechopen.73672

**Abstract**

The increase of carbon dioxide emissions is the most important contributor to climate change. A better use of produced energy, increasing systems efficiency and using renewable sources, can limit them. A key technological issue is to integrate a thermal energy storage (TES). It consists in stocking thermal energy through the heating/cooling of a storage material for future needs. Among various technologies, latent heat TES (LHTES) provides high energy storage density at constant temperature during melting/solidification of storage media. The bottleneck in the use of typical PCMs is their low thermal conductivity. To improve the heat exchange between heat transfer fluid and PCM, three methods are possible and here experimentally analyzed: conductivity systems enhancements; convective flows promotion in liquid phase; and improvement of PCM thermal properties including small amounts of nanoparticles. CFD models were used to evaluate physical phenomena that are crucial for optimized LHTES systems design. The study of the heat exchange mode allowed some useful indications to achieve an optimized LHTES, taking advantage by convective flows and conductivity promotion systems. The use of NEPCM, to maximize the stored energy density and realize compact systems, makes necessary the improvement of its thermal diffusivity. These will be the future research topics.

**Keywords:** heat exchange, latent heat, nanoparticles, phase change material, thermal energy storage

## 1. Introduction

The increased world energy demand is the most important contributor to climate change. A better use of the produced energy, by increasing the energy efficiency in industrial and civil applications, as well as the use of renewable sources, such as solar energy, can limit the carbon dioxide emissions and, consequently, the man-made greenhouse effect [1]. European Commission introduced in October 2014 new and ambitious targets for the year 2030 [2, 3]: 27% share for renewable energy penetration, 40% cuts in greenhouse gas (GHG) emissions, and 27% improvement in energy efficiency.

A key technological issue to reach these objectives is to integrate in the productive system an efficient and low-cost thermal energy storage (TES) [4, 5]. Thermal energy storage is a technology that consists in stocking thermal energy through the heating and cooling of a storage material. The energy stored in this way can be used for future needs in particular to face the fluctuating energy demand, increasing the efficiency of several systems. The heat can be stored in a heat storage material (HSM) in three different modes: as sensible heat (HSM temperature increasing), as latent heat (HSM phase change, i.e. solid-liquid), or as thermochemical energy (reversible thermochemical reactions).

Among these technologies, latent heat thermal energy storage (LHTES) provides, due to the high absorbed/released energy required by the phase change process of the material, a high-energy storage density at an almost constant temperature during the melting and the solidification of the storage media. These materials are called phase change materials (PCMs). However, in practice, in the place of a single temperature, the system operates in a temperature range, which includes the melting temperature. A PCM can store higher amount of heat if in comparison with a material using only sensible heat, and this leads to a significant decrease of the size and cost of the LHTES systems [6, 7].

PCMs are commonly used in applications for both thermal management and thermal energy storage. For example, LHTES systems can find application [7] in:

- small and large size solar thermal power plants, where the constant temperature of the supplied heat allows a more efficient operation of the gas turbine;
- in industrial plants, where the process heat, deriving from renewable sources, is provided at the required temperature allowing a wide range of processes: food (30–120°C), beverages (60–90°C), paper Industry (60–150°C), metal surface treatment (30–80°C), bricks and blocks curing (60–140°C), textile industry (40–180°C), chemical industry (60–260°C), plastic industry (60–220°C), and other industrial sectors (30–180°C).
- in district heating, industrial cooling, or waste heat recovering.

Typical HSM for medium-high applications are salts or mixtures thereof [8, 9]. The bottleneck of these PCMs is their low thermal conductivity which, combined with a high thermal capacity, leads to a low thermal diffusivity and, therefore, a low exploitation of the material, high

charging times, and low released power. The enhancement of the thermal conductivity of the PCMs is one of the most important topics in LHTES system design. Many development activities, indeed, are focused on this topic with the aim of creating materials with high latent heat, high specific heat, and high thermal conductivity.

To improve the heat exchange between the heat transfer fluid (HTF) and PCM, three methods deserve to be cited [10]:

**i.** Increase of the heat exchange surface through the introduction of suitable thermal conductivity promotion systems;

**ii.** Increase of the heat exchange coefficient by exploiting the development of convective flows inside the PCM during the solid-liquid phase change (convective thermal exchange);

**iii.** Increase the thermal conductivity of HSM by altering its properties through the introduction of small amounts of proper nanoparticles (nanoenhanced PCM (NEPCM)).

The effect of these solutions on heat transfer mode should be carefully analyzed to assess the advantages and disadvantages.

In the first part of this chapter, the commonly used storage media and the methods of increasing the conductivity will be illustrated. Subsequently, some experimental tests will be described, and the results discussed. Finally, after analyzing the numerical methodologies useful to simulate the highlighted physical phenomena, future steps for the development of innovative latent heat storage systems will be described.

## 2. Heat storage materials

The most common HSMs for medium-high applications are solar salts and their mixtures. They shows good thermal properties and low cost. **Table 1** summarizes some of these HSMs.

It was demonstrated that the main thermal properties of PCMs (in particular in the solar salts) can be enhanced with the addition of several kind of nanoparticles. Some of these properties are latent heat, specific heat, and thermal conductivity. In particular in this paragraph, it is reported how the enhancement of thermal properties is strictly related to some factors like the size, the type, and the weight percentage of nanoparticles, as well as synthesis protocol and the parameters used. For example, nanoparticles with a too little diameter may precipitate instead of dispersing in the liquid or a too high weight percentage can be responsible for a difficult nanoparticle dispersion.

As for the synthesis protocols, the NEPCM can be obtained with several experimental procedures. The most used is the two-step liquid solution method which involves the production of a solution and the use of ultrasound. In particular, in this case, the NEPCMs are prepared by dissolving 200 mg of salt and nanoparticles in solid state (as powder) into 20 ml of distilled water. The dispersion of the nanoparticles is ensured by the ultrasonication of the solution followed by water evaporation on hot plate.

| Composition | Melting temp, °C | Latent heat, J/g | Composition | Melting temp, °C | Latent heat, J/g |
|---|---|---|---|---|---|
| $LiNO_3$:$KNO_3$ 33:67 [a] | 0133 | 170 | NaOH:NaCl:$Na_2CO_3$ 86:8:6 [b] | 298 | 286 |
| $KNO_3$:$NaNO_2$:$NaNO_3$ 53:40:7 [a] | 142 | 80 | $NaNO_3$ | 307 | 183 |
| $LiNO_3$:$NaNO_3$ 49:51 [a] | 194 | 265 | $KNO_3$ | 337 | 100 |
| $LiNO_3$:NaCl 87:13 [a] | 208 | 369 | LiCl:KCl 58:42 [b] | 348 | 170 |
| $NaNO_3$:$KNO_3$ 54:46 [a] | 222 | 110 | $MgCl_2$:NaCl:KCl 63:23:24 [a] | 385 | 461 |
| $NaNO_2$:NaOH 80:20 [b] | 232 | 252 | KCl:$MgCl_2$:NaCl 20:50:30 [b] | 396 | 291 |
| NaOH:$NaNO_2$ 73:27 [b] | 237 | 272 | $Li_2CO_3$:$K_2CO_3$:$Na_2CO_3$ 31:35:34 [a] | 397 | 275 |
| NaOH:$NaNO_3$ 28:72 [b] | 246 | 225 | LiF:LiOH 80:20 [b] | 430 | 528 |
| $LiNO_3$ | 253 | 363 | Li:NaF:KF 29:12:59 [a] | 463 | 442 |
| $LiNO_3$:NaCl 93.6:6.4 [a] | 255 | 354 | $Li_2CO_3$:$K_2CO_3$ 47:53 [a] | 488 | 342 |
| LiCl:LiOH 37:63 [a] | 262 | 485 | $CaCl_2$:NaCl 55:45 [b] | 495 | 236 |
| $NaNO_3$:NaOH 41:59 [b] | 266 | 278 | $Na_2CO_3$:$Li_2CO_3$ 56:44 [a] | 496 | 368 |
| LiCl:$Ca(NO_3)_2$ 59:41 [b] | 270 | 167 | NaCl:$CaCl_2$ 33:67 [a] | 500 | 281 |
| $NaNO_3$-2NaOH [b] | 270 | 295 | $K_2CO_3$:NaF:KCl 62:17:21 [a] | 520 | 274 |
| LiOH:LiCl:KCl 62:36.5:1.5 [b] | 282 | 300 | $Li_2CO_3$:$Na_2CO_3$:$K_2CO_3$ 22:16:62 [a] | 580 | 288 |

[a]wt.%.
[b]mol.%.

**Table 1.** Main properties for some HSMs used as PCMs [11–14].

In general, a sonication is made by using sound energy to disperse particles into a material. When the ultrasonic frequencies are used, the process is called ultra-sonication. The aim of this method is to obtain a uniform dispersion of the nanoparticles, thus avoiding the formation of agglomerates (i.e., clusters of hundreds of single nanoparticles).

Different sonication times (100 and 200 min) and evaporation temperatures (60, 100, and 200°C) can be used in this procedure [15–17].

The typical salts used as PCMs in LHTES are nitrates, at medium-high temperatures (due to their melting temperature which is between 200 and 400°C), and carbonates and chlorides, at high temperatures (since their melting temperature is above 400°C). For example, the dispersion of 1 wt.% of $SiO_2$ nanoparticles into a mixture of $Li_2CO_3$ and $K_2CO_3$ (62:38) with a melting point of 488°C was done under sonication for 100 min followed by water evaporation at 200°C [15]. Above the melting point (in the range 525–555°C), the specific heat of the NEPCM is enhanced by 19–24%. The enhancement was attributed to the formation of a substructure close to the nanoparticles and to the high specific surface energy of the nanoparticles. By increasing the nanoparticles, percentage (1.5 wt.% instead of 1 wt.%) of the same

nanoparticles into the same molten salt mixture different results can be obtained by changing the protocol parameters [16, 17]. In particular, with 200 min and 60°C, a specific heat increase of 34% in solid phase and 101% in liquid phase can be achieved. The morphology of the NEPCMs is characterized by the formation of needle-like structures of nanoparticles in the salt mixture. These structures could be responsible of the specific heat enhancement. Moreover, slow water evaporation (i.e. at lower temperature) seems to be more effective in increasing the specific heat of the salt due to the reduced presence of agglomerates. Other kind of nanoparticles can also be used. A low amount of graphite nanoparticles (0.1 wt.%) added into the same eutectic salt ($Li_2CO_3$: $K_2CO_3$ 62:38) may produce an increase of the specific heat of 40 and 57% in solid and liquid phase, respectively [18]. Chloride salts and their eutectic mixtures can also be used as HSM at high temperature. An eutectic mixture of barium chloride, sodium chloride, calcium chloride, and lithium chloride ($BaCl_2$:NaCl:$CaCl_2$:LiCl 34.59:12.52:40:12.89) has a melting point of 378°C. The addition of 1 wt.% of $SiO_2$ nanoparticles to this mixture showed an increase of the specific heat of about 14.5% [19].

The nanoparticle size can also affect the thermal behavior of molten salts and nanoparticles. It seems that higher specific heat increase is obtained with higher nanoparticle diameter. This trend was shown by studying nanofluids based on the common binary nitrate salt of $NaNO_3$:$KNO_3$ (60:40) having a melting temperature of about 225°C by using the two-step liquid solution method. Lu and Huang [20] used $Al_2O_3$ nanoparticles with 13 and 90 nm diameter, while Dudda and Shin [21] used $SiO_2$ nanoparticles (1 wt.%) with 5, 10, 30, and 60 nm in diameter. The possible explanation of this effect is that nanoparticles with little diameter (<10 nm) tend to precipitate or form agglomerates, thus preventing a good dispersion into the molten salt, which is a fundamental step to achieve thermal properties enhancement.

Several experimental studies have been conducted by University of Perugia and ENEA in order to develop NEPCM as HSMs. In one of these [22], $SiO_2$, $Al_2O_3$, $TiO_2$, and a mixture of $SiO_2$-$Al_2O_3$ nanoparticles (82–86% silica, 14–18% alumina) were added to the salt mixture $NaNO_3$-$KNO_3$ (60:40). The NEPCMs were obtained by the two-step liquid solution method described above with 100 min of dispersion and water evaporation at 200°C.

Some considerations could be found. First of all, the NEPCMs showed the highest improvement of the specific heat with 1 wt.% of nanoparticles added, while 0.5 and 1.5 wt.% were not considered effective. Second, the type of nanoparticle played an important role: $TiO_2$ did not increase the Cp of nitrate salts, while $SiO_2$ $Al_2O_3$ showed the greatest enhancement (+22 and +57% in solid and liquid state). Since no substructure was formed in this case, the observed enhancement of heat capacity was attributed to the formation of a solid-like nanolayer on the surface of the nanoparticle.

In a recent study, another HSM was developed through water solution method by using $KNO_3$ as molten salt (melting point of 334°C) and 1 wt.% of $SiO_2$, $Al_2O_3$, and a mixture of $SiO_2$-$Al_2O_3$ as nanoparticles [23]. The HSM has an increased specific heat with silica and silica-alumina nanoparticles (+9.5% and +4.7%, respectively). In any case, the two-step method involves the use of high amount of water and the evaporation of the water can be expensive and time consuming. In other words, in industrial scale, it should be tried to produce NEPCMs with easier methods. Few studies report the production of nanofluids based on molten salt and

nanoparticles without water by mixing them with the ball milling procedure (i.e., directly in solid state). In this study [24], a ball-mill with 9 mm stainless steel bearing was used to mix the powder salts and the nanoparticles (CuO and $TiO_2$). With this procedure and materials, the NEPCMs obtained showed higher latent heat (+2.4 and +3.8%) and specific heat.

Recently, a new mixing methodology was developed by University of Perugia and ENEA [25]. This technique does not involve the use of water, since salts and nanoparticles are mixed together directly at high temperature (i.e., in liquid state). $NaNO_3$:$KNO_3$ (60:40) and 1.0 wt% of nanoparticles (silica, alumina and a mixture of silica/alumina as above) were mixed together in powder and then heated above the melting temperature (at 300°C) by using a twin screw microcompounder (**Figure 1**). The presence of a recirculating channel ensures the recycling of the NEPCM and the good dispersion of nanoparticles. The materials were mixed at screw speed of 100 and 200 rpm, for 15 and 30 min. After this heating, the mixture is then cooled down at room temperature and ground to powder. The thermal properties of the NEPCMs produced in this way depend on the type of nanoparticle and the time and speed used to mix them. A good HSM was obtained with silica/alumina nanoparticles mixed for 30 min at 200 rpm, reaching a high increase of $C_p$ (+52.1% in solid phase and +18.6% in liquid phase) and good increase of the heat of fusion (+4.7%). The thermal storage capability of molten salts and nanoparticles can be also calculated and evaluated as the integration of the heat flow curve between the minimum and maximum working temperatures. The stored heat was found to enhance by 13.5%.

Another important property of the HSM is their latent heat. The advantage of the increase of latent heat is the increased storage heat capability of the material per unit volume. About the latent heat enhancement, there is lack of information. However, some studies performed by University of Perugia reported an increase of 15% mainly with silica-alumina nanoparticles in nitrate mixture [22] and also in $KNO_3$ as molten salt having a melting point of 334°C (the latent heat increased by 12%). In both studies, the NEPCMs were produced in water solution [23]. It was shown that the stored heat of molten salts as $NaNO_3$-$KNO_3$ [22] and $KNO_3$ [23] is increased with the addition of 1.0 wt.% of $SiO_2$-$Al_2O_3$ and $SiO_2$.

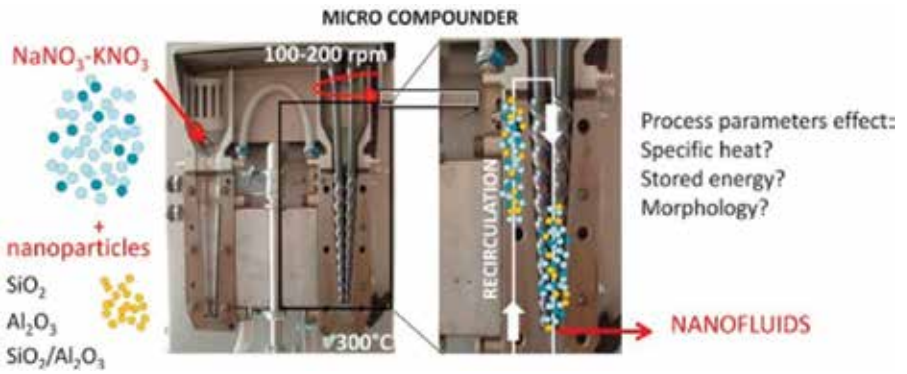


**Figure 1.** Mixing of nanoparticles and the salt mixture at high temperature in a twin screw microcompounder [21].

Another fundamental property of heat storage materials is their thermal conductivity. However, for many PCMs (especially molten salts), it needs to be increased. Thus, the main idea to increase this property is to combine these PCMs with highly conductive nanomaterials [26]. The research on other nanofluids is wide, but only few studies were performed in particular on molten salts with nanoparticles to enhance the thermal conductivity of the pure materials. One of these showed that only 1 wt.% of $SiO_2$ nanoparticles may enhance the thermal conductivity of the eutectic mixture of carbonates ($Li_2CO_3$:$K_2CO_3$ 62:38) by 47% at 150°C and 37% at 300°C with respect to the base salt and the thermal diffusivity by 28 and 25% at 150 and 300°C, respectively [27]. The formation of a percolation network was considered responsible of the enhancement of the thermal conductivity and diffusivity of the nanocomposite (as previously reported about the specific heat enhancement). Recently, University of Perugia [28] produced NEPCMs starting from the nitrate mixture ($NaNO_3$:$KNO_3$ 60:40). Only 1.0 wt.% of silica-alumina nanoparticles (82–86% silica, 14–18% alumina) were dispersed into the salt mixture in a concentrated water solution (from 100 to 500 g/l). The salts and the nanoparticles were mixed by a mechanical stirrer, and the NEPCMs produced showed a higher thermal conductivity value in comparison to the base salt mixture (up to +25%). Moreover, it increased by increasing the aqueous solution concentration (from 100 to 500 g/l), as well as thermal diffusivity (up to +47%).

## 3. Enhancement of heat exchange in LHTES

The improvement of thermal exchange between heat transfer fluid and PCM is one of the main themes in development of LHTES systems [29]. Commonly, used PCMs show a low conductivity of 0.5–1 W/m K. Therefore, the design of the heat exchanger is dominated by the task to identify effective solutions to increase the equivalent thermal conductivity within the heat storage material [30]. In the previous paragraph, the possibility to act on the material itself by altering its thermal properties by adding small amounts of nanoparticles (NEPCM) was evaluated. In this section, however, two other methods to increase the apparent conductivity of the thermal storage medium were analyzed: introducing a system to promote the conductivity and favoring a convective heat exchange in the liquid phase of PCM.

### 3.1. Promoting thermal conductivity

Different solutions can be applied to promote thermal conductivity or to improve heat exchange and increase power level [11, 31]:

- Increasing of heat transfer area: the contact area of the heat exchanger between HTF and PCM is enlarged to reduce the average distance for heat diffusion within the PCM. Possible implementations of this approach can use either finned tubes or capsules;
- Composite material with increased thermal conductivity: a material showing a high thermal conductivity is added to the PCM. The PCM can be infiltrated in a porous matrix made up of the additional material, or the two components can be mixed as powders, fibers, or small particles;

- Intermediate heat transfer medium liquid/gaseous: the PCM and a heat exchanger are arranged in a container filled with a medium that transfers the energy between these two components. The heat transport involves the phase change of the heat transfer medium.

A **sandwich structure** is an approach to increase the effective thermal conductivity of the PCM, integrating highly conductive materials layers inside the PCM. The layers are arranged in the heat transport direction (**Figure 2a**). The application of tubes with wings embedded in a PCM is described as a sandwich concept. This concept has been developed, since it seems to be the most promising option for making efficient and low-cost latent heat storage systems [11, 12, 32].

The choice of steel would be a simple solution as well as finned steel tubes are standard components for heat exchangers. Instead, graphite or aluminum sheets are chosen as materials for wings due to their high thermal conductivity. To obtain the same heat transfer performance in comparison with the graphite or aluminum fins, the steel fins require a higher volume and, therefore, significantly higher costs, also due to the higher density (**Table 2**). The costs are proportional to the $c/\lambda$ factor, where $\lambda$ is the thermal conductivity and c is the volume specific cost of the fins material.

Mounting the fins on the pipes is a key issue for the sandwich concept. If the material of the fins is different from the material of the pipes two other phenomena can occur: a different thermal expansion between the used materials and a galvanic corrosion (the damage induced when two dissimilar materials are coupled in a corrosive electrolyte). In addition, the application of fins made of expanded graphite offers several advantages beyond a good thermal conductivity. Expanded graphite has good chemical stability with nitrates and nitrites at temperatures up to 250°C, and galvanic corrosion does not occur when it is in contact with steel tubes. Because graphite laminae exhibit a high degree of flexibility and they are often used as a sealing material, a tight contact between the tubes and the fins can easily be achieved [32]. The highest specific price, compared to stainless or carbon steel, is largely compensated by its low density and high thermal conductivity. However, graphite is stable with nitrates only below 250°C. For higher temperature applications, the use of metallic fins is necessary [11]. **Figure 2b** shows semiindustrial applications of this concept.

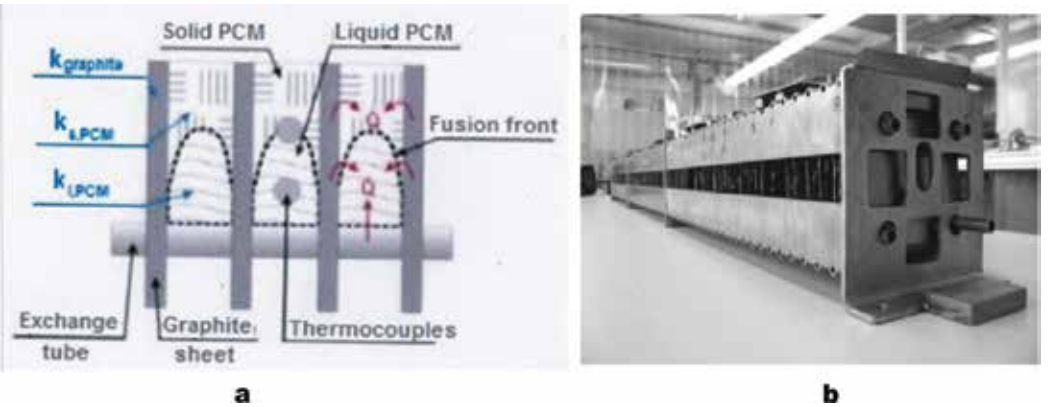


**Figure 2.** Functional scheme and test module of the LHTES sandwich concept [29, 31, 32].

| | Graphite foil | Aluminum | Stainless steel | Carbon steel | Copper |
|---|---|---|---|---|---|
| Thermal conductivity $\lambda$ (W/m K) | 150 | 200 | 20 | 30 | 350 |
| Density $\rho$ (kg/m$^3$) | 1000 | 2700 | 7800 | 7800 | 8800 |
| Estimated volume specific costs $c$ (€/m$^3$) | 10,000 | 7000 | 20,000 | 15,000 | 40,000 |
| Estimated $c/\lambda$ (€K/W m$^2$) | 66.7 | 35.0 | 1000 | 500 | 114.3 |

**Table 2.** Main properties for materials used in LHTES sandwich systems [31, 32].

A second solution is to pack the PCM into capsules in order to reduce the maximum distance for heat transfer or to increase the heat exchange area: this concept is called **macroencapsulation** of the storage medium [11]. **Figure 3** shows an example of LHTES with macrocapsules used in a laboratory scale experiment. In this case, the cylindrical capsules have a length of 0.5 m and a diameter of 15–25 mm and they are filled with a $NaNO_3$-$KNO_3$ eutectic mixture. The capsules are arranged in parallel and integrated inside a tank. Due to PCM specific volume variations that can reach up to 10% during phase change, the tubes are not fully filled. A volumetric gas fraction of about 20% is required within the rigid capsules to limit the increase in pressure during PCM melting.

Because of the corrosive behavior of some PCM salts, it is necessary to provide a certain minimum thickness of the wall and avoid a flexible encapsulation. However, this concept is not considered a promising solution due, in particular, to some economic aspects and the following disadvantages [11]:

- The amount of material required for pressure capsules is significant, if steel is used: the steel mass is almost equivalent to the mass of PCM;
- The volume fraction of PCM in the pressure tank may be less than 40%;
- The filling and sealing procedure with molten PCM are complex;
- HTF contamination with PCM should be avoided due to leakage from the capsules: this requires high standards of quality with consequent further increase in costs.

Thermal conductivity can also be improved by using **composite materials** in which the properties of a high latent heat of a PCM are combined with that of a good thermal conductivity of an additive. Said composite materials are manufactured in blocks and subsequently assembled together with the tube assembly (**Figure 4**).

If the operational temperature range is 120–300°C, nitrates or nitrites and various types of graphite are currently being used. Graphite was chosen because of its high thermal conductivity and chemical stability. The objective is generally to obtain a composite material with an effective thermal conductivity in the range of 5–15 W/m K using a small amount of graphite to obtain a high capacity and a low cost of the LHTES system. The fraction of graphite mass significantly influences the effective thermal conductivity. The composite material is

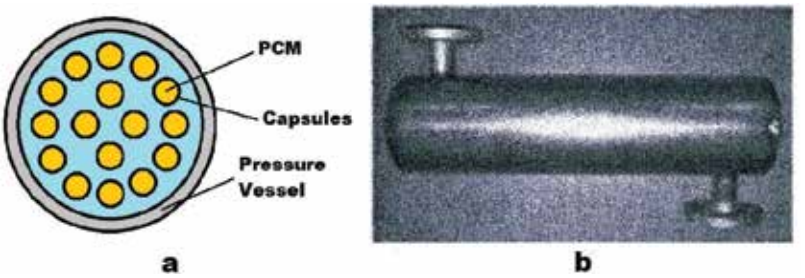


**Figure 3.** PCM capsules array and external containers [12, 31].

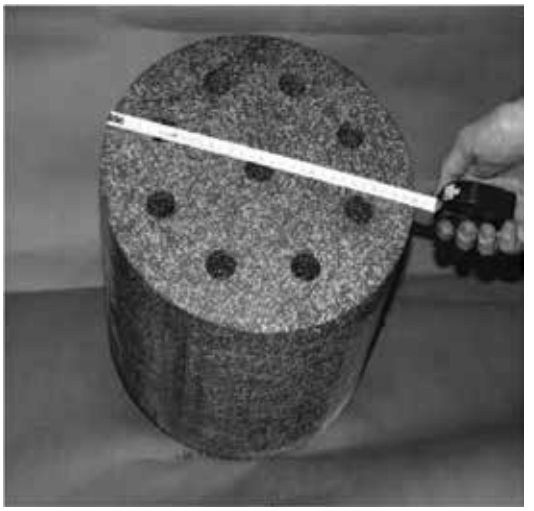

**Figure 4.** Example of composite material (expanded graphite) with PCM in a laboratory scale element [29, 31].

produced by compression of PCM powders and expanded graphite. The development of an efficient HSM requires the limitation of graphite content because of material costs (ratio of specific expanded graphite/PCM costs is about 20:1) and the reduction in volumetric storage capacity. An important aspect is also the cyclic behavior of composite material. The separation of the components must not be the result of repeated charge/discharge. Indeed, during some experiments, described in literature [11], significant PCM loss occurred, about 40% of nitrate salt separated from graphite. There are several possible causes for the salt loss of the storage module. These causes include the requirement for an empty volume for salt expansion, degassing caused by impurities and moisture in the salts, and poor testability of alkaline metal nitrate salts on graphite and their good wettability on metallic surfaces (tendency to the sliding). Probably, the salt leakage was caused by a combination of these critical phenomena.

### 3.2. Convective heat exchange

The heat transfer efficiency between the HTF and PCM strongly affects the performance of the charging/discharging cycles of an LHTES system, especially during melting/solidification

phases. During melting, the PCM has to be heated by the HTF (charge process), the heat flows toward the PCM by conduction and later by natural convection. The solid PCM near the heat exchanger surface heats up and then starts to melt, and the thickness of the liquid region increases over time at fluid-solid interfaces. As the thermal conductivity of liquid PCM is less than that of solid PCM, the heat transfer by conduction becomes almost negligible as the melting process moves forward, and the movement of the fluid in terms of convection must also be taken into consideration.

Convective flows are a result of the varying density of the PCM in function of temperature. The whole mass of fluid is subject to a downward gravitational pull. Consequently, lighter portions of fluid will be subject to Archimedes' upward buoyant force. The nonhomogeneity in temperature causes the same in density [10]. The heat transfer to the PCM followed three regimes [33]: conduction; mixed conduction and convection, where conduction domination was gradually replaced by convection when a sufficiently large amount of liquid had formed; and convection. Regarding solidification, the HTF must be heated. A solid layer was produced on the surface of the heat exchanger on the PCM side that affected the heat transfer by conduction. This is the reason why it is important to enhance the thermal conductivity of the LHTES system. The transition from a conductive to a convective regime produced a significant increase in thermal exchange with a reduction in charging and discharging times and consequent increase in available thermal power and system efficiency. The conditions necessary to establish these convective motions have been extensively studied both experimentally [30, 34–36] and numerically [37–41]. The last goal is to promote this sort of heat exchange within the LHTES to achieve an optimized and efficient system.

A preliminary experimental test of PCM melting was performed in ENEA in a small tubular reactor in a temperature range between 180 and 300°C. The experiment also included the cooling down of the system. Only the time period of the fusion phase was taken into account. The PCM was a mixture of nitrate salts, whose composition is $NaNO_3$-$KNO_3$ (60:40%wt), the dimensions of the AISI 316 reactor were 66 mm internal diameter, 70 mm external diameter, and 310 mm high. It contained about 2 kg of molten salts, and the tubular reactor was equipped with an external heating element, made in kanthal, placed along the wall. Instrumentation for the acquisition of the temperature and pressure was also present.

There are 18 thermocouples for temperature measurement inside the reactor: they are placed on six planes. Each plane contains three thermocouple tubes positioned at 120 degrees from each other at three different radial distances.

For the melting test, the reactor was loaded with 2 kg of PCM in order to have a uniform composition. The PCM was heated up to 300°C and then cooled down.

- The heating from 180 to 300°C was set without programming any temperature ramp on the controller. This is the reason why it overshoots the desired temperature value.
- During the heating phase, the salts started to melt in the temperature range of 220–240°C. In **Figure 5**, the blue dotted lines correspond to the melting temperature interval, and the blue line is the time of the melting process.

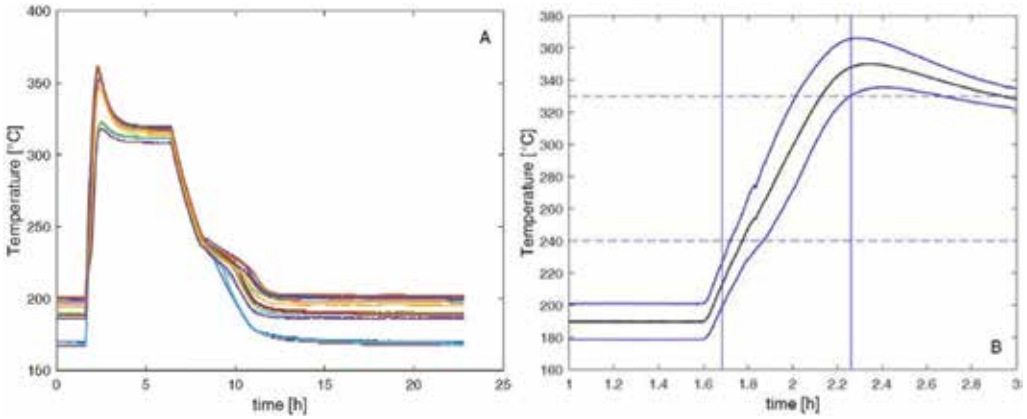


**Figure 5.** (A) All of the 18 thermocouples over experimental test time; (B) The black line is the mean temperature value; and the blue line is the standard deviation ± σ.

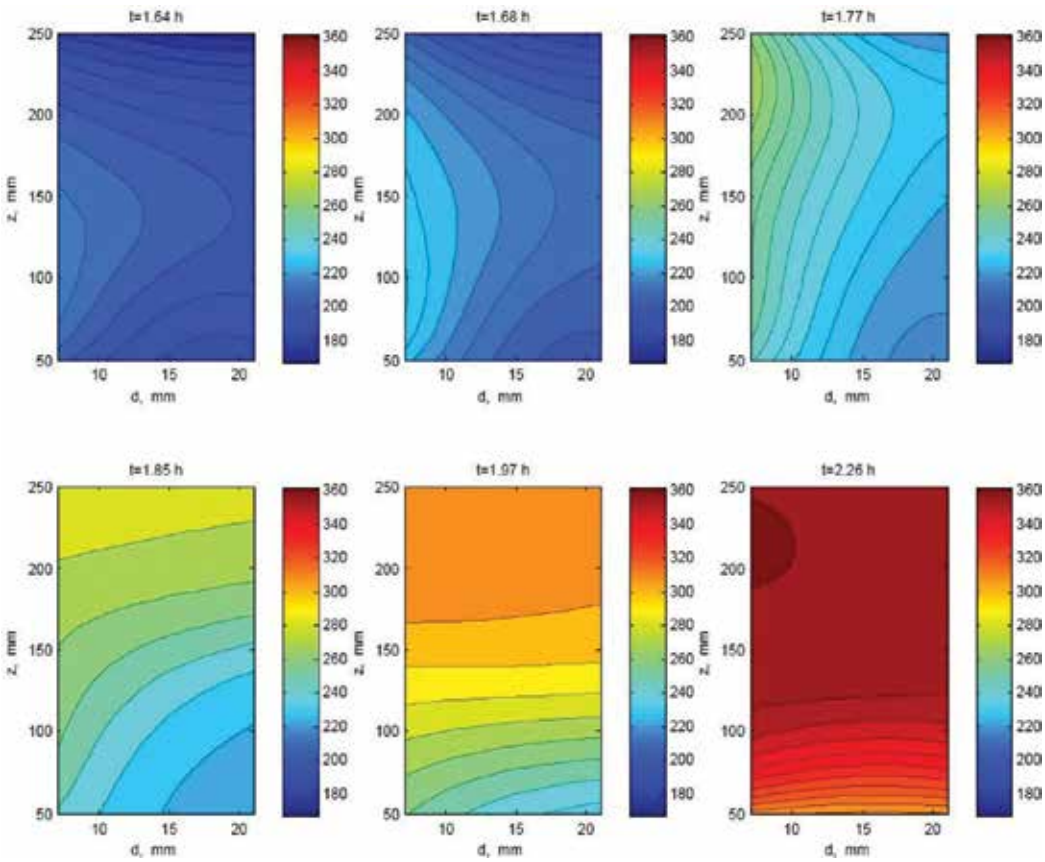


**Figure 6.** Temperature contour lines inside the reactor for 6 different times during the melting process. d(mm) is the distance from the wall heated by electrical heater and z(mm) is the height.

- Isotherm at 300°C for 3 h 20 min.
- The cooling down of the system from 300 to 180°C was by natural convection at room temperature (after approximately 5 h). During the cooling down phase, the PCM solidified within the same range of temperature.

Only the melting process was taken into consideration, the temperature contour lines inside the reactor are described in **Figure 6**. The melting process started after 1 h 46 min, and all of the experimental temperature data are reported in function of d and z for six different times as the fusion took place. At 1 h 38 min, the PCM was solid, and shortly thereafter, it started to melt; at 1 h 45 min, the solid phase started to collapse. Five minutes later, the solid phase was bound at the bottom right. After 2 h, it was completely liquid and homogenization by convection started, which was in turn induced by internal temperature gradients. At 2 h 15 min, the PCM homogenized by simple conduction with the presence of a convective cell at the top of the reactor. Moreover, the liquid phase pushed the solid downward, and the heat flux is orthogonal to the temperature contour lines.

## 4. Experimental tests on simple LHTES

An experimental system (**Figure 7a**), whose operating temperature varies in the range 150–300°C, was installed in ENEA CR Casaccia to carry out a cognitive survey of the involved phenomena. It consists of a series of stainless steel cylinders (**Figure 8a**) able to contain about 2.5 l of material, an heating/cooling circulator to handle thermal oil used as transfer fluid to charge and discharge it, four electro-valves to allow different oil circulations, a flowmeter, as well as 32 thermocouples to detect the temperature evolutions. The thermocouples inside the cylinder (**Figure 7b**) were equally spaced both axially and radially in such a way that they have a homogeneous temperature record in order to properly analyze their developments within the material. Eventually, a SW interface, based on LabView®, permits to control the system also in remote. The pipe, where the oil (Therminol 66) flows, together with the cylinder containing it, is a shell and tube type exchanger. In order to study the effect of the exchange surface, the external area of the tube in the cylinder can be plain or finned (**Figure 8b**). These cylinders were then insulated with 10 cm of Rockwool and covered by an aluminum sheet (**Figure 8c**).

A thermocryostat Julabo® HT30M1CU ensures the heating and cooling, as well as the handle of the oil thanks to an integrated centrifugal pump, which allows a volume flow rate up to 11 l/min, ensuring a turbulent flow. This equipment, with a 3 kW heating power and a 15 kW cooling power, is able to heat a thermal fluid up to 400°C, but, in our case, the oil was wormed up to 300°C to avoid its cracking. Four kinds of tests were carried out, each one using three cylinders in series of same type:

1. PCM in the cylinder with plain exchanger tube inside;
2. PCM in the cylinder with finned exchanger tube inside;

3. NEPCM (PCM doped with 1%wt of nanoparticles, 20–200 nm, of $SiO_2$-$Al_2O_3$) in the cylinder with plain exchanger tube inside;
4. NEPCM in the cylinder with finned exchanger tube inside;

Every test has been conducted 2–3 times to verify the repeatability of the results. During the tests, the thermocryostat was programmed in order to allow the oil to ensure the following temperature trend, where seven distinct phases can be clearly identified: (a) heating phase from room temperature to 200°C (1 h), (b) maintaining temperature at 200°C (10 h), (c) heating phase from 200 to 280°C (1 h), (d) charging phase at 280°C (8 h), (e) cooling phase from 280 to 150°C, (f) system discharging phase at 150°C (8 h), and finally, (g) cooling phase (4 h). **Figure 9** shows the temperature evolutions in the middle section of a cylinder (**Figure 7b**). In case of test with more cycles, the phases c-d-e-f were replicated (**Figure 10**).

A comparison between tests 1 and 2 points out that, in the test using finned tube as exchanger, the temperature trend of the HTF in the zones near the exchanger (blue line) is closer to the oil in the tube. Thus, it shows a better thermal exchange, surely due to the kind of exchange surface;

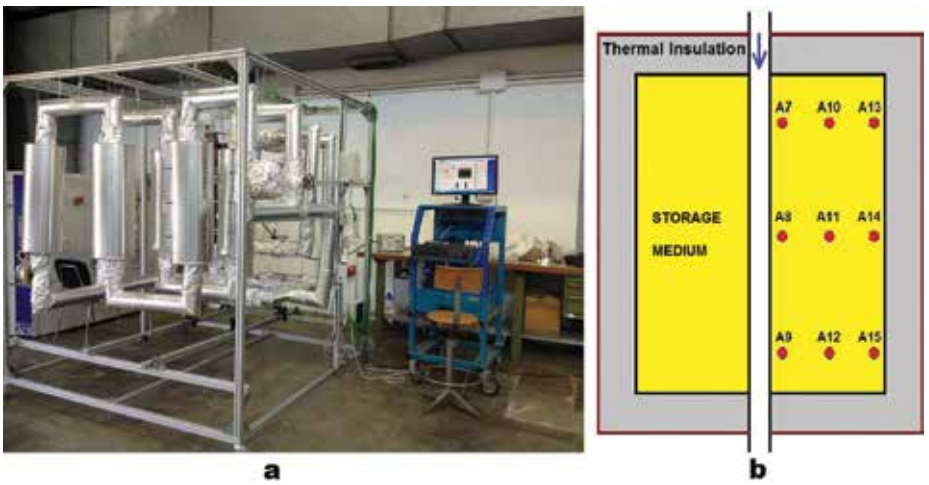


**Figure 7.** ATES plant (a) and thermocouple positioning inside a reference cylinder (b).

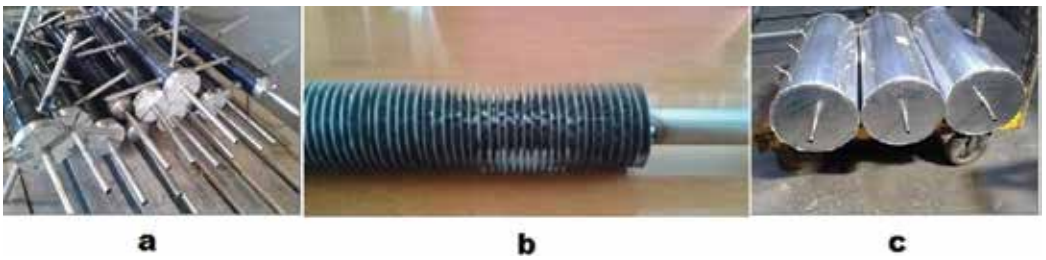


**Figure 8.** LHTES shell and tube configuration: (a) elementary systems; (b) finned tube; (c) complete systems.

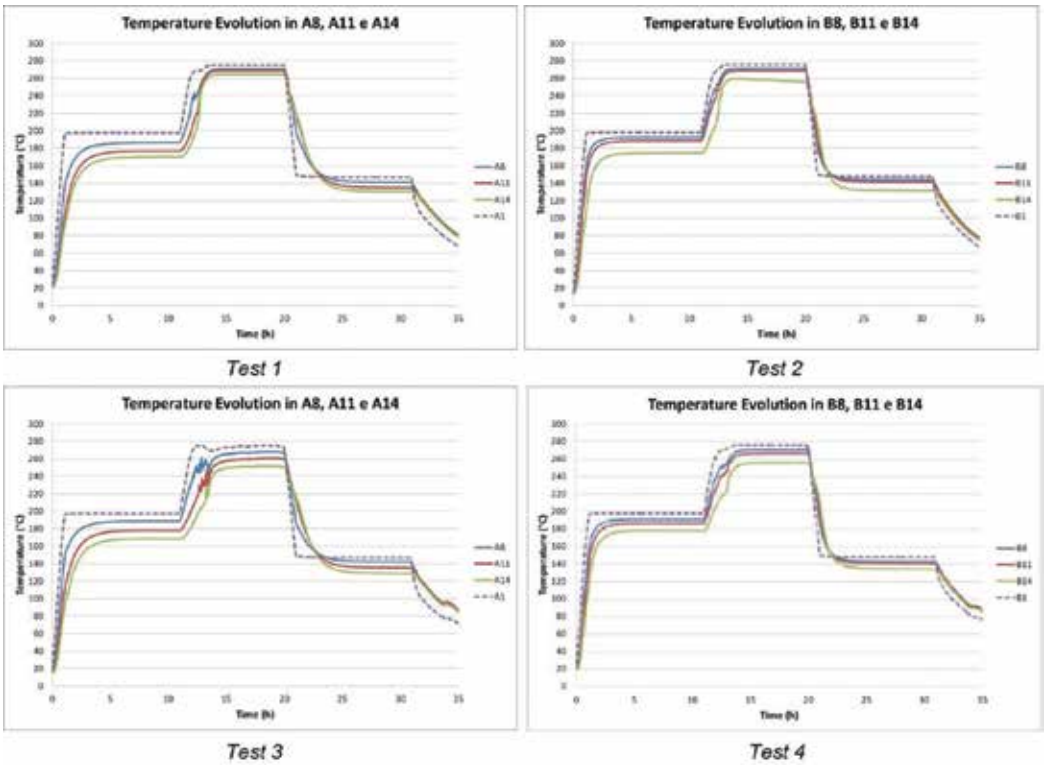


**Figure 9.** HSM temperatures evolution in the middle section of the first TES [42].

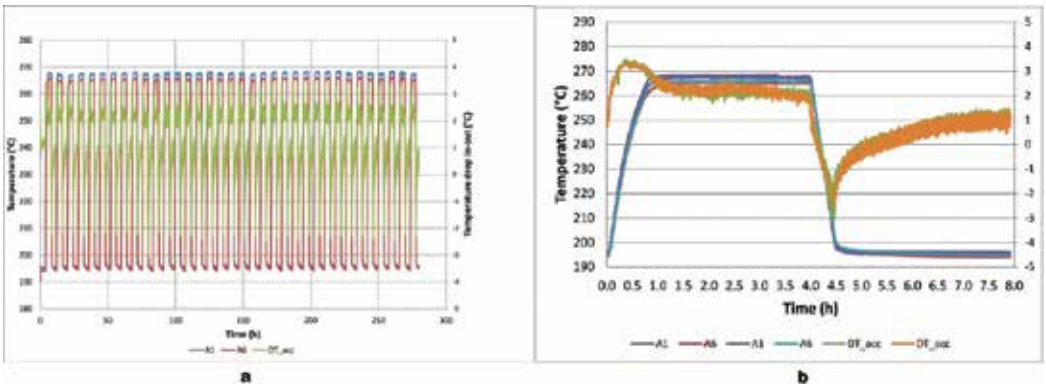


**Figure 10.** (a) Input (A1) and output (A6) temperature evolution and temperature drop in storage system and (b) temperature in-out HTF and their difference.

nevertheless, the temperature gradient increases, as it goes to the peripheral areas, which means a worse heat absorption within the medium. This phenomenon could be explained also by the Agyenim observations, in fact he claims [9]: "*Phase change problems, first treated as pure conduction controlled, has in recent times moved to a different level of complexity with added convection in the*

*melt being accounted for*". This phenomenon was not detected, in general, if finned tubes were used (test 2 and 4), probably for the physical limitations of the fins. These convective flows, however, were not found even in the NEPCM with plain exchanger tube, as it can be easily seen by observing test 3, where the green line is more distant from the others than in test 1. In this case, the presence of nanoparticles significantly increases the viscosity [9, 43, 44] of the fluid and probably inhibits the starting of the abovementioned flows [40]. Thus, we can affirm that, when the PCM is in liquid phase and there are no physical limitations (i.e. with plain tubes), the low thermal conductivity ($\lambda$) and diffusivity ($\alpha = \lambda(\rho c_p)^{-1}$) are counterbalanced by the start of convective flows thus improving the heat transfer. In NEPCM, despite a substantial invariance of the thermal diffusivity, the thermal capacity and the correlated thermal effusivity, $e = (\lambda\rho c_p)^{1/2}$, are increased. So, in this case, the storage material better exchanges thermal energy with its surroundings (e.g., exchanger) but not inside itself (depending on the diffusivity).The use of finned tubes highlights the promotion of the thermal conductivity, and so the charging and discharging times are lower and substantially independent from the storage medium. It is worth to notice that finned tubes make discharge rate faster because the insulation effect, due to the salt solidification on the wall of the exchanger tube, is compensated by the action of the fins. They in fact improve the thermal exchange for the increased surface. In any case, the TES system with NEPCM and finned tubes through the greater heat capacity, coupled with the lower discharge times, allows the system to deliver a higher average project power.

Cyclability tests (**Figure 10a**) performed on the NEPCM showed the substantial invariance of the storage medium behavior along the cycles. **Figure 10b**, in particular, emphasizes the perfect overlap of the temperature differences between inlets and outlets at 10th and 30th cycle. This makes it well to hope that nanostructured material keeps its features in time.

## 5. Numerical analysis on LHTES thermal behavior

The correct evaluation of the physical phenomena, that are at the base of the LHTES systems, is crucial for the design of optimized LHTES systems. Since computational fluid dynamics (CFD) models to simulate the thermofluid dynamics behavior of the LHTES system is essential for a good design of these systems, in this section, two models are briefly described. They were developed, by the use of COMSOL Multiphysics® software, ver. 5.2, to simulate the heat storage process for two different geometrical configurations.

Two different geometrical configurations were considered for the LHTES system. In the first one (Model 1), the heat exchange between the heat transfer fluid, oil, and the PCM, "solar salts" ($NaNO_3$-$KNO_3$), occurs through tubes, whose outer wall is smooth. In the second geometry (Model 2), the tubes have a series of transversal fins on the outer surface, so as to improve the thermal exchange with the PCM. In particular, it was considered a section of steel tube of external diameter of 16 mm, thickness 1 mm, and length 500 mm, surrounded by a tubular crown of PCM of external diameter 70 mm. In the finned configuration, a series of transversal fins of 1 mm thickness and 10 mm height were inserted on the outer surface of the tube and placed at constant interval of 50 mm. Both systems have axial symmetry, and so two 2-D axial symmetry models have been made. Furthermore, since the comparison of the thermofluid

dynamic behavior of PCM is the most important issue, only this material has been simulated. **Figure 11** shows the two models with a mesh detail.

The PCM was modeled as a constant-density fluid, and the buoyancy force was simulated by inserting the vertical component of a volume force equal to $\rho \cdot g \cdot \alpha \cdot (T - T_0)$, where $\rho$ is the density, g is the gravity acceleration, and $\alpha$ is the thermal expansion coefficient at the reference temperature $T_0$. The phase change condition has been simulated through the use of the liquid fraction ($\beta$), defined as: $\beta = 0$ for $T \leq T_{sol}$, $\beta = (T - T_{sol})/(T_{liq} - T_{sol})$ for $T_{sol} < T < T_{liq}$ and $\beta = 1$ for $T \geq T_{liq}$; where $T_{sol}$ is the temperature at which the solid material begins the liquefaction process, and $T_{liq}$ is the temperature at which the material has completed the liquefaction process. The fluid-dynamic behavior of phase change is simulated by inserting the dissipative term $F = [(1-\beta)^2/(\beta^3 + \varepsilon)] \cdot A_{mush} \cdot u$ in the equation of conservation of momentum; where $\varepsilon$ is a very small number (0.001), introduced in the equation to avoid division for zero as $\beta = 0$, $A_{mush}$ is the "mushy zone constant", equal to 100,000 kg/(m$^3$s), and u is the velocity of the fluid. The thermodynamic behavior associated with absorption and release of latent heat ($L_{fus}$) has been simulated by adding, in the transition zone between $T_{sol}$ and $T_{liq}$, to the specific heat of PCM the term $L_{fus}/(T_{liq} - T_{sol})$. The external walls have been simulated as adiabatic surfaces, while the wall corresponding to the surface of the steel tube has been considered as a temperature-controlled wall in both models. The temperature evolution on this wall provides a first linear rise step, from the initial minimum temperature of 200°C to the maximum temperature of 250°C in 1 h and a subsequent step at the maximum temperature for 3 h. Then, it follows a linear descent ramp from the maximum value to the minimum temperature value in 1 h and a step at the minimum temperature for 3 h. The total time of the simulated test is 8 h. **Figure 12** shows the distributions of liquid fraction of PCM, for both models, at time t = 3900 s, and **Figure 13** shows the velocity in the complete models and in their upper part always at t = 3900 s.

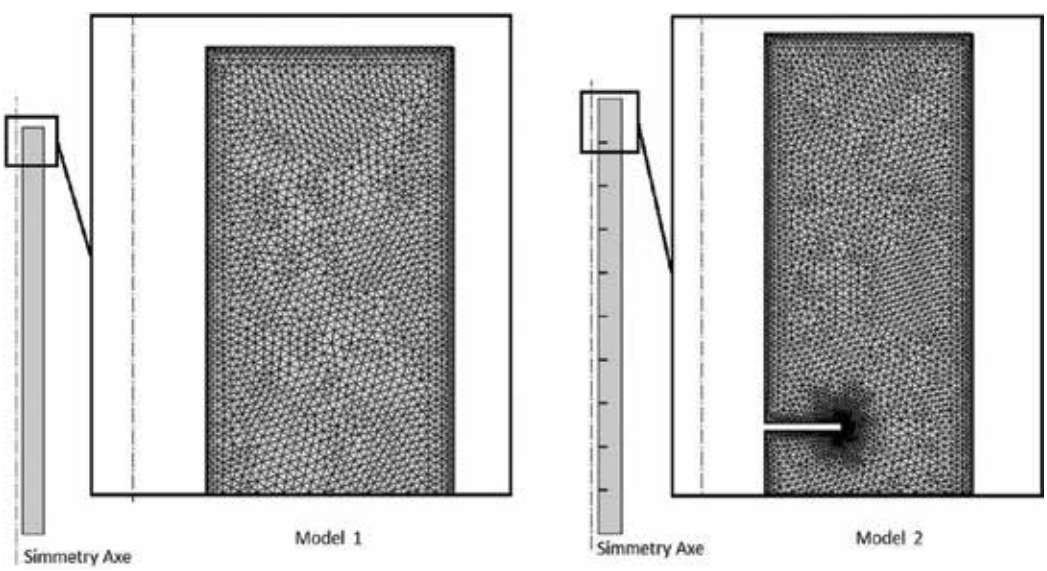


**Figure 11.** CFD models with a mesh detail.

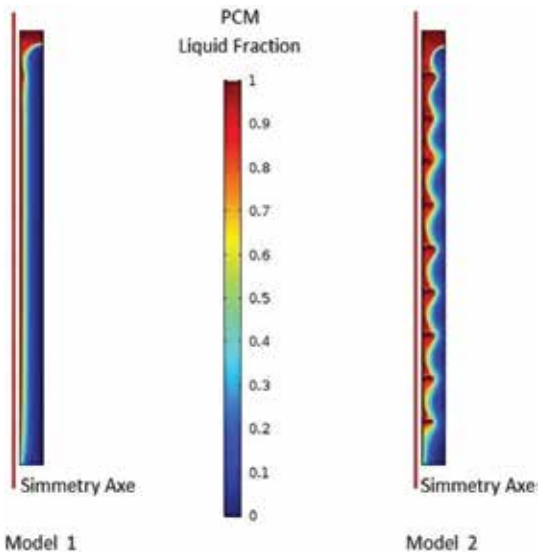


**Figure 12.** PCM liquid fraction at t = 3900 s.

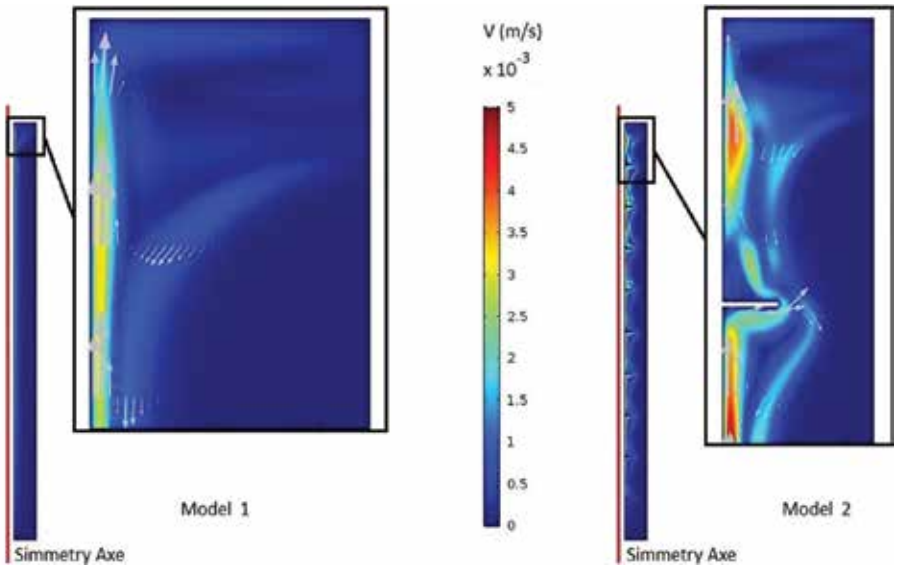


**Figure 13.** Velocity at t = 3900 s.

**Figure 14** shows the comparison between the time evolutions of the melted PCM in the two simulations during the entire charge-discharge cycle. **Figure 15** shows the comparison between the time evolutions of the energy stored by the system in the two models. For comparison, the energy is reported as a percentage of the total energy that can be stored in each of the two systems.

Comparing the results obtained by the two CFD simulations, it is possible to see how the presence of the fins on the outer surface of the steel tube strongly increases the efficiency of the system.

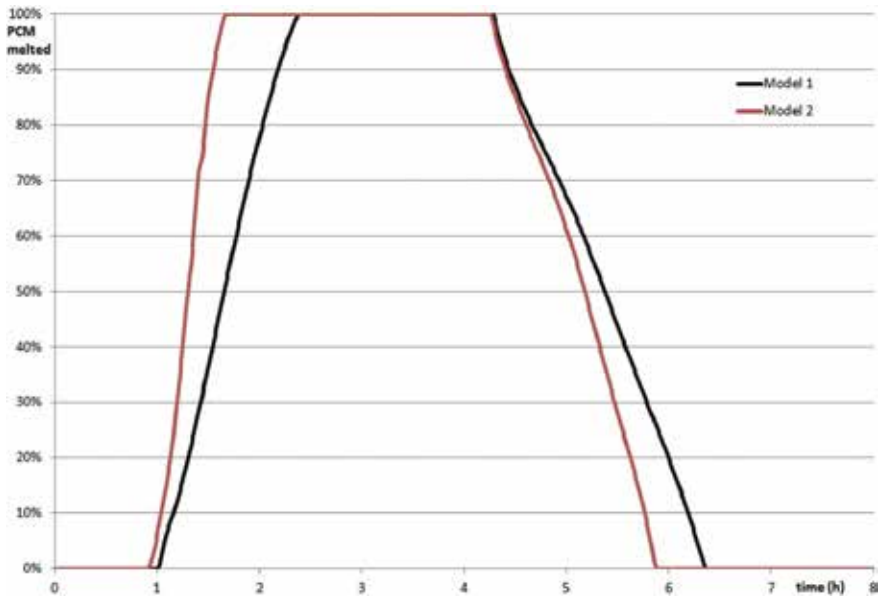


**Figure 14.** Time evolution of melted PCM.

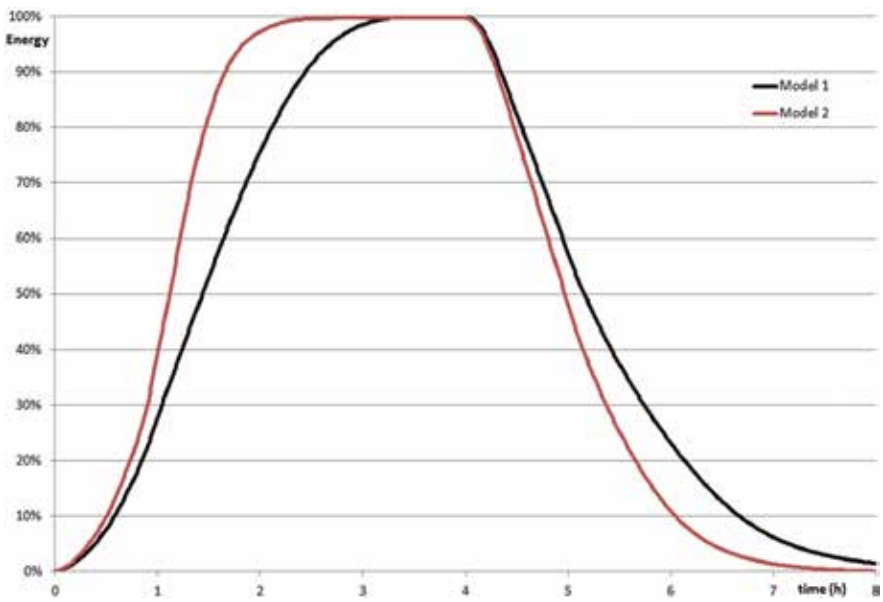


**Figure 15.** Time evolution of stored energy.

## 6. Conclusions and future developments

Thermal energy storage is a key technological issue to have an efficient use of the energy and reduce the carbon dioxide emissions and greenhouse effect. Latent heat storage offers

the possibility of designing much smaller TES systems and thus decreasing the cost of stored energy. However, to develop an efficient LHTES system is necessary to select or synthetize an appropriate heat storage material (PCM) with high thermal properties and to increase the HTF-PCM heat exchange, actually limited by the PCM low thermal conductivity/diffusivity. In particular, it is worth to pay attention to the selection of the materials in order to have good thermal properties for storing a large density of energy. For this purpose, a proper synthesis of new PCMs with increased thermal properties by adding little amount of nanoparticles (NEPCMs) can be convenient. In addition, the heat exchange surface plays an important role through the introduction of suitable thermal conductivity promotion systems, and so its design must be well evaluated and optimized, even in the light of the possible exploitation of the development of convective flows inside the PCM during the solid-liquid phase change. Both experimental and theoretical analyses to deepen these phenomena are necessary, and at this purpose, an experimental facility called ATES was developed by ENEA to take into account these phenomena and produce data for elaborating numerical analysis to carefully analyze the advantages and disadvantages of the various solutions and design innovative LHTES systems.

The study on the heat storage materials and heat exchange mode has allowed to obtain some useful indications on the LHTES design and optimization. It should take advantage by the presence of convective flows and conductivity promotion systems to facilitate the heat exchange. Instead, the use of NEPCM as a storage medium, useful to maximize the stored energy density and realize compact systems, makes necessary to improve its thermal diffusivity: this could be done by adding carbon-based nanoparticles to the PCM because they show a high thermal conductivity. Among these, carbon nanotubes (CNTs) and graphene nanoplatelets (GNP) can be used.

These will be the main research topics for the development of new concepts of LHTES.

## Acknowledgements

The authors would like to acknowledge the 2014 Annual Research Plan of the Electric System Research Program (RSE) of the Italian Ministry of Economic Development and the EU through the 7th FP in the frame of the STAGE-STE Project (Ctr. Nr. 609837) for the financial support of this work.

## Author details

Adio Miliozzi[1]*, Raffaele Liberatore[1], Daniele Nicolini[1], Manila Chieruzzi[2], Elisabetta Veca[1], Tommaso Crescenzi[1] and Luigi Torre[2]

*Address all correspondence to: adio.miliozzi@enea.it

1 ENEA, Italian National Agency for New Technologies, Energy and Sustainable Economic Development, Casaccia Research Centre, Rome, Italy

2 Civil and Environmental Engineering Department, University of Perugia, Terni, Italy

## References

[1] Miliozzi A, Liberatore R, Giannuzzi GM, Veca E, Nicolini D, Lanchi M, Chieruzzi M. ENEA research and innovation on Thermal Energy Storage for CSP plants. In: 16th CIRIAF National Congress, Sustainable Development, Human Health and Environmental Protection; April 7-9, 2016; Assisi (Italy). 2016

[2] EU Commission. Climate strategies & targets. 2030 Climate & energy framework. Available from: https://ec.europa.eu/clima/policies/strategies/2030_en [Accessed: Feb 2017]

[3] EU Commission. Climate strategies & targets. 2020 Climate & energy package. Available from: https://ec.europa.eu/clima/policies/strategies/2020_en [Accessed: Feb 2017]

[4] Miliozzi A, Chieruzzi M, Torre L, Kenny JM. Nanofluids with enhanced heat transfer properties for thermal energy storage. In: Tiwari A, Mishra YK, Kobayashi H, Turner APF, editors. Intelligent Nanomaterials. 2nd Ed. Hoboken, NJ, USA: John Wiley & Sons, Inc.; 2016. p. 295-360. ISBN: 978-1-119-24248-2

[5] Salomoni VA, Majorana CE, Giannuzzi GM, Miliozzi A, Nicolini D. New trends in designing parabolic trough solar concentrators and heat storage concrete Systems in Solar Power Plants. In: Rugescu RD, editor. Solar Energy. InTech; 2010. p. 267-292. ISBN: 978-953-307-052-0

[6] Chieruzzi M, Veca E Miliozzi A, Torre L. Phase change materials for latent heat storage: research and future trend. In: 16th CIRIAF National Congress, Sustainable Development, Human Health and Environmental Protection; April 7-9, 2016; Assisi (Italy). 2016

[7] Fleischer AS, editor. Thermal Energy Storage Using Phase Change Materials - Fundamentals and Applications. SpringerBriefs in Applied Sciences and Technology. New York, Dordrecht, London: Springer Heidelberg; 2015. 94 p. DOI: 10.1007/978-3-319-20922-7

[8] Liu M, Saman W, Bruno F. Review on storage materials and thermal performance enhancement techniques for high temperature phase change thermal storage systems. Renewable and Sustainable Energy Reviews. 2012;**16**:2118-2132

[9] Agyenim F, Hewitt N, Eames P, Smyth M. A review of materials, heat transfer and phase change problem formulation for latent heat thermal energy storage systems (LHTESS). Renewable and Sustainable Energy Reviews. 2010;**14**:615-628

[10] Jegadheeswaran S, Pohekar SD. Performance enhancement in latent heat thermal storage system: A review. Renewable and Sustainable Energy Reviews. 2009;**13**:2225-2244

[11] Steinmann WD, Laing D, Tamme R. Latent heat storage systems for solar thermal power plants and process heat applications. Journal of Solar Energy Engineering. 2010;**132**:1-5

[12] Tamme R, Bauer T, Buschle J, Laing D, Muller-Steinhagen H, Steinmann WD. Latent heat storage above 120°C for applications in the industrial process heat sector and solar power generation. International Journal of Energy Research. 2008;**32**:264-271

[13] Michels H, Pitz-Paal R. Cascaded latent heat storage for parabolic trough solar power plants. Solar Energy. 2007;**81**(6):829-837

[14] Kenisarin MM. High-temperature phase change materials for thermal energy storage. Renewable & Sustainable Energy Reviews. 2010;**14**(3):955-970

[15] Shin D, Banerjee D. Enhanced specific heat of silica Nanofluid. Journal of Heat Transfer-Transactions of the Asme. 2011;**133**(2):024501(4 pages)

[16] Shin D, Banerjee D. Enhanced specific heat capacity of Nanomaterials synthesized by dispersing silica nanoparticles in eutectic mixtures. Journal of Heat Transfer-Transactions of the Asme. 2013;**135**(3)

[17] Shin D, Banerjee D. Effects of silica nanoparticles on enhancing the specific heat capacity of carbonate salt eutectic (work in progress). The International Journal of Structural Changes in Solids. 2010;**2**(2):25-31

[18] Jo B, Banerjee D. Enhanced specific heat capacity of molten salt-based nanomaterials: Effects of nanoparticle dispersion and solvent material. Acta Materialia. 2014;**75**:80-91

[19] Shin D, Banerjee D. Enhancement of specific heat capacity of high-temperature silica-nanofluids synthesized in alkali chloride salt eutectics for solar thermal-energy storage applications. International Journal of Heat and Mass Transfer. 2011;**54**(5-6):1064-1070

[20] Lu M, Huang C. Specific heat capacity of molten salt-based alumina nanofluid. Nanoscale Research Letters. 2013;**8**:292(7 pages)

[21] Dudda B, Shin D. Effect of nanoparticle dispersion on specific heat capacity of a binary nitrate salt eutectic for concentrated solar power applications. International Journal of Thermal Sciences. 2013;**69**:37-42

[22] Chieruzzi M, Cerritelli GF, Miliozzi A, Kenny JM. Effect of nanoparticles on heat capacity of nanofluids based on molten salts as PCM for thermal energy storage. Nanoscale Research Letters. 2013;**8**(1):448

[23] Chieruzzi M, Miliozzi A, Crescenzi T, Torre L, New Phase KJMA. Change material based on potassium nitrate with silica and alumina nanoparticles for thermal energy storage. Nanoscale Research Letters. 2015;**10**(1):984

[24] Lasfargues M, Geng Q, Cao H, Ding Y. Mechanical dispersion of nanoparticles and,its effect on the specific heat capacity of impure binary nitrate salt mixtures. Nanomaterials. 2015;**5**(3):1136-1146

[25] Chieruzzi M, Cerritelli GF, Miliozzi A, Kenny JM, Torre L. Heat capacity of nanofluids for solar energy storage produced by dispersing oxide nanoparticles in nitrate salt mixture directly at high temperature. Solar Energy Materials and Solar Cells. 2017;**167**:60-69

[26] Khodadadi JM, Babaei LFH. Thermal conductivity enhancement of nanostructure-based colloidal suspensions utilized as phase change materials for thermal energy storage: A review. Renewable and Sustainable Energy Reviews. 2013;**24**:418-444

[27] Shin D, Banerjee D. Enhanced thermal properties of SiO2 nanocomposite for solar thermal energy storage applications. International Journal of Heat and Mass Transfer. 2015;**84**:898-902

[28] Chieruzzi M, Miliozzi A, Crescenzi T, Kenny JM, Torre L. Synthesis and characterization of nanofluids useful in concentrated solar power plants produced by new mixing methodologies for large-scale production. Journal of Heat Transfer. 2018;**140**(4):042401(13 pages)

[29] Laing D. Storage development for direct steam generation power plants. In: Parabolic Trough Technology Workshop; March 9, 2007, Golden CO, USA. 2007

[30] Fan L, Khodadadi JM. Thermal conductivity enhancement of phase change materials for thermal energy storage: A review. Renewable and Sustainable Energy Reviews. 2011;**15**:24-46

[31] Steinmann WD, Tamme R. Latent heat storage for solar steam systems. Journal of Solar Energy Engineering. 2008;**130**:1-5

[32] Steinmann WD, Laing D, Tamme R. Development of PCM storage for process heat and power generation. Journal of Solar Energy Engineering. 2009;**131**:1-4

[33] Agyenim F, Eames P, Smyth M. A comparison of heat transfer enhancement in a medium temperature thermal energy storage heat exchanger using fins. Solar Energy. 2009;**83**:1509-1520

[34] Agyenim F, Eames P, Smyth M. Experimental study on the melting and solidification behaviour of a medium temperature phase change storage material (Erythritol) system augmented with fins to power a LiBr/H2O absorption cooling system. Renewable Energy. 2011;**36**:108-117

[35] Jones BJ, Sun B, Krishnan S, Garimella SV. Experimental and numerical investigation of melting in a cylinder. International Journal of Heat and Mass Transfer. 2006;**49**:2724-2738

[36] Tan FL. Constrained and unconstrained melting inside a sphere. International Communication of Heat and Mass Transfer. 2008;**35**:466-475

[37] Fornarelli F, Camporeale SM, Fortunato B, Torresi M, Oresta P, Magliocchetti L, Miliozzi A, Santo G. CFD analysis of melting process in a shell-and-tube latent heat storage for concentrated solar power plants. Applied Energy. 2016;**164**:711-722

[38] Guo S, Li H, Zhao J, Li X, Yan J. Numerical simulation study on optimizing charging process of the direct contact mobilized thermal energy storage. Applied Energy. 2013;**112**:1416-1423

[39] Archibold AR, Rahman MM, Goswami DY, Stefanakos EK. The effects of radiative heat transfer during the melting process of a high temperature phase change material confined in a spherical shell. Applied Energy. 2015;**138**:675-684

[40] Sciacovelli A, Gagliardi F, Verda V. Maximization of performance of a PCM latent heat storage system with innovative fins. Applied Energy. 2015;**137**:707-715

[41] Seddegh S, Wang X, Numerical HAD. Investigation of heat transfer mechanism in a vertical shell and tube latent heat energy storage. Applied Thermal Engineering. 2015;**87**:698-706

[42] Miliozzi A, Liberatore R, Crescenzi T, Veca E. Experimental analysis of heat transfer in passive latent heat thermal energy storage systems for CSP plants. Energy Procedia. 2015;**82**:730-736

[43] Goharshadi EK, Ahmadzadeh H, Samiee S, Hadadian M. Nanofluids for heat transfer enhancement–a review. Physical Chemistry Research. 2013;**1**:1-33

[44] Bashirnezhad K, Bazri S, Safaei MR, Goodarzi M, Dahari M, Mahian O, Dalkiliça AS, Wongwises S. Viscosity of nanofluids: A review of recent experimental studies. International Communication of Heat and Mass Transfer. 2016;**73**:114-123. DOI: 10.1016/j.icheatmasstransfer.2016.02.005

Chapter 2

# High Temperature Energy Storage (HiTES) with Pebble Heater Technology and Gas Turbine

Dragan Stevanovic

Additional information is available at the end of the chapter

http://dx.doi.org/10.5772/intechopen.75093

**Abstract**

In modern power systems with high penetration of renewable energy generation, the energy storage is very important, not just for the load control for quite different time periods, but even in the frequency control. If it is missing, the anomalies occur, like the stagnant $CO_2$ emission, export of the overproduction under unfavourable conditions, curtailments of wind-mills and/or negative market prices for electricity. The new technology is a high temperature thermal electric energy storage. It is based on the combination of three state-of-the-art technologies: pebble-heater, radial gas-turbine and electric resistive heating. Due to very high temperature (1100°C), low exergy losses during the heat transfer and water injection in the gas-turbine process, the round-trip efficiency is high even with nowadays available components. With some moderate improvements of the gas-turbine it could be increased towards 60%, even at 2MW low generator capacity. The discharge time is 10 h; due to the modular design, it may increase to 20 or even 30 h. The analysis of LCOES (levelized cost of electricity storage) shows that even today that system could be used in a viable way in countries with high insolation or on sites where an autarchic power supply may replace expensive market electricity.

**Keywords:** energy storage, high temperature, pebble-heater, radial gas turbine, hot air turbine, resistive heating, power-to-heat-to-power, LCOES

## 1. Introduction

Energy storage is used to store an overproduction of electricity and to use it again in periods of higher power demand. The pumped hydro storage is one of the oldest systems, especially for mass storage, which has been in use for many years. Previously it was used only for load control, that is, for smoothening the electricity consumption, mostly between day and night,

in systems with higher capacities of base-load plants, like coal and nuclear power plants. Instead of reducing their output and entering into the zone of lower process efficiency, their overproduction was stored, always enabling the optimal operation parameters. Those were well-defined periods of time, well planned and without rush load changes.

### 1.1. Influence of renewable power generation

In the modern systems with high penetration of renewable energy generation, like from wind and solar, the situation has been drastically changed. Not the consumption, but the generation is now what has to be smoothened. Those changes may be very fast and may last very long, even several days or weeks. It means the modern power storage devices have to participate in the load control for quite different time periods but additionally even in the frequency control.

The problems with the intermittent generation do not start immediately after the installation of the first unit. Big power generation systems may absorb easily small disturbances in the system. It depends on many factors, but the experience shows that with about 20% penetration of the intermittent power generation, big problems occur. Then there is a strong need for higher usage of energy storage systems, together with other measures, like new grids, demand response, etc. Otherwise, curtailment or export under unfavourable conditions has to take place. However, it is important to understand the difference between the effects of new additional grids and the energy storage systems: With a grid, it is possible to transport a local power overproduction to some other areas with higher demand at that moment; however, a time shift, like with storage systems, is not possible. Moreover, new big grids implicitly lead to a more centralised generation, which was not the idea with the introduction of renewable power generation. Therefore, the best long-term solutions are energy storage systems that support distributed power generation.

### 1.2. Examples for the need of energy storage

In Germany, which is one of the leaders in the renewable power generation with some 33% in 2015, the opinion [1] was that in the next 10–20 years, there is no need for energy storage. That will change first when a very high share of renewable power generation (even 90%!) is reached. Meanwhile, in the last years, many anomalies that appeared on the market demonstrated that this is not the case. The electricity price on the stock market is falling, as the share of renewables is increasing. On the other hand, prices for industry and households increase with a rate of more than 5% per year. The net export is steadily growing but brings ever smaller income. The most important and the most absurd fact is that, in spite of all efforts with increasing the usage of renewable generation, the emission of $CO_2$ is more or less stagnant! That infliences fast changing in the previous opinion: it is now recognised that energy storage, together with new grids expansion, is the inevitable component of the German "Energiewende". That case of Germany was described in detail in [2], showing that 40% of intermittent renewable electricity cannot be used domestically and has to be exported. In 2016 that trend has continued, as presented in [3]. Although the yearly increase of intermittent electricity was small (only 4.0 TWh), all of that increase had to be exported! On the other hand, the curtailment of many wind mills occurs very often, as the last option to get rid of the electricity overproduction. The need for energy storage in Germany is obvious.

California is the US state with the highest penetration of wind and solar power generation. Contrary to Germany, they have started thinking about and analysing the potential problems of intermittent generation much earlier. The "Duck Chart" was created by the California Independent System Operator to show that increasing solar generation paired with conventional base-load plants that cannot be turned off (e.g. nuclear and less flexible natural gas) can cause over-generation in the afternoons during certain months [4]. The chart shows that the shape of the net load curve begins to shift dramatically in 2015 due to increasing solar generation and there is potential for over-generation during the afternoons beginning in 2018. An especially big problem is a very fast ramping between 17 and 19 h (13.5 GW in 2 h!). To solve those potential problems, several measures were planned, like demand response, import/export, curtailment and energy storage. Being unfavourable measures, import/export and especially curtailment were minimised. Nowadays California is the area with the most installed energy storage systems, and several new projects are planned.

In some areas of Chile, there is a locally very high penetration of the solar power generation, based on photovoltaic systems. As the insolation is very high, the price of that electricity is low (<3 ₵ /kWh). However, every day at around noon, the market price goes into the negative area, as there are not enough consumers when the generation reaches its daily maximum. Therefore, there are some projects for energy storage facilities and some new generation facilities but based on concentrated solar power (CSP) with integrated molten salt storage.

Many countries with high insolation will be very soon in the same situation. In fact, many of them are waiting on a suitable solution for the energy storage in order to start a wide range of usage of solar power, which is a very competitive solution there.

### 1.3. Thermal energy storage

There are many technologies for energy storage. Some are suitable for long-term storage, the other for short-term and some of them even for the frequency control, with very fast response time. They are all using different principles, and therefore they have different advantages and disadvantages. Roughly, there are mechanical, chemical, electrical and thermal storage technologies.

Thermal energy storage is mostly famous for the molten salt facilities. They are used almost exclusively with the concentrated solar power (CSP) systems, where solar heat is stored and later used for power generation through the steam turbine cycle. The efficiency is about 32–36%, and the investment cost is still high. Due to the storage capacity of up to 10 h (some special cases), they are attractive, as that is the only available technology nowadays to store solar power for a longer period. There is also development to transform the electricity into heat and store it underground in some rocks or gravels (see the web presentation of Siemens [5]). Afterwards, that heat is used to generate electricity, again over a steam turbine cycle. In that case, the temperature is limited to 600°C. The HiTES system [6] has a considerably higher temperature: up to 1100°C. The leading idea is that the exergy of stored heat is much higher at elevated temperatures. The quality of heat at 600°C is about 65%, while at 1100°C it is already 80% [7]. That makes it possible to reach a higher round-trip efficiency, even with heat storage systems. That system is presented in more details in the next chapters.

## 2. Components of the HiTES system

**Hi**gh **T**emperature **E**nergy **S**torage (or shortly HiTES) is a new technology for energy storage based on three technologies that are state of the art:

- Pebble heater technology
- Radial gas turbine
- Electric resistive heating

Those three technologies are combined in a new system, which suits well for medium-term storage, from several minutes up to several days. Electricity is used to heat up the heat storage material (pebbles) in a high temperature pebble heater by electric resistance heaters, during periods with electricity overproduction. If there is a need for additional electricity, a gas turbine coupled with a generator will produce it from the stored high temperature heat.

### 2.1. Why high temperature?

It is a common truth that heat is the lowest form of energy. It means the electricity may be transformed into heat with high efficiency, but transforming heat into electricity will be coupled with high losses. However, temperature defines the quality of heat, as shown in **Figure 1** [8]. It is not the same if one transforms electricity to heat at 2000°C or at 100°C. Moreover, heat available at 10,000°C has higher exergy than the natural gas, for example. Therefore, the common opinion mentioned here at the beginning is not generally right, but depends strongly on temperature. That is the reason why the electricity transformation into high temperature heat has been selected in this storage process.

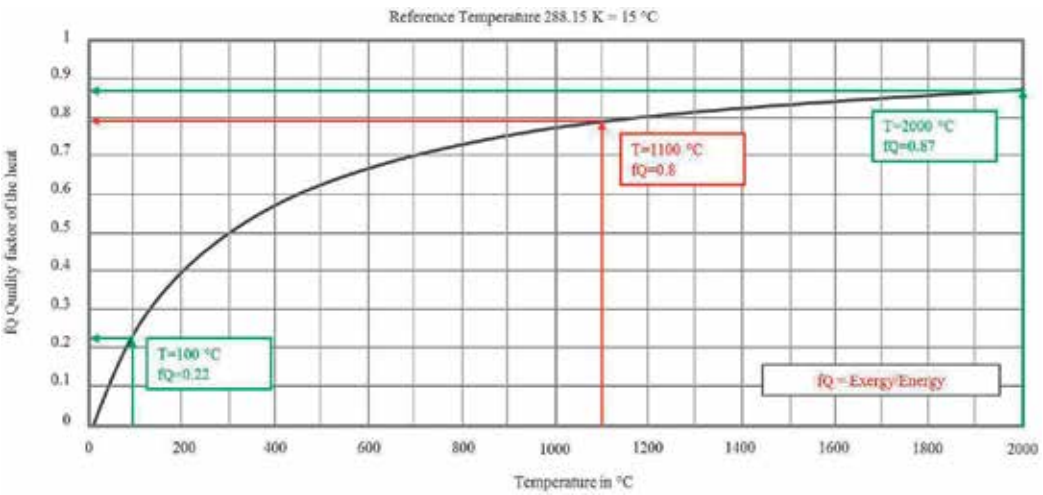


**Figure 1.** The thermodynamic quality factor of heat, indicating the fraction of exergy in the amount of energy (adapted from Klimstra [8]).

Material is the limiting factor—is not easy to realise, for example, 2000°C. In the case of HiTES, it is 1100°C: all available components are made of material that can withstand it, and the quality factor is still very high (0.8).

### 2.2. Why pebble heater technology?

The pebble heater technology has been selected as it is very suitable for high temperatures, and due to high heat exchange surface, it produces very low exergy losses. Such an example is presented in **Figure 2**. A heating gas enters the bed with 1350°C and has 160°C at the outlet. During the next phase, a gas which has to be heated (air in this case) has 90°C at the inlet and leaves the bed with 1280°C. The temperature difference between those two gases is only 70 K on both sides of the pebble bed. That gives an exergy efficiency of 95.2%. It is even less than 50 K in many applications. The recorded minimum was 15 K, leading to the exergy efficiency of above 98%.

Those characteristics make the pebble heater technology very efficient for the applications like thermal oxidizers (recuperation efficiency above 98% [9]), hot gas supply at temperatures above 1400°C (even $H_2$ has been preheated), steam superheating (1200°C) for some special chemical reactions, steel converters [10, 11], blast furnaces [12], regenerative burners [13], etc. For HiTES technology, the pebble heater is a component which is crucial for reaching high process efficiency. For more details about that technology, see Chapter 3.

### 2.3. Why radial gas turbine?

That type of gas turbine sets has been selected due to its extraordinary reliability recorded even in extreme conditions on oil rigs and gas fields, from sea platforms till Siberia. Despite small capacity (approx. 2 MW electric) and its simplicity, a modern design leads to

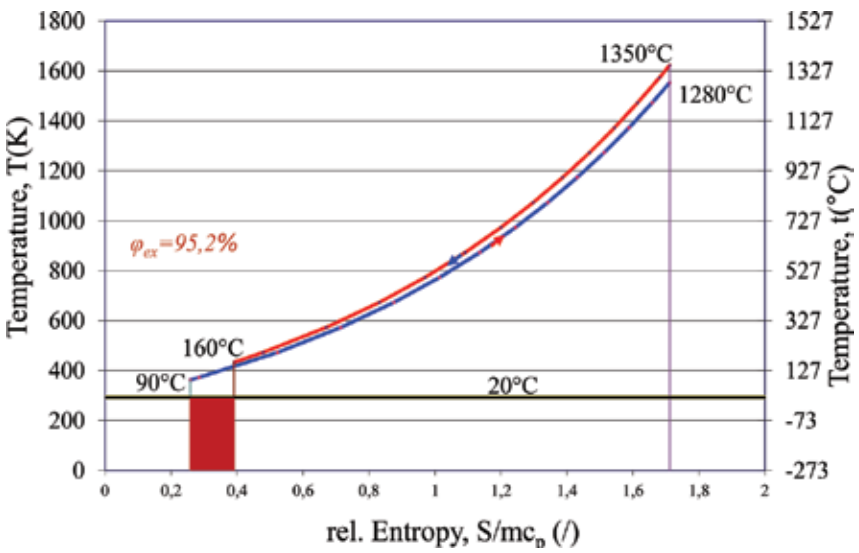


**Figure 2.** Entropy increase during the heat transfer in a pebble heater.

**Figure 3.** Rotor of a radial gas turbine with expander (left) and compressor (right) [14].

the efficiency of even 25% in a simple open cycle. They are very robust, have single shaft with cold end drive, have easy maintenance, have low lube oil consumption and have long inspection intervals. The models present on the market (produced by OPRA from the Netherlands and Dresser-Rand with its production facilities in Norway) have proven its abilities in much more than 1000 units built. The design for external firing, which is required for the HiTES system, is now also available. **Figure 3** [14] presents a modern all-radial design (expander, compressor and shaft).

## 3. Pebble heater

The name "pebble heater" is already known in the field of regenerative heat exchangers. It may operate at high temperatures for heating and cooling gaseous media by means of bulk material consisted of spherical balls, called pebbles. That is common for the previous and the new design of the pebble heater.

The most important difference is the flow direction: the bulk material is fixed between two vertical, concentric and permeable cylinders (hot and cold grid), so that the fluid flows radially. At the first sight, small difference results in further extraordinary advantages. As there is no danger of fluidization, the flow velocity may be increased, and smaller pebbles may be used. That improves dramatically the heat transfer, especially through very high ratio of surface to volume, that is, specific surface. With those characteristic it is easy to reach a thermal recuperation efficiency of 95%; even 98% has been achieved with a unit in operation. As a result, the exergy losses are small, and the temperature difference between two gases (heating and cooling) is as little as 20 K—all that at temperatures up to 1500°C!

That intensive heat transfer results in a temperature gradient as high as 2000 K/m. Therefore the bed of pebbles is thin, and the pressure drop stays low or acceptable. The units are compact, which lead to low investment cost—the most important fact for investors.

### 3.1. Physical description

Outside, the pebble heater is a cylindrical vessel. Inside, there are two permeable grids with a pebble bed fixed in between. The inner grid (hot grid) is always at high temperature. It is composed of high-quality ceramic bricks. Each brick has a hole that ends with a honeycomb segment, in order to prevent the pebble fluidization. Those bricks are tested up to 1500°C, first in an industrial scale pilot facility and later in tenths of industrial facilities. The improved quality of the honeycomb segments will enable higher temperatures, up to 1700°C, as required for some special applications.

The outer grid is on the cold side and therefore referred as the cold grid. It is constructed of a perforated steel plate. There is no possibility for pebbles to fluidize or circulate, as they are fixed between those two grids. The cold grid temperature is usually held under 250°C. In such cases, the material for the outer vessel may be a conventional steel. Moreover, the outer insulation is not required, only some touch protection in some cases. Indeed, as presented in blue in **Figure 4**, some fire-clay insulation is only required at the hot gas inlet/outlet (bottom) and for the so-called dome, which closes the hot grid on the top.

In the case of applications with very high temperatures, the bed of alumina pebbles (>99% $Al_2O_3$) is the best choice. They are very resistant to the thermal shocks, so that the temperature

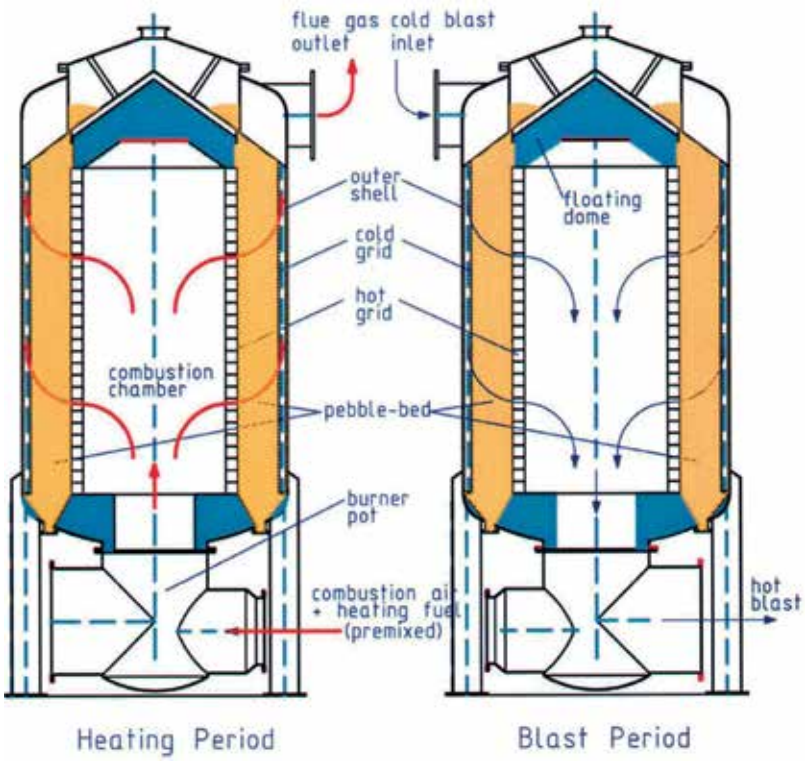


**Figure 4.** Pebble heater with radial design [12].

cycling of even over 400 K cannot cause any damage. In the case of less demanding applications, bulk materials like fire-clay balls or even river gravels are much cheaper solution.

The thermal expansion of the hot grid does not cause any sealing or stress problem, as it may expand together with the "floating" dome upwards freely; see **Figure 4**.

### 3.2. Operation of pebble heater

Being a regenerative heat exchanger, at least two units of pebble heater are required for a continuous operation. One unit is producing hot gas (blast), while one or more units are reheated. After a certain time, the reheated unit will switch to the blast phase, and the other unit will switch to the reheating phase. On that way a continuous supply of hot gas is secured.

The operation of pebble heater during those two phases is seen in **Figure 4**. In the case that the heating gas is a combustion product, the combustion takes place mainly in the chamber inside the hot grid. Flue gases enter the bed through the hot grid. Flowing radially through the bed, flue gases leave their heat to it and have a low temperature at the end of the bed. Cooled gases pass upwards, through the gap between the cold grid and the outer wall of the vessel, towards the exit.

When the bed is fully reheated, the burner stops, and the vessel is pressurised at the cold blast pressure. Then it enters and flows in opposite direction: first it distributes in the gap around the pebble bed and then passes through it. Heat is now transferred in reverse direction, from the pebbles to the gas. In the chamber inside the hot grid, the hot blast is collected and flows out through the hot blast main.

In some cases an existing waste hot gas may be used for reheating phase. Then there is no need for a burner, as the pebble heater recuperates the waste heat from that gas and uses it for preheating air or some other gas.

### 3.3. Mathematical modelling of pebble heater

To simulate the operation of such pebble heater with radial flow, the mathematical model has been developed, based on Crank-Nicholson numerical method [18].

The heater is axial-symmetric, and the upper and bottom walls are adiabatic, so the heat is transferred just in radial direction. Due to a very high specific surface available for the heat transfer (usually between 500 and 1000 $m^2/m^3$), the difference between gas and pebble temperature is almost negligible when compared to the temperature change during each phase. Vortmeyer and Schäfer have presented a so-called "homogeneous" model [15], which uses only one energy balance equation and gives good results in such cases. Originally, the equation of Vortmeyer and Schäfer describes a cylindrical pebble bed with axial flow. For the radial geometry, it was rewritten as follows:

$$\frac{1}{r}\frac{\partial}{\partial r}\left(r\,\Lambda_r\frac{\partial T}{\partial r}\right) = \frac{\partial}{\partial r}\left(m_o\,c_{Pf}\,T\right) + \left[(1-\psi)\,\rho_s\,c_s + \psi\rho_f\,c_{Pf}\right]\frac{\partial T}{\partial t} \tag{1}$$

with the following notation: $r$ is the radial coordinate; $t$ – time; $\Lambda_r$ – "effective" heat conductivity; $T$ – temperature; $m_o$ - mass flux of gas; $\Psi\psi$ - void fraction (i.e. bed porosity); $c_s$, $c_{Pf}$ – specific heat (solid and gas phase, respectively); $\rho_s$,$\rho_f$ – density (solid and gas phase, respectively).

All physical properties, including the "effective" heat conductivity, are functions of the temperature and indirectly of the radial coordinate, as temperature changes significantly with the radial position. Due to the change of the flow cross section with the radial coordinate, the mass flux of gas is also a function of the radial position. The "effective" heat conductivity in radial direction ($\Lambda_r$), which is introduced in this model, differs from the "classical" heat conductivity in the usual *Fourier* equation as it includes the effects of convection and radiation, besides the heat conductivity of fluid and solid. One can find several correlations for those terms in the literature. The correlations given by Bauer [16] and Till [17], which are valid up to a *Péclet* number of $Pe = 30$, are used here.

Eq. (1) is a partial differential equation of the second order. To solve it, one initial and two boundary conditions are required. The initial condition is some given temperature distribution over the bed radius. The boundary conditions are heat fluxes on the hot and cold end (i.e. hot and cold grid), which have to be defined.

As the "effective" heat conductivity and gas flux are not constant, there is not an analytical solution for Eq. (1). That type of *Fourier* equation may be effectively solved by using the Crank–Nicolson numerical method, as shown in [18]. That method is implicit, which is its main advantage, because it enables long time steps with good stability of the calculation process. Based on that method, a numerical code for simulation of the pebble heater operation has been developed, with typical results of the characteristic temperature profile through the bed given in **Figure 5**.

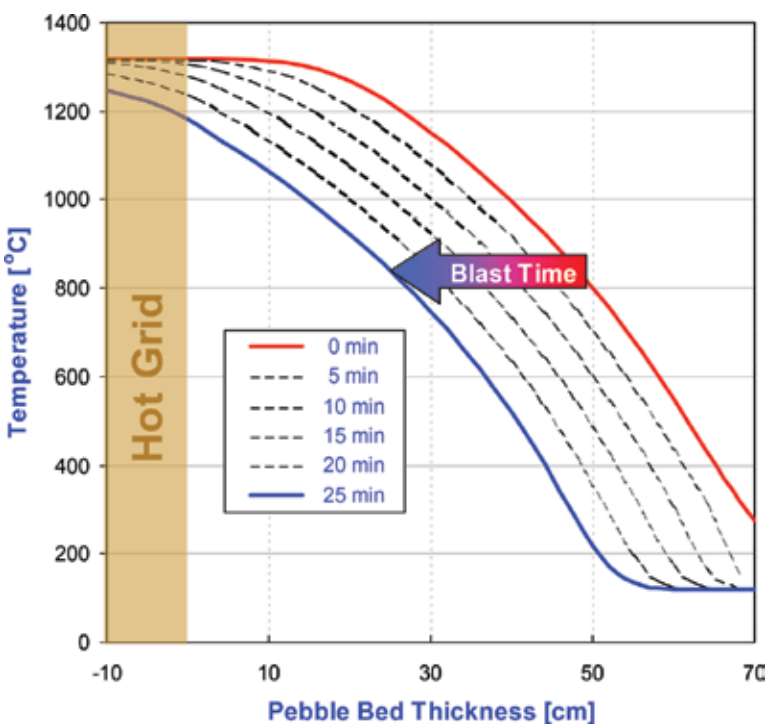


**Figure 5.** Typical temperature distribution inside the pebble heater.

Solving the energy Eq. (1) runs side by side with calculating the pressure drop through the pebble bed, through integration of the following equation:

$$\frac{dp}{dr} = \frac{1}{\psi^2} \mu\xi \frac{\rho\, w_o^{\,2}}{2\, D_e} \tag{2}$$

with following parameters: $p$ – pressure; $\mu\xi$ – friction and path factor; $w_o$ – gas velocity; $D_e$ – equivalent pebble diameter.

The usual way for calculating the friction and path factor $\mu\xi$ is the famous Ergun equation [19]. The comparison with measured values has shown that the correlation of Kast [20] is more accurate. Based on own measurements, the new correlations have been defined, which give even better results. Especially in the case of irregular shape of pebbles, those advantages were distinct.

### 3.4. Performance of pebble heater

**Figure 5** presents the typical, S-shaped temperature profile inside the bed, which is an extraordinary characteristic of the pebble heater technology. It arises from the intensive heat transfer and resulting low temperature difference between gas and solid phases. That S-shape enables a temperature change of more than 400 K in the middle of the bed, and correspondingly high storage capacity, while the hot grid (and hot blast at the exit) exhibits a very moderate temperature drop.

Therefore the hot blast temperature stays almost constant at the first two thirds of the blast phase. Only in the course of the last third of the blast phase, there is a more intensive drop of the blast temperature ($\Delta T$ = 30–100 K, in different designs and operation mode. The same is with the temperature changes on the cold), usually in the range $\Delta T$ = 100–150 K. That is the reason for low mean value of the flue gas temperature and resulting low exit loss.

An extensive test series on the pilot unit PH 104 (10,000 $m_{i.N.}^3$/h) has proven the extraordinary characteristics of this new concept of heat regenerators:

- Between 92 and 95% of thermal recuperation efficiency
- Ability to sustain high temperature operation
- Stability of the hot blast temperature

In that test series, all main operational parameters (like blast rate, cycling time, flame temperature, etc.) were modified from test to test, in order to cover any possible operating condition. Those tests have proved that the recuperation efficiency of the pebble heater overpasses by far the efficiency of the modern stoves, even with recuperative heat exchangers for preheating combustion air and/or fuel gas.

In the meantime, since 1996 more than 20 facilities have been built. Most of them were used as thermal oxidizers; however, the biggest units are for hot blast supply for iron and steel industry. In the next years, even bigger units are expected to replace the old Cowper technology for blast furnaces.

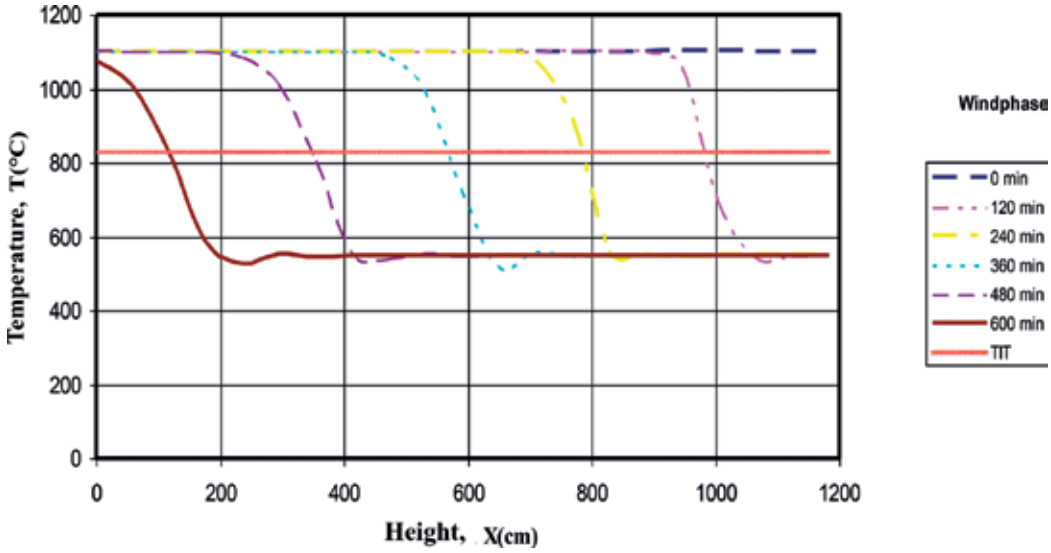


**Figure 6.** Typical temperature distribution inside the storage tower during 10 h discharging.

### 3.5. Application for energy storage

The extraordinary characteristics of the pebble heater technology are of decisive importance for the energy storage concept presented in this article. Each storage module consists of four smaller pebble heaters for the gas turbine recuperation (temperature range up to 550°C) and one more than 12 m tall electrically heated pebble heater. Small pebble heaters are in operation during gas turbine operation, and they are intermittent in charging-discharging operation, with time sequences of about 30 min.

The big pebble heater (or storage tower) is electrically charged when the gas turbine is out of operation. During that time (up to 10 h per tower), the temperature of pebbles rises from 550°C towards 1100°C. When the gas turbine is in operation, it delivers the high temperature compressed air for the turbine drive.

**Figure 6** gives the typical temperature distribution inside such storage tower with a column of 12 m filled with 12 mm pebbles, during a discharging phase of 10 h. At the beginning, all pebbles are at the highest temperature of 1100°C. Then the compressed air with 550°C enters from the bottom (the right side of **Figure 6**) and flows upwards (to the left side). It is heated to 1100°C and the pebbles are cooled down. The S-type temperature profile is established, resulting with stable outlet temperature for a long time.

## 4. Operation of HiTES

The principles of HiTES operation are based on the patent document [6] and given in [7]. When the system is charging, only one pebble heater (PH-E in **Figure 7**) is in use. Electrical heaters

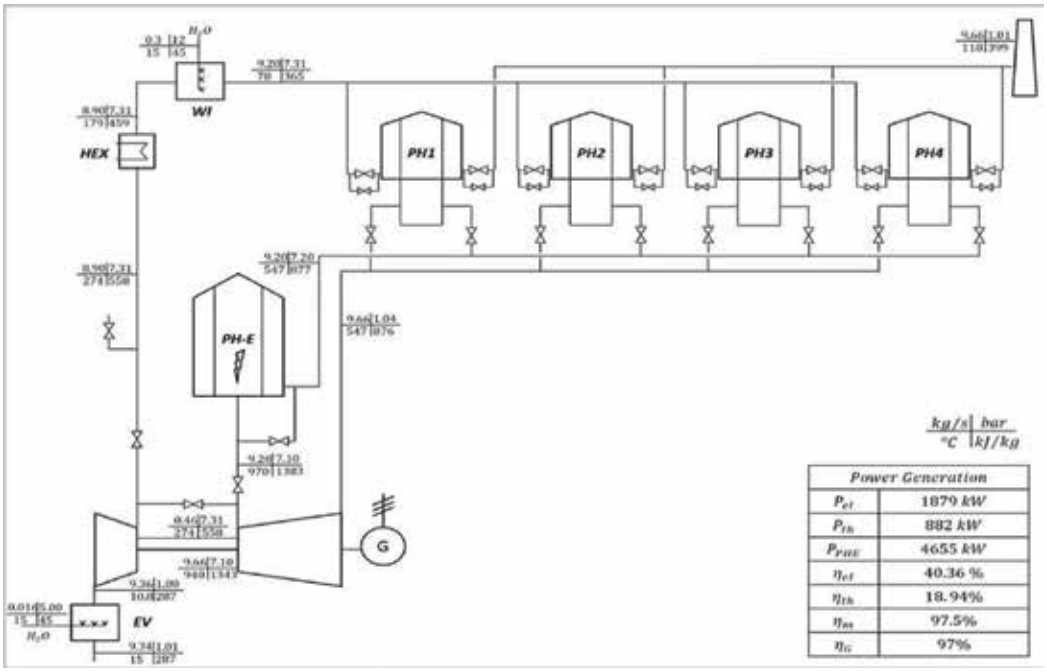


**Figure 7.** Flow diagram and nominal process parameters of HiTES [7].

heat up the storage material from 550 to 1100°C. That is very important for achieving good round-trip efficiency, as the charging electricity is stored only in form of high temperature heat.

When the system is discharging, all system components presented in **Figure 7** are in use. First, the low temperature pebble heaters (PH1…PH4) preheat compressed air to 550°C, and then it enters the high temperature PH-E where it is preheated to the end temperature of 1100°C. Hot compressed air enters the gas turbine and expands there, releasing mechanical work for compressor and generator drive. Expanded exhaust air heats up again the low temperature storage PH1…PH4. That heat is used later for preheating the compressed air, by activating the set of presented valves. In that way, always one pebble heater is in compressed air loop, and the remaining three are in the exhaust air phase. When a certain time (e.g. 20 min) has elapsed, another PH changes over to the compressed air loop, and the previous PH goes to the exhaust air loop and so on.

In the first step, it is preferred to use a radial gas turbine existing on the market, instead of developing a new one. Even the existing gas turbine (2 MW output power) in the HiTES system will reach approx. 40% of the round-trip efficiency that enables the profitability of the first units. After the maturity of this technology is proved in the industrial application, a new or modified gas turbine will be used, leading to higher efficiency and increased profitability of the system.

Some additional components have to be introduced with the existing gas turbine model in order to reach that high round-trip efficiency. Those are the fogging of the inlet air and compressed air cooling with water injection. The following description gives more precise process parameters (based on the ISO conditions 15°C, 1.013 bar abs).

When the system is discharging, the ambient air at 15°C, 1.013 bar absolute and a relative humidity of 60% enters into the compressor. In front of compressor, that air is cooled down by fogging. On one hand that decreases the compression work, and on the other hand, the fogging increases the mass flow by increasing the density. At the compressor outlet, the air has 7.3 bar and 275°C. The subsequent heat exchanger takes out some amount of heat from the compressed air, and by water injection, the further cooling is achieved. It is possible to inject 0.3 kg/s of water, before reaching the dew point temperature. Again, that leads to the higher mass flow rate and lower temperature of the compressed air. That injected water can be considered as a replacement for the fuel mass flow missing in such application of the gas turbine. In that way, the compressor and the expander work very close to the design point. The cooling of air entering the pebble heaters PH1…PH4 is important for the efficient heat transfer, as it leads to lower outlet temperatures during the exhaust air phase, meaning lower heat losses. Such preconditioned compressed air passes through one of the pebble heaters (PH1…PH4). Due to previously described advantages of the pebble heater technology, the air is preheated almost to the turbine exhaust temperature, leading to the high recuperation of the gas turbine cycle. After the low temperature PH, the compressed air flows through the high temperature pebble heater (PH-E), where it is heated further to 1100°C. In front of the expander, the air temperature is adjusted to the required inlet parameters (970°C), by controlling the bypass valve. That air is mixed with the turbine cooling air, preventing the overheating of the turbine guide blades. In that way, the turbine inlet temperature (TIT) of 940°C is reached. At the turbine outlet, the expanded air is at about ambient pressure and 540°C. It flows through the remaining three pebble heaters and heats up the pebbles. Thus it is cooled down to about 110°C and with that temperature leaves the system through the chimney.

Starting from the nominal turbine output of 2 MW and the round-trip efficiency of 40%, the suitable high temperature storage capacity of pebble heater PH-E is 50 MWh (i.e. 10 h heating with 5 MW of input power). In that case the discharging phase may deliver maximum 20 MWh of electricity (again 10 h with 2 MW electrical power). In a modular concept of the facility, two or three identical PH-E may be coupled with one gas turbine set. Respectively, the output of 2 MW power may be delivered for 20 or even 30 h.

With the refractory inside the PH-E made of high-quality fibre modules, the storage time of the high temperature heat may be from several minutes up to several days. **Figure 8** presents the temperature drop through such refractory over 5 days. Storing times longer than 7 days are not feasible, due to considerable efficiency reduction, as approx. 1% of stored heat would be lost per storage day. It means that after 5 days, some 5% of heat would be lost, as presented in **Figure 9**, leading to the reduction of the round-trip efficiency from 40 to 38%. The results presented in both **Figures 8** and **9** are based on the heat transfer calculations for a cylindrical structure with inside refractory made of silica-based fibre modules. According to the product sheet of a famous refractory supplier, those modules have an excellent heat conductivity coefficient. Although it increases with the temperature, at 1100°C it is only 0.25 W/mK (at 200°C 0.05 W/mK). That temperature dependence is taken into account in the calculations.

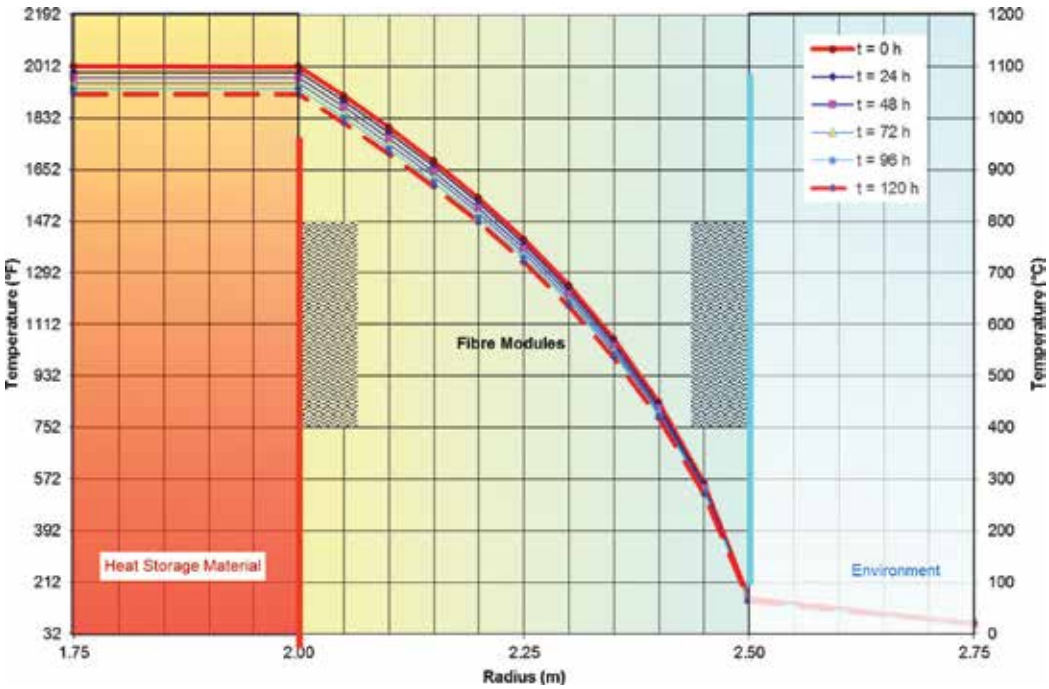


**Figure 8.** Temperature drop through the refractory of high-quality fibre modules, over 5 days.

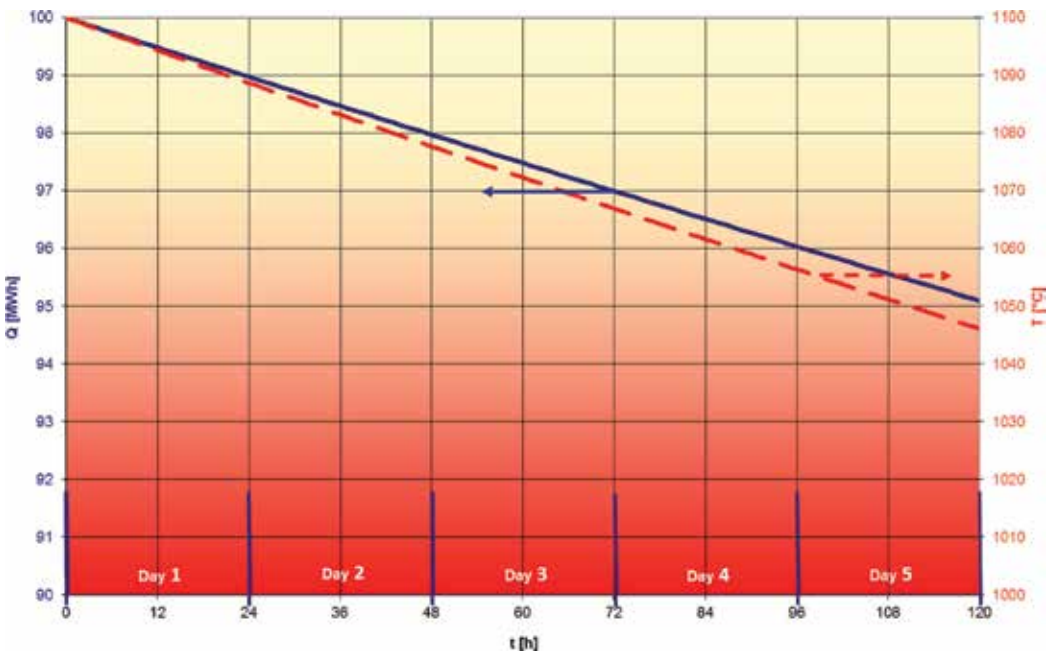


**Figure 9.** Decrease of stored heat due to heat losses and the drop of temperature inside the storage tower, during 5 days.

## 5. System improvements

As mentioned previously, some well-known measures may improve the actual round-trip efficiency of the existing process. Those measures and their effects, including the turbine optimization, have been analysed in [21]. In some cases those improvements may be done with the existing gas turbine; in other words it would be required to make more or less complex optimizations or design changes. In the case of the existing design, the pressure ratio was 7.27 and the isentropic compressor efficiency 80.89%. The turbine mass flow was 9.663 kg/s and the isentropic turbine efficiency 83.96%. For the improved optimised designs, the same characteristics were assumed, except that in the case of "pressure ratio", it was reduced to 3.5. Here follows a short overview of those measures, and the summary at the end gives the effect of all measures that could be applied simultaneously on the existing or on the related improved designs.

### 5.1. Fogging or evaporative cooling

Fogging is a measure well analysed in theory [22–24] and successfully used nowadays. It brings the biggest effects in climates with hot and dry ambient air. The compressor inlet air is saturated with water, which causes its temperature to drop, as the water evaporation takes the energy from it. The wet bulb temperature is the resulting temperature, causing the mass flow to rise due to the density increase. For example, for ambient air at 15°C and the relative humidity of 60%, the wet bulb temperature comes to 10.8°C. Respectively, the compression energy drops and the turbine efficiency increases.

### 5.2. Water injection

Water injection into the compressed air makes the same effect as the evaporative cooling. Due to water evaporation, the temperature drops. Although that evaporation energy is lost for the external heat usage, the mass flow rate and the heat capacity increase and so the turbine power releases, too.

The compressor work stays constant, and the generator gets the whole increase of the turbine output, leading to the higher power generation efficiency.

### 5.3. Turbine inlet temperature, TIT

An increased TIT leads to a higher inlet enthalpy and increases the specific turbine work. The robustness of materials is improving continuously with the progress in material science. Presently, some expander rotors operate with the turbine inlet temperature of 1050°C, without blade cooling. Therefore it seems just a matter of time until 1100°C will be reached, maybe with some additional measures, like blade coating. That would be another significant step forward compared to 970°C in the nowadays available gas turbine.

### 5.4. Pressure ratio

It is well known that in a simple cycle, there is always an optimum pair of the pressure ratio and the inlet gas turbine temperature. However, that optimum is not the same for a recuperated gas

cycle. There, the optimum pressure ratio depends on the recuperation efficiency and is much lower for the same inlet temperature. The gas turbine in consideration here is optimised for a simple cycle operation, and the selected pressure ratio of 7.27 is too high for the recuperated cycle. If it would be reduced to, e.g. 3.5, the efficiency would rise by 8.8% points.

### 5.5. Wet compression

A further improvement at the compressor inlet may be reached by wet compression. In that case water is sprayed above the saturation point into the inlet air. It is oversaturated with small droplets, which evaporate during the compression and therefore cool the air inside the compressor. The effects are similar to those of fogging, i.e. water injection, as the higher density and increased flow rate improve the efficiency.

As presented in several literature references [22–26], the droplet size is the most important factor for the impact of the water injection, as it defines the evaporation rate. A maximum of 3% water can be sprayed, when a pressure ratio is about 7 [23]. In case of the HiTES cycle, that is about 0.3 kg/s. The increase of electric power is about 320 kW, while the power generation efficiency climbs by 6.2% points.

### 5.6. Intercooling

The intercooling is an old and well-known method for improving the gas turbine cycle. The compressor is divided in two units, and between them there is a heat exchanger where the air is cooled. Due to the intercooling, the compression work is reduced in the second compressor by the higher density, as the air temperature is lower. The available shaft power for the generator increases due to the higher difference between the expander and the compressor power. In the case of a recuperative cycle, there is not a negative impact of the lower compressor outlet temperature. The electric efficiency and the generator power increase drastically.

### 5.7. Summary of all improvem.5ents

The summary of all those improvements is presented in **Figure 10** [21]. In the "uprate" scenario, all measures that may be done with the existing gas turbine are collected. As the round-trip efficiency would rise to 44.6%, it is obvious that the effect is not negligible.

Contrary to those measures, considerable design improvements and/or optimizations are required for the scenarios "Future I", "Future II" and "Future III". In all three scenarios, TIT is raised to 1100°C, and therefore at least some improved materials are required, together with an optimised expander design. The pressure ratio is reduced to 3.5 in the "Future I" scenario, increasing the efficiency to 53.7%.

Only in the scenario "Future II" the wet compression is used. The pressure ratio is preserved at the old value of 7.3, and therefore the efficiency with 51.9% is lower than in the previous case. The advantage is that the power output jumps to above 2.8 MW (+50% compared to the actual case). At least a new design of the gear box and power generator would be needed.

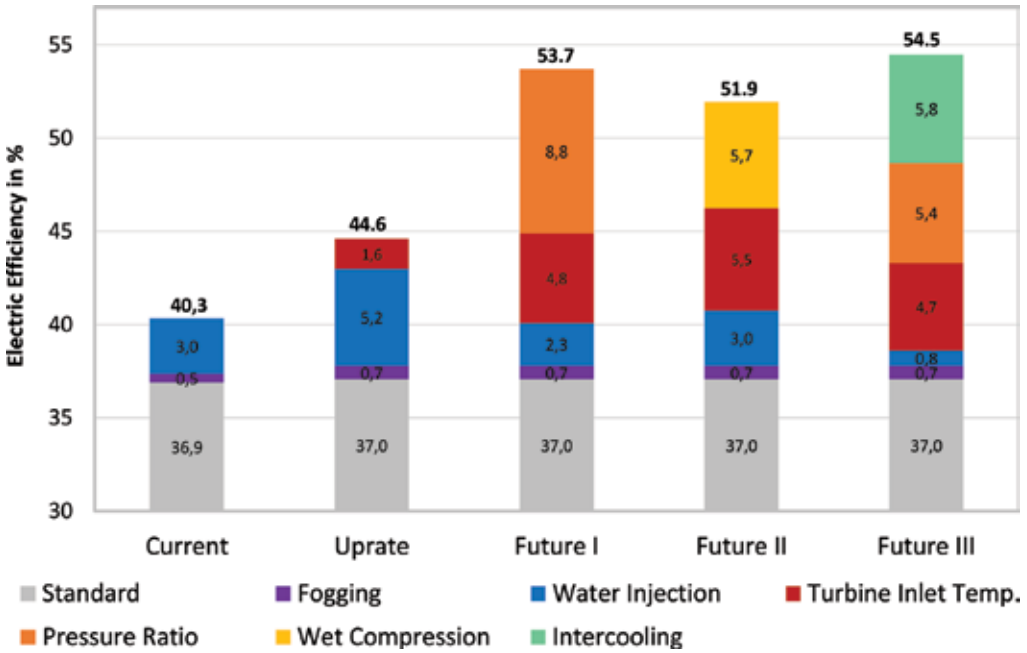


**Figure 10.** Potential improvements of HiTES cycle efficiency [21].

The scenario "Future III" includes the effects of intercooling together with reduced pressure ratio. The total pressure ratio is achieved in two stages with equal pressure ratios of 1.87 but reduced again to 3.5. The compressed air cools down to 37°C by water injection between two compressor units. The power output is above 2.5 MW (+35% compared to the actual case), and the round-trip efficiency rises to 54.5%.

The advantage is that all those improvements are not a special technological challenge and the robustness and simple design of the original gas turbine can be preserved. Eventual higher costs (e.g. expander blades for higher inlet temperature) will be overwhelmed by the increase in the power output, so that the specific costs will not rise.

## 6. Levelized cost of electricity storage

The round-trip efficiency is usually the first criterion for comparing different energy storage technologies. The concern is to keep the electricity losses induced by the storage at a minimum. However, in order to achieve the economic viability of the storage system, the investment cost has to be acceptable, too. Therefore some authors use the specific investment costs per kWh of stored electricity, and the others prefer the specific investment costs per 1 kW of the output (or input) capacity. The problem is that comparisons based on such different criteria give quite different results.

Using the levelized cost of electricity (LCOE) is the most correct approach for that comparison. It is similar to the model used for costs of electricity from power plants. It includes all relevant parameters: capital expenditure (*CAPEX*), annual operational expenditure (*OPEX*), energy output $W_{el}$, interest rate $i$ and the lifespan $n$ in years [7]. Due to some differences compared to the electricity production costs, the LCOE has to be extended with the characteristics of energy storage systems: costs of the input electricity $\sigma$ and the round-trip efficiency $\eta_{el}$. The resulting formula for the levelized cost of electricity storage (LCOES) is given in Eq. (3):

$$\mathrm{LCOES} = \frac{\mathrm{CAPEX}}{W_{el}} \frac{i \cdot (1+i)^n}{(1+i)^n - 1} + \frac{\mathrm{OPEX}}{W_{el}} + \frac{\sigma}{\eta_{el}} \tag{3}$$

The above formula is the most objective way for comparing the energy storage technologies. However, all technology details have to be known and well analysed for a correct comparison. There is a difference between the capacity which is achievable in praxis and the nominal discharge capacity of some technologies. In such cases there is a drastic reduction in the lifespan if the full discharge cycles would performed regularly. For example, it is well known that in the case of chemical batteries, there is a significant difference in the capacity at the beginning and at the end of their lifespan. Therefore, a realistic pair of capacity and lifespan must be selected in such cases.

With LCOES it is possible to analyse the whole complexity of the energy storage. In the available literature, there are data about many available storage technologies that vary for more than a factor 2 in some cases. On the other hand, some important parameters, like the specific

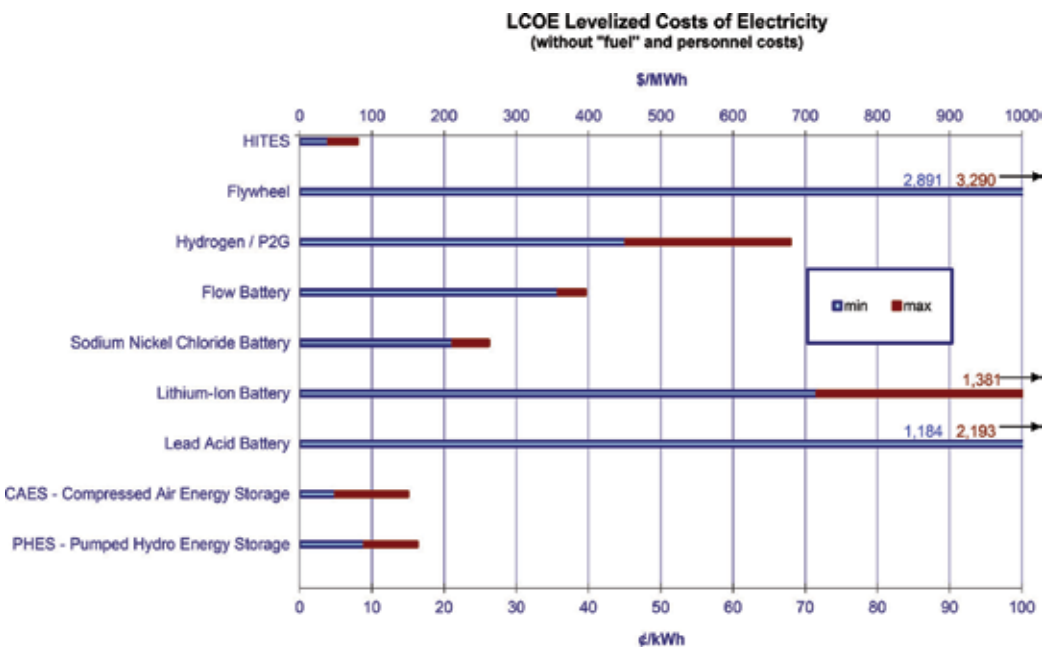


**Figure 11.** Comparison of LCOES for different storage technologies, based on data from [27].

investment cost and the efficiency, are subjected to steady improvements. Therefore, it is difficult to calculate reliable value of LCOES for the related technology and to compare them. As an example, **Figure 11** gives such a comparison, based on data from [27]. The following parameters are taken the same for all technologies:

- Power output 2 MW
- Time on power generation 4150 h/a
- Power generation 8300 MWh/a
- Life time 25 years (if lower, related investment cost increased)
- Loan cost 6.5% interest rate, 10 years long

For the simplicity of presentation, those figures do not include the price of the input electricity, nor the eventual cost for personnel operating the storage plant. The minimal (blue) and maximal (red) costs are presented, illustrating the wide range of different input data. Therefore, in order to point out the most important parameters, in **Figure 12** only two technologies are compared, taking into account the costs of the input electricity (i.e. the influence of the round-trip efficiency) as well. Those two energy storage systems are compared:

- One high specific investment cost of 1600 €/kWh and with 85% round-trip; the cost may be reduced to 800 €/kWh due to the further development.
- The other system has a considerably lower round-trip efficiency of 40% but also lower the specific investment cost of 250 €/kWh (e.g. HiTES with 20 h discharge time); the round-trip efficiency may be improved to 50 and 60%, retaining the same specific cost.

The change of storage cost LCOES (€/MWh) is given with presented curves, as a function of the input electricity cost (also €/MWh). The development of the solar and wind generation technologies in the last years has resulted in a tendency of steady price reduction of generated electricity. The lowest recorded prices from a photovoltaic system are 25 €/MWh in Chile and 20.7 €/MWh in Abu Dhabi, and just recently 15.3 €/MWh have been bided in Saudi Arabia [29]. Moreover, due to high penetration of intermittent renewable power generation in some energy systems, it happens more and more often that the stock market prices are negative. Therefore, the negative input electricity prices are plotted, as well.

Two important conclusions may be drawn from the graph in **Figure 12** [28]:

- The specific investment costs are more important than the efficiency; the improvements in the investment cost are more important than the improvements in the efficiency; of course that is limited to the values which are common for the contemporary systems.
- With the falling prices of renewable generation, the above effect becomes more and more important: the efficiency is not as important as the investment cost. (In the case of negative cost of the input electricity, lower efficiency gives lower LCOES.)

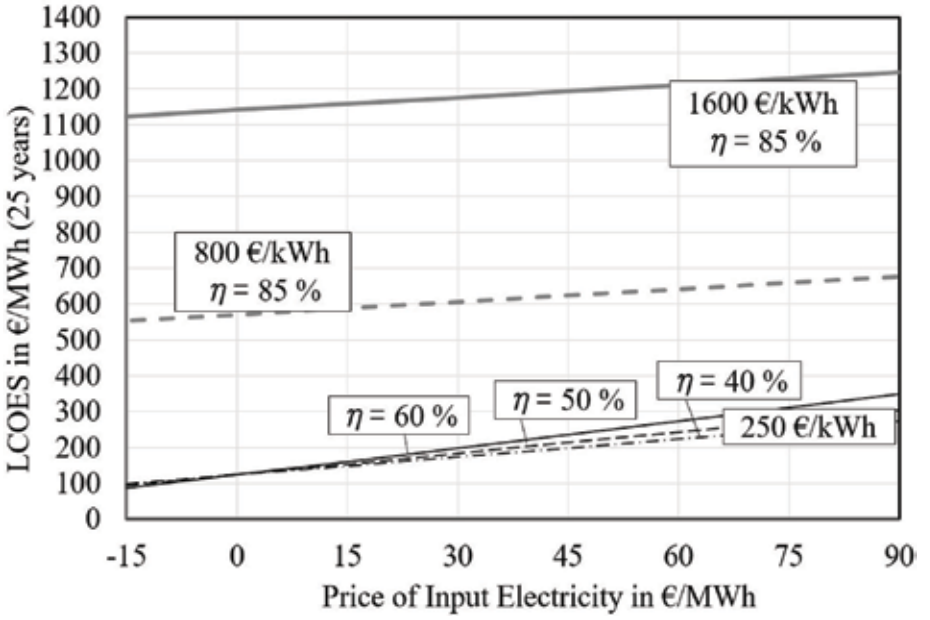


**Figure 12.** Influence of specific investment, efficiency and price of input electricity on LCOES [28].

The further improvements of HiTES should go in direction indicated in the presented analysis: reduction of investment costs before the efficiency improvements. It is not allowed to pay the efficiency improvements with increased investment cost. The main potential for the reduction of the specific investment costs is an increased number of installed units.

## 7. Concluding remarks

Without energy storage, it is impossible to implement the generation of renewable electricity based on intermittent sources like wind and solar. Although there are many different technologies available nowadays, they are still not widely used, as they are still very expensive and not suitable for distributed power generation. One possibility with a huge potential is the HiTES technology, which is attractive because of its relative low specific investment cost, its long discharge time (10, 20 or even 30 h) and its potential to improve its efficiency easily towards 60%. Thus, its round-trip efficiency is considerably higher than the efficiency of some other long discharge systems, like power-to-gas, or molten salt. With its relatively low capacity compared to CAES and PHES, it is especially suitable for distributed generation. That shows how the previously developed technology for biomass CHP [30, 31] may be adjusted for new tasks, preserving its simplicity and improving the efficiency.

The analysis of LCOES, which is the best comparison criteria, shows that those systems are more favourable than the battery storage. Even today, that system could be used in a viable manner in countries with high insolation. In combination with photovoltaic plants, it gives lower cost of the electricity supply than concentrated solar plants (CSP).

The specific investment cost is considerably more important than the round-trip efficiency. With the steadily falling prices of the renewable generation, that effect will become more and more pronounced.

## Author details

Dragan Stevanovic

Address all correspondence to: office@pebble-heater.com

Engineering and Consulting/Energy and Environment, Sulzbach-Rosenberg, Germany

## References

[1] Fürstenwerth D, Waldmann L. Stromspeicher in der Energiewende. Study of Agora Energiewende, Berlin; September 2014

[2] Stevanovic D. Energiewende – German energy transition – Integration of Renewable Electricity. Industrial Energy and Environmental Protection in South Eastern Europe, IEEP-2015; 24-27 June 2015; Zlatibor, Serbia. 2015

[3] Graichen P, Marthe Kleiner M, Podewils Ch. Die Energiewende im Stromsektor: Stand der Dinge 2016. Berlin: Agora Energiewende; January 2017

[4] Loutan C. Overcoming grid intermittancy. CAISO California Independent System Operator, CA, CSP Today; 26-27 June 2013; Mandalay Bay, Las Vegas. 2013

[5] SIEMENS. 2016. web-site: http://www.siemens.com/press/WindEnergy2016

[6] Stevanovic D, Brotzmann K. "Stromspeicherung über thermische Speicher und Luft-turbine", Patent application DE102013017010A1. German Patent and Trade Mark Office, Munich 2013 (also: "Storing energy using a thermal storage unit and an air turbine", US patent application US2016/0237892A1, 2016); 2013

[7] Stevanovic D, Rembold T. High temperature energy storage based on hot air turbine and pebble-heater technology. 4th International Symposium on Environment Friendly Energies and Applications EFEA-2016; 14-16 September 2016; Belgrade. 2016

[8] Klimstra J. Energy, exergy or economy? Cogeneration & On-Site Power Production; July–August 2014; PennWell. 2014. pp. 22-27

[9] Stevanovic D, Faßbinder H-G. Regenerative thermal oxidizers based on the pebble-heater technology. 5th European Conference on Industrial Furnaces and Boilers – INFUB 5; 11-14 April 2000; Porto, Portugal. 2000

[10] Wimmer G, Pastucha K, Kluge J, Fleischanderl A, Spiess J. Jet process for highest scrap and DRI rates in converter. 1st ESTAD & 31st JSI; 7-8 April 2014; Paris, France. 2014

[11] Günther C et al. Increased scrap rate to the BOF process by application of hot air post combustion – PS-BOP project. 1st ESTAD & 31st JSI; 7-8 April 2014; Paris, France. 2014

[12] Brotzmann K, Stevanović D. Pebble-Heater als Alternative zum klassischen Winderhitzer—Erzeugung von Hochtemperatur-Heißwind. VDEh-Fachausschußbericht 1.031, Juli 1998; Düsseldorf. 1998

[13] Stevanovic D, Fischer W. Pebble-heater twins with fluid dynamic valve—An efficient possibility for high combustion air preheating. In: 6th European Conference on Industrial Furnaces and Boilers—INFUB 6; 2-5 April 2002; Estoril, Portugal. 2002

[14] DRESSER-RAND. KG2 Gas Turbines for Power Generation. March 31, 2016. http://dresser-rand.es/products/turbo/gasturbine/KG2-3E.php

[15] Vortmeyer D, Schäfer RJ. Equivalence of one- and two-phase models for heat transfer processes in packed beds: One dimensional theory. Chemical Engineering Science. 1974;**29**:485

[16] Bauer R. Wärmeleitung in durchströmten Schüttungen. Chapter Mh. In: VDI-Wärmeatlas, 5th ed. Düsseldorf, Germany: VDI-Verlag; 1988

[17] Till K. Modellierung und Berechnung turbulenter Strömungen mit chemischer Reaktion in Festbettreaktoren [Dr.-Ing. dissertation]. Merseburg, Germany: Fakultät für Technische Wissenschaft und Mathematik; 1981

[18] Stevanovic D, Studovic M. Method for transient fuel element response evaluation. In: 5th National Conference on Heat and Nuclear Engineering Problems of PRB; Varna, Bulgaria. 1981

[19] Ergun S. Fluid flow through packed columns. Chemical Engineering Progress. 1952; **48**:89-94

[20] Kast W. Druckverlust bei der Strömung durch Schüttungen, Chapter Le. In: VDI-Wärmeatlas. 4th ed. Düsseldorf, Germany: VDI-Verlag; 1984

[21] Rembold T. Power storage by a high temperature thermal storage and a hot air turbine [MSc thesis]. Faculty of Mechanical and Environmental Engineering, OTH Amberg-Weiden; March 2016

[22] Lechner C, Seume J. Stationäre Gasturbinen, 2nd ed. Berlin, Heidelberg, Germany: Springer; 2010

[23] Kim KH, Perez-Blanco H, 2007, "Potential of regenerative gas-turbine systems with high fogging compression", Applied Energy. 2007;**84**(1):16-28

[24] Khan JR. Fog cooling, wet compression and droplet dynamics in gas turbine compressors [dissertation]. New Orleans, USA: University of New Orleans; 2009

[25] Eisfeld T. Experimenteller Untersuchung der Aerodynamik einer mit Wassertropfen beladenen Luftströmung in einem ebenen Verdichtergitter [dissertation]. Hamburg, Germany: Helmut-Schmidt-University/Universität der Bundeswehr Hamburg; 2011

[26] Zheng Q, Li M, Sun Y. Thermodynamic performance of wet compression and regenerative (WCR) gas turbine. In: ASME Turbo EXPO 2003, Collocated with the 2003 International Joint Power Generation Conference. 2003. pp. 813-820

[27] Pimlott S. Five Minute Guide: Electricity Storage Technologies. ARUP; March 9, 2015. http://publications.arup.com/Publications/A/A_five_minute_guide_to_electricity_storage.aspx

[28] Stevanovic D. Energy storage for integration of renewable electricity—Case of HiTES. In: Industrial Energy and Environmental Protection in South Eastern Europe, IEEP-2017; 21-24 June 2017; Zlatibor, Serbia

[29] Dipaola A. Saudi Arabia gets cheapest bids for solar power in auction. Bloomberg Markets. October 3, 2017. https://www.bloomberg.com/news/articles/2017-10-03/saudi-arabia-gets-cheapest-ever-bids-for-solar-power-in-auction

[30] Stevanovic D. Innovative biomass power plant based on pebble-heater technology and hot air turbine. Power Gen; Brussels, Belgium; 2001

[31] Stevanovic D. Method and device for converting thermal energy from biomass into mechanical work. United States Patent Application US2012/0137701A1. June 7, 2012

Chapter 3

# Technologies for Seasonal Solar Energy Storage in Buildings

Uroš Stritih and Urška Mlakar

Additional information is available at the end of the chapter

http://dx.doi.org/10.5772/intechopen.74404

**Abstract**

Thermochemical heat storage is a very promising technology that enables us to save the excess heat produced during summer time for the needs in the winter, when we have higher heating needs. Thermochemical heat storage bases and an overview of thermochemical materials (TCMs), suitable for the solar energy storage, are given. Choosing a suitable adsorbent and adsorbate is very important. The most important properties of the substance are high energy density for high thermal storage, low charging temperature for low energy consumption, high uptake of sorbate kg(sorbate)/kg(sorbent) and environmental safety and easy to handle-nonpoisonous. The paper also presents the differences between the closed and the open sorption system. The biggest difference between those two systems is the importance of sorbent, which in case of open systems means that sorbent must be environmentally friendly. Also, various closed and open systems are presented.

**Keywords:** thermochemical heat storage, adsorption, solar energy, open and closed systems

## 1. Introduction

In 2030 Energy Strategy, European Union (EU) set a goal to achieve the following 3 major targets by 2030:

- To reduce at least 30% of greenhouse gas (GHG) emissions, compared to 1990 levels
- 27% increase of the share of renewable energy sources in final energy consumption
- To achieve at least 27% increase of energy efficiency

The key to achieve these goals is improving the building energy performance, because buildings are responsible for 36% of $CO_2$ emissions and 40% of energy consumption in the EU [1, 2]. Since solar energy has a lot of potential, it would be smart to use more of it. Because of the mismatch between the availability of the source and the energy needs of the building, the use of heat storage technologies is needed to realize its potential.

Heat storage can be achieved by different chemical or physical processes. Depending on how heat is stored, we distinguish two basic methods: sensible and latent physical heat storage. Sensible storage is achieved by the temperature change of the storage material. The amount of energy stored depends on the temperature rise and specific heat of the storage material (stored energy per unit volume or mass). Latent heat storage depends on heat interactions associated with phase change of the material (at constant temperature), usually from liquid to solid, and vice versa. Due to higher thermal energy change during phase change, compared to temperature rise of storage material in sensible heat storage, latent heat storage allows higher heat densities. Nevertheless, in practice, the use of sensible heat storage systems predominates due to better and higher thermal stability and cheaper storage materials, compared to phase change materials (PCMs).

In addition to these two storage methods, we also know thermochemical heat storage systems, which are not yet available on the market. In thermochemical heat storages are involved reversible chemical reactions. During the charging stage, heat is usually from the collector supplied to the storage material, which triggers desorption of the water vapor, which is endothermic reaction. As long as the products of endothermic reaction are separated, the supplied heat can be stored for an arbitrary time (almost) without losses. This and a several times higher stored thermal energy density (**Figure 1**) make thermochemical materials (TCMs) a promising option for mid- and long-term heat storage.

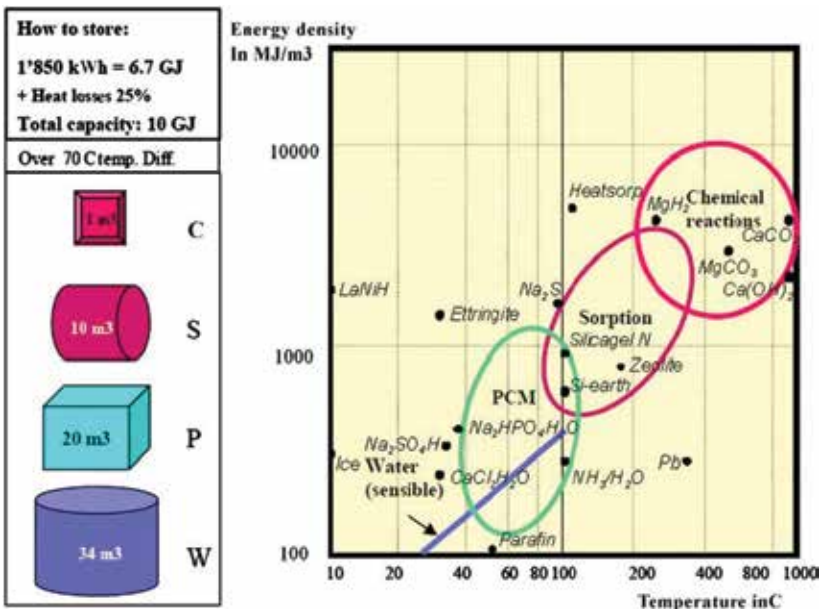


**Figure 1.** Energy density of thermal storage technologies [4].

In this paper, a review of thermochemical heat storage technologies and systems with solar energy utilization in buildings, regarding TCMs with a charging temperature below 140°C, is presented [3]. The paper is organized as follows: Section 2 sums up the fundamentals of thermochemical heat storage and contains an overview of TCMs suitable for solar energy storage. Section 3 presents possible system configurations for thermochemical heat storage and evaluates applications appropriate for reducing the energy needs of buildings. An overview of models for predicting and optimizing the performance of thermochemical storage systems is included in Section 4. Section 5 concludes the paper.

## 2. Thermochemical heat storage

### 2.1. Basics

Thermochemical heat storage is generally classified under chemical heat storage processes (**Figure 2**). Under the term thermochemical heat storage, we usually summarize sorption heat storage processes. Some authors (e.g., [4]) also mention thermochemical storage without sorption but with no exact definition of the latter. Sorption can be defined as a phenomenon of fixation of a gas by a substance in solid or liquid phase [5]. We differ between absorption and adsorption. Absorption is used when we have substance in gas phase and substance in liquid (usually) or solid phase. The substance in gas phase enters a liquid or solid and in the process changes the composition of the liquid or solid [6], while adsorption is defined as a gaseous substance that binds to the surface of a solid or porous material [4]. Further, adsorption is divided into chemical adsorption or chemisorption and physical adsorption or physisorption. The attraction between substances is caused by different forces, in physisorption by Van der Waals forces and in case of chemisorption by valence forces, which create stronger bonds. Because of stronger bonds, the chemisorption processes are able to reach higher thermal energy densities than physisorption. Chemisorption processes are also reversible, which makes them suitable for heat storage applications. In the following section, only reversible sorption processes are presented.

Reversible sorption heat storage processes can be written in the following way:

$$AB + Q \leftrightarrow A + B \tag{1}$$

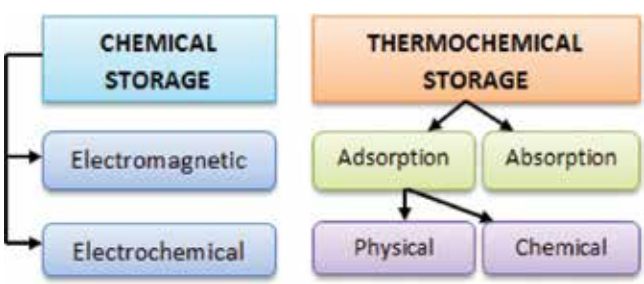


**Figure 2.** Classification of chemical heat storage.

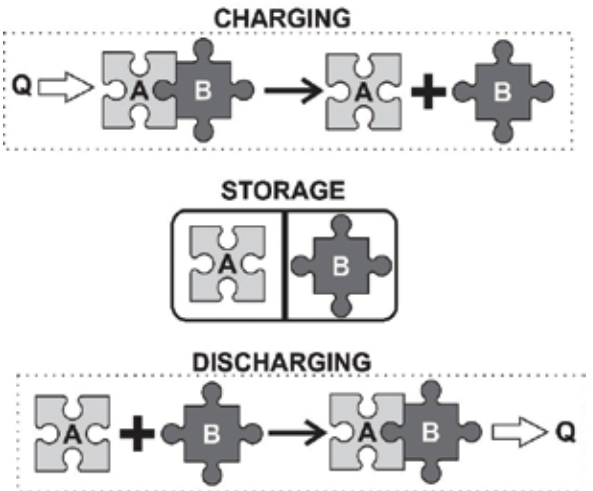


**Figure 3.** Thermochemical heat storage cycle has three stages: charging stage, storage stage and discharging stage.

where, AB is a compound of components A and B. When AB is split into A and B with energy input (Q)-this is called a "charging stage." Then, A and B are stored separately (storage state). At a discharge when A and B are in contact, they form AB with energy released (Q)-this is called "discharging state" (**Figure 3**). Storage materials consist of component A also called adsorbent and component B also called adsorbate. In charging stage, adsorbate is desorbed from adsorbent, and then in discharging stage, adsorbate is adsorbed on the surface of adsorbent. For adsorbate in desorbed state, term adsorptive is also used. In heat storage applications, mainly water (vapor) is used as adsorbate because of its availability (i.e., cheap) and nontoxicity.

The heat needed for desorption can be divided into three parts [5]:

$$Q = Q_{sens} + Q_{cond} + Q_{bind} \tag{2}$$

here, $Q_{sens}$ represents the sensible heat needed to heat the absorbent to the temperature needed for desorption. $Q_{cond}$ is the heat needed to vaporize the adsorbate, while $Q_{bind}$ is the heat required to overcome the sorption forces. The latter is therefore usually termed as binding heat. As seen from **Figure 4**, $Q_{bind}$ decreases with the increase of sorbate concentration. This means that more is needed at the beginning of the charging process when the sorbate concentration is low. For heat storage applications, the contribution of $Q_{bind}$ must be as low as possible compared to $Q_{cond}$ since it results in lower temperatures required for desorption [7].

### 2.2. Reactants

Knowledge on materials is a prerequisite to design thermal storage systems and their components. Different sorption working pairs or reactants have been studied for thermal energy

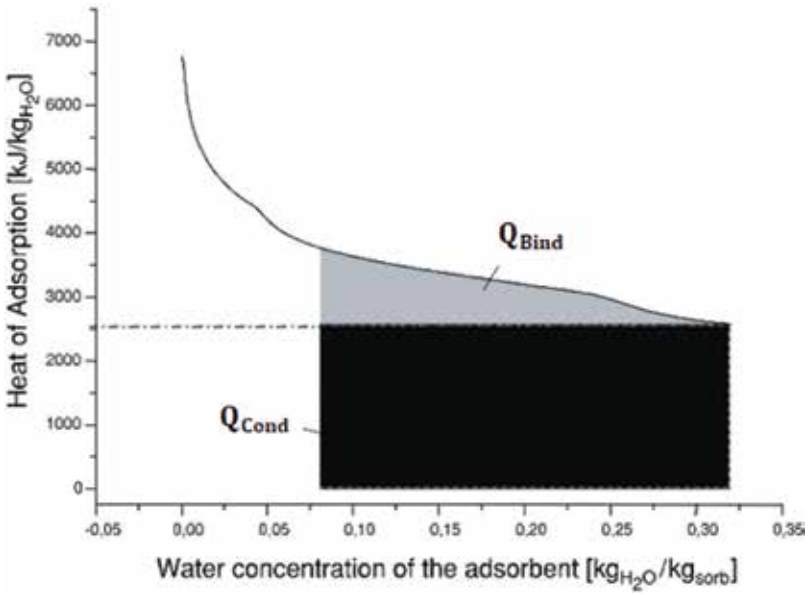


**Figure 4.** Break down of the required heat for desorption for zeolite as an example [5].

storage applications. The sorbents with the highest potential in sorption storage systems are crystalline and amorphous materials and their composites with hygroscopic inorganic salt hydrates. But the abovementioned materials do not meet the requirements for large-scale applications yet [3]. Through the literature [4, 7–11], the following requirements for materials have been exposed:

- High energy density for high thermal storage-thermal energy density at the operating temperature (kWh/m$^3$, Wh/kg)
- Low charging temperature for low energy consumption
- High uptake of sorbate kg(sorbate)/kg(sorbent)-if water is the sorbate, a high selectivity for water
- Thermal and chemical stability-no deterioration
- High thermal conductivity for high heat transfer
- High heat and mass transfer of the working fluid to the sorbent
- Moderate operating pressure range
- Low regeneration time
- Noncorrosive
- Environmental safety and easy to handle-nonpoisonous
- Low cost-low price per kWh heat stored

The abovementioned material requirements of sorption properties represent the foundation of selecting appropriate TCM for application. But complete evaluation of sorption material properties demands precise measurements of sorption isotherms, isobars and isosteres under a wide range of pressures and temperatures [9]. The energy storage densities and charging/discharging temperatures of some materials suitable for thermochemical heat storage are listed in **Table 1**. The most promising materials have low charging temperatures and high energy storage densities.

| Phenomena | Sorbent | Sorbate | Charging temperature (°C) | Discharging temperature (°C) | Energy density (kWh/m³) |
|---|---|---|---|---|---|
| Adsorption | | | | | |
| | silica gel | $H_2O$ | 88 | 32 | 50–125 |
| | zeolite 13X | $H_2O$ | 160–180 | 20–40 | 97–160.5 |
| | zeolite 4A | $H_2O$ | 180 | 65 | 130–148 |
| | zeolite 5A | $H_2O$ | 80–120 | 20–30 | 83 |
| | zeolite MSX | $H_2O$ | 230 | | 154 |
| | APO-n | $H_2O$ | 95–140 | 40 | 240 |
| | SAPO-n | $H_2O$ | 95–140 | 40 | — |
| | MeAPO-n | $H_2O$ | 95–140 | 40 | — |
| Absorption | | | | | |
| | $CaCl_2$ | $H_2O$ | 45–138 | 21 | 120–381 |
| | LiCl | $H_2O$ | 66–87 | 30 | 253–400 |
| | $LiCl_2$ | $H_2O$ | 46–87 | 30 | 253 |
| | LiBr | $H_2O$ | 40–90 | 30 | 252–313 |
| | NaOH | $H_2O$ | 50–95 | 70 | 154–250 |
| | $SrBr_2$ | $H_2O$ | 80 | — | 60–321 |
| Chem. react. | | | | | |
| | $BaCl_2$ | $NH_3$ | 56–70 | 40 | 787 |
| | $CaCl_2$ | $NH_3$ | 95–99 | — | 673 |
| | $CaSO_4$ | $H_2O$ | — | 89 | 390 |
| | $CuSO_4$ | $H_2O$ | 92 | — | 575 |
| | $Li_2SO_4$ | $H_2O$ | 103 | — | 255 |
| | $MgCl_2$ | $H_2O$ | 130–150 | 30–50 | 556–695 |
| | $MgSO_4$ | $H_2O$ | 122–150 | 120 | 420–924 |
| | $MnCl_2$ | $NH_3$ | 152 | — | 624 |
| | $Na_2S$ | $H_2O$ | 80–95 | 80–110 | 780 |

**Table 1.** Materials used in thermochemical heat storage studies.

Because of good properties, water is the most used sorbate for seasonal solar energy storage in buildings. Water is environmentally friendly and cheap, which satisfies most conditions. Hence, hydrophilic materials such as silica gels are appropriate for the counterpart reactant or the sorbent. Silica gels have high affinity to water vapor, large water sorption capacity at low humidity, easy regeneration and low cost, but they provide low material energy densities, because of the low hydrophilic characteristic within the working window [10]. Therefore, the application prospect of silica gels in solar energy storage is obscure. Because of the strong interaction between electrostatically charged framework and the water molecules, zeolites are more hydrophilic than silica gels [12]. Because of that, their desorption or charging temperature needs to be higher, which can be altered with dealumination, ion exchange or the variation of the aluminum-silicon ratio [12–14]. Impregnated mesoporous silicates with hygroscopic salts are another option [15–19] to increase performance of the sorption reaction and enhance heat and mass transfer. Nevertheless, these composite materials have some disadvantages such as they suffer from leakage of salt species and are also corrosive due to the contained salts [20].

Some authors [3, 13, 21–23] favor microporous aluminophosphates (APO-n) and their modified analogs (SAPO-n and MeAPO-n) to modified zeolites, because of lower discharging temperatures and higher energy densities. The main focus in research of materials suitable for heat storage applications has been to increase the uptake of sorbate (water) with incorporating silicon or metal cations in aluminophosphates [3, 24, 25]. The performance of the latter substances usually degrades after a few charging/discharging cycles because of framework structure degradation and dislodgement of incorporated cations from the framework [13, 21, 24, 25]. However, the main limitation of aluminophosphates compared to zeolites (and silica gels) is their high synthesis cost [10, 12].

As we can see in **Table 1**, mostly used sorbents in absorption heat storage studies are calcium chloride ($CaCl_2$), lithium chloride (LiCl), lithium bromide (LiBr) and sodium hydroxide (NaOH) and almost all use water as sorbate. Of the listed substances, NaOH is a base while the other compounds are hygroscopic salts and are thus applied in the form of solutions. Advantages of strong bases and acids are higher water uptake and low cost, but they also have disadvantages like corrosiveness, need of higher charging temperature, etc.

In contrast to sorption processes, chemical reactions are characterized by a change in the molecular configuration of the compound involved during the reactions. Based on the material, chemical reactions have great storage potential. But their performance in applications does not perform well, and after several initial cycles, the reaction is very difficult to continue due to swelling, deliquescence and agglomeration. Thus, the performance of material in applications needs further investigation [7]. Furthermore, because chemical reactions induce volume modification of the solid, an obvious hysteresis may exist.

Sorption processes are more suitable for low temperature applications such as seasonal solar energy storage, then chemical reactions, because they require lower activation energy. In the subsequent sections, only heat storage applications utilizing solid-gas adsorption processes are discussed, because liquid-gas absorption systems have limitations with corrosion and crystallization issues.

## 3. Sorption storage systems

According to the system design, sorption thermal storage systems can be divided into open and closed systems. The biggest difference between those two systems is the importance of sorbent, which is usually in gaseous phase and interacts with atmospheric environment, so it is not isolated, which means it is important that the sorbate is environmentally friendly. Meanwhile, closed system is isolated and we need storage for the storage material (sorbate). In contrast, the working fluid vapor is released to the environment in open systems, which means that only water (vapor) can be used as the sorbate.

Closed system generally consists of two vessels that are connected (**Figure 5**), namely, a condenser/evaporator where liquid water is collected and a reactor that consists of reactive sorbent. Desorption in the reactor and a phase change in the condenser take place in the charging process. Sorbate exits from the sorbent when heat source with high temperature (e.g., solar energy from solar collector) is supplied to the reactor. Low temperature level in a condenser causes liquefying of vapor where the condensation heat is released into the heat sink. The flow from reactor and the condenser is prevented with the valve after charging process is finished and in such a way the heat is stored. When head demand occurs, the flow from condenser/evaporator to the reactor is established again by opening the valve. The discharging process works in a reverse direction, whereby an additional low-temperature heat source is needed for water evaporation. Closed systems allow adjusting the operating pressure of the working fluid and are able to reach higher output temperatures for heating applications compared to open systems [7, 11]. However, the regeneration of closed systems usually requires a higher temperature level. Therefore, closed systems are appropriate especially for small-scale applications.

In open systems (**Figure 5**), a dry air stream is guided into a reactor filled with sorbent during the charging process. Water adsorbed/absorbed by the sorbent is extracted by the hot air and exits the reactor bed. Hereby, the air is adiabatically cooled. During discharging, cold humid air stream enters into the (desorbed) reactor. Part of the water vapor in the air is attracted

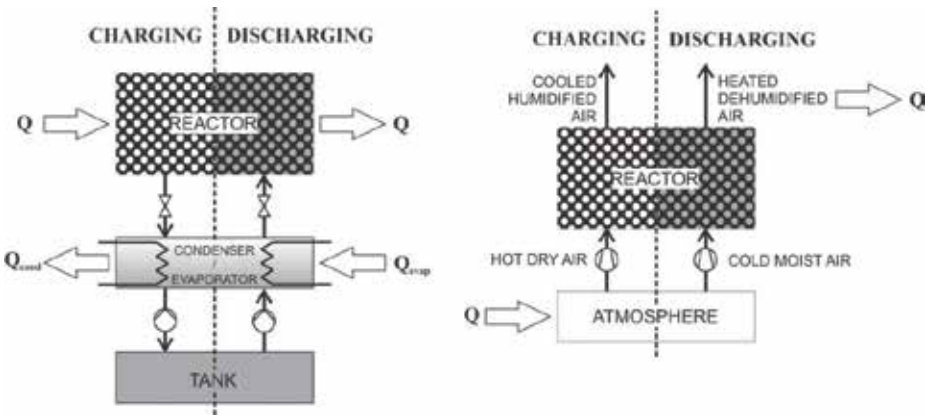


**Figure 5.** Operation principle of sorption storage systems: (left) closed, (right) open [11].

by the sorbent. The air temperature increases, due to the released sorption heat. Weather conditions limit the operation of open systems. For a good discharging rate, the ambient air humidity must be sufficient. Thus, the air must be additionally humidified when the ambient moisture content is insufficient. Compared to closed system, the open system has many advantages, such as the design is simpler, which in the end means cheaper, because they do not require the use of condensers, evaporators and working fluid storage reservoirs. However, the main advantage of using the open system configuration is the better heat and mass transfer conditions, because the heat transfer fluid (air) is in direct contact with the solid reactant, while closed systems require a separate heat transfer loop and hence a heat exchanger in the reactor (heat transferred mainly by conduction). On the other side, open systems may suffer from high energy consumption for overcoming pressure losses through the reactor, which is reflected in higher fan power thereby in higher electrical energy usage.

The main objective of this section is to review the available equipment used for sorption heat storage, especially concerning gas-solid reactors for solar energy utilization.

### 3.1. Closed systems

A closed adsorption system with silica gel-$H_2O$ as the working pair suitable for the long-term storage of low-temperature heat was developed within the HYDES project [26–28]. The developed storage system consists of multiple storage units combined with solar collectors (**Figure 6**). Each storage unit includes an absorber with an integrated heat exchanger, which is connected through a valve to a combined evaporator/condenser unit. Both the high-temperature heat for desorption and the low-temperature heat for evaporation heat are provided by the solar collectors. To study the performance of the proposed design, a prototype with two sorption storage units with a combined volume of 1.25 $m^3$ (1.1 $m^3$ of silica gel) connected to solar collectors with an area of 20.4 $m^2$ was installed in a low energy house to provide heating and domestic hot water production. Two heat sink options for condensation were provided, namely, a 10 $m^3$ rainwater reservoir for simultaneous condensation (with desorption) and water from the solar plant loop (as in evaporation) for asynchronous condensation. The experimentally determined storage density of silica gel was around 20% lower from the theoretically expected value (i.e., 123 kWh/$m^3$ compared to 150 kWh/$m^3$).

The follow-up project of HYDES was called MODESTORE [26–29]. Within this project, a second-generation storage module prototype was developed (**Figure 7**). To improve the performance, the reactor and the condenser/evaporator were combined in a single casing, thereby achieving a significantly more compact design. The reactor contains a spiral heat exchanger containing the silica gel, whereby a channel in the center is left free for vapor diffusion. In contrast to the HYDES prototype, where the evaporator was submerged at the bottom of the reservoir for the entire water for adsorption, only a small amount of water was pumped into the evaporator area at the bottom of the storage module, which significantly improved the heat transfer. The volume of laboratory-tested prototype was approximately 350 L, while the reactor contained around 200 kg of silica gel. The experimental performance of the prototype was unsatisfactory, since the energy storage density of silica gel on the prototype scale was below that of water sensible storage (50 kWh/$m^3$). The discrepancy between the material and

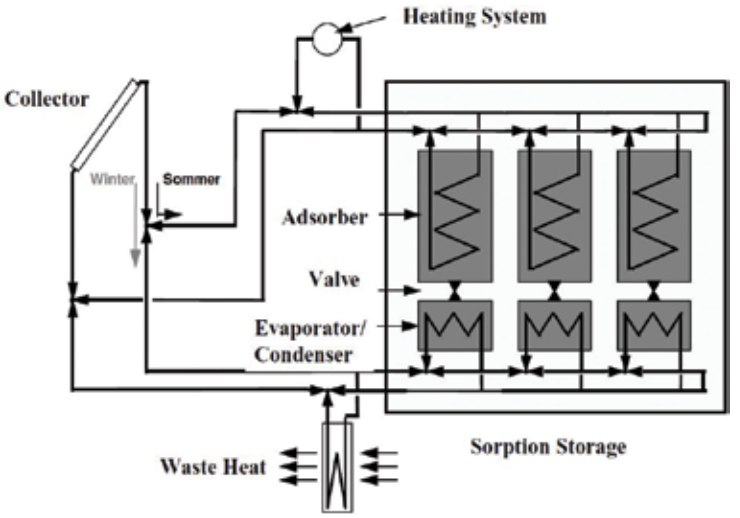


**Figure 6.** HYDES seasonal storage system concept [27].

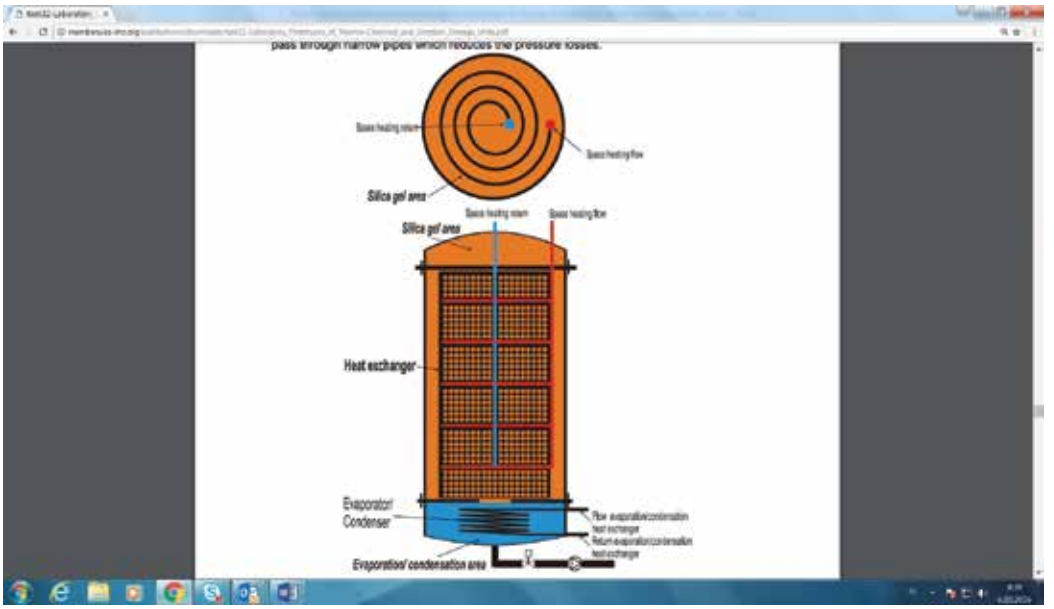


**Figure 7.** Scheme of the MODESTORE storage module prototype [29].

system scale energy densities was due to the adsorption conditions required to guarantee desorption under the temperature provided by the solar collectors and the heat sinks (i.e., silica gel water content between 3 and 13%). The authors therefore declared the working pair silica gel-$H_2O$ as unsuitable for solar energy storage systems for building applications. Stritih and Bombač [30] came to the same conclusion with a similarly designed closed storage unit prototype with silica gel-$H_2O$ working pair, but on a smaller scale (5.7 kg of silica gel).

Schreiber et al. [31] developed a laboratory-scale closed heat storage unit with zeolite 13X and water as the adsorption pair suitable for cogeneration in industrial batch processes (i.e., brewery). The design of the storage unit is similar to that of the MODESTORE prototype, since the absorber and evaporator/condenser unit are integrated into a single container (**Figure 8**) without valves in between. In contrast to the MODESTORE module, a lamellae heat exchanger is used in the reactor bed, while thermal oil was used as the heat transfer fluid to allow temperatures higher than 100°C. For the evaporator/condenser heat exchanger, water was used as the heat transfer fluid. The absorber contained 20 kg of zeolite. In the experiment, the heat supply was provided via an electric heater, while the heat demand was emulated using a water reservoir, which was heated during the discharging process. Measurements were conducted with constant power of the electric heater. The temperature was 120°C during adsorption, while the charging temperature was up to 200°C (i.e., too high for solar energy storage). Three temperature profiles for evaporation/condensation were tested, namely, 60/90°C, 90/60°C and 90/90°C. The results of the study showed a strong dependence between the storage unit performance and the evaporation/condensation temperatures, whereby a low evaporation temperature proved to be crucial.

Lu et al. [32] developed a closed adsorption cold storage system also using zeolite 13X and water as a working pair. The system has been installed in an internal combustion engine locomotive for producing chilled water for air conditioning the driver's cab. In contrast to the previously mentioned closed system with zeolite-$H_2O$ working pair [31], the evaporator and condenser are separate units, since the evaporator is used to absorb heat from the cabin (**Figure 9**). During charging, the adsorbent bed is heated by the locomotive's internal combustion engine exhaust gasses, while ambient air is used to cool the condenser and the adsorber

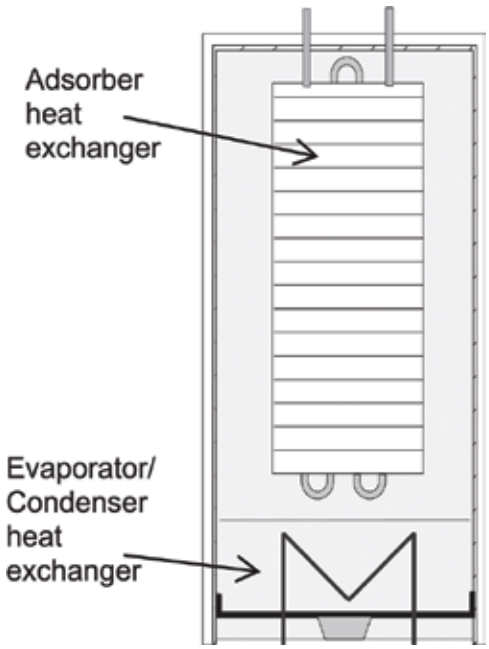


**Figure 8.** Scheme of the closed zeolite-$H_2O$ heat storage unit [31].

during discharging. The prototype system was filled with 140 kg of zeolite grains and 185 kg of water. The system reached an average cooling power of 4.1 kW, while a maximum storage capacity of 5.5 kWh was obtained at an adsorption bed temperature of 125°C. Since the expected maximal storage capacity was 23.3 kWh, the authors concluded that heat and mass transfer of the adsorber need to be improved for better performance.

Lass-Seyoum et al. [33, 34] developed a large-scale adsorption storage system (volume 750 L) with water and an unspecified porous material as the adsorption pair. The storage systems consist of two subsystems connected by a valve, i.e., the storage reactor and the evaporator/condenser unit (**Figure 10**). The reactor contains a copper matrix heat exchanger, which enables to reach a relatively uniform temperature distribution in the reactor (**Figure 10**). Solar thermal heat pipes with a capacity of 4 kW served as the high temperature source. Several dynamic performance tests were carried out. The maximum charging temperature varied between 100 and 120°C, while the maximum discharging temperatures lied in the interval 65–70°C. The daily average heat output ranged between 2.5 and 3 kW. The achieved material energy storage density was 30–40% lower than the values expected from laboratory tests due to the significantly lower charging temperatures (laboratory 220–250°C). For this reason, the authors intend to use a storage material more suitable for the available charging temperature range in the developed storage system.

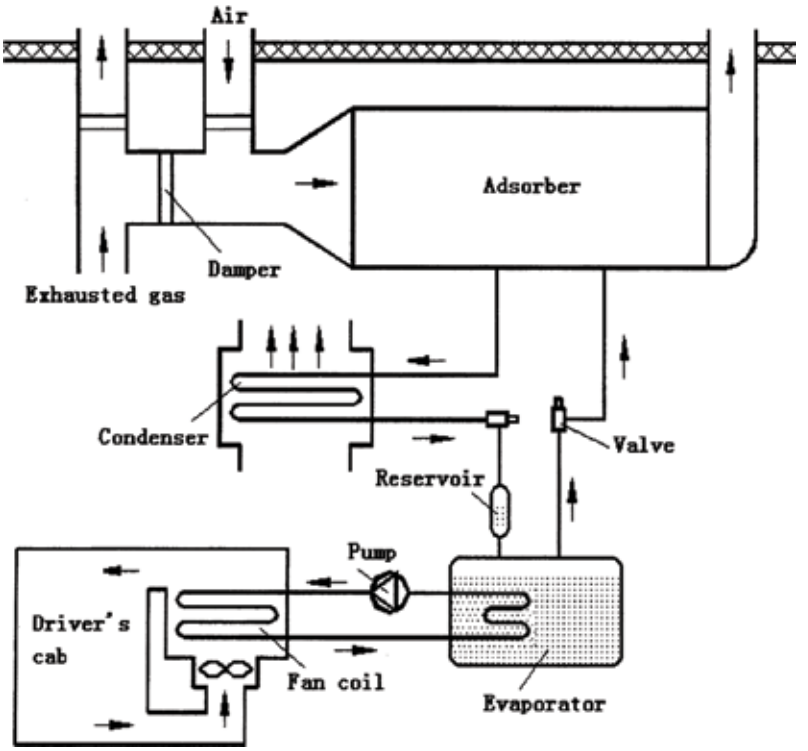


**Figure 9.** Closed adsorption cold storage system [32].

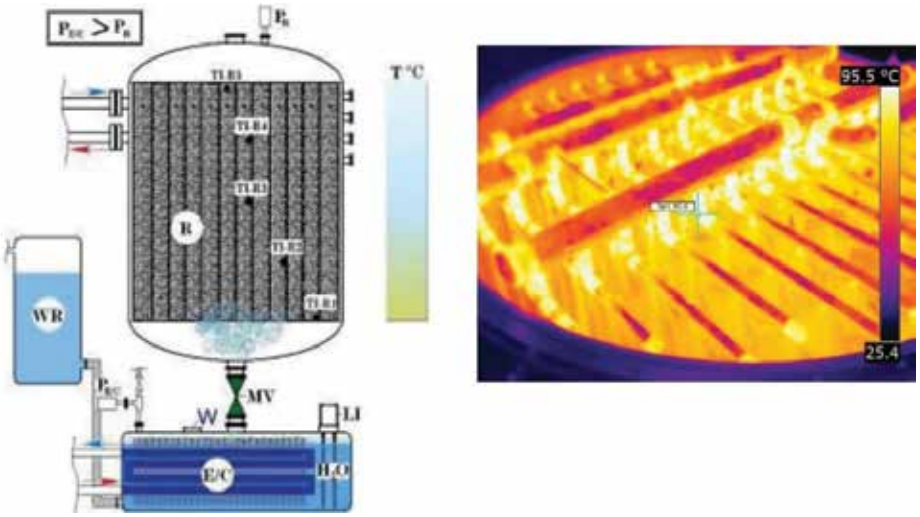


**Figure 10.** 750 L closed adsorption heat storage prototype: (left) scheme [33]; (right) temperature distribution inside the reactor [34].

TNO [35–37] developed and built modular seasonal storage system, whereby zeolite 5A and water were chosen as the reactants. The system basically consists of two separate cylindrical vessels, i.e., heat storage (reactor) and evaporator/condenser (single) unit, connected to a high- and low-temperature heat source. The reactor is built of parallel arranged and finned heat exchangers packed with zeolite (**Figure 11**), placed in a stainless steel vessel. The evaporator/condenser unit consists of a combination of a copper fin connected on one side to a copper spiral and a capillary working material on the other side with a heat exchange area of 1.4 $m^2$ (**Figure 11**). A prototype filled with 41 kg of zeolite corresponding to a storage capacity of 3 kWh was constructed, consisting of one reactor and one evaporator/condenser unit. A 12 kW electrical heater served as the high temperature source, while thermostatic water bats were used as a low-temperature heat source (evaporator) and/or heat sink (condensation, discharging). Although the test results were in accordance with expectations, i.e., maximal heat storage 4 kWh and heat output between 0.7 and 1.6 kW, the system energy density was around 73% lower than the material energy density (22 versus 83 kWh/$m^3$). The authors expect that an approximately 60% performance increase can be achieved by optimizing the system.

### 3.2. Open systems

Within the project MONOSORP [38, 39], an open adsorption heat storage with zeolite 4A and water as adsorption pair was developed. The storage system was designed for the inclusion in a building ventilation system with heat recovery. During discharging, the exhaust air flow is blown through the sorption material, which leads to a rise in temperature and dehumidification. The leaving air stream is then guided into an air to air heat exchanger (**Figure 12**) where it releases heat to the fresh air stream. Because the air that exits the sorption material is not appropriate for direct ventilation of the building, the heat recovery with fresh air through the

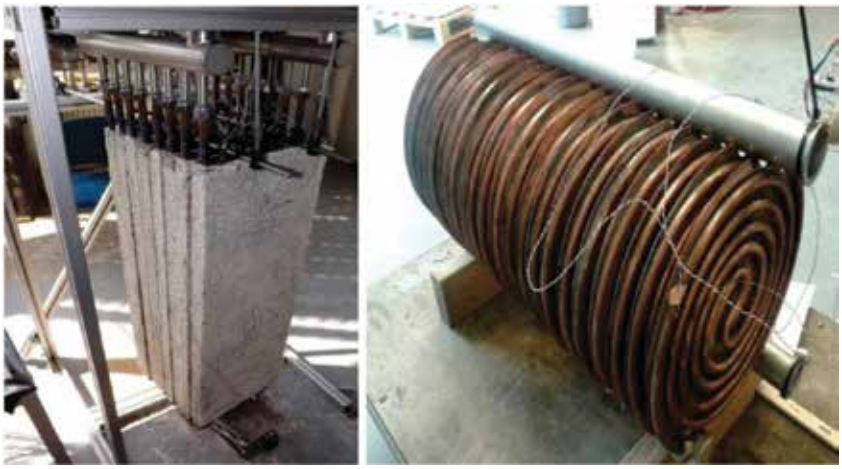

**Figure 11.** TNO adsorption storage module: (left) adsorber/desorber unit; (right) evaporator/condenser unit [37].

heat exchanger is taking place. To achieve a good heat transfer between air flow and sorption material, honeycomb monoliths with a numerous straight, small channels (large contact area) were developed and made by extrusion of zeolite 4A powder (**Figure 12**). Apart from the good heat transfer, the main advantage of these structures is the low pressure loss. The only required component aside from the monolith container is a water to air heat exchanger (**Figure 12**), which is connected to solar collectors (i.e., high-temperature heat source). Since a desorption temperature above 160°C was required, only evacuated tube collectors were suitable. The laboratory prototype (**Figure 12**) with storage volume of 100 L (62 kg of zeolite) was built and connected to 4.4 $m^2$ of collectors via a finned tube heat exchanger. For air to air heat recovery, a plate heat exchanger was used. Both heat exchangers were commercially available, not specifically designed for adsorption heat storage. The prototype preformed satisfactory with an energy density of 130 $kWh/m^3$ (without sensible heat) and a heat output between 1 and 1.5 kW, whereby a maximal temperature lift of 22°C was achieved. The charging rate on the other side ranged from 2 to 2.5 kW. The discharging rate could be increased with additional humidification of the exhaust air. Apart from this, the major drawbacks of the proposed systems are the high desorption temperature and the high material and production costs.

The follow-up project of MONOSORP is called SolSpaces [40, 41]. Within SolSpaces, a new solar heating system, including adsorption storage for seasonal energy storage with binderless zeolite 13X as adsorbent, has been developed. The system concept is similar to the MONOSORP project with the difference that air solar collectors were used (**Figure 13**), therewith eliminating the need for a water to air heat exchanger. The projects also differ in the reactor design. In contrast to MONOSORP, a packed bed of zeolite spheres is used instead of honeycomb monoliths. The storage has been further subdivided into smaller segments (**Figure 13**) to improve the thermal performance (i.e., reduced heat capacities and heat losses). The developed system has been built up in full scale in a research building with vacuum tube air collectors for testing and demonstration. Although the building has an area of only 43 $m^2$, it is comparable to larger buildings, since it has a relatively high specific heat demand due to a large surface-to-volume

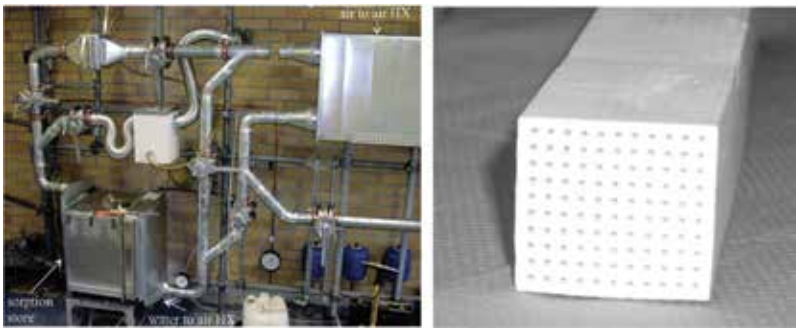

**Figure 12.** MONOSORP prototype: (left) laboratory setup; (right) zeolite monolith [39].

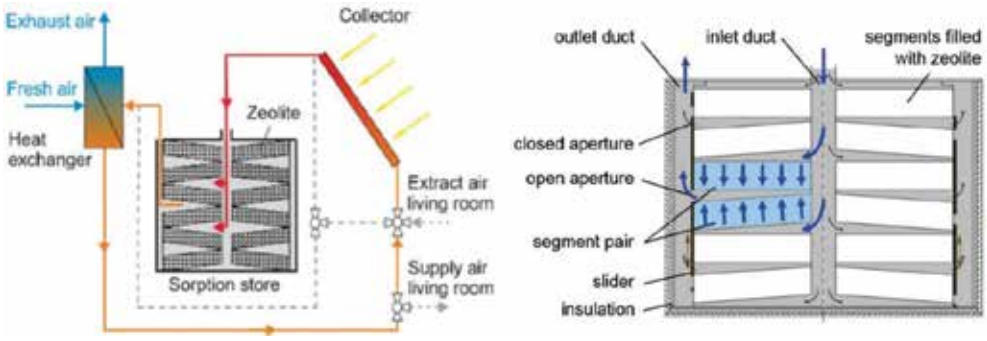


**Figure 13.** SolSpaces project: (left) heating system scheme; (right) vertical cut through the storage systems [40].

ratio. The built storage unit has a total volume of 8 $m^3$ and is filled with 4.3 $m^3$ of zeolite grains (diameter 2 mm) with a heat storage capacity of around 700 kWh. The unit is divided into four quadrants according to the top view and each quadrant itself is subdivided into six segments as is shown in cross-section on right side of **Figure 13**. Each of the two stacked segments form a pair (12 pairs total). The selection of the segment pairs is realized through the opening and closure of apertures in the outlet ducts by a slider mechanism, which is the only moving part within the reactor. Airflow inlet is at the top of the inlet duct, which is placed at the center of the unit. The airflow exits the inlet duct through one of the four ducts on the vertical edges. Airflow can pass through each segment pair individually so the segment pairs can be adsorbed and desorbed separately. On the right side of **Figure 13**, the airflow through the unit is shown for a middle segment pair, which is colored blue. On an exemplary (discharging) operation day, the discharging rate varied between 565 and 790 W, while a temperature lift between 22 and 28°C was achieved. The experiments also showed that the flow through two segments of a segment pair is quite homogeneous, meaning that the charging and discharging process takes place simultaneously in both segments. The authors plan to further monitor the developed system also during the discharging period. Same as for the MONOSORP prototype, the heat output could be increased with humidifying the exhaust air stream before it enters the storage unit. Dividing the unit into segments gives lower pressure drop of air through the unit, greater heat transfer and no dead volume of sorption material.

Within the CWS [42–46] project, a seasonal solar storage system for a composite material of zeolite and salt was developed. The system was designed for integration in a solar combi-system, i.e., solar collectors alternatively heat the combined storage tank or supply the heat required for desorbing the storage material. The main difference from the previously mentioned projects lies in the design of the sorption storage unit. In contrast to the MONOSORP and SolSpaces units, where sorption reactions occur within the storage vessel, the CWS storage unit consists of an external reactor in which the adsorption/desorption takes place and a separate storage vessel for hydrated and dehydrated storage material as well as a material transport system (**Figure 14**). The reactor consists of two chambers: one chamber to load the material and one chamber to regenerate it. Both chambers are separated by an air to HTF (e.g., water, oil) heat exchanger (**Figure 14**). During the reaction, the material is filled into the reactor from the top and emptied through the outlet at the bottom, driven only by gravity. The air enters the reactor from the side. The laboratory prototype reactor with a storage volume of 20 L was built with the flow cross-section area of 0.25 $m^2$ and length of 80 mm. A thermostat connected to an air to oil heat exchanger in the reactor was used alternately as heat source or heat sink. The experiment was carried out with zeolite 13X as the adsorbent. Although the prototype suffered from significant heat losses (37% of released heat) due to the uninsulated reactor, the prototype achieved a satisfactory heat output of 750 W and a 30°C temperature lift.

ZAE Bayern designed and installed an adsorption storage system with zeolite 13X as adsorbent for providing space heating and cooling to a school and jazz club connected to district heating system [27, 47]. The built storage system contains 7000 kg of zeolite and consists of three cylindrical storage modules connected in series: a humidifier, water reservoir (for humidification) and a control unit (**Figure 15**). The storage units are connected to the district heating system via a heat exchanger on the supply side and a combined air/radiator/floor heating system on the demand side. The storage system is used as a buffer between the district heating system and space heating

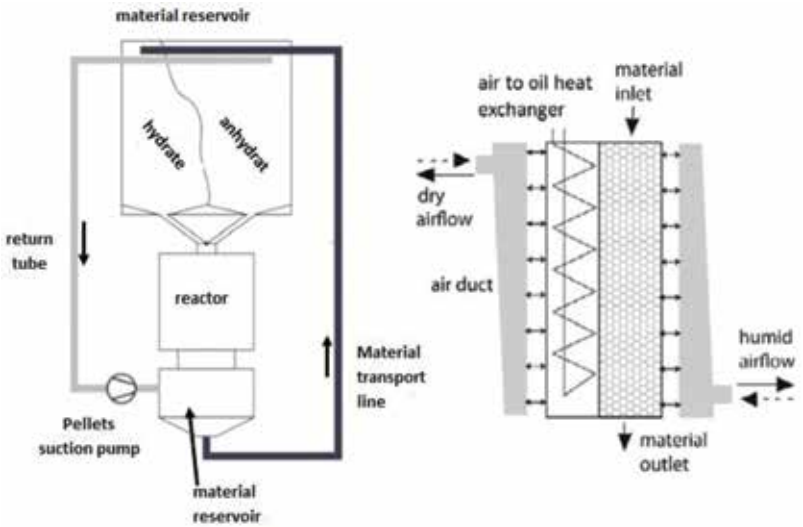


**Figure 14.** Separate adsorption storage: (left) unit concept; (right) reactor design [45].

system of the school. The storage is charged by the district heating system during off-peak periods (desorption temperatures between 130 and 180°C), while during peak hours, the building heating system can be powered only by the energy stored in the zeolite, thereby reducing the peak power demand of the district heating system. During monitoring, the system reached a 19% lower energy density than the theoretical maximum value, namely 124 kWh/m$^3$. In order to use the storage system as a desiccant cooling device for the mentioned jazz club, the system was additionally upgraded with a heat recovery device (exhaust air) to cool the dried supply air exiting the zeolite modules and a supply air humidifier to adiabatically cool the air afterward. The heat recovery device consisted of an exhaust air humidifier with an integrated heat exchanger and the supply air heat exchanger, which were connected by a fluid circuit. Three desorption temperatures were tested, namely 130, 100 and 80°C. The corresponding achieved energy densities (in the same order) are as follows: 168, 105 and 100 kWh/m$^3$. Although higher energy densities were achieved at higher desorption temperatures, the best overall system performance (COP) was achieved at the lowest tested desorption temperature (i.e., 0.87). The rough economic analysis showed that the payback time of the installed adsorption storage system was estimated to be 7–8 years and is dependent on the price reduction for the off-peak thermal energy, the investment costs and the number of storage cycles. The authors concluded that the system performance could further be enhanced with an improvement and simplification of the operation control strategies.

Zettl et al. developed a revolving drum reactor for open adsorption heat storage systems [48, 49]. The reactor was designed as a slowly rotating cylindrical drum to enable a steady mixing of the storage material in granular form in order to reach homogeneous temperatures and to avoid overhydration of the storage material. Air is supplied/extracted from the reactor through pipe-in-pipe air inlet/outlet construction, whereby the supply air is blown through the outer part while the extracted air leaves the reactor through the central pipe (**Figure 16**). The main advantage of this design is that in contrast to fixed bed reactors no reaction front is formed, since adsorption takes place throughout the whole storage material volume due to bed rotation. The laboratory prototype reactor with a maximum design heat output of 1.5 kW was built (**Figure 16**). It was filled with 70 L of a granular storage material, i.e., alternately zeolite 4A (53 kg) and zeolite MSX (50 kg), covering a volume fraction of about 80% of the interior.

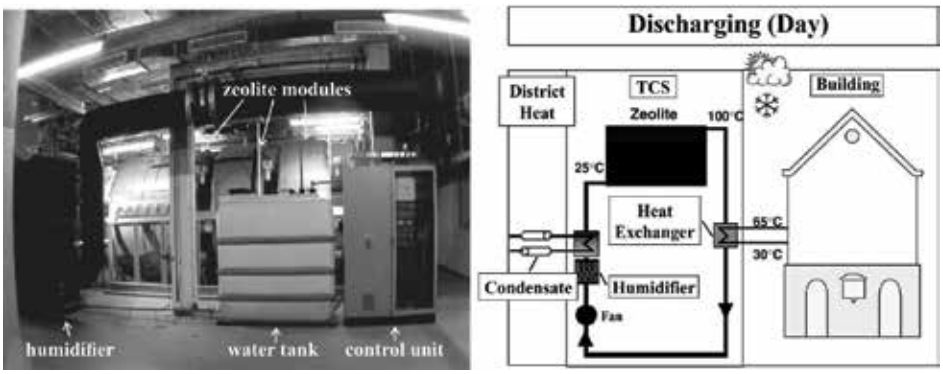


**Figure 15.** Large-scale open adsorption storage system connected to district heating system [47].

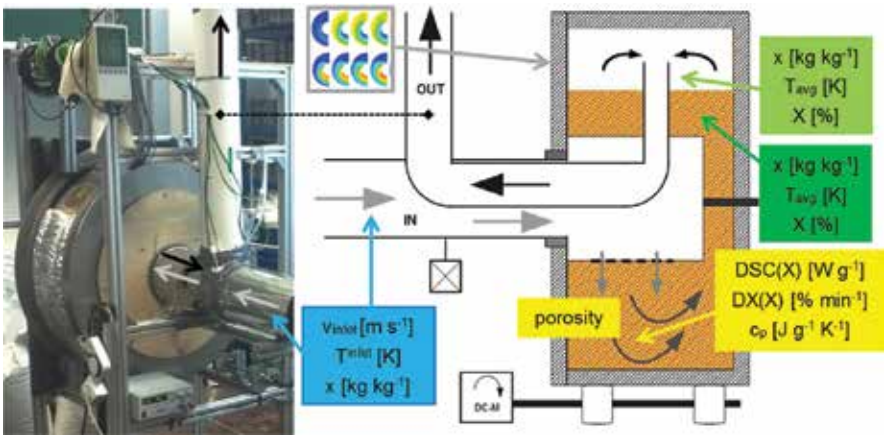


**Figure 16.** Revolving drum reactor: (left) laboratory setup; (right) cross-section sketch [49].

Special care was taken in the design of the reactor interior to avoid abrasion of the storage material (e.g., no sharp edges). Only adsorption was monitored in the reactor, desorption took place in a conventional drying oven prior to the adsorption tests. During the adsorption tests, the inlet air was adiabatically humidified. Both materials reached a comparable maximum temperature lifts of 36°C. The test with zeolite 4A generated 10.5 kWh of heat and 11.9 kWh was reached with zeolite MSX, which correspond to a stored energy density of 148 kWh/m$^3$ for zeolite 4A and 154 kWh/m$^3$ for zeolite MSX. The average heat output during the tests was 1.2 kW, while the combined electric energy use for drum rotation and fan operation was around 100 W. The authors plan to upscale the developed reactor to a realistic size, with which airflow velocity, pressure drop of airflow and specific fan power will be reduced. Special care will be taken on the containment material to guarantee loss-free storage. With upscaling of the storage unit, 16 m$^3$ storage volume filled with zeolite and material dehydration at 180°C would be required

**Figure 17.** Experimental setup of an open adsorption storage system with reactors in parallel configuration [50].

to achieve energy savings of 80%. But for realistic evaluation, other aspects of investigation needs to take place like efficient desorption and building integration.

Johannes et al. [50] designed a high-powered energy-dense zeolite heat storage system with the intention to shave the electricity peak loads in a house by reducing the heating part of the demand. A packed bed reactor system was built containing 80 kg of zeolite 13X, which was split into two equal-sized reactors, in order to test serial and parallel configurations of reactors. The whole system consists of two reactors and ducts to drive the airflow into the reactors (**Figure 17**). An air treatment system was used to prepare (i.e., heat and/or humidify) the airflow during the experiments. Several tests have been carried out both during discharging and charging at various flow rates, relative humidity and temperatures of hydration. The experiments revealed that serial configuration of reactors is unsuitable because the thermal mass of the second reactor draws heat from the first one in serial configuration, which results in a unstable maximum heat output during discharging. For parallel configuration, the results show that the reactor is able to supply a constant power of 2.25 kW for more than 2 hours, while the COP varied between 1.7 and 6.8 depending on the air temperature during charging and air humidity during discharging. For the next step, the authors plan to validate a numerical model of the system to further optimize the developed storage system as well as to numerically asses the performance when coupled to a building.

Within the FlowTCS project [51], an open adsorption storage system with an external reactor configuration has been developed, whereby zeolite and salt-impregnated zeolite were used as the sorbent. The storage system consists of a reactor with approximately 30 L of zeolite and the adsorbent storage reservoir with a volume of 200 L, thereby achieving a high flexibility regarding both storage capacity and heat output. The reactor is designed as a quasicontinuous cross-flow reactor, i.e., the adsorbent flows down through the reactor led by gravity and controlled by a rotary valve through which it is discharged out of the reactor (**Figure 18**).

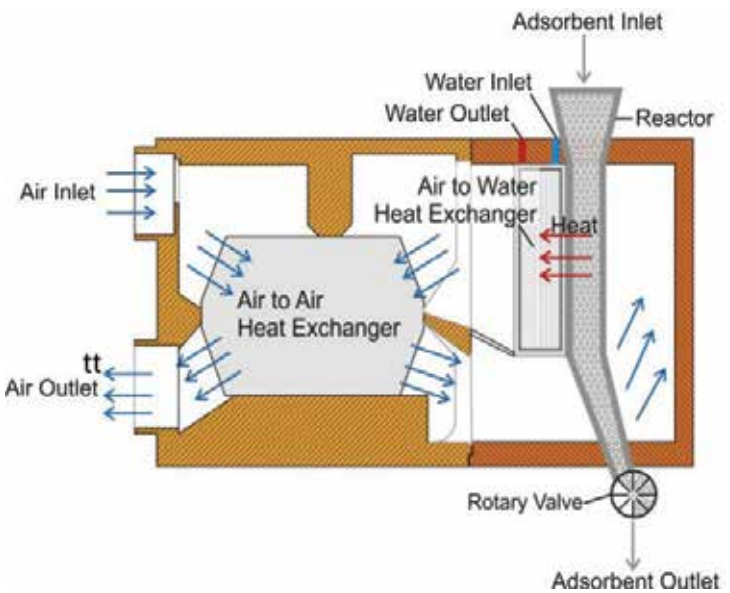


**Figure 18.** External reactor concept during discharging [51].

The heat released during discharging is transported to the heating system/buffer store via an air to water heat exchanger. During charging, the air is heated up in the air to water heat exchanger. For heat recovery, an air to air heat exchanger was additionally integrated into the reactor unit. The storage system was experimentally tested by varying the air humidity and the heating demand. The system performance was in compliance with the theoretically expected thermal power and temperature lift based on the heat storage density of the adsorbent. The developers further plan to increase the system compactness, reduce heat losses and lower the charging temperature and also to test the concept in an in situ setup.

## 4. Conclusions

Thermochemical heat storage is considered as the only storage concept with a potential for long-term low-temperature heat storage of high enough storage density to be also economically attractive. In this paper, thermochemical heat storage technologies and systems were reviewed. The studies were reviewed based on used storage materials, system configuration as well as models to predict and optimize system performance. Emphasis was placed on systems suitable for solar energy utilization in buildings.

In the paper, an overview of working pairs studied for thermochemical heat storage and transformation applications was given, but none of the presented materials meet the requirements for large-scale low-temperature heat storage applications due to unsuitable operating conditions (i.e., too high charging temperature), too low energy density and discharging temperature, corrosiveness, thermal/chemical instability, environmentally unfriendly production or high cost. The most promising are solid materials that participate in reversible chemical and physical sorption processes with water vapor as sorbate. The focus of material research has been on zeolites and their composites with hygroscopic inorganic salt hydrates and on microporous aluminophosphates. Nevertheless, one issue is common to all sorption storage materials, i.e., the discrepancy between the material and system energy storage density.

One of the main reasons that the prototypes do not achieve the storage capacity expected based on the material energy storage density is insufficient heat and mass transfer inside the reactor. In this regard, open reactor concepts have an advantage over closed reactor configuration, since the heat transfer fluid is in direct contact with the solid reactant, while closed systems require a separate heat transfer loop and hence a heat exchanger in the reactor. Additionally, the design of open systems is much simpler and consequently cheaper compared to closed systems, because they do not require the use of condensers, evaporators and working fluid storage reservoirs.

However, weather conditions are limiting the operation of open systems, i.e., supply air must be humidified when the ambient moisture content is insufficient (e.g., during winter). Another issue limiting the performance of sorption storage systems is the sensible heat loss during charging and discharging as a consequence of heating up the sorbent material and consequently the reactor to the charging/discharging temperature. Therefore, modular, moving beds and fluidized bed reactors are favorable. Also, attention should be paid on building reactors from materials with lower thermal mass, yet with comparable thermal conductivity, than the usually used steel alloys.

Since seasonal storage requires a steady and continuous heat output when discharging, the reactor bed must be optimized in such a way that it guarantees a constant flow rate to enable stable heat output during discharging. In order to achieve this without sacrificing the heat storage unit, compactness numerical modeling techniques have to be employed in the reactor design phase. The review of literature indicates that in the majority of solid-gas adsorption processes modeling efforts, the Dubinin-Polanyi theory is applied for describing adsorption equilibria, while Darcy's law and LDF model are used to predict the pressure gradient inside the adsorbent bed and the adsorption rate.

To conclude, the storage materials represent a bottleneck for the development of thermochemical heat storage systems. Therefore, in order to achieve the commercial breakthrough of thermochemical heat storage systems, a bottom-up approach of storage material engineering is needed, i.e., during material development, the required material characteristics have to be redefined according to the dynamics of the thermochemical process in the particular storage design, thereby obtaining a better understanding of the relations between material synthesis procedures, structural properties and system-level properties. In addition, a significant performance increase can also be expected from the optimization of the storage system's control strategies.

## Author details

Uroš Stritih* and Urška Mlakar

*Address all correspondence to: uros.stritih@fs.uni-lj.si

Faculty of Mechanical Engineering, University of Ljubljana, Ljubljana, Slovenija

## References

[1] European Commision. Directive 2002/91/EC of the European Parliament and of the council of 16 December 2002 on the energy performance of buildings. Official Journal of the European Union. 2002:65-71. DOI: 10.1039/ap9842100196

[2] EU. Directive 2010/31/EU of the European Parliament and of the council of 19 may 2010 on the energy performance of buildings (recast). Official Journal of the European Union. 2010:13-35. DOI: 10.3000/17252555.L_2010.153.eng

[3] Ristić A, Logar NZ, Henninger SK, Kaučič V. The performance of small-pore microporous aluminophosphates in low-temperature solar energy storage: The structure-property relationship. Advanced Functional Materials. 2012;**22**:1952-1957. DOI: 10.1002/adfm.201102734

[4] N'Tsoukpoe KE, Liu H, Le Pierres N, Luo L. A review on long-term sorption solar energy storage. Renewable and Sustainable Energy Reviews. 2009;**13**:2385-2396. DOI: 10.1016/j.rser.2009.05.008

[5] Hauer A. Sorption theory for thermal energy storage. Thermal Energy Storage for Sustainable Energy Consumption. 2007:393-408. DOI: 10.1007/978-1-4020-5290-3_24

[6] McGlashan ML. Manual of symbols and terminology for physicochemical quantities and units. Pure and Applied Chemistry; 1970

[7] Yu N, Wang RZ, Wang LW. Sorption thermal storage for solar energy. Progress in Energy and Combustion Science. 2013;**39**:489-514. DOI: 10.1016/j.pecs.2013.05.004 Review

[8] Bales C. Thermal properties of materials for thermo-chemical storage of solar heat. Development. 2005;**20**

[9] Aydin D, Casey SP, Riffat S. The latest advancements on thermochemical heat storage systems. Renewable and Sustainable Energy Reviews. 2015;**41**:356-367. DOI: 10.1016/j.rser.2014.08.054

[10] Tatsidjodoung P, Le Pierres N, Luo L. A review of potential materials for thermal energy storage in building applications. Renewable and Sustainable Energy Reviews. 2013;**18**:327-349. DOI: 10.1016/j.rser.2012.10.025

[11] Solé A, Martorell I, Cabeza LF. State of the art on gas-solid thermochemical energy storage systems and reactors for building applications. Renewable and Sustainable Energy Reviews. 2015;**47**:386-398. DOI: 10.1016/j.rser.2015.03.077

[12] Henninger SK, Jeremias F, Kummer H, Schossig P, Henning HM. Novel sorption materials for solar heating and cooling. Energy Procedia. 2012;**30**:279-288. DOI: 10.1016/j.egypro.2012.11.033

[13] Henninger SK, Schmidt FP, Henning HM. Water adsorption characteristics of novel materials for heat transformation applications. Applied Thermal Engineering. 2010;**30**:1692-1702. DOI: 10.1016/j.applthermaleng.2010.03.028

[14] Henninger SK, Schmidt FP, Nunez T, Henning HM. Monte Carlo investigations of the water adsorption behavior in MFI type zeolites for different Si/al ratios with regard to heat storage applications. Adsorption. 2005;**11**:361-366. DOI: 10.1007/s10450-005-5951-2

[15] Gordeeva YIALG, Resticcia G, Cacciola G. Selective water sorbents for multiple applications, 5-libr confined in mesopores of silica-gel-sorption properties. Reaction Kinetics and Catalysis Letters. 1998;**63**:81-88

[16] Levitskij EA, Aristov YI, Tokarev MM, Parmon VN. "Chemical heat accumulators": A new approach to accumulating low potential heat. Solar Energy Materials & Solar Cells. 1996;**44**:219-235. DOI: 10.1016/0927-0248(96)00010-4

[17] Mrowiec-Białoń J, Jarzębski AB, Lachowski AI, Malinowski JJ, Aristov YI. Effective inorganic hybrid adsorbents of water vapor by the sol–gel method. Chemistry of Materials. 1997;**9**:2486-2490. DOI: 10.1021/cm9703280

[18] Aristov YI. $SiO_2$–LiBr nanocomposite sol–gel adsorbents of water vapor. Preparation and Properties. 1999;**503**:500-503

[19] Zhu D, Wu H, Wang S. Experimental study on composite silica gel supported CaCl2 sorbent for low grade heat storage. International Journal of Thermal Sciences. 2006;**45**:804-813. DOI: 10.1016/j.ijthermalsci.2005.10.009

[20] Ponomarenko IV, Glaznev IS, Gubar AV, Aristov YI, Kirik SD. Synthesis and water sorption properties of a new composite "CaCl2 confined into SBA-15 pores". Microporous and Mesoporous Materials. 2010;**129**:243-250. DOI: 10.1016/j.micromeso.2009.09.023

[21] Henninger SK, Munz G, Ratzsch KF, Schossig P. Cycle stability of sorption materials and composites for the use in heat pumps and cooling machines. Renewable Energy. 2011;**36**:3043-3049. DOI: 10.1016/j.renene.2011.03.032

[22] Lohse U, Löffler E, Kosche K, Jänchen J, Parlitz B. Isomorphous substitution of silicon in the erionite-like structure AIP04-17 and acidity of SAPO-17. Zeolites. 1993;**13**:549-556. DOI: 10.1016/0144-2449(93)90232-R

[23] Rajić N, Gabrovšek R, Ristić A, Kaučič V. Thermal investigations of some AlPO and MeAPO materials prepared in the presence of HF. Thermochimica Acta. 1997;**306**:31-36. DOI: 10.1016/S0040-6031(97)00292-X

[24] Floquet N, Coulomb JP, Dufau N, Andre G, Cnrs CRMC, De Luminy C, Cedex M. Structure and dynamics of confined water in AlPO 4-5 zeolite. The Journal of Physical Chemistry. B. 2004;**108**:13107-13115

[25] De Geus A. Development of a seasonal thermochemical storage system. Energy Procedia. 2012;**30**:207214. DOI: 10.1016/j.egypro.2012.11.025

[26] Gartler G, Jähnig D, Porkarthofer G, Wagner W. Development of a High Energy Density Sorption Storage System, EuroSun; 2004. http://download.aee-intec.at/0uploads/dateien7.pdf

[27] Hauer A. Adsorption Systems for Tes—Design and Demonstration Projects. Thermal Energy Storage for Sustainable Energy Consumption. 2007;**13**:409-427. DOI: 10.1016/0378-7788(89)90020-0

[28] Wagner W, Jähnig D, Isaksson C, Hausner R. Modularer Energiespeicher nach dem Sorptionsprinzip mit hoher Energiedichte (MODESTORE), Berichte Aus Energie - Und Umweltforsch; 2006

[29] Bales C, Gantenbein P. Laboratory prototypes of thermo-chemical and sorption storage units ,Report B3—IEA SHC Task 32, Rep. B3—IEA SHC Task 32; 2007

[30] Stritih U, Bombač A. Description and analysis of adsorption heat storage device. Journal of Mechanical Engineering. 2014;**60**:619-628. DOI: 10.5545/sv-jme.2014.1814

[31] Schreiber H, Graf S, Lanzerath F, Bardow A. Adsorption thermal energy storage for cogeneration in industrial batch processes: Experiment, dynamic modeling and system analysis. Applied Thermal Engineering. 2015;**89**:485-493. DOI: 10.1016/j.applthermaleng.2015.06.016

[32] Lu YZ, Wang RZ, Zhang M, Jiangzhou S. Adsorption cold storage system with zeolite-water working pair used for locomotive air conditioning. Energy Conversion and Management. 2003;**44**:1733-1743. DOI: 10.1016/S0196-8904(02)00169-3

[33] Lass-Seyoum A, Blicker M, Borozdenko D, Friedrich T, Langhof T. Transfer of laboratory results on closed sorption thermo-chemical energy storage to a large-scale technical system. Energy Procedia. 2012;**30**:310-320. DOI: 10.1016/j.egypro.2012.11.037

[34] Lass-Seyoum A, Borozdenko D, Friedrich T, Langhof T, Mack S. Practical test on a closed sorption thermochemical storage system with solar thermal energy. Energy Procedia. 2016;**91**:182-189. DOI: 10.1016/j.egypro.2016.06.200

[35] Cuypers R, Maraz N, Eversdijk J, Finck C, Henquet E, Oversloot H, Van't Spijker H, De Geus A. Development of a seasonal thermochemical storage system. Energy Procedia. 2012;**30**:207-214. DOI: 10.1016/j.egypro.2012.11.025

[36] Finck C, Van Spijker H, De Jong A, Henquet E. Design of a modular 3 kWh thermochemical heat storage system for space heating application, SESB- 2nd Int. Conf. Sustain. Energy Storage; 2013

[37] Finck C, Henquet E, Van Soest C, Oversloot H, De Jong AJ, Cuypers R, Van T'Spijker H. Experimental results of a 3 kWh thermochemical heat storage module for space heating application. Energy Procedia. 2014;**48**:320-326. DOI: 10.1016/j.egypro.2014.02.037

[38] Kerskes H, Heidemann W, Müller-Steinhagen H. MonoSorp - Ein weiterer Schritt auf dem Weg zur vollständig solarthermischen Gebäudeheizung. In: Tagungsband Zum 14. Symp. Thermische Solarenergie, Otti-Technologie-Kolleg, Regensburg; 2004. pp. 169-173

[39] Kerskes H, Sommer K, Müller-Steinhagen H. MonoSorp Integrales Konzept zur solarthermischen Gebäudeheizung mit MonoSorp; 2007

[40] Weber R, Asenbeck S, Kerskes H, Drück H. SolSpaces – Testing and performance analysis of a segmented sorption store for solar thermal space heating. Energy Procedia. 2016;**91**:250-258. DOI: 10.1016/j.egypro.2016.06.214

[41] Mette B, Kerskes H, Drück H. Concepts of long-term thermochemical energy storage for solar thermal applications – Selected examples. Energy Procedia. 2012;**30**:321-330. DOI: 10.1016/j.egypro.2012.11.038

[42] Mette B, Kerskes H, Drück H. Experimental and numerical investigations of different reactor concepts for thermochemical energy storage. Energy Procedia. 2014;**57**:2380-2389. DOI: 10.1016/j.egypro.2014.10.246

[43] Kerskes H, Mette B, Bertsch F, Asenbeck S, Drück H. Development of a thermo-chemical energy storage for solar thermal applications. In: Proc. O ISES Sol. World Congr. 2011, Kassel; 2011. http://archive.iea-shc.org/publications/downloads/Task42-Development_of_a_Thermo-Chemical_Energy_Storage_for_Solar_Thermal_Applications.pdf

[44] Kerskes H, Bertsch F, Asenbeck S, Mette B, Drück H. Abschlussbericht CWS- Chemische CWS Verbundvorhaben chemische Wärmespeicherung mittels reversibler Feststoff-Gasreaktionen, Stuttgart; 2012

[45] Kerskes H, Mette B, Bertsch F, Asenbeck S, Drück H. Chemical energy storage using reversible solid/gas-reactions (CWS) - results of the research project. Energy Procedia. 2012;**30**:294-304. DOI: 10.1016/j.egypro.2012.11.035

[46] Mette B, Asenbeck S, Kerskes H, Drück H. Effizienzsteigerung thermochemischer Energiespeicher für solare Anwendungen durch Reduzierung der Regenerationstemperatur. In: 23. OTTI-Symposium Thermische Solarenergie, Bad Staffelstein; 2013

[47] Hauer A. Thermal energy storage with zeolite for heating and cooling applications. In: Proc. 7th Int. Sorption Heat Pump Conf. ISHPC, Shanghai; 2002. pp. 385-390

[48] Englmair G, Zettl B, Lager D. Characterisation of a rotating adsorber designed for thermochemical heat storage processes. In: Proc. EuroSun 2014 Conf., Aix-les-Bains; 2014. pp. 1-8. DOI: 10.18086/eurosun.2014.10.12

[49] Reichl C, Lager D, Englmair G, Zettl B, Popovac M. Fluid dynamics simulations for an open-sorption heat storage drum reactor based on thermophysical kinetics and experimental observations. Applied Thermal Engineering. 2016;**107**:994-1007. DOI: 10.1016/j.applthermaleng.2016.06.119

[50] Johannes K, Kuznik F, Hubert JL, Durier F, Obrecht C. Design and characterisation of a high powered energy dense zeolite thermal energy storage system for buildings. Applied Energy. 2015;**159**:80-86. DOI: 10.1016/j.apenergy.2015.08.109

[51] van Helden W, Yamaha M, Rathgeber C, Hauer A, Huaylla F, Le Pierrès N, Stutz B, Mette B, Dolado P, Lazaro A, Mazo J, Dannemand M, Furbo S, Campos-Celador A, Diarce G, Cuypers R, König-Haagen A, Höhlein S, Brüggemann D, Fumey B, Weber R, Köll R, Wagner W, Daguenet-Frick X, Gantenbein P, Kuznik F. IEA SHC task 42 / ECES annex 29 – Working group B: Applications of compact thermal energy storage. Energy Procedia. 2016;**91**:231-245. DOI: 10.1016/j.egypro.2016.06.210

Section 2

# Electrical Energy Storage

Chapter 4

# A Novel Highly Integrated Hybrid Energy Storage System for Electric Propulsion and Smart Grid Applications

Alessandro Serpi, Mario Porru and Alfonso Damiano

Additional information is available at the end of the chapter

http://dx.doi.org/10.5772/intechopen.73671

**Abstract**

This chapter addresses potentialities and advantages of a highly integrated hybrid energy storage system (HESS) for electric propulsion and smart grids. This configuration consists of a highly integrated battery-ultracapacitor system (HIBUC) and aims to benefit from the advantages of both passive and active HESS configurations. Particularly, the integration of the ultracapacitor module (UM) within the DC-link of the DC/AC multilevel converter enables the decoupling between DC-link voltage and energy content without the need for any additional DC/DC converter. As a result, HIBUC benefits from simplicity and energy flow management capabilities very similar to those achieved by passive and active HESS configurations, respectively. This is highlighted properly by a theoretical analysis, which also accounts for a comparison between HIBUC and both passive and active HESS configurations. Some HIBUC application examples are also reported, which highlight the flexibility and potentialities of HIBUC for both electric propulsion systems and smart grids.

**Keywords:** batteries, energy management, energy storage, electric vehicles, modeling, smart grids, supercapacitors, ultracapacitors

## 1. Introduction

Electric energy storage systems (ESSs) are widely recognized as one of the most promising technology for enabling the transition toward a sustainable energy system [1–3]. Particularly, transportation electrification is pushing toward progressive improvements of ESS technologies, especially for light- and heavy-road electric vehicles: these have to rely on on-board ESSs

for guaranteeing long mileage and short charging time. Consequently, high efficiency, low costs, small volumes, and weights are desirable. The employment of ESSs is increasingly considered also for such systems that have been propelled electrically since a long time, such as railway and ships, in order to increase system efficiency and fuel economy, as well as ensuring reliable operation of on-board power systems [4–6]. In this context, both hybrid and all-electric ships are expected to be appealing in the forthcoming future. Similarly, ESSs are a key point for designing more electric aircrafts, in which pneumatic and hydraulic actuators are being replaced with electrical ones [7]. Therefore, on-board ESSs should start the engines, maintain DC-link voltage constant over dynamic operations, and, above all, guarantee emergency power supply. ESSs can be employed successfully also for addressing several issues affecting modern power systems, such as reduced level of power quality, massive growth of distributed generation, and high penetration of renewable energy sources [8–10]. Particularly, integrating the massive and increasing share of photovoltaic and wind power plants installed all over the world is one of the main challenges for future power systems, which will be faced resorting to smart grid and microgrid concepts. In this context, ESSs are the ideal solution for mitigating power fluctuations, storing overproduction, and releasing it when required, improving overall reliability and power quality.

An ESS consists of two main stages, i.e., the power conversion system and the energy storage unit, as shown in **Figure 1**. The power conversion system is generally represented by a power electronic converter, which has to regulate ESS voltage and current levels in order to match application requirements. Whereas, the energy conversion occurs within the energy storage unit, which exchange electrical energy only, storing it into different forms (mechanical, chemical, magnetic, etc.).

There are several ESSs available on the market, which are generally classified in accordance with their energy/power density (Wh/l, W/l) or specific energy/power (Wh/Kg, W/Kg), as highlighted in **Figure 2** [11, 12]. High-energy density ESSs are able to provide large amount of energy but over long time periods, as occurring for the majority of electrochemical batteries. These are the first ESS introduced on the market and still represent the most widespread. Electrochemical batteries can be further classified based on the chemical reaction they exploit. Lead acid (PbA) is probably the most-known technology; it is being widely used on vehicles for starting, lighting, and ignition purposes. PbA batteries are currently employed when sizes and weights are not an issue, such as isolated power systems and UPSs, whereas, lithium-ion

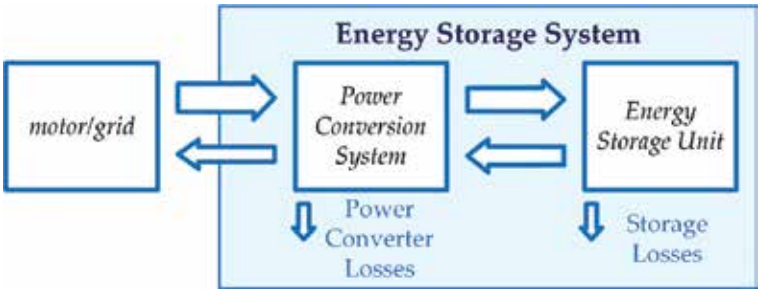


**Figure 1.** ESS schematic representation.

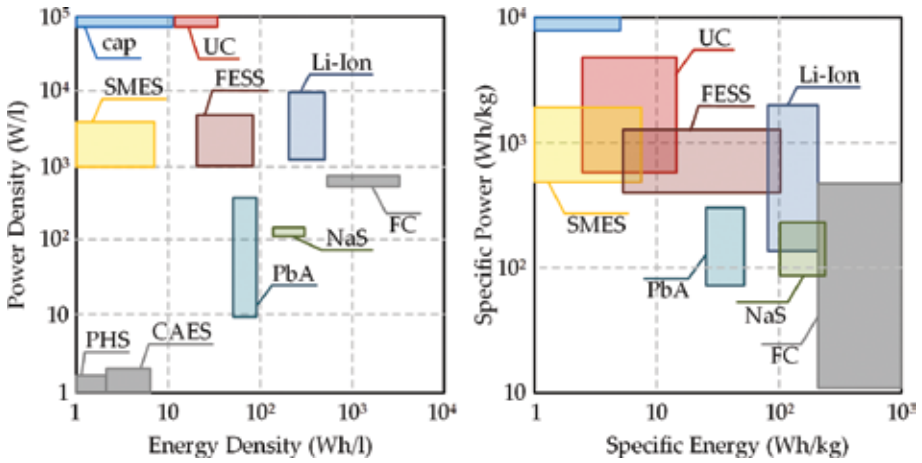


**Figure 2.** Energy/power density (left) and specific energy/power (right) of ESSs on Ragone plots: pumped hydroelectric storage system (PHS), compressed air energy storage system (CAES), and fuel cell (FC).

batteries (Li-ion) are surely the best solution for modern electric vehicles due to their very high-energy density and specific energy. However, sodium-based batteries may be preferred when high capacity is required, namely for load leveling and renewable energy sources integration. Despite their advantages, electrochemical batteries generally suffer from low power capabilities; thus, even if research is focused on improving power density, they are not yet the best solution for high-power applications [13, 14].

Differently from electrochemical batteries, high-power density ESSs can provide much little amount of energy but in very short times, which is the case of flywheel energy storage system (FESS), superconducting magnetic energy storage system (SMES), and ultracapacitors (UCs). Particularly, FESS is characterized by very high efficiency, long life expectancy, and low environmental impact. However, it presents a quite high self-discharge rate and also suffers from safety issues as far as high speeds are concerned [15–17]. Regarding SMES, a cryogenic system ensures the superconducting state of coils. Consequently, losses are due to power converters only, leading to a very high overall efficiency. Other advantages consist of fast response and wide power range, as well as long lifespan. Nevertheless, SMES is very expensive due to the high costs of both superconductors and cryogenic system; thus, although it has been recently tested for power quality and voltage stabilization in both transmission and distribution systems, it is still employed in military applications mostly [18–20]. The main advantages of UCs are high-power capability, quite long life cycle and no memory effect, but they cannot store great amount of energy unless big and costly UC modules are used. Thus, UCs have been used for power quality applications and for handling small regenerative braking on electric propulsion systems [21–23].

Based on the previous considerations, it can be stated that a single ESS technology hardly matches both energy and power application requirements. Particularly, electrochemical batteries are very suitable for providing energy services, in which high-energy storage capability is mandatory. On the other hand, FESS, SMES, and UCs are more appropriate for power services,

when high-power rates are required for very short times. In addition, further constraints may regard efficiency, life cycle, and cost, which might make one ESS technology unsuitable. In this regard, a viable and promising solution is the employment of a hybrid energy storage system (HESS), which consists of combining high-energy and high-power density ESSs in order to benefit from the advantages of different ESS technologies [24–27]. As a result, HESS may bring increased performances, higher efficiency, longer lifetime, reduced costs, and more appropriate design and sizing. Among all the ESS combinations, HESSs made up of electrochemical batteries and UCs are the most popular and promising solutions because of the perfect complementarity between their features [28–30].

Consequently, this chapter focuses on HESS made up of a battery pack (BP) and an ultracapacitor module (UM). Particularly, a brief overview of main HESS configurations and management approaches is provided in Section 2. Then, Section 3 focuses on a highly integrated HESS configuration [31–33], in which BP and UM are coupled only by means of a multilevel converter. This highly integrated battery-ultracapacitor system (HIBUC) is also compared to those described in Section 2, highlighting its most important advantages. In Section 3, two HIBUC application examples are also presented and discussed based on numerical simulations. Concluding remarks are reported in Section 4.

## 2. Overview on hybrid energy storage systems

Considering a hybrid energy storage system (HESS) made up of a battery pack (BP) and an ultracapacitor module (UM), a number of configurations have been proposed in the literature, which differ from each other mainly due to the number of power electronic converters involved. Particularly, no or few power electronic converters entail simple configurations, but poor flexibility and energy management. As the number of power electronic converters increases, energy management capability, and, thus, HESS exploitation increase, but at the cost of increased complexity, costs, volumes, and weights. The following sections investigate the most important HESS configurations, as well as their management and control strategies, by highlighting their most important advantages and drawbacks.

### 2.1. HESS configurations

HESS configurations can be roughly classified into passive and active configurations; in passive HESS, BP and UM are directly coupled to the DC-link of the DC/AC converter, as depicted in **Figure 3** [34, 35]. Therefore, BP and UM share the same voltage, which generally varies with BP state-of-charge. As a result, UM voltage cannot vary independently, resulting in its poor energy exploitation. Still referring to **Figure 3**, the following relationships can be introduced:

$$V_b = r_b i_b + L\frac{di_b}{dt} + V_{DC} \tag{1}$$

$$C_u\frac{dV_u}{dt} = i_b - i_P. \tag{2}$$

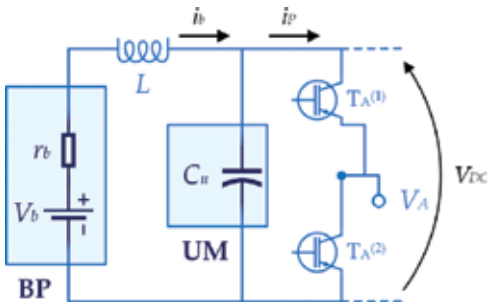


**Figure 3.** Schematic representation of passive HESS configuration.

Particularly, a simple but effective BP model has been considered, which consists of a voltage source $V_b$ series-connected with an internal resistance $r_b$, while $i_b$ is the battery current. BP is coupled to the DC-link through an inductive filter, whose inductance $L$ should prevent $i_b$ from unsuitable sudden variations, $V_{DC}$ being the DC-link voltage. Referring to Eq. (2), $C_u$ denotes the capacitance of the UM, whereas $i_P$ denotes the power current, which is proportional to the power drawn or delivered by the DC/AC converter. The DC-link energy content $E_{DC}$ and its time-variation can be expressed, respectively, as:

$$E_{DC} = \frac{1}{2} C_u V_{DC}^2 \tag{3}$$

$$\frac{dE_{DC}}{dt} = V_{DC}(i_b - i_P). \tag{4}$$

The comparison between Eq. (2) and Eq. (4) reveals a significant coupling between $E_{DC}$ and $V_{DC}$, which cannot be varied within a wide range. This results in a poor UM exploitation, as well as in an unsuitable energy management, which are the main drawbacks of this HESS configuration. Consequently, in spite of its simplicity and cheapness, passive HESS configuration is rarely used due to weak performances that make it not suitable for most applications.

Much better performances can be achieved by semi-active and active HESS configurations, which exploit one or more DC/DC converters for decoupling BP and UM [36–43]. Particularly, **Figure 4** shows an active parallel configuration, in which BP and UM are parallel-connected to the DC-link both through DC/DC converters. Referring to this configuration, the following relationships can be introduced:

$$\tilde{V}_b = L\frac{d\tilde{i}_b}{dt} + V_{DC} \ , \quad C\frac{dV_{DC}}{dt} = \tilde{i}_b + \tilde{i}_u - i_P \tag{5}$$

in which, $C$ is the capacitance of the DC-link, which is much smaller than $C_u$. Whereas

$$\tilde{V}_b = \frac{1}{k_b}(V_b - r_b i_b) \ , \quad \tilde{i}_b = k_b i_b \tag{6}$$

$$V_{DC} = \frac{1}{k_u} V_u \ , \quad \tilde{i}_u = -k_u C_u \frac{dV_u}{dt}. \tag{7}$$

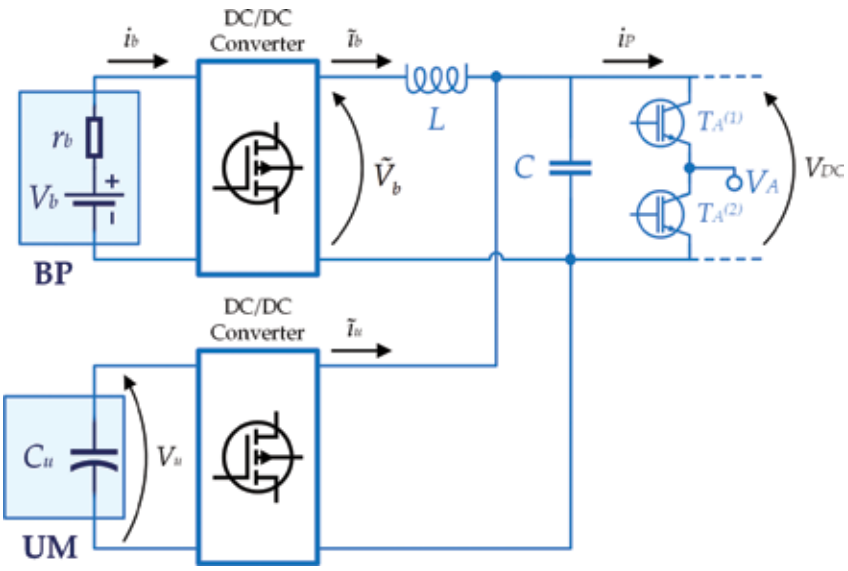


**Figure 4.** Schematic representation of active parallel HESS configuration.

Particularly, Eqs. (6) and (7) have been achieved by assuming ideal DC/DC converters, which have been modeled by simple gains ($k_b$ and $k_u$ for BP and UM, respectively). Therefore, the combination of Eq. (5) with Eqs. (6) and (7) leads to the following expressions:

$$V_b = r_b i_b + k_b^2 L \frac{d i_b}{dt} + k_b V_{DC} \tag{8}$$

$$C \frac{dV_{DC}}{dt} = k_b i_b - k_u C_u \frac{dV_u}{dt} - i_P. \tag{9}$$

Regarding the DC-link energy content, it should account not only for $C$, but also for $C_u$ in order to make the comparison with all HESS configurations consistent. Consequently, $E_{DC}$ and its time derivative can be expressed as

$$E_{DC} = \frac{1}{2} C V_{DC}^2 + \frac{1}{2} C_u V_u^2 \tag{10}$$

$$\frac{dE_{DC}}{dt} = V_{DC}(k_b i_b - i_P). \tag{11}$$

Therefore, considering both Eqs. (9) and (11), it can be seen that $V_{DC}$ and $E_{DC}$ can be controlled independently by setting the duty cycles of the DC/DC converters properly. However, Eqs. (9) and (11) are characterized by increased complexity compared to passive HESS configurations. Furthermore, these equations highlight a significant coupling among all system variables, which makes control system design a not trivial issue. Consequently, advanced management and control systems are required in order to exploit active HESS configurations properly.

### 2.2. HESS management and control

As far as semi-active or active HESS configurations are concerned, the management and control system cover a fundamental role for exploiting the HESS at the maximum extent. Particularly, an appropriate selection of HESS management strategy is of paramount importance, even from the design stage, especially for sizing BP and UM properly in accordance with target performances, and technical and economic constraints. It is fundamental also for assuring HESS efficiency, reliability, and durability.

Referring to **Figure 5**, HESS management consists mainly of a sharing criterion for splitting the overall HESS energy flow between BP and UM. Literature review reveals that several approaches have been proposed in order to exploit BP and UM inherent features to the maximum extent, preventing them from unsuitable operation as well. In this regard, UM generally handles fast power fluctuations, whereas BP copes with the average power demand. This principle is the basis of the simplest HESS management strategy known as frequency-based management (FBM); this consists of splitting the overall power demand into high- and low-frequency components, which have to be tracked by UM and BP, respectively [44, 45]. An alternative approach is the so-called rule-based management (RBM), which exploits the single ESSs in accordance with an appropriate order of priority by means of a pre-set of rules [46, 47]. In this regard, it is worth noting that FBM and RBM may be combined to each other or with fuzzy logic algorithms in order to account for ESS constraints and to improve overall HESS performances [48–51].

Although FBM and RBM are intuitive, simple, and easy to implement, they generally do not lead to optimal solutions. For this reason, another popular approach is determining BP and UM reference power profiles by minimizing suitable cost functions over a given time horizon. Hence, different optimal solving techniques can be used, such as model predictive control, mixed-integer/linear programming, nonlinear programming, and dynamic programming [52–55]. However, such solving techniques are generally complex to implement and quite time-demanding. Consequently, heuristic approaches have been also proposed, like genetic algorithms and particle swarm optimization, which achieve sub-optimal solutions but faster and with less computational efforts [56–58]. As a result, very complex and sophisticated cost functions can be considered, which can account for many system constraints and goals. The

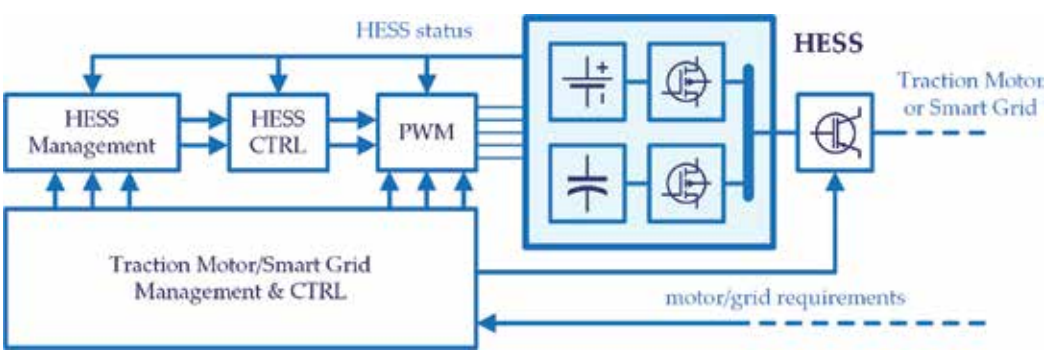


**Figure 5.** Schematic representation of an HESS management and control system.

main advantage of these approaches consists of enabling HESS to provide multiple services in an optimal manner, by both economic and technical points of view; this aspect makes HESS very competitive, especially for smart grid applications.

## 3. A novel highly integrated HESS

In order to overcome the issues arising from both passive and active HESS configurations, a highly integrated solution has been proposed by the authors in [31–33], whose schematic representation is depicted in **Figure 6**. It consists of coupling a BP with an UM through a multilevel converter, namely a three-level neutral-point-clamped converter (NPC). The key feature of the proposed highly integrated battery-ultracapacitor system (HIBUC) is the full integration of UM within the DC-link of the NPC, which decouples the overall DC-link voltage ($V_{DC}$) from its energy content ($E_{DC}$). As a result, HIBUC energy flow management is quite similar to that achieved with active HESS configurations without resorting to any DC/DC converter, as detailed in the following sections.

### 3.1. HIBUC modeling

Still referring to **Figure 6**, the DC-link of HIBUC is split into high-side and low-side due to the three-level configuration: high-side consists of the UM, whose overall voltage and capacitance are denoted by $V_u$ and $C_u$, respectively, while the low-side is made up of conventional capacitors, $V$ and $C$ being the corresponding voltage and capacitance. Hence, HIBUC main equations can be expressed as

$$V_b = r_b i_b + L\frac{di_b}{dt} + V_{DC} \ , \quad V_{DC} = V_u + V \tag{12}$$

$$C_u\frac{dV_u}{dt} = i_b - i_H \ , \quad C\frac{dV}{dt} = i_b - i_L. \tag{13}$$

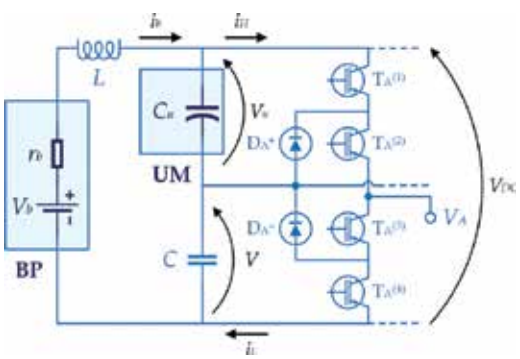


**Figure 6.** The highly integrated HESS configuration proposed in [31–33].

Whereas, the overall DC-link energy content can be determined easily as

$$E_{DC} = \frac{1}{2} C_u V_u^2 + \frac{1}{2} C V^2. \tag{14}$$

Based on both Eqs. (12) and (13), the dynamic equation of the DC-link voltage can be achieved as

$$C_{DC} \frac{dV_{DC}}{dt} = i_b - i_{DC} \ , \quad C_{DC} = \frac{C_u C}{C_u + C} \ , \quad i_{DC} = \frac{C}{C_u + C} i_H + \frac{C_u}{C_u + C} i_L \tag{15}$$

where $C_{DC}$ and $i_{DC}$ are defined as the equivalent DC-link capacitance and current, respectively. Furthermore, by time-differentiating Eq. (14) and combining the result with (13), the following relationship is achieved:

$$\frac{dE_{DC}}{dt} = V_{DC}(i_b - i_P) \ , \quad i_P = \frac{V_u}{V_{DC}} i_H + \frac{V}{V_{DC}} i_L. \tag{16}$$

Hence, Eq. (16) reveals that $E_{DC}$ depends on both $i_b$ and $i_P$. However, since the latter is generally imposed by the application requirements, $E_{DC}$ can be regulated successfully through $i_b$ only, while $V_{DC}$ can be driven independently by means of $i_{DC}$, as pointed out by Eq. (15). This occurs as far as $i_{DC}$ and $i_P$ differ from each other. Otherwise, both $V_{DC}$ and $E_{DC}$ time variations would be proportional to the difference between $i_b$ and $i_P$, thus $E_{DC}$ and $V_{DC}$ control decoupling cannot be achieved. Therefore, considering both Eqs. (15) and (16), the following relationship can be introduced:

$$\begin{bmatrix} i_{DC} \\ i_P \end{bmatrix} = A \cdot \begin{bmatrix} i_H \\ i_L \end{bmatrix} \ , \quad A = \begin{bmatrix} \frac{C}{C_u + C} & \frac{C_u}{C_u + C} \\ \frac{V_u}{V_{DC}} & \frac{V}{V_{DC}} \end{bmatrix} \tag{17}$$

Consequently, since $A$ must be non-singular, the following constraint is achieved:

$$CV - C_u V_u \neq 0 \tag{18}$$

Hence, if Eq. (18) is satisfied, $i_{DC}$ and $i_P$ can differ from each other; this does not occur in conventional NPC configurations, which are characterized by equal voltages and capacitances. Whereas, HIBUC suitably exploits DC-link capacitance and voltage unbalances, leading to a decoupled control of $V_{DC}$ and $E_{DC}$.

#### *3.1.1. Comparison with passive and active HESS configurations*

In order to highlight the advantages of HIBUC compared to passive and active HESS configurations, reference can be made to the per unit DC-link energy content ($e_{DC}$), which is defined as follows:

$$e_{DC} = \frac{E_{DC}}{\frac{1}{2} C V_{DC}^2} \tag{19}$$

Hence, considering Eqs. (3), (10), and (14), the following results are achieved:

$$e_{DC}^{(P)} = \alpha \ , \quad \alpha = \frac{C_u}{C} \tag{20}$$

$$e_{DC}^{(A)} = 1 + \alpha \xi^2 \ , \quad \xi = \frac{V_u}{V_{DC}} = k_u \tag{21}$$

$$e_{DC}^{(H)} = \alpha \cdot \xi^2 + (1 - \xi)^2 \ , \quad \xi = \frac{V_u}{V_{DC}} \tag{22}$$

where the superscripts (*P*), (*A*), and (*H*) denote passive, active and HIBUC configuration, respectively. In addition, $\alpha$ is the capacitance factor, which is much greater than 1 because $C_u$ is much greater than *C*. Furthermore, $\xi$ is the UM voltage share, which is equal to $k_u$ in the case of active HESS configuration. It is worth noting that $\xi$ ranges from 0 to 1 for the HIBUC configuration and that the same reasonably occurs also for active HESS configurations.

Hence, considering the $e_{DC}$ evolutions with $\xi$ depicted in **Figure 7**, different considerations can be made for each HESS configuration and for a given $\alpha$ value. Particularly, referring to passive HESS configuration at first, $e_{DC}$ does not depend on $\xi$, as already pointed out by Eq. (20). This is because the voltage across UM always equals $V_{DC}$, thus $\xi = 1$ over any operating conditions. As a consequence, once $\alpha$ has been set, $E_{DC}$ can vary only with $V_{DC}$. However, since $V_{DC}$ should be kept almost constant in order to supply the converter properly, a poor UM exploitation is achieved, as expected.

Considering now active HESS configuration, minimum and maximum $e_{DC}$ values are always achieved for $\xi = 0$ and $\xi = 1$, respectively, as pointed out in the following:

$$\breve{\xi} = 0 \qquad \rightarrow \qquad \breve{e}_{DC}^{(A)} = \min_{0 \le \xi \le 1} \left\{ e_{DC}^{(A)} \right\} = 1 \tag{23}$$

$$\widehat{\xi} = 1 \qquad \rightarrow \qquad \widehat{e}_{DC}^{(A)} = \max_{0 \le \xi \le 1} \left\{ e_{DC}^{(A)} \right\} = 1 + \alpha \tag{24}$$

Therefore, the maximum exploitation of the DC-link energy content can be achieved by varying $\xi$ within [0,1] as

$$\Delta\xi = \widehat{\xi} - \breve{\xi} = 1 \qquad \rightarrow \qquad \Delta e_{DC}^{(A)} = \widehat{e}_{DC}^{(A)} - \breve{e}_{DC}^{(A)} = \alpha \tag{25}$$

Hence, differently from passive HESS configuration, active configuration enables the DC-link energy content to vary with $\xi$ without the need of changing $V_{DC}$. However, it is worth noting that the operating range of $\xi$ is much narrower than [0,1] because $\xi$ equals $k_u$, which is constrained by DC/DC converter maximum and minimum duty cycle capabilities.

Focusing now on the HIBUC configuration, the minimum $e_{DC}$ value is achieved in correspondence of the following $\xi$ value:

$$\breve{\xi} = \frac{1}{1 + \alpha} \qquad \rightarrow \qquad \breve{e}_{DC}^{(H)} = \min_{0 \le \xi \le 1} \left\{ e_{DC}^{(H)} \right\} = \frac{\alpha}{1 + \alpha} \tag{26}$$

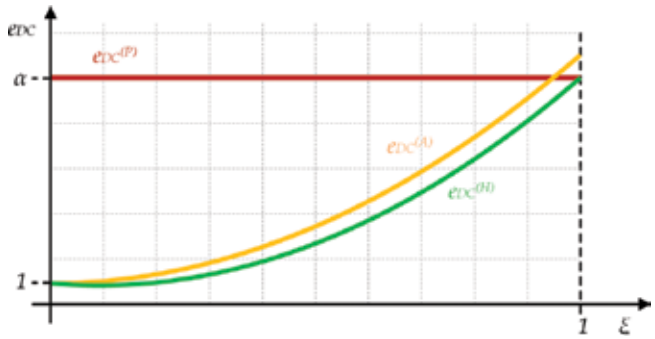


**Figure 7.** The $e_{DC}$ evolutions with $\xi$ for $\alpha$ = 10: passive, active, and HIBUC configurations.

Whereas, given that $\alpha$ is greater than 1, the maximum $e_{DC}$ value is reached for $\xi = 1$, as pointed out in the following:

$$\widehat{\xi} = 1 \qquad \rightarrow \qquad \widehat{e}_{DC}^{(H)} = \max_{0 \le \xi \le 1} \left\{ e_{DC}^{(H)} \right\} = \alpha \tag{27}$$

Consequently, maximum exploitation of the DC-link energy content is achieved if $\xi$ varies as follows:

$$\Delta\xi = \widehat{\xi} - \check{\xi} = \frac{\alpha}{1+\alpha} \qquad \rightarrow \qquad \Delta e_{DC}^{(H)} = \widehat{e}_{DC}^{(H)} - \check{e}_{DC}^{(H)} = \frac{\alpha^2}{1+\alpha} \tag{28}$$

The evolutions of both $\Delta\xi$ and $\Delta e_{DC}$ with $\alpha$ are depicted in **Figure 8**. Particularly, for low $\alpha$ values, active HESS configuration shows superior performances compared to HIBUC, which is characterized by limited UM voltage range, and thus, poor DC-link energy exploitation. However, HIBUC performances rapidly increase with $\alpha$, they becoming very close to those achieved by active HESS configurations for relatively high $\alpha$ values. Since $\alpha$ should be quite high due to the huge capacitance of UM, e.g., hundreds or even thousands, HIBUC is a very competitive solution even versus active HESS configuration because it can assure very similar performances in terms of energy flow management. In addition, HIBUC benefits also from a multilevel converter, whose increased complexity and costs are counterbalanced by improved output voltage and current waveforms due to the availability of multiple voltage levels.

### 3.2. HIBUC management and control

The overall HIBUC management and control scheme is depicted in **Figure 9**. The comparison with **Figure 5** reveals some differences, especially due to the high degree of integration among all HIBUC components. Particularly, the NPC has to account for HIBUC needs in terms of energy flow management, thus it cannot be driven only in accordance with application requirements. Regarding the HIBUC management block, it has to synthesize the most suitable BP current profile ($i_b^*$) based on the chosen HIBUC management approach; this is then tracked

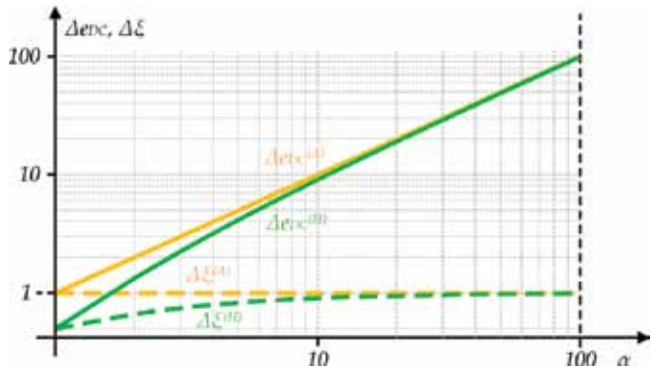


**Figure 8.** The evolutions of both $\Delta\xi$ (dashed lines) and $\Delta e_{DC}$ (solid lines) with $\alpha$: active and HIBUC configurations.

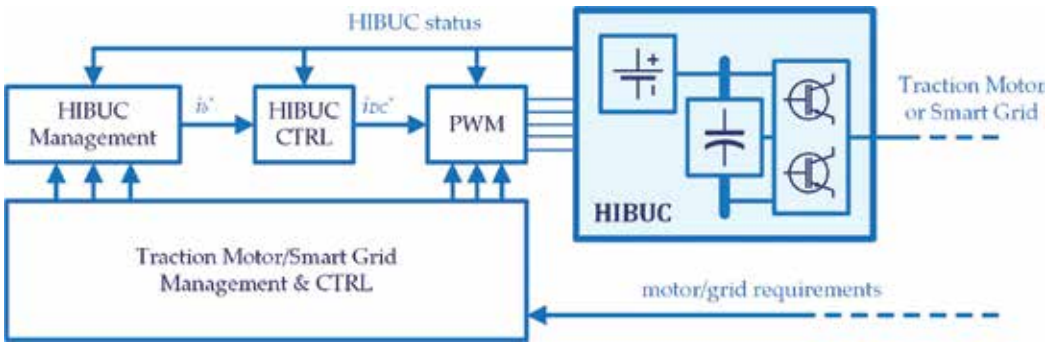


**Figure 9.** General overview of the HIBUC management and control scheme.

by means of the HIBUC control system, which can be designed in accordance with both Eqs. (12) and (15). As a result, a suitable $i_{DC}^*$ is achieved, whose implementation is guaranteed by means of advanced PWM patterns that account for both HIBUC and application requirements, as well detailed in [33, 59, 60].

In conclusion, the structure of both HIBUC management and control blocks generally depends on the specific application, as well as on the kind of power and energy services HIBUC has to provide. For this reason, two application examples are reported in the following, for each of which a much in-depth analysis of these blocks is presented, as well as some simulation results.

### *3.2.1. Electric propulsion system*

The HIBUC management and control blocks for the highly integrated electric propulsion system proposed in [31–33] are depicted in **Figure 10**. Focusing on the HIBUC energy management at first, the idea is to exploit the UM over acceleration and regenerative braking mainly. Consequently, the reference $E_{DC}$ profile is set in accordance with the actual motor/vehicle speed ($\omega_m$), namely $E_{DC}$ should decrease properly as $\omega_m$ increases in order to enable UM to release its energy content gradually during acceleration, as well as storing it back

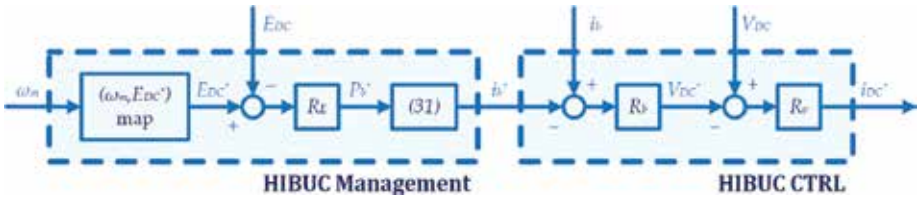


**Figure 10.** The HIBUC management and control scheme for an electric propulsion system.

during regenerative braking. In this regard, different maps can be chosen depending on UM sizing and on the kind of assistance it has to provide to BP in supplying the traction motor over these operating conditions, as pointed out in [32].

Once $E_{DC}$* has been set, its tracking can be accomplished through a PI regulator ($R_E$), which can be designed in accordance with Eq. (16), but expressed as

$$\frac{dE_{DC}}{dt} = P_b - P_P \ , \quad P_b = V_{DC} i_b \ , \quad P_P = V_{DC} i_P. \tag{29}$$

Then, in order to overcome the dependence of $P_b$ from $V_{DC}$, it is possible to multiply (12) by $i_b$ and substituting the result in Eq. (29), leading to the following expression:

$$P_b = i_b(V_b - r_b\, i_b) - \frac{1}{2} L \frac{di_b^2}{dt} \simeq i_b(V_b - r_b\, i_b) \tag{30}$$

in which, the magnetic energy variation related to the inductive filter can be neglected safely due to the relative low inductance value. As a result, the reference $i_b$ value can be computed as follows:

$$i_b^* = \frac{V_b}{2r_b} - \sqrt{\left(\frac{V_b}{2r_b}\right)^2 - \frac{P_b^*}{r_b}}. \tag{31}$$

Regarding the HIBUC control block, it consists of two nested control loops: the external loop regulates $i_b$ through $V_{DC}$ by means of a PI regulator, which can be designed easily based on Eq. (12). As a result, a reference DC-link voltage profile is achieved, whose tracking is demanded to the internal loop; this determines the most suitable reference $i_{DC}$ profile by means of another PI regulator, which is designed in accordance with Eq. (15).

In order to highlight the effectiveness of the proposed configuration, a simulation study has been performed in MATLAB-Simulink, whose main parameters are reported in **Table 1**. While simulations results are depicted in **Figures 11–15**. Particularly, each variable is shown in per unit with reference to the corresponding base value shown in **Table 1**. Focusing on **Figure 11** at first, different speed profiles have been considered for simulating a start and stop of the vehicle, which are characterized by decreasing ramp times (5 s for case 1, 4 s for case 2, and 3 s for case 3). While the corresponding motor torque evolutions are depicted in **Figure 12**. The latter reveals higher torque demands as soon as faster speed variations are required, namely from case 1 to case 3, as expected. Considering the current evolutions shown in **Figure 13**, it

| EPS parameters and rated values | | | | | | | | | |
|---|---|---|---|---|---|---|---|---|---|
| | $T_{e,n}$ | $\omega_{m,n}$ | $P_{m,n}$ | $V_b$ | $r_b$ | $L_b$ | $I_b$ | $C_u$ | $C$ |
| Value | 110 | 3500 | 40.3 | 450 | 0.4 | 15 | 89.6 | 1.7 | 1.6 |
| Units | Nm | rpm | kW | V | Ω | mH | A | F | mF |

**Table 1.** Parameters and rated values of the electric propulsion system.

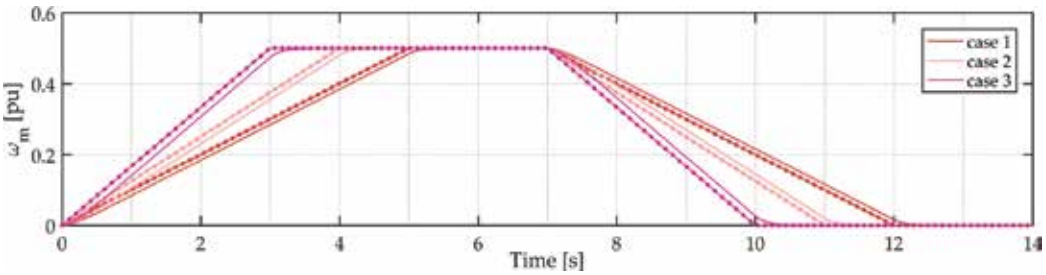


**Figure 11.** Motor speed evolution achieved over vehicle start and stop.

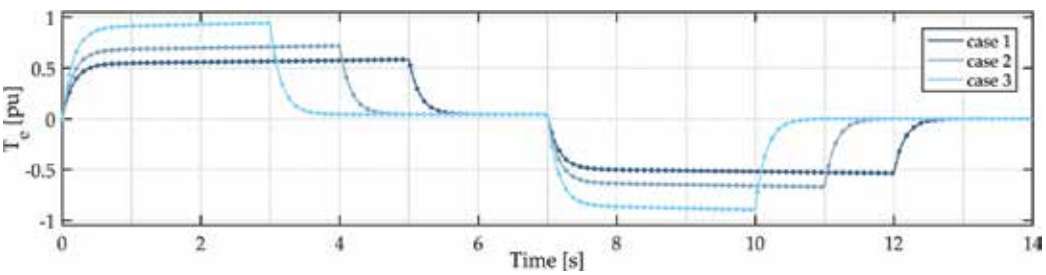


**Figure 12.** Motor torque evolution achieved over vehicle start and stop.

can be seen that high power demands occur during both vehicle acceleration and braking, especially in comparison with steady state vehicle power requirements. However, BP is prevented from coping with such high and fast power variations, as proved by the low battery current profiles achieved in all cases and still shown in **Figure 13**. This is due to UM, which is discharged and charged appropriately in accordance with the ($\omega_m$, $E_{DC}^*$) map, as highlighted in **Figure 14**. In addition, **Figure 15** shows that $V_u$ is reduced during vehicle acceleration, but $V$ is increased simultaneously. Consequently, $V_{DC}$ can be kept sufficiently high in order to prevent unsuitable and fast BP current variations. Similar considerations can be made during regenerative braking, in correspondence of which UM is recharged, while BP current is slowly driven to zero. As a result, HIBUC enables the UM to supply the motor on its own mostly during both vehicle acceleration and regenerative braking, thus preventing BP from an unsuitable exploitation.

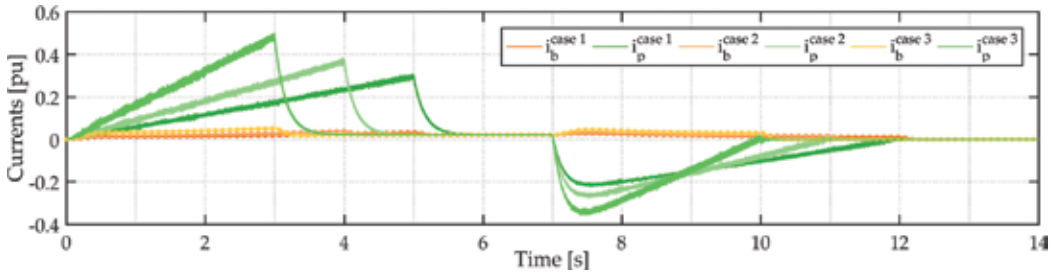


**Figure 13.** Power and battery current evolutions over vehicle start and stop: $i_P$ (green) and $i_b$ (gold).

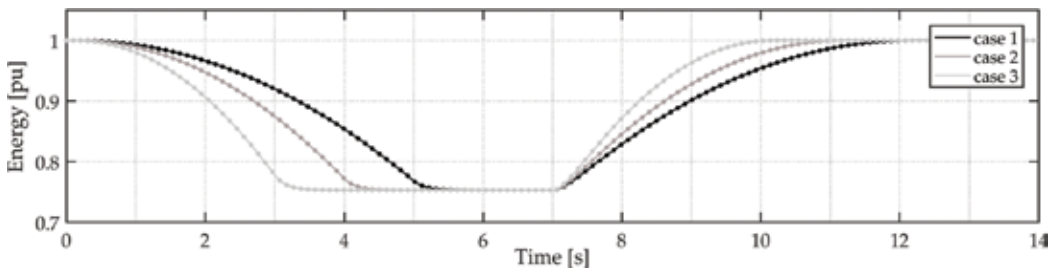


**Figure 14.** DC-link energy variations over vehicle start and stop.

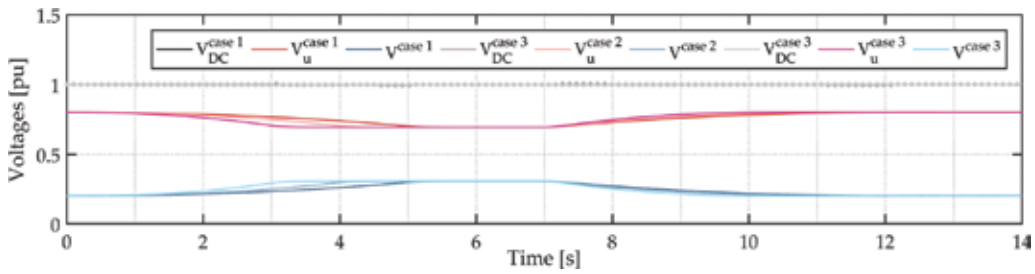


**Figure 15.** DC-link voltage evolutions over vehicle start and stop: $V_{DC}$ (gray), $V_u$ (red), and $V$ (blue).

### *3.2.2. Smart grid*

The HIBUC management and control blocks for a smart grid are depicted in **Figure 16**. Particularly, it differs from **Figure 10** only in terms of HIBUC management because the tracking of both $i_b^*$ and $V_{DC}^*$ does not depend on the specific application. Therefore, focusing on the HIBUC management only, it can be seen that a frequency-based management approach has been followed [61], namely the smart grid reference active power profile ($P_e$*) is processed by an appropriate low-pass filter in order to extract low-frequency components only. These are further processed by the energy management block, which has to synthesize the reference BP

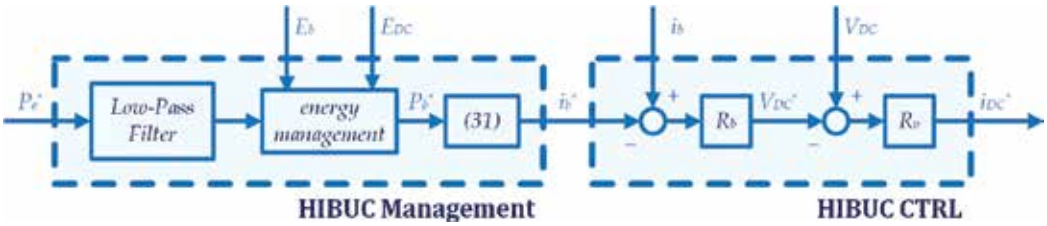


**Figure 16.** The HIBUC management and control scheme for a smart grid.

power profile in accordance with BP energy and power constraints. As a result, the UM has to cope with high-frequency power components only, which are generally characterized by poor energy content. However, since UM has to compensate for system losses, forecasting errors, and relatively low BP dynamic performances, the energy management block accounts also for the DC-link and, thus, the UM energy content in defining the reference BP power profile. Hence, if UM energy level is too low, additional power is delivered by BP with the aim of restoring an intermediate UM energy content. The opposite occurs when UM is almost fully charged, namely BP should draw energy from UM in order to preserve its continuous operation. As a result, the HESS configuration is exploited properly, not only by differentiating the kind of services BP and UM have to provide, but also by enabling a mutual support between the single ESSs.

A simulation study has been carried out in MATLAB-Simulink with reference to the main parameters shown in **Table 2**. Particularly, HIBUC has been sized differently from the previous application (electric propulsion system), especially in terms of voltage and capacitance ratings, in order to better match the new application requirements. Simulation results are depicted in **Figures 17–21**; all the results are expressed in per unit with reference to the corresponding base values shown in **Table 2**. Simulations refer to several active and/or reactive smart grid power variations, as highlighted in **Figure 17**. In addition, after 3 s, a noise signal has been added to the reference active power in order to test HIBUC performances in preventing BP from coping with such high-frequency power fluctuations. Still focusing on **Figure 17**, it can be seen that a very fast and suitable reference power tracking is achieved. This is mainly due to the fast UM dynamic response, while a much slower BP power response is achieved due to the employment of a low-pass filter, as highlighted in **Figure 18**. Particularly, the low-pass filter prevents BP from quickly reacting to reference active power variations, as well as from coping with the noise signal added to the reference active power; this is handled by UM on its own mostly, as still highlighted in **Figure 18**.

| **MG parameters and rated values** | | | | | | | | | |
|---|---|---|---|---|---|---|---|---|---|
| | $P_{e,n}$ | $V_{line}$ | $f_{line}$ | $V_b$ | $r_b$ | $L_b$ | $I_b$ | $C_u$ | $C$ |
| Value | 40 | 230 | 50 | 1000 | 0.4 | 15 | 40 | 141 | 0.94 |
| Units | kW | Vrms | Hz | V | Ω | mH | A | mF | mF |

**Table 2.** Parameters and rated values of the smart grid scenario.

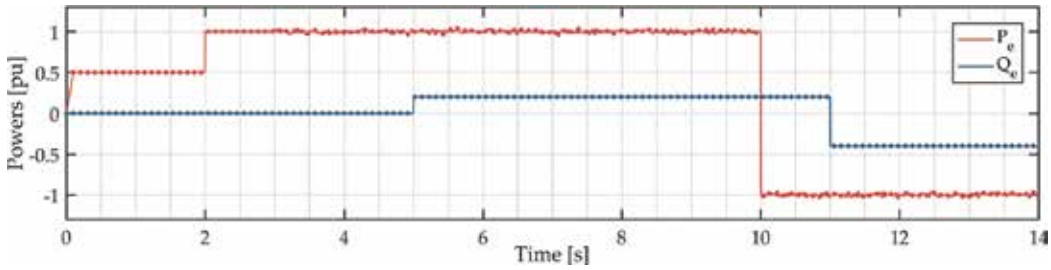


**Figure 17.** Active and reactive power profiles of the smart grid.

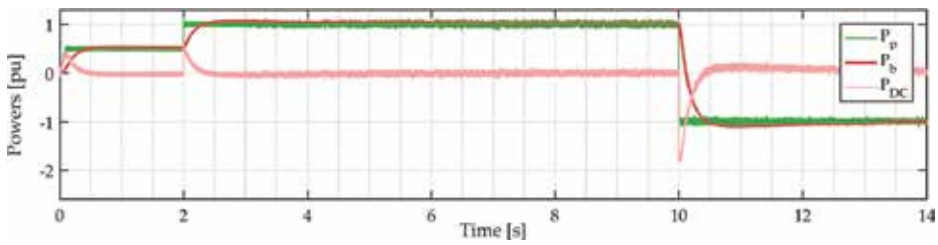


**Figure 18.** Active powers: $P_P$ (green), $P_b$ (red), and $P_{DC}$ (pink).

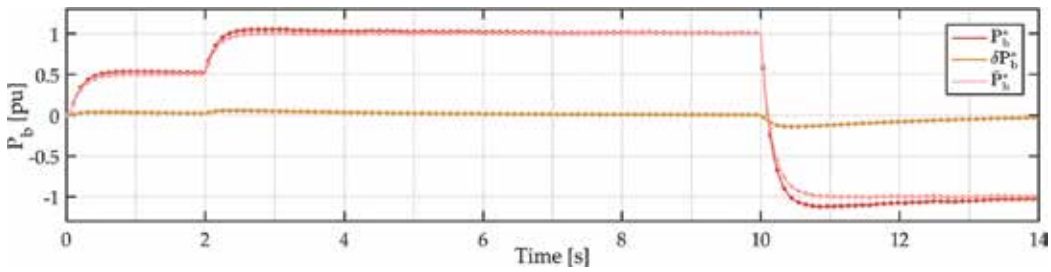


**Figure 19.** Reference active power components provided by BP: $P_b^*$ (red), $\delta P_b^*$ (gold), and $\overline{P}_b^*$ (pink).

Focusing now on the BP reference power profile, it is made up of two contributions, as pointed out in **Figure 19**: one comes from the low-pass filter ($\overline{P}_b^*$), whereas the other contribution ($\delta P_b^*$) is provided by a DC-link energy loop similar to that shown in **Figure 10**. Particularly, $\delta P_b$* enables BP to slowly drive the UM energy to a suitable intermediate reference value, as shown in **Figure 20**. This occurs by varying $V_u$ and $V$ suitably, as highlighted in **Figure 21**. It is worth noting that UM may be fully charged or discharged if this control loop is not employed and, thus, unable to cope with fast active power decrease or increase, respectively. In addition, $\delta P_b^*$ accounts also for system losses that, if ignored, would force UM to be fully discharged. In conclusion, it is also worthy of note that reactive power variations do not affect both BP and UM power profiles significantly, as highlighted by the comparison between **Figure 17** and **Figure 18**.

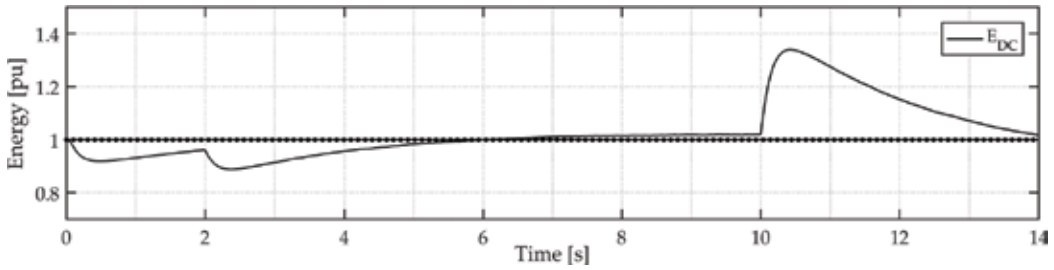


**Figure 20.** DC-link energy variations.

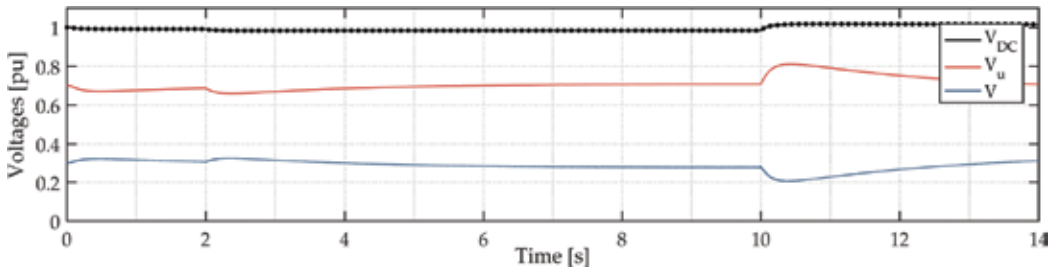


**Figure 21.** DC-link voltages: $V_{DC}$ (gray), $V_u$ (red), and $V$ (blue).

## 4. Conclusion

This chapter has addressed the potentialities and advantages of a highly integrated battery-ultracapacitor system (HIBUC). Particularly, HIBUC benefits from the advantages of both passive and active hybrid energy storage system (HESS) configurations, namely a relative simple structure and an effective energy flow management of both the battery pack (BP) and the ultracapacitor module (UM). This has been proved by the analytical comparison among all the above-mentioned configurations, which reveals HIBUC as a very suitable and competitive solution, especially when high UM capacitance is concerned. In addition, HIBUC is also very flexible, as proved by the two application examples, namely an electric propulsion system and a smart grid. For each of these, HIBUC management and control approaches have been presented and discussed, providing some simulation results as well. These highlight the high level of integration achieved in each application, especially in the design of the HIBUC management stage, which should be done in accordance with the specific application requirements.

## Acknowledgements

This work has been developed within the project "Design and Implementation of a Novel Hybrid Energy Storage System for Microgrids," which is funded by the Sardinian Regional Government (Regional Law no. 7, August 7, 2007) under the Grant Agreement n°68 (Annuity 2015).

## Author details

Alessandro Serpi[1,2]*, Mario Porru[1,2] and Alfonso Damiano[1]

*Address all correspondence to: alessandro.serpi@diee.unica.it

1 Department of Electrical and Electronic Engineering, University of Cagliari, Cagliari, Italy

2 NEPSY srl, Cagliari, Italy

## References

[1] Huggins RA. Energy Storage. Boston, MA: Springer US; 2010

[2] Barnes FS, Levine JG. Large Energy Storage Systems Handbook. Boca Raton, FL: CRC Press; 2011. 254p

[3] IEA (International Energy Agency). Technology Roadmaps—Energy Storage. 2014

[4] Apsley JM, Gonzalez-Villasenor A, Barnes M, Smith AC, Williamson S, Schuddebeurs JD, et al. Propulsion drive models for full electric marine propulsion systems. IEEE Transactions on Industry Applications. 2009 Mar;**45**(2):676-684

[5] Arboleya P, Bidaguren P, Armendariz U. Energy is on board: Energy storage and other alternatives in modern light railways. IEEE Electrification Magazine. 2016 Sep;**4**(3):30-41

[6] Abad G, editor. Power Electronics and Electric Drives for Traction Applications. 1st ed. Chichester, UK: Wiley; 2016. 648p

[7] Tariq M, Maswood AI, Gajanayake CJ, Gupta AK. Aircraft batteries: Current trend towards more electric aircraft. IET Electrical Systems in Transportation. 2017;**7**(2):93-103

[8] Li R, Zhou F. Microgrid Technology and Engineering Application. Oxford, UK: Elsevier; 2015. 200p

[9] Gao DW. Energy Storage for Sustainable Microgrid. Oxford, UK: Academic Press; 2015. 153p

[10] Tan X, Li Q, Wang H. Advances and trends of energy storage technology in microgrid. International Journal of Electrical Power & Energy Systems. 2013 Jan;**44**(1):179-191

[11] Zakeri B, Syri S. Electrical energy storage systems: A comparative life cycle cost analysis. Renewable and Sustainable Energy Reviews. 2015 Feb;**42**:569-596

[12] Luo X, Wang J, Dooner M, Clarke J. Overview of current development in electrical energy storage technologies and the application potential in power system operation. Applied Energy. 2015 Jan;**137**:511-536

[13] Vazquez S, Lukic SM, Galvan E, Franquelo LG, Carrasco JM. Energy storage systems for transport and grid applications. IEEE Transactions on Industrial Electronics. 2010 Dec; **57**(12):3881-3895

[14] Boicea VA. Energy storage technologies: The past and the present. Proceedings of the IEEE. 2014 Nov;**102**(11):1777-1794

[15] Awadallah MA, Venkatesh B. Energy storage in flywheels: An overview. Canadian Journal of Electrical and Computer Engineering. 2015 Spring;**38**(2):183-193

[16] Gayathri NS, Senroy N, Kar IN. Smoothing of wind power using flywheel energy storage system. IET Renewable Power Generation. 2017;**11**(3):289-298

[17] Gee AM, Dunn RW. Analysis of trackside flywheel energy storage in light rail systems. IEEE Transactions on Vehicular Technology. 2015 Sep;**64**(9):3858-3869

[18] Ali MH, Wu B, Dougal RA. An overview of SMES applications in power and energy systems. IEEE Transactions on Sustainable Energy. 2010 Apr;**1**(1):38-47

[19] Liu Y, Tang Y, Shi J, Shi X, Deng J, Gong K. Application of small-sized SMES in an EV charging station with DC bus and PV system. IEEE Transactions on Applied Superconductivity. 2015 Jun;**25**(3):1-6

[20] Song M, Shi J, Liu Y, Xu Y, Hu N, Tang Y, et al. 100 kJ/50 kW HTS SMES for micro-grid. IEEE Transactions on Applied Superconductivity. 2015 Jun;**25**(3):1-6

[21] Grbovic PJ. Ultra-Capacitors in Power Conversion Systems: Applications, Analysis, and Design from Theory to Practice. Chichester, UK: Wiley-IEEE Press; 2014. 336p

[22] Jayasinghe SDG, Vilathgamuwa DM. Flying supercapacitors as power smoothing elements in wind generation. IEEE Transactions on Industrial Electronics. 2013 Jul;**60**(7): 2909-2918

[23] de la Torre S, Sánchez-Racero AJ, Aguado JA, Reyes M, Martínez O. Optimal sizing of energy storage for regenerative braking in electric railway systems. IEEE Transactions on Power Apparatus and Systems. 2015 May;**30**(3):1492-1500

[24] Aktas A, Erhan K, Ozdemir S, Ozdemir E. Experimental investigation of a new smart energy management algorithm for a hybrid energy storage system in smart grid applications. Electric Power Systems Research. 2017 Mar 1;**144**:185-196

[25] Hannan MA, Hoque MM, Mohamed A, Ayob A. Review of energy storage systems for electric vehicle applications: Issues and challenges. Renewable and Sustainable Energy Reviews. 2017 Mar 1;**69**:771-789

[26] Chong LW, Wong YW, Rajkumar RK, Rajkumar RK, Isa D. Hybrid energy storage systems and control strategies for stand-alone renewable energy power systems. Renewable and Sustainable Energy Reviews. 2016 Dec;**66**:174-189

[27] Zimmermann T, Keil P, Hofmann M, Horsche MF, Pichlmaier S, Jossen A. Review of system topologies for hybrid electrical energy storage systems. Journal of Energy Storage. 2016 Nov;**8**:78-90

[28] Dougal RA, Liu S, White RE. Power and life extension of battery-ultracapacitor hybrids. IEEE Transactions on Components and Packaging Technologies. 2002 Mar;**25**(1):120-131

[29] Gao L, Dougal RA, Liu S. Power enhancement of an actively controlled battery/ultracapacitor hybrid. IEEE Transactions on Power Electronics. 2005 Jan;**20**(1):236-243

[30] Lukic SM, Cao J, Bansal RC, Rodriguez F, Emadi A. Energy storage systems for automotive applications. IEEE Transactions on Industrial Electronics. 2008 Jun;**55**(6):2258-2267

[31] Porru M, Serpi A, Marongiu I, Damiano A. A novel hybrid energy storage system for electric vehicles. In: Proceedings of the 41th Annual Conference of the IEEE Industrial Electronics Society (IECON 2015); Yokohama, Japan; 2015. pp. 3732-3737

[32] Porru M, Serpi A, Damiano A. Smart energy management of HESS-based electric propulsion systems for urban mobility. In: Proceedings of the 42nd Annual Conference of the IEEE Industrial Electronics Society (IECON 2016); Florence, Italy; 2016. pp. 4453-4458

[33] Porru M. Management and Control of Energy Storage Systems for Stationary and Automotive Applications [Internet] [PhD Dissertation] [Italy]. Department of Electrical and Electronic Engineering, University of Cagliari; 2015. Available from: http://veprints.unica.it/1117/

[34] Ma T, Yang H, Lu L. Development of hybrid battery–supercapacitor energy storage for remote area renewable energy systems. Applied Energy. 2015 Sep 1;**153**:56-62

[35] Pagano M, Piegari L. Hybrid electrochemical power sources for onboard applications. IEEE Transactions on Energy Conversion. 2007 Jun;**22**(2):450-456

[36] Wang B, Xu J, Cao B, Ning B. Adaptive mode switch strategy based on simulated annealing optimization of a multi-mode hybrid energy storage system for electric vehicles. Applied Energy. 2017 May 15;**194**:596-608

[37] Min H, Lai C, Yu Y, Zhu T, Zhang C. Comparison study of two semi-active hybrid energy storage Systems for hybrid electric vehicle applications and their experimental validation. Energies. 2017 Feb 28;**10**(3):279

[38] Song Z, Hofmann H, Li J, Han X, Zhang X, Ouyang M. A comparison study of different semi-active hybrid energy storage system topologies for electric vehicles. Journal of Power Sources. 2015 Jan 15;**274**:400-411

[39] Hredzak B, Agelidis VG, Jang M. A model predictive control system for a hybrid battery-ultracapacitor power source. IEEE Transactions on Power Electronics. 2014 Mar;**29**(3):1469-1479

[40] Choi M-E, Kim S-W, Seo S-W. Energy management optimization in a battery/supercapacitor hybrid energy storage system. IEEE Transactions on Smart Grid. 2012 Mar;**3**(1):463-472

[41] Tankari MA, Camara MB, Dakyo B, Lefebvre G. Use of ultracapacitors and batteries for efficient energy management in wind-diesel hybrid system. IEEE Transactions on Sustainable Energy. 2013 Apr;**4**(2):414-424

[42] Bellache K, Camara MB, Dakyo B. Transient power control for diesel-generator assistance in electric boat applications using supercapacitors and batteries. IEEE Journal of Emerging and Selected Topics in Power Electronics. 2017;**PP**(99):1

[43] Araújo RE, de CR, Pinto C, Melo P, Freitas D. Combined sizing and energy management in EVs with batteries and supercapacitors. IEEE Transactions on Vehicular Technology. 2014 Sep;**63**(7):3062-3076

[44] Mendis N, Muttaqi KM, Perera S. Management of battery-supercapacitor hybrid energy storage and synchronous condenser for isolated operation of PMSG based variable-speed wind turbine generating systems. IEEE Transactions on Smart Grid. 2014 Mar;**5**(2):944-953

[45] Kollimalla SK, Mishra MK, Narasamma NL. Design and analysis of novel control strategy for battery and supercapacitor storage system. IEEE Transactions on Sustainable Energy. 2014 Oct;**5**(4):1137-1144

[46] Zeng A, Xu Q, Ding M, Yukita K, Ichiyanagi K. A classification control strategy for energy storage system in microgrid. IEEJ Transactions on Electrical and Electronic Engineering. 2015 Jul;**10**(4):396-403

[47] Wang G, Ciobotaru M, Agelidis VG. Power smoothing of large solar PV plant using hybrid energy storage. IEEE Transactions on Sustainable Energy. 2014 Jul;**5**(3):834-842

[48] Tummuru NR, Mishra MK, Srinivas S. Dynamic energy management of renewable grid integrated hybrid energy storage system. IEEE Transactions on Industrial Electronics. 2015 Dec;**62**(12):7728-7737

[49] Ye Y, Sharma R, Garg P. An integrated power management strategy of hybrid energy storage for renewable application. In: Proceedings of the 40th Annual Conference of the IEEE Industrial Electronics Society (IECON 2014); Dallas, USA; 2014. pp. 3088-3093

[50] Wang S, Tang Y, Shi J, Gong K, Liu Y, Ren L, et al. Design and advanced control strategies of a hybrid energy storage system for the grid integration of wind power generations. IET Renewable Power Generation. 2015 Feb;**9**(2):89-98

[51] Mohamed A, Salehi V, Mohammed O. Real-time energy management algorithm for mitigation of pulse loads in hybrid microgrids. IEEE Transactions on Smart Grid. 2012 Dec;**3**(4):1911-1922

[52] Garcia-Torres F, Bordons C. Optimal economical schedule of hydrogen-based microgrids with hybrid storage using model predictive control. IEEE Transactions on Industrial Electronics. 2015 Aug;**62**(8):5195-5207

[53] Laldin O, Moshirvaziri M, Trescases O. Predictive algorithm for optimizing power flow in hybrid ultracapacitor/battery storage systems for light electric vehicles. IEEE Transactions on Power Electronics. 2013 Agosto;**28**(8):3882-3895

[54] Larsson V, Johannesson L, Egardt B. Analytic solutions to the dynamic programming subproblem in hybrid vehicle energy management. IEEE Transactions on Vehicular Technology. 2015 Apr;**64**(4):1458-1467

[55] Shen J, Khaligh A. A supervisory energy management control strategy in a battery/ultracapacitor hybrid energy storage system. IEEE Transactions on Transportation Electrification. 2015 Ottobre;**1**(3):223-231

[56] Herrera V, Gaztanaga H, Milo A, Saez-de-Ibarra A, Etxeberria I, Nieva T. Optimal energy management of battery-supercapacitor based light rail vehicle using genetic algorithms. IEEE Transactions on Industry Applications. 2016;**PP**(99):1

[57] Rouholamini M, Mohammadian M. Heuristic-based power management of a grid-connected hybrid energy system combined with hydrogen storage. Renewable Energy. 2016 Oct;**96**(Part A):354-365

[58] García-Triviño P, Llorens-Iborra F, García-Vázquez CA, Gil-Mena AJ, Fernández-Ramírez LM, Jurado F. Long-term optimization based on PSO of a grid-connected renewable energy/battery/hydrogen hybrid system. International Journal of Hydrogen Energy. 2014 Jul 15;**39**(21):10805-10816

[59] Porru M, Serpi A, Marongiu I, Damiano A. An improved DC-link voltage equalization for three-level neutral-point clamped converters. In: Proceedings of the 10th Conference on PhD Research in Microelectronics and Electronics (PRIME 2014); Grenoble, France; 2014. pp. 1-4

[60] Porru M, Serpi A, Marongiu I, Damiano A. A novel DC-link voltage and current control algorithm for neutral-point-clamped converters. In: Proceedings of the 40th Annual Conference of the IEEE Industrial Electronics Society (IECON 2014); Dallas, USA; 2014. pp. 4521-4527

[61] Porru M, Serpi A, Salimbeni, A., Damiano, A. An advanced frequency-based energy management of hybrid energy storage systems for microgrids. In: Proceedings of the 43rd Annual Conference of the IEEE Industrial Electronics Society (IECON 2017); Beijing, China; 2017

Chapter 5

# Synergetic Control of a Hybrid Battery-Ultracapacitor Energy Storage System

Rached Dhaouadi, Kamyar Khosravi and Yoichi Hori

Additional information is available at the end of the chapter

http://dx.doi.org/10.5772/intechopen.73673

**Abstract**

This chapter presents a synergy-based cascade control scheme for a hybrid battery-ultracapacitor (UC) energy storage system. The purpose is to improve the dynamic response of the battery-based energy storage system using an ultracapacitor module as an auxiliary energy storage unit. A bidirectional DC-DC converter is designed to interface between the ultracapacitor module and the main DC-bus. The control scheme is based on a fast inner current control loop using sliding mode control and an outer loop for DC-bus voltage regulation using synergy-based control. The improvement in performance is demonstrated through simulation and experiments. The results show that the DC-bus voltage is well regulated under external load disturbances with fast dynamic transients. The ultracapacitor module is able to absorb the sudden load variations and limit the battery power requirements by maintaining an optimal power balance between the two embedded storage units. The performance of the proposed synergy-based controller is compared with the standard PI controller, and its ability to achieve optimal transient performance is verified.

**Keywords:** DC-DC converter, hybrid energy storage system, synergetic control, ultracapacitor

## 1. Introduction

The rapid development of the automotive industry has resulted in a variety of technological enhancements in electric vehicles (EV), which have significantly improved fuel consumption and reduced emissions. However, EV technology still faces many challenges such as long drive

range, long battery operating life, and high charge–discharge cycle rate in order to recover as much of the vehicle's kinetic energy as possible and supply high peak energies on demand [1–4].

For the EV operation, it is important to predict the battery energy demand for a specific trip. However, the stochastic driving cycles and unpredictable power demand may lead to a fast discharge action of batteries, resulting in an energy shortage to complete the given trip. A backup energy storage unit is therefore necessary to supply a stable and reliable power to the vehicle and improve the steady-state and dynamic behavior under different operating conditions [5, 6].

Ultracapacitors (UCs) are nowadays recognized as a viable auxiliary power source with outstanding power characteristics. They have been integrated successfully with energy storage systems for many industrial applications such as electric vehicles and photovoltaic energy systems [7–13]. The inclusion of UC can be very useful to maintain stability in electrical power systems with distributed generation by enhancing the output from lead-acid batteries and intermittent renewable resources.

In electric vehicles, the main power source is usually a lithium-ion battery, or a fuel cell, and the mechanical load is coupled to a permanent-magnet synchronous machine (PMSM) through an inverter. To extend the driving range of the vehicle and enable more efficient use of the batteries, a UC module is used as an auxiliary power source connected to the DC-bus through a bidirectional DC-DC converter. This configuration allows obtaining an optimized charge/discharge operation to smooth the power fluctuations and reinforce the DC-bus during the load transients [14–17].

During the last decade, different control techniques based on adaptive control theory, sliding mode control, fuzzy logic, and neural networks have been proposed for the control of DC-DC power converters [18, 19]. The main objective of such nonlinear controllers is to provide the control support for boost-type converters to improve their controllability and performance for large operating ranges.

Recently, the synergetic control appears to be a novel effective approach to deal with many nonlinear control problems due to its optimality property and its inherent robustness to disturbances. The synergetic control was developed by Kolesnikov et al. [20] on the basis of the standard variable structure control. The method was later applied to a number of industrial processes, including problems in energy conversion [21–25]. In [24], the authors presented the optimization characteristic of the synergetic control method and showed that the control law can be derived using the analytical design of aggregated regulators (ADAR) method and calculus of variation principles.

The main features of synergetic control are that it is well-suited for digital implementation; it gives constant switching frequency operation and gives better control of the off-manifold dynamics. Switching converters have intrinsic nonlinear and time-varying characteristics, which make the synergetic controller to also be a well-suited control scheme. The other important advantages of this control approach are order reduction, decoupling design procedure, and insensitivity to parameter variation.

This chapter presents a new control scheme to improve the dynamic response of a battery-based energy storage system using an UC module as an auxiliary energy storage unit. This chapter represents a preliminary study for EV applications. The primary objective is to improve both the vehicle range and the battery cycle life through optimal management of the onboard power and energy, and realize full utilization of the installed storage capacities.

The originality of the proposed technique is the procedure to develop the synergy-based cascade control scheme and to devise the link between the system variables to have an accurate control of the DC-bus voltage and an optimal management of the power flow between the battery, UC module, and load. Additionally, our contribution extends the analysis of the synergy-based cascade control scheme by providing a proof of the controller stability using Lyapunov theory.

A prototype hybrid battery/UC system is developed to perform experimental analysis and validate the proposed controller. Experimental results and a comparison with the standard PI controller are given to validate the optimal transient performance of the synergy-based controller.

The proposed synergy-based control scheme is shown to have the following characteristics:

- Synergetic control improves the dynamic response of the UC energy storage system.
- UC absorbs sudden load variations and limits battery power requirements.
- The control scheme maintains an optimal power balance between the storage units.
- Synergy-based control is robust to external load disturbances and UC voltage variation.

## 2. Hybrid energy storage system

**Figure 1** shows the proposed topology used for electric vehicles. The system has a DC-coupled structure where a UC module is used as an auxiliary power source and connected to the

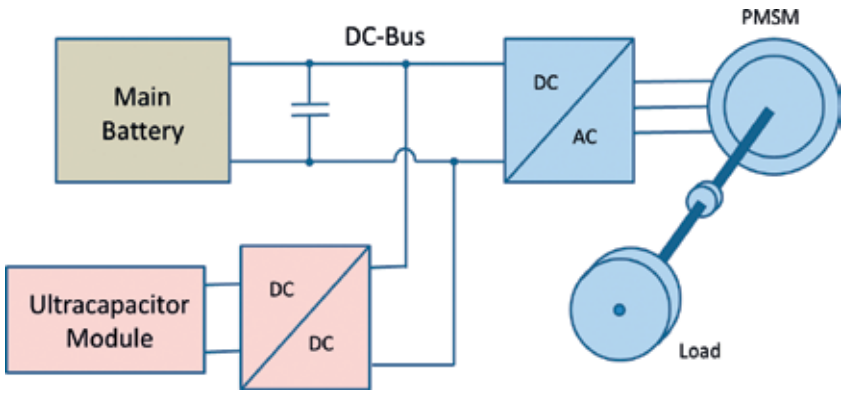


**Figure 1.** Topology of the hybrid energy storage system.

DC-bus through a bidirectional DC-DC converter. The proposed hybrid energy storage system is designed to have high efficiency and regenerative energy capture capability. These two features represent the key elements with respect to energy saving in electric vehicles. The battery is the main DC power source that forms the DC-bus. Various loads including the AC drive motors and auxiliary electrical loads are fed from the DC-bus through DC-AC and DC-DC converters. The AC drive motors represent the main load. A UC is interfaced to the DC-bus through a bidirectional DC-DC converter to control the energy transfer between the battery and the UC module. The power converter circuit consists of two MOSFET switches in a bridge configuration combined with an inductor and a capacitor as shown in **Figure 2**. The converter is connected to the UC module on the low-voltage side and to the lead-acid battery on the high-voltage side. The circuit is controlled through a PWM signal generated by the hysteresis current controller.

The power converter regulates the energy flow to and from the UC in two modes of operation: buck and boost, depending on the direction of the inductor current. The converter operates in the boost mode when energy is transferred from the UC to the battery.

On the other hand, the converter operates in the buck mode when energy is transferred from the battery to the UC, or if energy is recovered from the load (regenerative breaking). The power converter is assumed to operate in continuous conduction PWM mode while switching between two states depending on the status of the switches $(Q_1, Q_2)$.

In the first PWM state, $Q_1$ is ON and $Q_2$ is OFF, while in the second PWM state, $Q_1$ is OFF and $Q_2$ is ON. In the boost mode of operation, the converter circuit is described by the following equations:

$$L\frac{di_L}{dt} = v_c - (R_s + R_L)i_L - v_0(1-u), \tag{1}$$

$$C_f\frac{dv_0}{dt} = i_L(1-u) - i_0 + i_b, \tag{2}$$

$$C_s\frac{dv_c}{dt} = -i_L, \tag{3}$$

where u is the average control factor of the switch $Q_2$, $L$ is the inductance, $C_s$ is the ultracapacitance, $C_f$ is the filter capacitance, $R_L$ is the internal inductor resistance, $i_b$ is the battery current, $i_L$ is the inductor current, $i_0$ is the load current, $v_0$ is the output voltage, $v_c$ is the ultracapacitor voltage, and $R_s$ is the internal resistance (ESR) of the ultracapacitor.

In the literature, different electro-circuit models for UC behavior simulation are available. These models have different degrees of complexity and simulation qualities [26–27]. In this chapter, the focus is on the validation of the synergy-based controller concept, the UC is modeled as a pure supercapacitance in series with the equivalent ESR. The measured UC voltage is given by:

$$\begin{aligned} v_s &= v_c + R_s i_{sc} \\ i_{sc} &= -i_L \end{aligned}, \tag{4}$$

where $i_{sc}$ is defined as the UC current. A positive $i_{sc}$ means that the UC is charging, while a negative $i_{sc}$ means that the UC is discharging.

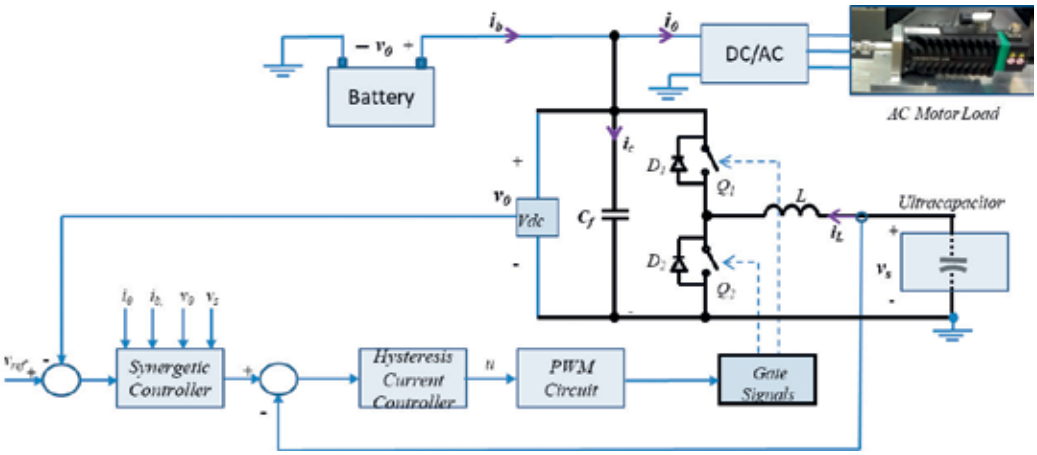


**Figure 2.** Block diagram of the proposed synergy-based hybrid energy storage system.

The battery is modeled by an equivalent RC circuit with a series–parallel branch as given by Eq. (5). $C_b$ represents the charge storage capacity of the battery, $R_b$ is the internal series resistance (ESR), and $R_d$ is used to model the long-term storage performance of the battery [13].

$$\begin{aligned} &C_b \frac{dv_b}{dt} + \frac{v_b}{R_d} + i_b = 0 \\ &v_0 = v_b - R_b i_b \end{aligned} . \tag{5}$$

The state space equations of the energy storage system can be obtained by taking $i_L$, $v_0$, $v_c$, and $v_b$ as state variables, and considering the load current $i_0$ as the system input:

$$\frac{d}{dt}\begin{bmatrix} i_L \\ v_0 \\ v_c \\ v_b \end{bmatrix} = \begin{bmatrix} -\frac{(R_s + R_L)}{L} & -\frac{\overline{u}}{L} & \frac{1}{L} & 0 \\ \frac{\overline{u}}{C_f} & -\frac{1}{R_b C_f} & 0 & \frac{1}{R_b C_f} \\ -\frac{1}{C_s} & 0 & 0 & 0 \\ 0 & \frac{1}{R_b C_b} & 0 & -\frac{1}{C_b}\left(\frac{1}{R_b} + \frac{1}{R_d}\right) \end{bmatrix} \begin{bmatrix} i_L \\ v_0 \\ v_s \\ v_b \end{bmatrix} + \begin{bmatrix} 0 \\ -\frac{1}{C_f} \\ 0 \\ 0 \end{bmatrix} i_0, \tag{6}$$

where $\overline{u} = 1 - u$ is the switch control signal.

## 3. Cascade control scheme with sliding mode current control

The DC-bus voltage regulation is achieved by using a cascade control structure with a fast inner current control loop and an outer synergy-based voltage control loop. The current control loop is implemented using a sliding mode scheme to achieve a fast-response and robust performance. As a result, the inductor current is controlled to follow the reference

current $I_r$, within a given tolerance band, in order to charge or discharge the ultracapacitor and keep a regulated output DC-bus voltage $v_0$. The main objective is to keep the output voltage at the desired value even under external disturbances and load variations. **Figure 2** shows the overall control scheme of the energy management system.

First, a current switching line is defined

$$S(x) = I_r - i_L = 0, \tag{7}$$

where $I_r > 0$ is the reference current. Sliding motion exists in the region where $v_s < v_0$. The condition $\frac{dS}{dt} = 0$ is obtained by using Eq. (1):

$$\frac{v_0}{L}(1-u) - \frac{v_s}{L} = 0. \tag{8}$$

The equivalent control is

$$0 < u_{eq} = 1 - \frac{v_s}{v_0} < 1. \tag{9}$$

The hysteresis current controller is a very high gain controller permitting the measured current to properly track the reference signal with high accuracy. Therefore, if the tolerance band is very small, the current control loop can be approximated by a unity block. Hence, the converter equations reduce to $i_L \approx I_r$ and $u = u_{eq}$.

In EV applications, a sudden acceleration or deceleration is equivalent to a step load torque change. Therefore, a variable load current can be used to represent the nonlinear DC-AC converter characteristics together with the AC motors.

The energy storage system model is next modified to include the load as a variable resistance $R_0$. The load current can then be expressed as: $i_0 = \frac{v_0}{R_0}$.

The resulting converter equations are nonlinear in terms of the output voltage $v_0$.

$$\begin{cases} \dfrac{dv_0}{dt} = -\dfrac{1}{C_f}\left(\dfrac{1}{R_b} + \dfrac{1}{R_0}\right)v_0 + \dfrac{1}{R_b C_f}v_b + \dfrac{1}{C_f}\left(\dfrac{v_s}{v_0}\right) I_r \\ \dfrac{dv_b}{dt} = \dfrac{1}{R_b C_b}v_0 - \dfrac{1}{C_b}\left(\dfrac{1}{R_b} + \dfrac{1}{R_d}\right)v_b \\ \dfrac{dv_c}{dt} = -\dfrac{1}{C_s}I_r \end{cases}. \tag{10}$$

The Lyapunov stability method is next used to analyze the voltage Eqs. (10). The output voltage equation is the main nonlinear equation and can be written in the following form:

$$\frac{dv_0}{dt} = \frac{a}{v_0} - bv_0 + d, \tag{11}$$

where $a = \frac{1}{C_f} I_r v_s$, $b = \frac{1}{R_0 C_f}$, and $d = \frac{1}{C_f} i_b$.

Next, a Lyapunov function is defined as

$$F = \frac{1}{2b}\left(v_0 - \sqrt{\frac{a}{b}}\right)^2. \tag{12}$$

Then

$$\dot{F} = \frac{1}{b}\left(v_0 - \sqrt{\frac{a}{b}}\right) \times \frac{dv_0}{dt} = \frac{1}{b}\left(v_0 - \sqrt{\frac{a}{b}}\right)\ \left(\frac{a}{v_0} - bv_0 + d\right), \tag{13}$$

which can be rewritten in the following form:

$$\dot{F} = -\frac{1}{v_0}\left(v_0 - \sqrt{\frac{a}{b}}\right)\ \left({v_0}^2 - \frac{d}{b}v_0 - \frac{a}{b}\right) = -\frac{1}{v_0}\left(v_0 - \sqrt{\frac{a}{b}}\right)\ f(v_0). \tag{14}$$

The roots of the function $f(v_0) = 0$ are

$$\begin{cases} v_{01} = \frac{1}{2}\left(R_0 i_b - \sqrt{{R_0}^2 i_b^2 + 4R_0 I_r v_s}\right) \\ v_{02} = \frac{1}{2}\left(R_0 i_b + \sqrt{{R_0}^2 i_b^2 + 4R_0 I_r v_s}\right) \end{cases}. \tag{15}$$

The stability condition of the system Eq. (10) is guaranteed if $\dot{F} < 0$. This condition is satisfied if

$$v_0 > \frac{1}{2}\left(R_0 i_b + \sqrt{{R_0}^2 i_b^2 + 4R_0 I_r v_s}\right)\ . \tag{16}$$

## 4. Synergetic control

The synergetic control scheme is next developed by analyzing the reduced system voltage equations with sliding mode current control as described by (10). The nonlinear system can be written in the following form:

$$\dot{x} = f(x, w, t), \tag{17}$$

where $x = [v_0\ \ v_s]^t$ is the state vector, $v_0$ is the system output, and $w = I_r$ is the system input.

The objective is to devise a control law $I_r = f(v_0, v_s)$ that optimizes the required voltage regulation $v_0 = v_{0r}$ under different operating conditions.

Let $L(t, \sigma, \dot{\sigma})$ be a function with continuous first and second derivatives with respect to all of its arguments. The objective is to find the function $\sigma(x(t))$ that is continuously differentiable for $t_0 \le t \le t_f$ and satisfy boundary conditions $\sigma(t_0) = \sigma_0$ and $\sigma(t_f) = \sigma_f$, for which the functional

$$J = \int_{t_0}^{t_f} L(t, \sigma(t), \dot{\sigma}(t))dt = \int_{t_0}^{t_f} \left(T^2\dot{\sigma}^2 + \sigma^2\right)dt, \tag{18}$$

is minimum, where $T = T^T > 0$ is a symmetric positive parameter to be designed. Then, $\sigma(t)$ is a minimizer of the functional $J$ if it is a solution of the following linear differential equation

$$T\dot{\sigma} + \sigma = 0, \tag{19}$$

where $T$ is a design parameter that sets the speed of convergence to the desired manifold.

Next, define the macro-variable $\sigma$ as

$$\sigma = v_0 - v_{0r} + k_1(v_s - v_{sr}) + k_2 \int_0^t (v_0 - v_{0r})dt. \tag{20}$$

The reference voltage $v_{0r}$ can be selected to be the nominal DC-bus voltage with no load when the UC is in the charging mode. On the other hand, the reference voltage $v_{sr}$ is selected as the rated voltage of the UC. Next, the macro-variable derivative is obtained using the chain rule of differentiation.

$$\dot{\sigma} = \frac{d\sigma}{dx}\ \dot{x}. \tag{21}$$

Using (18)–(21) and solving for the reference current $I_r$ yields

$$I_r = \frac{1}{\frac{k_1}{C_s} - \frac{v_s}{C_f v_0}} \times \left[\frac{i_b - i_0}{C_f} + \left(k_2 + \frac{1}{T}\right)(v_0 - v_{0r}) + \frac{k_1}{T}(v_s - v_{sr}) + \frac{k_2}{T}\int (v_0 - v_{0r})dt\right]. \tag{22}$$

This synergetic control law will force the system to operate on the manifold $\sigma(x) = 0$. In addition, the control law will impose a well-controlled dynamic behavior off the manifold.

Next, the control law designed earlier is shown to be globally asymptotically stable. Consider the positive definite candidate Lyapunov function V is defined by

$$V(x) = \frac{1}{2}\sigma^2(x). \tag{23}$$

Then, the total time derivative of V along the trajectories of $\sigma(x)$ is given by

$$\dot{V} = \sigma(x)\dot{\sigma}(x) = -\frac{1}{T}\sigma^2(x) < 0 \qquad \forall\sigma \neq 0, \tag{24}$$

which shows that the system (10) will converge to the manifold $\sigma(x) = 0$ asymptotically.

## 5. Optimized control law

The synergy-based control strategy presented earlier uses a cascade control structure where the output voltage is regulated by the outer loop via the inductor current which is tightly

controlled by a faster inner loop. This strategy is shown to give a good transient performance. However, it is very sensitive to the UC voltage $v_s$, since this voltage is continuously changing due to charging and discharging actions. To overcome this drawback, an optimized control law is adopted by filtering the UC voltage $v_s$ to detect and use the low-frequency variation instead of the actual voltage.

The new manifold is then updated as

$$\Psi = v_0 - v_{0r} + k_1 v_{sf} + k_2 \int_0^t (v_0 - v_{0r}) dt, \tag{25}$$

where $v_{sf}$ is the filtered UC voltage. A first order low-pass filter is used with a cut-off frequency $\omega_f$ and a transfer function

$$G_f(s) = \frac{\omega_f}{s + \omega_f}. \tag{26}$$

## 6. Simulation results

The proposed synergetic control law is validated first using computer simulation. The closed loop system behavior is evaluated by checking the system robustness to step load disturbances. The simulation results are next validated on an experimental prototype system with the same input parameters.

**Figure 3** shows the system performance when starting at no load, and then the load current is changed from 0 to 2.6 A. It can be observed that initially the DC-bus voltage $v_0$ is stabilized at the desired reference value of 32.7 V. Next, due to the sudden variation in load, the voltage is disturbed and goes through a fast transient. The synergetic controller is able to minimize the

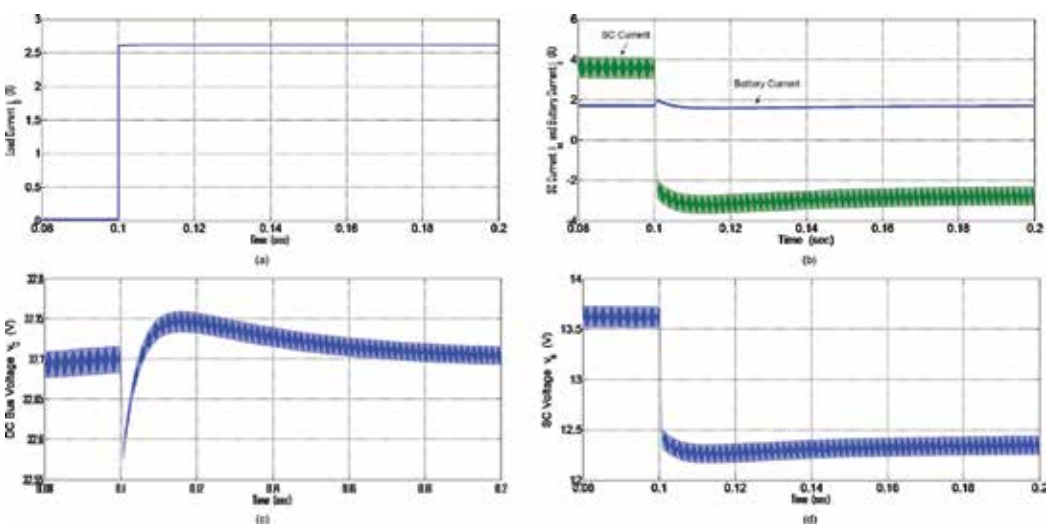


**Figure 3.** System response to a step load current with optimized control law. (**a**) Load current $i_0$; (**b**) DC-bus voltage $v_0$; (**c**) battery current $i_b$ and SC current $i_{sc}$; and (**d**) SC voltage $v_s$.

voltage fluctuation, and the voltage is regulated back to the reference value. The peak-to-peak voltage variation is

$$\Delta v_0 = \frac{v_{0\max} - v_{0\min}}{v_{0r}} = 0.56\%. \tag{27}$$

The sudden load increase at $t = 0.1s$ is quickly supplied by the UC, which is discharged through the inductor. The battery shows only a small variation in current which contains only a low-frequency component needed for voltage regulation. This response is a good feature of the proposed control system that would help extend the battery operating life. The results clearly illustrate that the optimized control system has a very good robust performance to load uncertainty. The incorporation of the low-pass filter allows tracking the voltage changes with fast transient response and very small steady-state error.

## 7. Experimental results and discussion

In this section, experimental results of the proposed synergy-based control scheme are provided to validate the theoretical design. **Figure 4** shows a general view of the actual hardware. The synergetic controller block is implemented by Eq. (22) as illustrated in **Figure 2**. The system parameters are given in **Table 1**.

The hybrid energy storage system prototype was developed using a bidirectional DC-DC converter module, a 36-V battery pack, and a 15-V UC bank formed by the series connection of six UCs with 2300 F each. The variable load is implemented by using two 25 Ω power resistors in parallel connected to the DC-bus. The control algorithms are developed on the eZdsp board from Texas Instruments based on the TMS320F28335 DSP and the dSPACE1104 development system. The TI DSP is solely dedicated to the current control loop, while the dSPACE1104 system is for the outer voltage control loop. The control code is developed by the operator on a laptop using Code Composer Studio and then downloaded on the TI-DSP for real-time operation.

The closed loop system behavior is analyzed by evaluating the transient response and steady-state response to step load disturbances. The first test examines the case where the DC-bus voltage is maintained at a constant value with no load and the battery is charging only the UC with a constant current.

The DC-bus voltage reference is set to a value $v_{0r} = 32.85V$ lower than the nominal value of the battery. The synergetic controller would then automatically set the charging current reference for the UC to maintain this DC-bus voltage level. The load is next changed abruptly as shown in the profile of **Figure 5**. Normally, this would require an abrupt change of the battery current to supply this sudden load disturbance. However, the system shows a very good robustness to this load disturbance, as the UC current changes rapidly from the charging mode to the discharging mode to supply the required additional load with the minimum effect on the battery current.

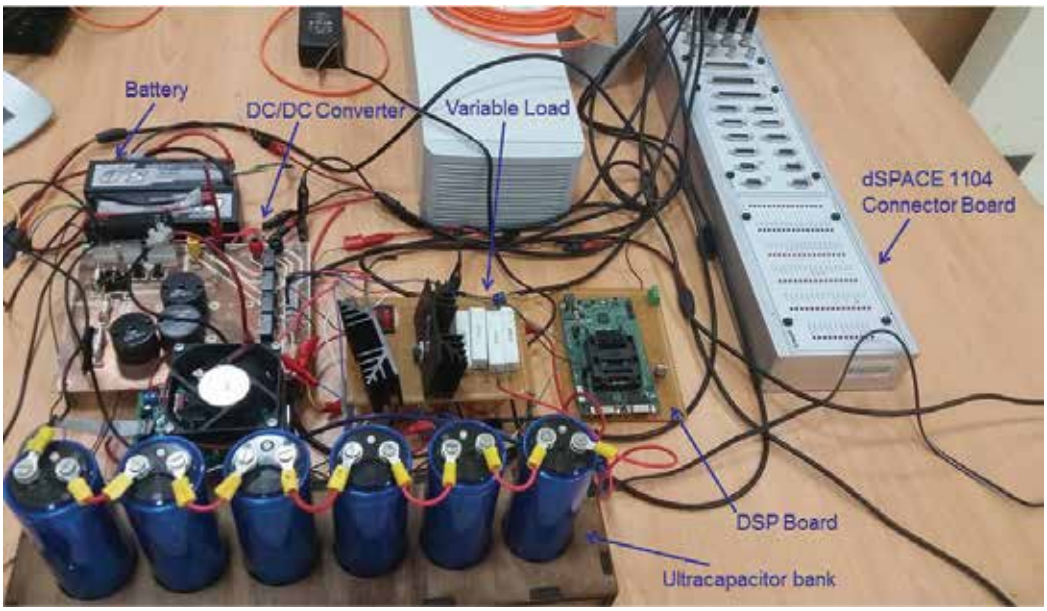


**Figure 4.** Hardware prototype of the proposed UC-based energy storage system.

| Symbol | Parameter | Value |
|---|---|---|
| $R_0$ | Resistive load | 25 Ω |
| $L$ | Inductance | 1.35 H |
| $R_L$ | Inductor Internal Resistance | 0.2 Ω |
| $C_s$ | UC Bank | 383.3 F |
| $R_s$ | UC Bank Internal Resistance | 0.2 Ω |
| $C_f$ | Output capacitor | 4700 μF |
| $v_{sn}$ | Nominal UC voltage | 15 V |
| $v_{bn}$ | Nominal battery voltage | 42 V |
| $C_b$ | Battery storage capacitor | 900 F |
| $R_b$ | Battery internal series resistance (ESR) | 0.4 Ω |
| $R_d$ | Battery storage resistance | 470 Ω |
| $T_s$ | Outer Loop Sampling time | 12.5 μs |
| $t_s$ | Current Control Loop Sampling Time | 5 μs |
| $\Delta i$ | Current controller Hysteresis band | 0.5 A |
| $T$ | Synergetic Controller Time Constant | 10 ms |
| $k_1$ | Synergetic Controller Gain | 0.01 |
| $k_2$ | Synergetic Controller Gain | 100 |

**Table 1.** Prototype system parameters.

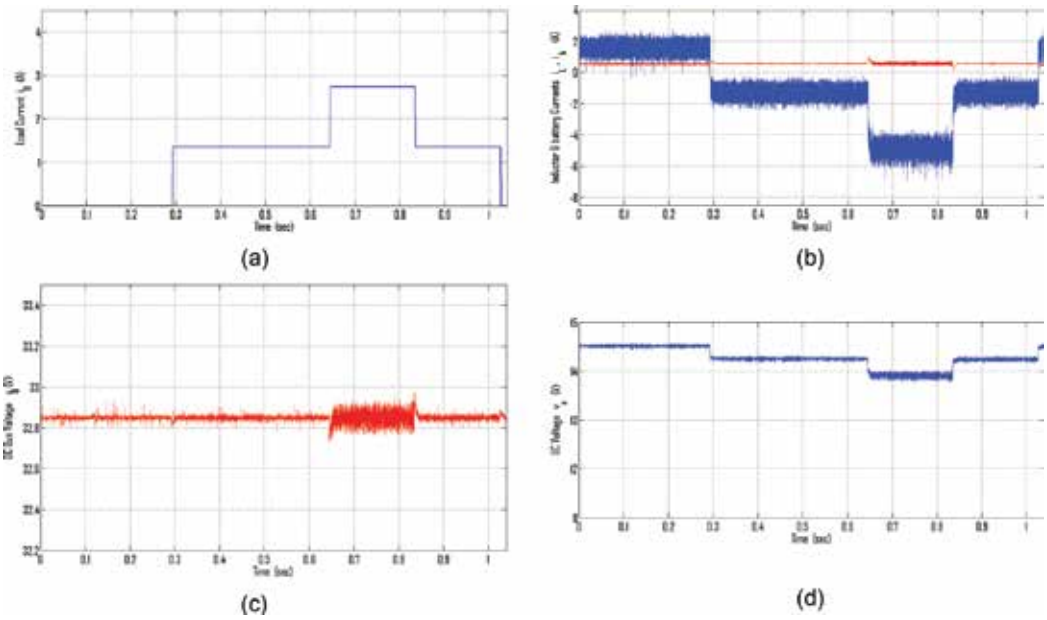


**Figure 5.** Experimental results with synergetic controller and variable load. (**a**) Load current $i_0$; (**b**) DC-bus voltage $v_0$; (**c**) battery current $i_b$ and SC current $i_{sc}$; and (**d**) SC voltage $v_s$.

The output voltage also maintains its steady-state value with minimum variation, except at large load, when the ripple voltage is increased. This is mainly due to the large inductor current ripple. Despite the large variation in load, the peak-to-peak voltage variation is

$$\Delta v_0 = \frac{v_{0\max} - v_{0\min}}{v_{0r}} = \frac{32.97 - 32.76}{32.85} = 0.73\%. \tag{28}$$

This result shows a very good agreement with the simulation results obtained in Section 5.

The transient performance of the proposed synergetic controller is next compared with the standard PI controller, and its ability to achieve optimal transient performance is verified. The PI voltage control loop is implemented using the measured output DC-bus voltage.

$$I_r = k_p(v_{0r} - v_0) + k_i \int_0^t (v_{0r} - v_0)dt. \tag{29}$$

**Figures 6** and **7** show the system response to a load step change for both controllers under the same operating conditions. The DC-bus voltage is regulated to follow a reference value $v_{0r} = 32.7V$. The PI controller gains were tuned to achieve a fast transient response while keeping the overshoot below 1%.

A step load change ($i_0$ = 2.56 A) is applied at t = 0.0047 s. For the PI controller, the DC-bus voltage is reduced due to this sudden load change as shown in **Figure 6b**. It goes through a transient and then recovers back to the reference value within 10.7 ms. For the synergetic

controller, the voltage deviation is smaller, and the transient response is faster with a settling time of 7.1 ms as shown in **Figure 7b**. The battery and supercapacitor currents' behavior can be compared by referring to **Figure 6c** and **Figure 7c**. In both cases, the UC current changes rapidly from the charging mode to the discharging mode to supply the required additional load current. However, it can be observed that the battery current shows a larger variation and

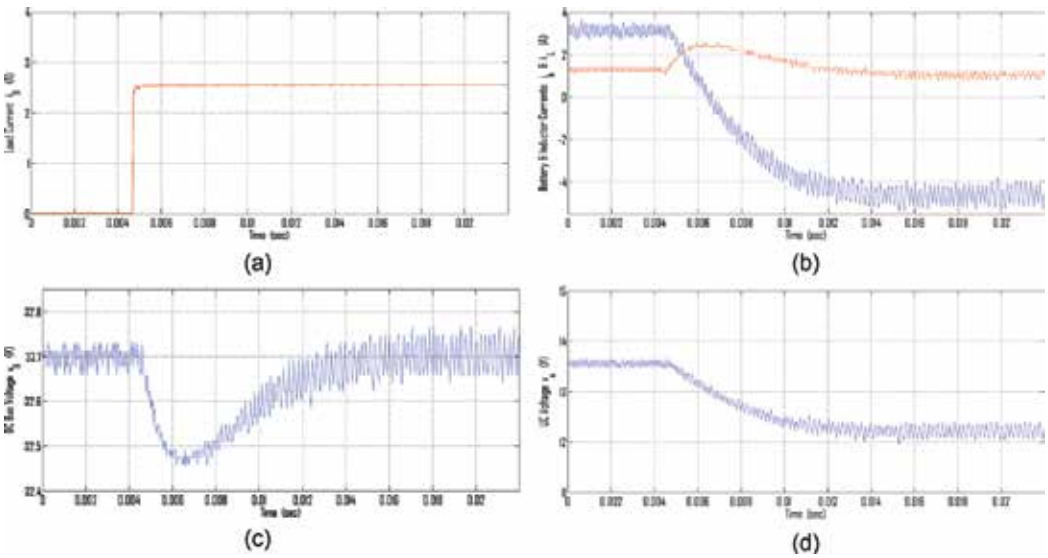


**Figure 6.** Experimental results with PI controller and a step load. (**a**) Load current ; (**b**) DC-bus voltage $v_0$; (**c**) battery current $i_b$ and SC current $i_{sc}$; and (**d**) SC voltage $v_s$.

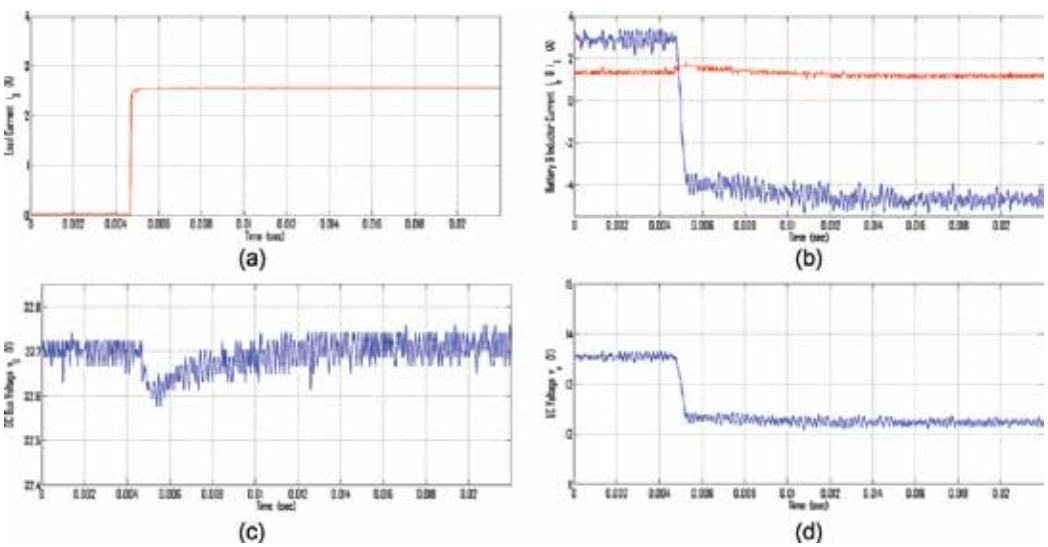


**Figure 7.** Experimental results with synergetic controller and a step load. (**a**) Load current $i_0$; (**b**) DC-bus voltage $v_0$; (**c**) battery current $i_b$ and SC current $i_{sc}$; and (**d**) SC voltage $v_s$.

a slower response for the case of the PI controller compared to the synergetic controller. The same behavior is observed for the UC voltage in **Figure 6d** and **Figure 7d**.

**Table 2** gives the peak-to-peak variations of the battery current and the DC-bus voltage for both controllers. It can be seen that the synergy-based controller has a much better transient performance and a higher robustness to disturbances than the PI controller.

| Controller | | PI controller | Synergetic controller |
|---|---|---|---|
| Battery current variation | $\Delta i_b = \frac{i_{b\max} - i_{b\min}}{i_{ss}}$ | 96.50% | 37.13% |
| DC-bus voltage variation | $\Delta v_0 = \left\lvert \frac{v_{0\max} - v_{0\min}}{v_{0r}} \right\rvert$ | 0.73% | 0.37% |
| Settling time | To reach steady state | 10.7 ms | 7.1 ms |

**Table 2.** Experimental results with PI controller and synergetic controller under variable load.

## 8. Conclusion

This chapter proposes a fast-response synergetic controller for a battery-ultracapacitor energy storage system. The synergy-based controller is developed to enhance the system robustness during the transient response of the DC-bus voltage tracking control. The ultracapacitor module is controlled to reinforce the DC-bus during the load transients and smooth the power fluctuations. The stability analysis of the nonlinear control scheme is derived using the Lyapunov theory. The effectiveness of the proposed control scheme is verified by simulations and by experiments on a prototype hybrid energy storage system and its advantages are indicated in comparison with the traditional PI control scheme. This work is intended as a preliminary study to optimize the performance of electric vehicles. It is believed that the presented technique will provide a strong foundation for the development of a range of full-field synergy-based control techniques in electric vehicles. The added advantages of this technique is that it has a cascade control structure which can be easily adapted and implemented on existing EV control systems. Only additional current and voltage sensors are needed to implement the feedback control loops. This could be a versatile tool to improve both the vehicle range and battery cycle life through optimal management of the onboard power and energy and realize full utilization of the installed storage capacities.

## Author details

Rached Dhaouadi[1]*, Kamyar Khosravi[1] and Yoichi Hori[2]

*Address all correspondence to: rdhaouadi@aus.edu

1 College of Engineering, American University of Sharjah, Sharjah, UAE

2 Graduate School of Frontier Science, The University of Tokyo, Chiba, Japan

## References

[1] Dyke KJ, Schofield N, Barnes M. The impact of transport electrification on electrical networks. IEEE Transactions on Industrial Electronics. 2010;**57**(12):3917-3926

[2] Sant AV, Khadkikar V, Xiao W, Zeineldin HH. Four-Axis vector-controlled dual-rotor PMSM for plug-in electric vehicles. IEEE Transactions on Industrial Electronics. 2015; **62**(5):3202-3212

[3] Huang W, Abu Qahouq JA. Energy sharing control scheme for state-of-charge balancing of distributed battery energy storage system. IEEE Transactions on Industrial Electronics. 2015;**62**(5):2764-2776

[4] Hu KW, Yi PH, Liaw CM. An EV SRM drive powered by battery/Supercapacitor with G2V and V2H/V2G capabilities. IEEE Transactions on Industrial Electronics. 2015;**62**(8): 4714-4727

[5] Shuai L, Corzine KA, Ferdowsi M. Unique ultracapacitor direct integration scheme in multilevel motor drives for large vehicle propulsion. IEEE Transactions on Vehicular Technology. 2007;**56**(4):1506-1515

[6] Dixon JW, Ortuzar ME. Ultracapacitors + DC-DC converters in regenerative braking systems. IEEE Aerospace and Electronic Systems Magazine. 2002;**17**(8):16-21

[7] Delille G, François B. A review of some technical and economic features of energy storage technologies for distribution system integration. Ecological Engineering and Environment Protection. 2009;**1**:40-48

[8] Zhang Z, Zhang X, Chen W, Rasim Y, Salman W, Pan H, Yuan Y, Wang C. A high-efficiency energy regenerative shock absorber using supercapacitors for renewable energy applications in range extended electric vehicle. Applied Energy. 2016;**178**:177-188

[9] Herrera V, Milo A, Gaztañaga H, Etxeberria-Otadui I, Villarreal I, Camblong H. Adaptive energy management strategy and optimal sizing applied on a battery-supercapacitor based tramway. Applied Energy. 2016;**169**:831-845

[10] Ma T, Yang H, Lu L. Development of hybrid battery–supercapacitor energy storage for remote area renewable energy systems. Applied Energy. 2015;**153**:56-62

[11] Abbey C, Joos G. Supercapacitor energy storage for wind energy applications. IEEE Transactions on Industrial Electronics. 2007;**43**(3):769-776

[12] Makhlouf M, Messai F, Benalla H. Modeling and simulation of grid-connected hybrid photovoltaic/battery distributed generation system. Canadian Journal on Electrical and Electronics Engineering. 2012;**3**(1):1-10

[13] Fakham H, Lu D, Francois B. Power control Design of a Battery Charger in a hybrid active PV generator for load-following applications. IEEE Transactions on Industrial Electronics. 2011;**58**(1):85-93

[14] Capasso C, Sepe V, Veneri O, Montanari M, Poletti L. Experimentation with a ZEBRA plus EDLC based hybrid storage system for urban means of transport. In: Proceedings of the 2015 International Conference on Electrical Systems for Aircraft, Railway, Ship Propulsion and Road Vehicles (ESARS); 3-5 March 2015; Aachen, Germany. IEEE; 2015. DOI: 10.1109/ESARS.2015.7101498

[15] Sanfélix J, Messagie M, Omar N, Mierlo JV, Hennige V. Environmental performance of advanced hybrid energy storage systems for electric vehicle applications. Applied Energy. 2015;**137**:925-930

[16] Capasso C, Veneri O, Patalano S. Experimental study on the performance of a ZEBRA battery based propulsion system for urban commercial vehicles. Applied Energy. 2017; **185**(2):2005-2018

[17] Krause A, Kossyrev P, Oljaca M, Passerini S, Winter M, Balducci A. Electrochemical double layer capacitor and lithium-ion capacitor based on carbon black. Journal of Power Sources. 2011;**196**(20):8836-8842

[18] Tan SC, Lai YM, Tse CK, Salamero LM, Wu CK. A fast-response sliding-mode controller for boost-type converters with a wide range of operating conditions. IEEE Transactions on Industrial Electronics. 2007;**54**(6):3276-3286

[19] Wai RJ, Chen MW, Liu YK. Design of adaptive control and fuzzy neural network control for single-stage boost inverter. IEEE Transactions on Industrial Electronics. 2015;**62**(9): 5434-5445

[20] Kolesnikov A. Synergetic control for electromechanical systems. In: Proceedings of the 15th International Symposium on Mathematical Theory of Networks and Systems (MTNS 2002); August 12–16, 2002; University of Notre Dame. 2002

[21] Kondratiev I, Santi E, Dougal R, Veselov G. Synergetic control for m-parallel connected DC-DC Buck converters. In: Proceedings of the 35th Annual IEEE Power Electronics Specialists Conference (PESC 04); 20-25 June 2004; Aachen, Germany: IEEE; 2004. p. 182-188. DOI: 10.1109/PESC.2004.1355739

[22] Santi E, Monti A, Li D. Synergetic control for power electronics applications: A comparison with the sliding mode approach. Journal of Circuits, Systems, and Computers. 2004; **13**(4):737-760

[23] Guangfu MA, Jing H, Gang L, Chuanjiang L. Adaptive synergetic optimal control for attitude tracking of rigid spacecraft. In: Proceedings of the 30th Chinese Control Conference; July 22–24, 2011; Yantai, China. 2011. p. 1865-1870

[24] Nusawardhana SAK, Crossley W. Nonlinear synergetic optimal control. Journal of Guidance, Control, and Dynamics. 2007;**30**(4):1134-1147

[25] Dhaouadi R, Hori Y, Huang X. Robust control of an ultracapacitor-based hybrid energy storage system for electric vehicles. In: Proceedings of the 13th IEEE International Workshop

on Advanced Motion Control, (AMC2014); March 14-16, 2014; Yokohama, Japan. IEEE; 2014. DOI: 10.1109/AMC.2014.6823275

[26] Buller S, Thele M, De Doncker RWAA, Karden E. Impedance-based simulation models of supercapacitors and Li-ion batteries for power electronic applications. IEEE Transactions on Industry Applications. 2005;**41**(3):742-747

[27] Zubieta L, Bonert R. Characterization of double-layer capacitors for power electronics applications. IEEE Transactions on Industry Applications. 2000;**36**(1):199-205

Section 3

# Integration of Energy Storage into Applications

Chapter 6

# Analysis of Various Energy Storage Systems for Variable Speed Wind Turbines

Youngil Kim and Robert J. Harrington

Additional information is available at the end of the chapter

http://dx.doi.org/10.5772/intechopen.72294

**Abstract**

During the high penetration of wind power, wind turbines can affect power quality directly due to an unstable and intermittency source. Voltage fluctuations, harmonics, and voltage drops might be factors in this environment. Energy storage systems (ESSs) with variable speed wind turbines (VSWTs) as a permanent magnetic synchronous generator (PMSG) and a doubly fed induction generator (DFIG) could be a solution to improve the power quality from the "variability" of wind power. This chapter investigates the proposed system, which comprises a hybrid ESS for the VSWT. It analyzes the ability of various ESSs (B, SC, and EDLC) based on VSWTs with various ESSs for power quality in terms of average THD (%) specified in reference to IEEE std-519-1992 and IEC 61400-21-Ed.2.0. In addition, this chapter investigates the DFIG with hybrid energy storage systems (Li ion battery and super capacitor ESS) for the economic evaluation in terms of payback time. The simulation results have been verified by a power system computer-aided design/electromagnetic transients direct current (PSCAD/EMTDC) to demonstrate the system performance under different scenarios.

**Keywords:** VSWT, hybrid ESS, total harmonic distortion, power quality, payback time, PSCAD/EMTDC

## 1. Introduction

The DOE's 2009 Annual Energy Outlook projected energy accumulation in the USA. The report describes that the future growth of domestic electric energy will increase by 26% for electricity sector by 2030. This might not only require additional generation capacity of 259 GW but also forecast to increase as 1.7% of total installed capacity until 2030 [1, 2]. Variable speed wind turbine prefers to the conventional operation to extract the maximum power from the unstable wind generation. Since speed of wind turbine is nonconstant, the generator should

be controlled by the power electronic circuit. Two variable speed wind turbines (VSWTs) on a principle of power electronics could be classified as DFIGs and PMSGs [3, 4].

DFIG-based wind turbine is a wound rotor induction generator. It consists of three-phase windings on the rotor and stator. The stator winding of the wind turbine is directly connected to the grid winding, while the rotor winding of the generator is fed by variable frequency bidirectional back-to-back PWM based on the voltage source converter, which consists of rotor side converter (RSC) and grid side converter (GSC). It has typically about 30% of nominal generator power [3, 4]. The synchronous machine has the ability to provide its own excitation on the rotor. Such excitation may be obtained by means of either a current carrying winding or permanent magnets (PMs) [5]. PM excitation avoids the field current supply or reactive power compensation facilities [2, 6–8]. PMSG is a permanent magnet synchronous machine with its stator windings connected to the grid through a frequency converter. Signal frequency is generated via the pulse width modulation (PWM) with the DC link of back-to-back voltage source converters (VSCs) consisting of machine side converter and grid side converter [9, 10].

There are several state-of-the-art technologies on wind power and energy storage to improve power quality and stability by optimal control of ESS [11–17], hybrid ESS [18, 19], and renewable forecasting modeling [20, 21]. It is widely popularized that an elaborately optimal control strategy for ESS is to smooth wind power fluctuations for the renewable energy [11–14]. Two configurations of DFIG-BESS for internal and external controllers have improved the capability integrated to the grid [15]. In [16], an optimal control scheduling was considered on the variable smoothing time constant and charging/discharging of power limits, which is to mitigate the wind power fluctuations, while extending the battery life cycle of the BESS. A control strategy of the ESS in the wind farm focused an open-loop optimal control scheme is to incorporate the operating limits of BESS based on the forecasted wind condition [17]. The author [18] introduced the hybrid energy storage system (HESS) to overcome the fast PV-wind power generation fluctuations by smart scheduling, which has a statistical approach for the capacity distribution of the HESS. However, they did not demonstrate real-time simulation with few limited cases. The control and energy management of the hybrid ESS (battery and super capacitor) with DFIG has coordinated the power flows and load demand [19]. Prediction scheme of wind power generation connected to battery ESS developed by using numeric weather prediction model which required to the input as detailed wind information [20]. However, they did not smooth to power variation scheme in this chapter. Energy management system of flywheel ESS used to fuzzy logic for two optimized models as constraint condition and determine optimization objective to control of FESS [21].

## 2. Configuration of the hybrid ESS of the variable speed wind turbines

The configuration of the HYESS-DFIG is illustrated in **Figure 1(a)**. DFIG is a variable speed wind turbine with a partial scale power converter in the rotor circuit. The main objective of the

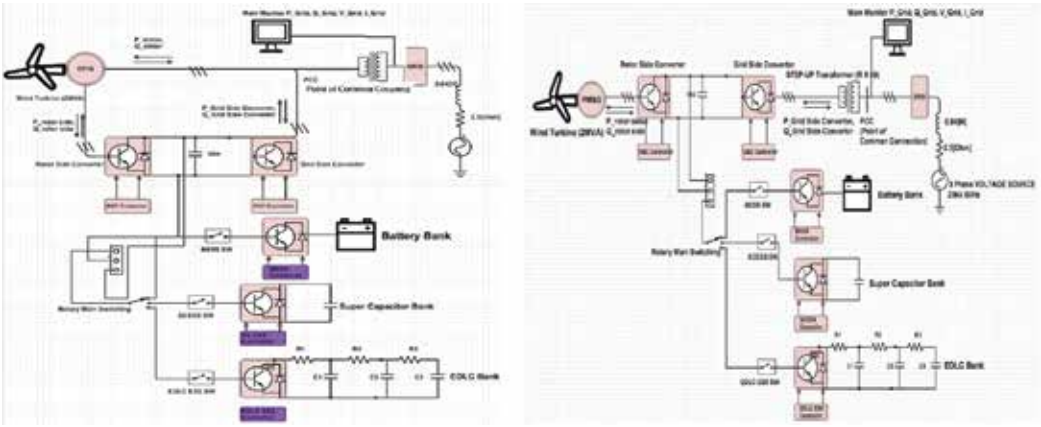


**Figure 1.** Block diagram of the hybrid energy storage system connected to the configuration variable speed wind turbines: (a) DFIG (left) and (b) PMSG (right).

| | |
|---|---|
| Generated Rated MVA | 2 [MVA] |
| Machine rated angular mechanical speed | 125.667 [rad/s] |
| Rotor radius | 44 [m] |
| Rotor area | 2124 [$m^2$] |
| Air density | 1.229 [$kg/m^3$] |
| Gear box efficiency | 0.97 [P.U] |
| Gear ratio-machine/Turbine | 60 |
| Equation for power coefficient | Mode 2 |

**Table 1.** PSCAD/EMTDC parameters of the wind turbine for DFIG, PMSG in the proposed systems [23].

RSC controller is to regulate active power (Ps) and reactive power (Qs) of the stator side independently, while the GSC controller is to keep the constant DC voltage ($V_{dc}$) to adjust reactive power (Qg) of the GSC, which transfers from the grid side [22]. **Figure 1(b)** describes that PMSG which is a variable speed wind turbine with a direct-drive generator connected to the grid through a full-scale power converter [2, 6]. Three different ESS such as battery (B), super capacitor (SC), and electrical dual layer capacitor (EDLC) were introduced in **Figure 1**. Each ESS controller comprised bank, inductance and two-quadrant DC/DC converter connected to the DC link as illustrated in **Figure 1**. Two DC/DC converter design includes two insulated gate Bi-polar junction transistors (IGBTs) diode switches as S1 and S2. To compare two different VSWTs, that is, DFIG and PMSG, three-phase voltage sources are employed at 20 kV, 60 Hz, 0.04 H, and 2.5 Ω, and PSCAD parameter of the wind turbine given in **Table 1**.

### 2.1. Model of the wind turbines

Variable speed wind turbine could be mathematically described by the follows (1), (2), (3). A wind turbine extracts kinetic energy ($P_{wind(kin)}$) from the swept area (Area) of the blades. The power of the airflow ($P_{airflow}$) is given by [3, 24]:

$$P_{air} = \frac{1}{2} \cdot \rho \cdot \text{Area} \cdot v^3 \tag{1}$$

where ρ, *Area*, *v* is the symbol of air density (approximately 1.225 kg/m$^3$), swept area of rotor $(m^2)$, upwind free wind speed (m/s), respectively.

The wind power ($P_{wind(kin)}$) transferred to the rotor of VSWT could be expressed by

$$P_{wind(kin)} = C_{pt}(\lambda, \beta) \cdot \frac{1}{2} \cdot \rho \cdot \text{Area} \cdot v^3 \tag{2}$$

where $C_{pt}(\lambda, \beta)$ is a power coefficient, $\lambda$ is a function of tip speed ratio , and β is pitch angle. Wind turbines are characterized by their aerodynamic torque or turbine torque as Ta [3, 24, 25]:

$$Ta = \frac{C_{pt}(\lambda, \beta) \frac{1}{2} \cdot \rho \cdot \text{Area} \cdot v^3}{\Omega_t} \tag{3}$$

where A is the maximum value of $C_{pt}$ defined by the Betz limit, which a turbine can never extract more than 59.3% of the power from an air stream [21, 25]. In reality, wind turbine rotors have maximum $C_p$ values in the range 25–45% [7].

### 2.2. Park's model of the VSWT

For our proposed system, the Park's model was used in VSWT (DFIG and PMSG) [3]. The voltage equations in the d, q axes-frame are given as follows [4, 5, 22, 26]:

$$V_d = \frac{d\phi_d}{dt} - \omega_r \phi_q + R_a I_d \tag{4}$$

$$V_q = \frac{d\phi_q}{dt} + \omega_r \phi_d + R_a I_q \tag{5}$$

$$\omega_r = \frac{d\theta}{dt} \tag{6}$$

$$\theta = \int_0^t \omega_r dt + \theta_0 \tag{7}$$

$\phi_d, \phi_q, I_d, I_q, V_d, V_q$ are the stator fluxes, current and voltage of the d and q components; $R_a$ is the stator resistance; $\omega_r$ is the rotor speed in electrical [radians/s]. The general Park's

model is used to explain about the control scheme of an induction machine. The equation of voltage vector in the DFIGs is expressed as follows [4, 5, 22, 26]:

$$V_s = R_s i_s + \frac{d\phi}{dt} + j\omega_s \varnothing_s \tag{8}$$

$$V_r = R_r i_r + \frac{d\phi}{dt} + j\omega_r \varnothing_r \tag{9}$$

$$\varnothing_s = L_s i_s + L_m i_r \tag{10}$$

$$\varnothing_r = L_m i_s + L_r i_r \tag{11}$$

The equivalent two-phase model of the symmetrical variable speed wind turbine (dq frame) used to synchronously rotating reference frame (dq frame) as follows [7]:

$$v_{sd} = R_s \cdot i_{sd} + \frac{d\phi_{sd}}{dt} - \omega_s \phi_{sq} \tag{12}$$

$$v_{sq} = R_s \cdot i_{sq} + \frac{d\phi_{sq}}{dt} + \omega_s \phi_{sd} \tag{13}$$

$$v_{rd} = R_r \cdot i_{rd} + \frac{d\phi_{rd}}{dt} - \omega_r \phi_{rq} \tag{14}$$

$$v_{rq} = R_r \cdot i_{rq} + \frac{d\phi_{rq}}{dt} + \omega_r \phi_{rq} \tag{15}$$

The stator and rotor fluxes using the synchronously rotating reference frame (d,q frame) are given as follows [5, 8, 9, 22]:

$$\begin{cases} \phi_{sd} = L_s i_{sd} + L_m i_{rd} \\ \phi_{sq} = L_s i_{sq} + L_m i_{rq} \end{cases} \tag{16}$$

$$\begin{cases} \phi_{rd} = L_r i_{rd} + L_m i_{sd} \\ \phi_{rq} = L_r i_{rq} + L_m i_{sq} \end{cases} \tag{17}$$

where $R_s, R_r$ indicate equivalent resistance of stator and rotor windings. $L_s, L_r, L_m$ indicate self and mutual inductances of stator and rotor windings, respectively. Ignoring the power losses in the stator and rotor resistances, the active and reactive powers from the stator are given by

$$P_S = \frac{3}{2}\left(v_{sd} \cdot i_{sd} + v_{sq} i_{sq}\right) \tag{18}$$

$$Q_S = \frac{3}{2}\left(v_{sd} \cdot i_{sd} - v_{sq} i_{sq}\right) \tag{19}$$

$$P_r = \frac{3}{2}\left(v_{rd} \cdot i_{rd} + v_{rq} i_{rq}\right) \tag{20}$$

$$Q_r = \frac{3}{2}\left(v_{rd} \cdot i_{rd} + v_{rq} i_{rq}\right) \tag{21}$$

The electromagnetic torque is given by [4, 5, 22, 26]:

$$T_e = \frac{3}{2} p \phi_s i_{sq} = -\frac{3}{2} p \phi_s \frac{L_m}{L_s} i_{rq} = -\frac{3}{2} p \frac{V_{sq}}{\omega_s} \frac{L_m}{L_s} i_{rq} \tag{22}$$

The synchronous model is also expressed in the (d,q) synchronous Park's model, and the voltage equations of the PMSG are represented as follows [7]:

$$\frac{di_{sd}}{dt} = \frac{1}{L_d}\left(-R_s i_{sd} + \omega L_q i_{sq} - V_{sd}\right) \tag{23}$$

$$\frac{di_{sq}}{dt} = \frac{1}{L_q}\left(-R_s i_{sq} - \omega_e L_d i_{sd} - V_{sq} + \omega_{PM} \varnothing_f\right) \tag{24}$$

where $V_{sd}$, $V_{sq}$, $i_{sd}$ and $i_{sq}$ are voltage and current for the d,q axis of the stator side. $\varnothing_f$ is the magnitude of the flux linkages by using the permanent magnetic flux [Web]; $\omega_{PM}$ is the value as rotating speed [rad/s] of the PMSG. The electromagnetic (EM) torque in the rotor could be expressed as follows [7]:

$$T_e = \frac{3}{2}\, p\, \varnothing_f i_{sq} \tag{25}$$

p is the number of pole pairs in the PMSG.

## 3. Modeling and control of the grid connected to various ESSs

Energy storage systems (ESSs) have a function of converting electrical energy from a power system network into a form that can be stored for converting back to electrical energy when needed [8, 9]. ESS has numerous applications including portable devices, smart grid, building integration, energy efficiency, transport vehicles, and stationary renewable energy resources [27]. In this chapter, only three different distributed ESSs for renewable generation systems were introduced as battery, super capacitor, and electrical dual layer capacitor [23]. **Table 2** summarizes the characteristics of three different ESSs.

### 3.1. Modeling and control of energy storage systems

**Figure 2** shows that each E-ES, for this study, consists of an energy source bank, an inductance and a two-quadrant DC/DC converter connected to the DC link. It also describes how the controller of the DC/DC buck-boost mode generates the gate signals for gate 1 and gate 2 [23].

| Categories | ESS Technology | Energy Related Cost ($/kwh) | Replacement Cost ($/kwh) | Energy Function | Charge (response) Time | Efficiency (%) |
|---|---|---|---|---|---|---|
| Chemical Energy Storage | Lead Acid B ESS | 300 | 300 | $E(t) = E_0 + \int v(t) \cdot i(t)dt$ | 1 min to 3 hours | 60~70% |
| | Lion and NaS B ESS | 500 | 500 | | | 70~80% |
| Magnetic Energy Storage | SC and EDLC ESS | 30,000 | 0 | $E(t)=\frac{1}{2} \cdot CV^2_{sc\ or\ EDLC}$ | 1 s to 1min | 70~80% |

**Table 2.** Properties of three different ESSs [23].

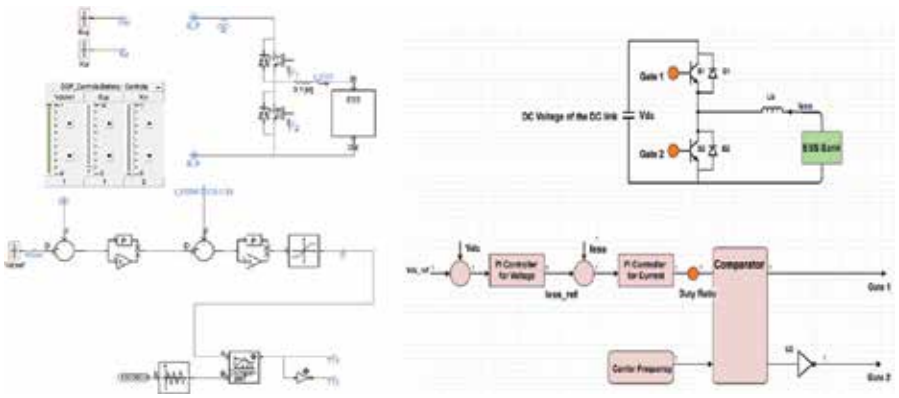

**Figure 2.** Block diagram of the ESS in PSCAD/EMTDC: modeling of ESS (upper) [14] and controller of ESS (lower) [29].

The reference value of the $i_{ess}$ can be made by using a voltage feedback control between $V_{dc\text{-}ref}$ and $V_{dc}$ with PI controller of the voltage. It can be expressed as follows [2, 25, 28]:

$$i_{ess\text{-}ref} = \left[k_{vp} + \frac{k_{vi}}{s}\right]\left(v_{dc\text{-}ref} - v_{dc}\right) \tag{26}$$

The inner current control loop using a PI controller of current can be produced by using the duty ratio to generate the gate-signal $i_{ess\text{-}ref}$, as given by Eq. (27) [2, 25, 28]:

$$D = \left[k_{bp} + \frac{k_{bi}}{s}\right]\left(i_{ess\text{-}ref} - i_{ess}\right) \tag{27}$$

Finally, the gate signal is generated by comparing the difference between the duty ratio and the carrier frequency.

### 3.2. Energy flow and Total harmonic distortion of various energy storage systems

The HYESS which is applied to the VSWT system uses DC-DC converters with controller of the ESS illustrated in **Figure 2**. When active power of DFIGs and PMSGs in the rotor side (Pr) or

stator side (Ps) is greater than active power of DFIG and PMSG on the grid side (Pg), the ESS charges the energy flow from the DC bus to the ESS Bank through the S1 switch and S2 diode [26, 29, 30].

Therefore, the source of ESS works to absorb active power from the DC voltage, while acts as a step-down converter when $V_{ess}$ boosts. The DC-DC converter design used as a buck converter circuit, and then D1 (duty ratio) of S1 in the buck mode can be computed by (28) [31]:

$$D1 = [V_{ess}/V_{dc}] \tag{28}$$

When Pg is bigger than Pr, the E-ES energy discharges through S1 and S2, and energy flows to the DC bus ($V_{dc}$) [27–29]. In this case, the converter acts as a boost converter mode [27–29]. The ESS bank serves as a source to supply active power, which results in the decrease of the voltage $V_{ess}$. The duty ratio D2 of S2 in the boost mode can be expressed as (29) [25]:

$$D_2 = 1 - D_1 \tag{29}$$

**Table 3** summarizes the energy flow in the two modes, that is, buck and boost modes.

The harmonic distortion of the voltage and current waveforms is generally expressed in terms of the fundamental frequency [32]. Power injection from the HY ESS affects the power quality, which is described as voltage and current THD. In Ref. [30], the practices and requirements for harmonic control in electrical power systems are established. **Figure 3** shows the PSCAD/EMTDC modeling for the voltage (Vg), current (Ig), and active power (Pg) of the THD measurement at the point of common connection (PCC) in the proposed system. With the increasing use of the nonlinear devices, harmonic distortion of the voltage waveform is a problem which is receiving the considerable attention. Any periodic waveform of nonsinusoidal form can be synthesized by expressing it as the sum of a series of harmonics of the fundamental frequency by using Fourier analysis (30) [31]:

$$f(t) = a_0 + a_1 \cos \omega t + a_2 \cos 2\omega t + a_3 \cos 3\omega t + \ldots + b_1 \cos \omega t + b_2 \cos 2\omega t + b_3 \cos 3\omega t + \ldots \tag{30}$$

where

$$a_0 = \frac{1}{T}\int_0^T f(t)dt, \quad a_n = \frac{2}{T}\int_0^T f(t)\cos n{\cdot}\omega t{\cdot}dt, \quad b_n = \frac{2}{T}\cdot\int_0^T f(t)\sin n{\cdot}\omega t{\cdot}dt$$

| Energy flow | Charge (Pr or Ps > Pg): From DC bus to the ESS | Discharge (Pr or Ps < Pg): From ESS to DC Bus |
|---|---|---|
| Bank | Sink as absorb active power | Source as supply active power |
| $V_{ess}$ | Increase | Reduce |
| Switch direction of two quadratic converters | S1 switch and S2 diode | S2 switch and S2 Diode |
| Converter act as | Buck converter as $V_{dc}$→reduce | Boost converter as $V_{dc}$→increase |

**Table 3.** Energy flow of the energy storage systems.

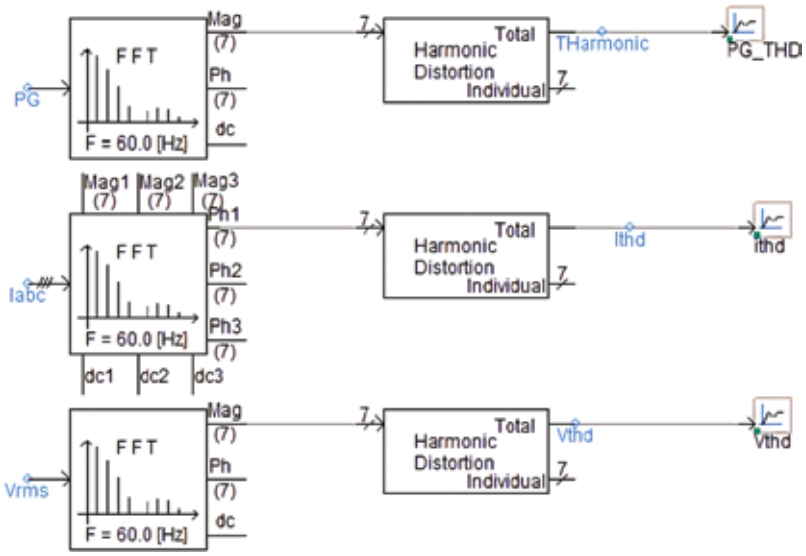


**Figure 3.** PSCAD modeling of 7th order 60 Hz for THD of active power, current, voltage at the PCC.

Total harmonic distortion (THD) is usually expressed as a percentage of fundamental voltage by the expression as (31):

$$\sqrt{\sum_{n=2}^{n=7}\left(\frac{V_n}{V_1}\right)^2} \times 100\% \tag{31}$$

where V1 = fundamental frequency voltage component, Vn = nth harmonic voltage component.

### 3.3. Battery energy storage systems (B-ESS)

Batteries have been widely used in many fields, which are referred to as electrical energy storage system, which accumulate electric energy in electrochemical form and delivers direct current (DC). The promising battery which is used as energy storage devices is lithium ion (Li-ion) battery. Due to high electrical potential and energy density of battery, Li-ion batteries are one of the promising solutions for the storage compared to other battery options. In addition, Li-ion batteries do not have poisonous metals (lead, mercury, or cadmium) and memory effect. The main disadvantage of Li-ion battery is the required high production cost [33]. The energy of battery could be calculated by (32):

$$E = IVh \tag{32}$$

where I (A) and V(V) are current and voltage of battery and h (hours) is the charging time. For this study, a Panasonic LJ-SK84A Li-ion storage battery system [34] is used to design about the modeling for the PSCAD battery as 8 KWh from 110 to 165 V in **Figure 4**.

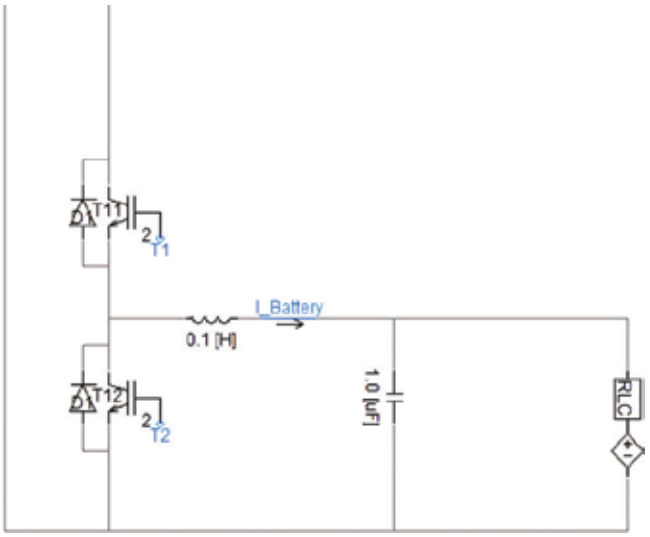


**Figure 4.** Modeling of PSCAD/EMTDC: BESS.

*3.3.1. State of charge*

In the Li-ion battery, over charging or over discharging could result in reducing the battery stack life and indirectly increasing the cost. However, accurate calculation of the state of charge (SOC: %) for battery ESS is essential for the battery outputs in powered system that aims at maximizing energy storage system's performance, extending battery life, and realizing the safe operation of the systems including EV, renewable generation, and building integration.

The SOC of the battery is defined as the ratio of the remaining capacity ($Q_{present}$) to the nominal capacity of the cell ($Q_{nominal}$). It could be described as (33)

$$\text{SOC}\ (\%) = \frac{Q\text{-}_{present}}{Q\text{-}nominal} \tag{33}$$

Q is usually measured in the unit of Ah or mAh.

The battery state of charge (SOC) estimation could be calculated by the Coulomb counting (CC) method through the integration of measured battery current or open circuit voltage (OCV) [35–37]. However, unknown initial SOC which caused by the measurement errors and noise in real practice can affect performance, which means unreliable SOC value results in reduced performance and potential risk to the battery system. Therefore, it is critical to develop algorithms that can estimate accurate SOC to improve the performance for the battery energy storage. There are several advanced methods which can be closer to true values over time to compensate for nonlinearity such as extended Kalman filter (EKF) and sigma-point (unscented) Kalman filter (SP/UKF) [35–37].

### 3.4. Super capacitor ESS

**Figure 5** describes about the super capacitors (SCs), which have higher power density, higher round trip efficiency, longer life cycle life, and lower capital cost per cycle than batteries [9, 37]. Therefore, SC is a good candidate for short-term storage (i.e., seconds to minutes). Assuming the initial voltage across the super capacitor ($C_{sc}$) is $V_{sc}$ (0) after charging for a period t, the instantaneous voltage across the capacitor $V_{sc}$ is given by (34)

$$V_{sc}(t) = V_{sc}(0) + \frac{I_L \cdot t}{C_{sc}} \tag{34}$$

where $I_L$ is the load current entering the capacitor from the unregulated power supply.

### 3.5. Electrical dual layer capacitor ESS

Capacitors composed of two conducting plates, which are separated by an insulating material [8, 29]. Conventional capacitors store little energy due to the limited charge storage areas and the separation distance between the two charged areas and the separation distance between the two charged plates [29, 38]. However, super capacitors based on the EDL mechanism can store significantly more energy because of the large interface area and the atomic range of charge separation distances [8]. A simple resistive capacitive equivalent circuit of the EDLC-cell is designed in PSCAD/EMTDC as shown in **Figure 5**.

## 4. Simulation results and discussion

Case I—Analysis of the Variable Speed Wind Turbines with Various ESSs for Power Quality in terms of THD (%).

The simulation results in Case I verify the performance of the hybrid ESS-VSWT by using the PSCAD design tool in terms of the THD (%). The mean wind speed is to make realistic results by using the PSCAD/EMTDC with random noise components during 60 s in **Figure 6**.

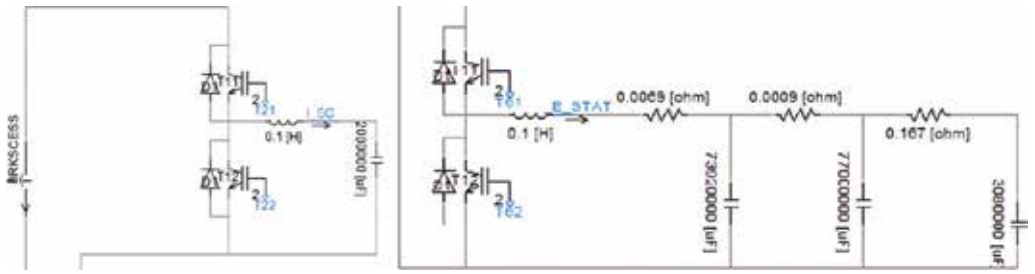


**Figure 5.** PSCAD modeling of the super capacitor as 2F and EDLC [9, 39].

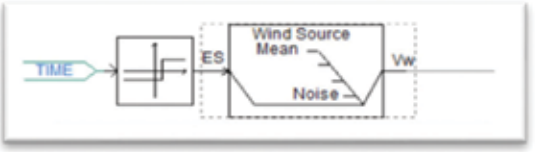


| Wind Source | |
|---|---|
| # of noise components | 50 |
| Noise Amplitude controlling Parameter | 1 rad/sec |
| Surface Drag Coefficient | 0.0192 |
| Turbulence Scale | 600 [m] |
| Random seed Number (1-99) | 3 |
| Time Interval for Random Generation | 4 [s] |

**Figure 6.** PSCAD modeling and noise component for the mean wind speed (10 m/s).

**Comparison of THD (%) with the HY ESS-VSWT (2 MW, 60 Hz, 10 m/s with random noise) during 60 s**

| | DFIG | | | PMSG | | |
|---|---|---|---|---|---|---|
| | **Avg THD for P** | **Avg THD for I** | **Avg THD for V** | **Avg THD for P** | **Avg THD for I** | **Avg THD for V** |
| No ESS | 3.61 | 6.90 | 9.73 | 14.12 | 4.38 | 7.37 |
| B- ESS | 2.90 | 4.44 | 4.58 | 11.31 | 2.78 | 4.94 |
| SC-ESS | 2.77 | 5.68 | 4.65 | 10.97 | 2.30 | 3.73 |
| E- ESS | 2.83 | 5.65 | 4.7 | 11.14 | 2.78 | 5.00 |
| B-SC ESS | 2.90 | 5.74 | 4.43 | 11.18 | 1.82 | 4.96 |
| B- E ESS | 2.89 | 5.75 | 4.69 | 11.14 | 2.79 | 4.93 |
| SC-E ESS | 3.02 | 5.73 | 4.60 | 11.23 | 2.77 | 3.71 |
| B-SC-E ESS | 3.05 | 6.06 | 4.60 | 1.42 | 1.82 | 3.71 |

**Table 4.** Comparison of THD at the PCC.

Power quality issue could be verified by the THD which was monitored at the point of common coupling (PCC) in the VSWT-HYESS as illustrated in **Figure 1**. The data (THD: %) in **Table 4** were extracted from using excel file and then taking an average value (THD: %) during 1 min.

### 4.1. The case of the DFIG-HYESS

**Figure 7** describes average THD (%) of a DFIG at the PCC for P, I, and V during 60 s. **Table 5** shows that average THD (%) of the DFIG is a greater than other DFIG-HYESS. This result showed that the proposed HY ESS-DFIG could improve the power quality by reducing the THD. SC-ESS (2.77%), B-ESS (4.4%), and B-SC ESS (4.43%) are the best choices to enhance power quality in the system, as shown in **Figure 8**.

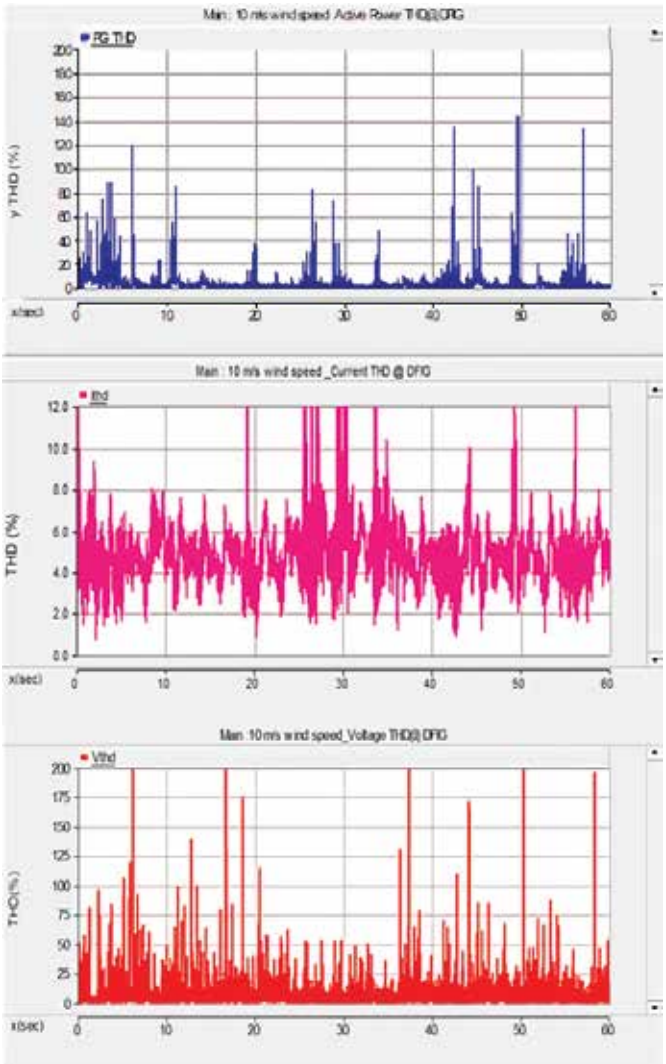


**Figure 7.** THD (%) of only DFIG during 60 second: active power THD (Pthd: upper), current THD (ithd: middle), voltage THD (Vthd: lower).

| Item | Cost ($) |
|---|---|
| Overnight cost of DFIG | 2949000.00 |
| Pb battery ESS | 16862.66 |
| Li-ion battery ESS | 11992.85 |
| Super capacitor ESS | 5574125.98 |

**Table 5.** Cost of 1.5 MW Wind Turbine [9].

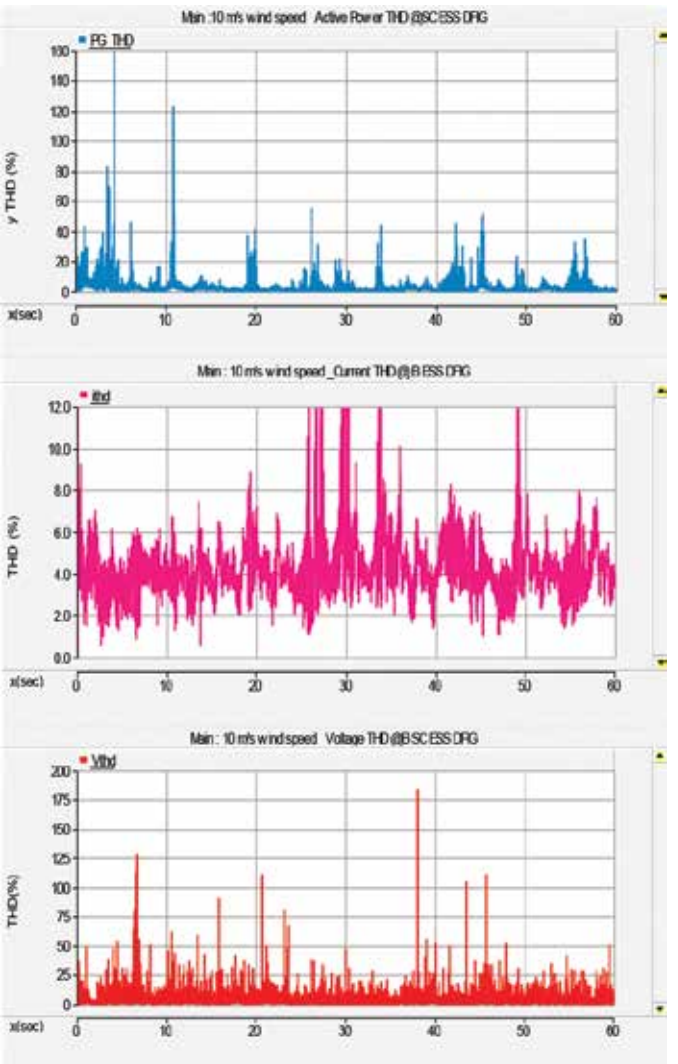


**Figure 8.** THD (%) of HY ESS DFIG during 60 secs: active power THD of SCESS, current THD of BESS, voltage THD of B-SC-E ESS.

### 4.2. In the HYESS-PMSG

**Table 5** shows that the average THD of PMSGs is bigger than HY ESS-PMSG. These results indicate that an ESS which reduces THD (%) is to be improved. SC-E-B ESS is the most effective option in reducing THD for the voltage (3.71%), current (1.82%), and active power (1.42%), as shown in **Figures 9** and **10**.

Case II– Financial analysis of the DFIG with two ESSs in terms of the payback time ($)

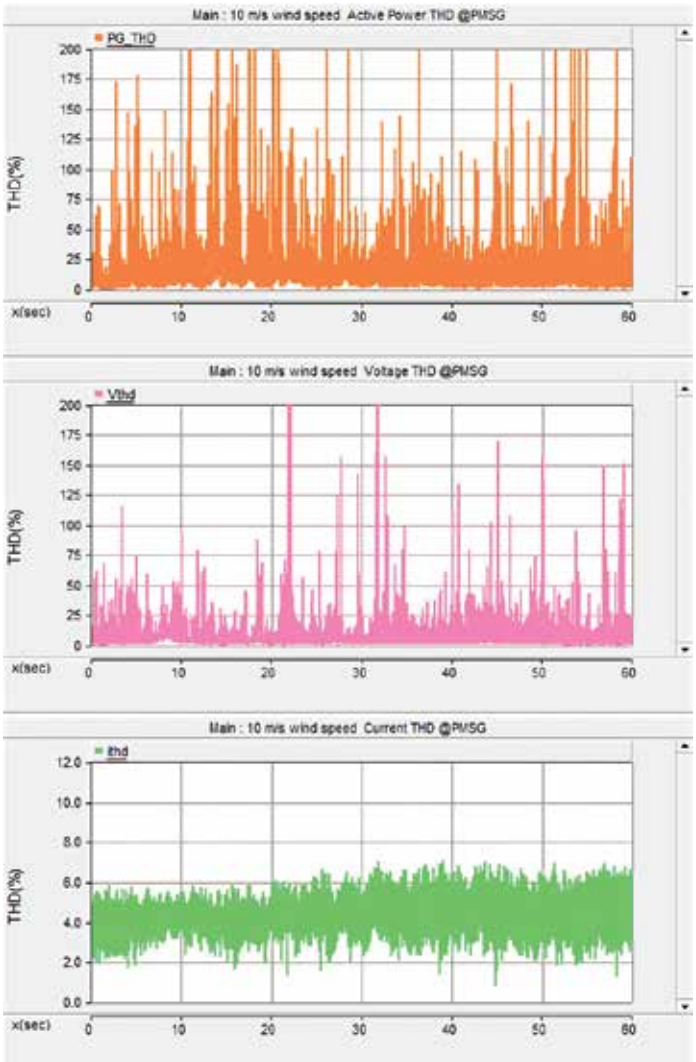


**Figure 9.** THD (%) of only PMSG during 60 s: active power THD (Pthd: upper), current THD (ithd: middle), and voltage THD (Vthd: lower).

Wind energy is free. However, financial analysis can be used to assess wind project investments such as how to screen cost and the benefits of the project. Regarding the financial analysis, the payback time depends on the amount of time to evaluate the performance of different ESSs such as super capacitor ESS (SCESS), battery ESS (BESS). Payback time is the time in which investors can recover all their investment. It depends on several factors such as O&M, inflation, and depreciation. It will show whether a project is worth establishing the investment to escape the risk. Shorter payback time indicates a more economical project. A 1.5 MW wind generator, which sells the electricity generated to utilities, can serve as an example. There are several manufacturers who provide large capacity DFIG. Generally, the overnight

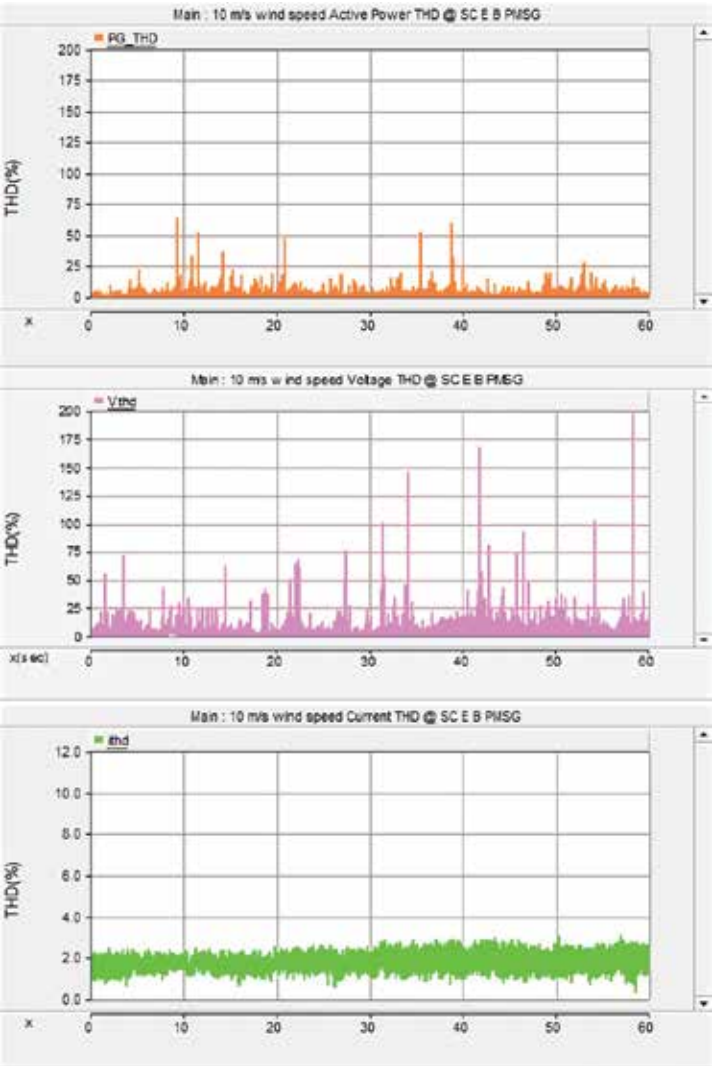


**Figure 10.** THD (%) of HYESS PMSG during 60 sec: active power THD of B-SC-E ESS, current THD of B-SC-E ESS, voltage THD of B-SC-E ESS.

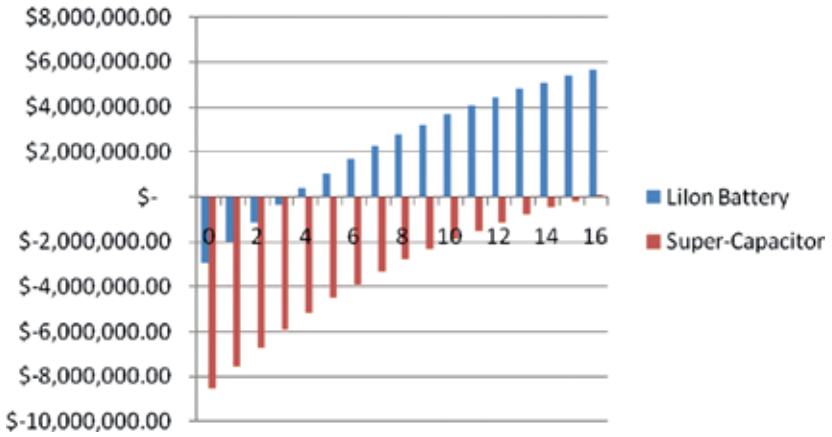


**Figure 11.** Accumulated cash flow.

cost of a wind generator is $1966/kW. The Cost of O&M per year was assumed as $30.98/kW-Year for this work to find payback time from the [39]. A 83.33 kWh super capacitor ESS and Li Ion battery are chosen [40, 41]. The discount rate is also assumed as 9%. The capital cost of a wind generator is provided in **Table 5**.

Payback time in terms of accumulated cash flow could be expressed as (35)

$$\left(\frac{1}{1 + Discount \quad Rate(0.9\%)}\right)^{year} = \text{Capital} \quad \text{Cost} + \text{Net Annual Saving}\ (1,032,838.80) \tag{35}$$

where capital cost is total overnight cost of DFIG ($) + cost of Li ion or SC ESS. The payback time for DFIG with Li ion ESS is 3.47 years; however, the payback time for DFIG with super-capacitor is 15.76 year as shown in **Figure 11**. If a hybrid ESS (B-SC) ESS is chosen, the payback time will be between 3.47 and 15.76 years, according to the proportion of BESS and SCESS given in this system.

## 5. Conclusion

This section analyzes the ability of various HY ESSs based on VSWTs to improve power quality in terms of THD under the same situations: three-phase voltage sources used at 20 kV, 60 Hz, 0.04 H, and 2.5 Ω. From the previous results, HYESS-VSWT has been verified to increase the power quality by reducing THD. SC-ESS (2.77%), B-ESS (4.4%), and B-SC ESS (4.43%) of the DFIG's case would be a better option to improve power quality for active power, voltage, and current, respectively, compared to other cases. In the case of the PMSGs, SC-E-B ESS indicated as the best option to reduce THD for voltage (3.71%), current (1.82%), and active power (1.42%). Compared to average active power THD of a DFIG as 3.61% and PMSG as 14.42% without ESS, a THD (%) for PMSG has lower power quality difference output as 10.81% compared to THD (%) of DFIG. This might be a converter configuration issue because

DFIGs are partially controlled by the back-to-back converter such as RSC and GSC, while PMSGs are directly connected through the back-to-back converter to the grid, which make 100% power rated. Regarding average THD, the PMSG-B E SC-ESS as 1.4% has the most outstanding output results compared to other options. Furthermore, the best option's values from the simulation results satisfy the IEEE Standard requirements, which should be less than 4% for current THD and 5% for voltage THD [30].

In addition, a DFIG with various ESSs is a financially attractive option if a chemical battery ESS is used. The payback time is acceptable, and it still has a benefit for the environment. If the new energy storage technology as a super capacitor is considered, the payback time right now is relatively long. However, if there is a technology breakthrough, the cost of a super capacitor will probably decrease and finally be financially attractive. Presently, a hybrid system will still be relatively affordable. This financial forecast helps achieve the high-power quality and reasonable payback time during the short period.

## Author details

Youngil Kim[1]* and Robert J. Harrington[2]

*Address all correspondence to: yikim01@gwmail.gwu.edu

1 Green Technology Center, Seoul, South Korea

2 The George Washington University, Washington, D.C., USA

## References

[1] US Department of Energy. Annual Energy Outlook 2009 with Projections to 2030. DOE/EIA- 282(2009). March 2009

[2] Mohd. Hasan Ali. Wind Energy Systems Solutions for Power Quality and Stabilization. CRC Press; 2012. Print ISBN: 978-1-4398-5614-7

[3] Anaya-Lara O, Jenkins N, Ekanayake J, Cartwright P, Hughes M. Wind Energy Conversion: Modeling and Control: Wiley. ISBN: 978-0-470-71433-1; August, 2009. 288 pp

[4] Mohd. Abdus Salam. Fundamental of Electrical Machines. 2nd ed: Alpha Science International Ltd. ISBN: 978-81- 8487-163-0; 2013. p. 416

[5] Kirtley JL. Electric Power Principles: Sources, Conversion, Distribution and Use. ISBN: 978-0-470-68636-2. September 2010: Wiley. pp. 159-163

[6] Li H, Chen Z. Overview of different wind generator systems and their comparisons. IET Renewable Power Generator. Jun 2008;**2**(2):123-138

[7] Jayalakshmi NS, Gaonkar DN, Sai Kiran Kumar K. Dynamic modeling and performance analysis of grid connected PMSG based variable speed wind turbines with simple power conditioning system. 2012 IEEE, International Conference on Power Electronics, Drives and Energy Systems. December 16-19, 2012, Bengaluru, India

[8] Muyeen SM, Takahashi R, Murata T, Tamura J. Integration of an energy capacitor system with a variable-speed wind generator. IEEE Transactions on Energy Conversion. Sep 2009; **24**(3):740-749

[9] Kim Y, Zhao J, Harrington RJ. Performance analysis of energy storage systems connected to a doubly fed induction generator. Green Energy and Systems Conference (IGESC), Long Beach, CA, 2015 IEEE, 9-9 Nov. 2015. pp. 30-34. DOI:10.1109/IGESC.2015.7359387

[10] Li S, Haskew TA, Swatloski RP, Gathings W. Optimal and direct-current vector control of direct-driven PMSG wind turbines. IEEE Transactions on Power Electronics. May 2012; **27**(5):2325-2337

[11] Yao DL, Choi SS, Tseng KJ, Lie TT. A statistical approach to the design of a dispatchable wind power-battery energy storage system. IEEE Transactions on Energy Conversion. Dec 2009;**24**(4):916-925

[12] Bludszuweit H, Domínguez-Navarro JA. A probabilistic method for energy storage sizing based on wind power forecast uncertainty. IEEE Transactions on Power Apparatus and Systems. Aug 2011;**26**(3):1651-1658

[13] Mercier P, Cherkaoui R, Oudalov A. Optimizing a battery energy storage system for frequency control application in an isolated power system. IEEE Transactions on Power Apparatus and Systems. Aug 2009;**24**(3):1469-1477

[14] Brekken TKA, Yokochi A, Von Jouanne A, Halamay DA. Optimal energy storage sizing and control for wind power applications. IEEE Transactions on Sustainable Energy. Jan 2011;**2**(1):69-77

[15] Sarrias-Mena R, Fernandez-Ramirez LM, Garcia-Vazquez CA, Jurado F. Dynamic evaluation of two configurations for a hybrid dfig-based wind turbine integrating battery energy storage system. Wind Energy. 2015;**18**(9):1561-1577

[16] Ding M, Chen Z, Su J, et al. Optimal control of battery energy storage system based on variable smoothing time constant. Automation of Electric Power Systems. Jan 2013;**37**(1): 19-25

[17] Teleke S, Baran ME, Bhattacharya S, Huang AQ. Optimal control of battery energy storage for wind farm dispatching. IEEE Transactions on Energy Conversion. Sep 2010; **25**(3):787-794

[18] Abbassi A, Dami MA, Jemli M. Statistical Characterization of Capacity of Hybrid Energy Storage System (HESS) to Assimilate the Fast PV-Wind Power Generation Fluctuations. 2017 International Conference on Advanced Systems and Electric Technologies (IC_ASET), Hammamet, Tunisia, 14-17 Jan. 2017

[19] Bouharchouche A, Berkouk EM, Ghennam T, Tabbache BA. Modeling and control of a Doubly Fed Induction Generator with Battery-Supercapacitor Hybrid Energy Storage for Wind Power Applications. In: Proc. POWERENG. 2013. pp. 1392-1397; 2013

[20] Luo W, Feng S, Ge W, Wang Z. Research on the control strategy of large-scale wind power energy storage system. IEEE Innovative Smart Grid Technologies. 2012:1-4, 2012

[21] Li J, Bi J, Yan G, Ge Y, Jin P. Research on improving power quality of wind power system based on the flywheel energy storage system. 2016 China International Conference on Electricity Distribution (CICED), 10-13 Aug 2016, Xi'an, China

[22] Ghennam T. Berkouk EM, Bruno F. Modeling and control of a doubly fed induction generator (DFIG) based wind conversion system power engineering, energy and electrical drives. 2009. POWERING09, pp. 507-512, Lisbon, 18-20 March 2009

[23] Kim Y, Harrington R. Analysis of various energy storage systems for variable speed wind turbines. IEEE Conference on Technologies for Sustainability – Engineering and the Environment (SusTech 2015), July 30-Aug 1, 2015 in Ogden, Utah

[24] Abad G, Lopez J, Rodriguez M, Marroyo L, Iwansk G. Doubly Fed Induction Machine: Modeling and Control for Wind Energy Generation. John Wiley & Sons; Sep 28, 2011

[25] Mohan NED. Power Electronics: A first Course. ISBN-13: 978-1118074800

[26] Lipo TA. Analysis of Synchronous Machines. 2nd ed: CRC Press; 2012

[27] Kalbat A. PSCAD simulation of grid-tied photovoltaic systems and Total Harmonic Distortion analysis. EPECS – 2013. pp. 1-6; 2013

[28] Jiang Z, Yu X. Modeling and control of an integrated wind power generation and energy storage system. Proc. Power Energy Soc. General Meeting. pp. 1-8. 2010-Jul-2630

[29] Qu L, Qiao W. Constant power control of DFIG wind turbines with super capacitor energy storage. IEEE Transactions on Industry Applications. January/February 2011;**47**(1)

[30] IEEE-std-519-1992

[31] Bollen MHJ. Understanding Power Quality Problems – Voltage Sags and Interruptions. John Wiley & Sons. ISBN: 0-7803-4713-7

[32] Arrillaga J, Watson NR. Power System Harmonics. 2nd ed; November, 2003. ISBN: 978-0-470- 85129-6. 412 pp

[33] Chakraborty S, Simoes MG, Kramer WE. Power Electronics for Renewable and Distributed Energy Systems: A Sourcebook of Topologies, Control and Integration. Springer-Verlag London: Springer. ISBN 978-1-4471-5103-6; 2013

[34] Panasonic Energy Solutions - Residential Storage Bat- Tery System, Panasonic Corporation; 2015

[35] Plett GL. Extended kalman filtering for battery management systems of LiPB-based hev battery packs, part 1. Background. Journal of Power Sources. 2004;**134**:252-261

[36] Plett GL. Extended kalman filtering for battery management systems of LiPB-based hev battery packs, part 2. Modeling and identification. Journal of Power Sources. 2004;**134**: 262-276

[37] Plett GL. Extended Kalman filtering for battery management systems of LiPB-based HEV battery packs part 3. State and parameter estimation. Journal of Power Sources. 2004; **134**:277-292

[38] Manitoba HVDC Research Center, https://hvdc.ca/pscad/

[39] Zhai Q et al. Cost benefit analysis of using clean energy supplies to reduce greenhouse gas emissions of global automotive manufacturing. Energies 4.10 (2011): 1478-1494

[40] Babazadeh H, Gao W, Wang X. Controller design for a hybrid energy storage system enabling longer battery life in wind turbine generators. North American Power Symposium (NAPS), IEEE; 2011

[41] Takahashi R et al. Efficiency calculation of wind turbine generation system with doubly fed induction generator. Electrical Machines (ICEM), 2010 XIX International Conference on. IEEE; 2010

Chapter 7

# Optimal Design and Operation Management of Battery-Based Energy Storage Systems (BESS) in Microgrids

Amjad Anvari-Moghaddam, Jeremy Dulout, Corinne Alonso, Bruno Jammes and Josep M. Guerrero

Additional information is available at the end of the chapter

http://dx.doi.org/10.5772/intechopen.71640

**Abstract**

Energy storage systems (ESSs) can enhance the performance of energy networks in multiple ways; they can compensate the stochastic nature of renewable energies and support their large-scale integration into the grid environment. Energy storage options can also be used for economic operation of energy systems to cut down system's operating cost. By utilizing ESSs, it is very possible to store energy in off-peak hours with lower cost and energize the grid during peak load intervals avoiding high price spikes. Application of ESSs will also enable better utilization of distributed energy sources and provide higher controllability at supply/demand side which is helpful for load leveling or peak shaving purposes. Last but not least, ESSs can provide frequency regulation services in off-grid locations where there is a strong need to meet the power balance in different operating conditions. Each of the abovementioned applications of energy storage units requires certain performance measures and constraints, which has to be well considered in design phase and embedded in control and management strategies. This chapter mainly focuses on these aspects and provides a general framework for optimal design and operation management of battery-based ESSs in energy networks.

**Keywords:** energy storage system, microgrid, optimal design and control, renewable energy integration, optimization

## 1. Introduction

Nowadays, due to the increased operation and maintenance cost and issues related to transportation of fuels, conventional ways of power generation are no longer an optimal solution.

With more concerns about environmental footprints and global warming together with the steady progress in green technologies, renewable energy resources (RESs) are deemed to be key enablers for sustainable energy development, cost-effective operations, and pollutant emission prevention. The use of RESs in an integrated framework with different energy sources not only enhances the system efficiency at different levels (e.g., energy generation, transmission, and distribution) but also improves the energy supply reliability and allows empowering of consumers in the different locations (such as suburban districts, countrysides, and remote/islanded areas). Additionally, with the complementary characteristics of energy storage systems (ESSs) and hybridization of energy systems, it is possible to offer more affordable and reliable source of power and introduce more controllability to the generation mix. More importantly, with the application of ESSs, the issues related to unpredictable nature of RESs (mainly solar and wind energy sources) can be resolved, and a smooth-running power supply can be guaranteed. On the other hand, implementation of an integrated energy system supported with ESSs allows energy saving at different scales. By proper charging/discharging of the ESSs, we can economically benefit from dispatching cheaper energy sources during peak load hours and saving excess energy during low-demand periods. It is noteworthy that the term "ESS" could have different definitions; however, in this chapter we are talking about a "commercially available technology that is capable of absorbing energy, storing it for a period of time, and thereafter dispatching the energy" [1]. It should be also noted that the system operation can be further improved if demand response programs (DRPs) are considered in energy management portfolio. DRPs will incentivize the users to reduce their energy consumption over peak times or to shift part of their consumptions to other time intervals for matching energy supply [2]. However, a good DRP should have two primary features: the first feature is defined as the *adaptability* to different consumers with different dispositions toward the DRP, and the second one is defined as the *adjustability* to time preferences of consumers. This means that each consumer should be able to easily shift his/her demand from the high-price hours to the favorite hours according to his/her lifestyle [3]. With this introduction on advantages of renewable energy integration and reliable backup through energy storage options, this chapter discusses different battery-based ESS (BESS) technologies and presents potentials of BESS in distribution systems. Moreover, different design criteria and methodologies for ESS sizing and planning are proposed, and a general framework for optimal operation management and control of BESSs in energy networks is developed.

## 2. Criteria and methodologies for battery sizing and planning

This section provides an overview of criteria and methods that should be used to optimally size and use a battery energy storage system (BESS) for different applications.

### 2.1. Battery technologies

A battery is constituted of electrochemical cells connected in series, parallel, or both in order to obtain the desired capacity and voltage output. A cell consists of a set of two electrodes

(oxidizer and reducer) in contact with an electrolyte and converts chemical energy into electric energy (and vice versa for rechargeable cells) [3–5]. Since the end of the eighteenth century with the development of the Volta pile, "voltaic pile," numerous designs of batteries have been invented (with different electrode materials, electrolytes, casings, separators, management systems, etc.). Hundreds of systems have been created, but almost 20 of them are currently commercialized (mainly derived from lead, zinc, nickel, or lithium materials) [6]. As presented in **Figure 1**, electrochemical cells can be classified into three main families:

- Flow batteries (also called redox flow batteries) are based on two electrolytes stored in external tanks. The electrolytes are pumped into an electrochemical cell in order to produce electricity. The energy density depends on the size of the tanks, and the power density depends on the rate of chemical reactions occurring in the electrochemical cell. These batteries can be fast to recharge by changing the electrolytes. In general, the chemical reactions are reversible.
- Primary batteries cannot be easily and efficiently recharged so they are usually only discharged once and discarded. They are often used in portable electric devices such as lighting, cameras, toys, and also in-home automation sensors (e.g., smoke and movement detectors). They offer a good energy density and a good shelf life.
- Secondary batteries are rechargeable and can perform a large number of cycle charge/discharge (100–1000). The market of rechargeable batteries comprises a very wide range of applications such as powering portable electronic devices, electric vehicles, storing surplus of energy from photovoltaic systems, etc. Since 1990, the average growth rate of rechargeable battery pack market is 5% per year [7]. For decades, lead-acid batteries (such as valve regulated and sealed) have been leading, by far, the global market of rechargeable batteries. Since the end of the 1990s, lithium-ion batteries have been gradually preferred to nickel-cadmium (Ni-Cd) and nickel-metal hydride (Ni-MH) batteries

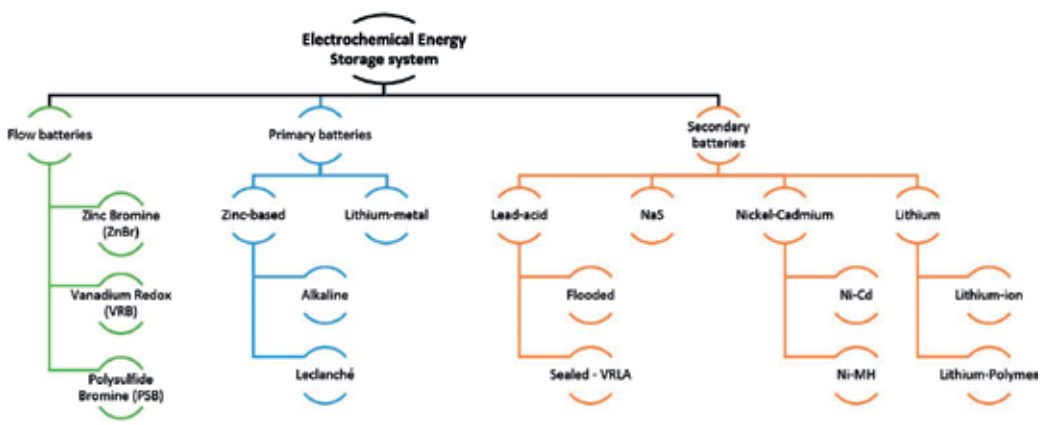


**Figure 1.** Main different electrochemical technologies.

in portable devices [7]. The historical development of the main battery chemistries and the key issues to create sustainable batteries with always higher performances are well presented in Ref. [8].

In this chapter, the analysis will be focused on secondary batteries, especially on lead-acid and lithium-ion batteries, the most popular technologies (because of an attractive price for the first cited and because of high performances in terms of energy and power densities for the latter). The main useful characteristics of a BESS, when selecting a technology, are listed below:

- **Response time:** a BESS has to charge/discharge in a given period (e.g., fast response time from milliseconds to seconds is needed to remove power fluctuations inherited from renewable source production).
- **Capital cost:** depending on the application, different costs are useful to be considered such as the cost of rated power (€/kW), the cost of rated capacity (€/kWh), and the cost on the long run (€/(cycle kWh)).
- **Operation and maintenance (O&M) cost:** every BESS has its proper O&M requirements. It is difficult to find a clear trend in the literature because it is highly dependent on the location (labor costs) and on the age of the facility.
- **Specific energy (Wh/kg) and specific power (W/kg):** enables to know the BESS weight that achieves power and energy requirements of the application. Energy and power densities, respectively, in Wh/l and W/l, are other metric representative of the volume aspect.
- **Cycling lifetime (number of cycles):** maximum number of cycles that the BESS can perform.
- **Calendar lifetime (years):** maximum shelf life of the BESS.
- **Cycle efficiency (%):** also named round-trip efficiency, the energy discharged by the BESS is lower than the energy initially charged into it. This parameter can be measured by calculating the ratio between energies discharged to the energy charged $E_{out}/E_{in}$. This calculation should not take into account self-discharge.
- **Self-discharge:** due to parasitic chemical reactions, the charges stored in the BESS decrease. This process can be accelerated or slowed not only by external conditions (e.g., temperature, humidity) but also by operating conditions (e.g., state of charge (*SOC*) of the battery, previous rate of charge, etc.).
- **Operating temperature (°C):** some parameters such as the efficiency, the available capacity, and the lifetime depend on the operating temperature range of the BESS.
- **Environmental impact and safety:** the extraction of the main components and manufacturing processes of batteries have different impacts on the environment from a technology to another. These impacts can be expressed as an energy consumption or a mass of GHG emissions [9]. The toxicity of some materials and the stability of the battery (e.g., thermal runaway of lithium batteries with cobalt-based cathode) can be a crucial issue depending on the application.

- **Maturity:** a strong scientific background is behind mature technologies which benefit from numerous user experiences. Only incremental improvements are expected. In comparison, a new technology is evolving fast thanks to breakthrough advances.

### 2.2. Potentials of BESS in distribution systems

Grid-scale storage facilities through the world have been gathered in a large database from the US DOE [10]. A full description is given for most of them such as the date of creation, the location, the technology, the rated capacity, the rated power, the use cases, a picture of the project, etc. It appears that the global storage resource is small (the operational maximum power storage is around 170–180 GW, corresponding to less than 1% of our energy production). The main storage technology (in terms of rated power) is by far pumped hydro (~96%), but electrochemical projects are the most numerous (nearly 1000) and represent nearly 2% of the total rated power. As listed in [10–12], a BESS can provide numerous benefits such as:

- **Environmental:** integration of renewable sources (the variability of these sources threatens the grid stability), replacement of diesel generators (in off-grid sites), pollution reduction (by reducing peak demand often met with harmful and costly plants), etc.
- **Societal:** electricity supply in remote areas, reliability improvement (possibility to maintain the grid stability or operate separately from the utility in a so-called islanded mode), duration of outages decreased (ESS can perform a black start), etc.
- **Economic:** energy cost decrease (due to electric energy time-shift that enables to buy cheap energy and then sell and/or use it when it is expensive), the use of expensive thermal power plant diminution (with advanced energy management strategies), electric peak demand flattening, power factor correction, transmission and distribution (T&D) investment deferral, etc.

Every actor of electricity from the end user to the utility operator may find one or more benefits to install a BESS facility [12]. Indeed, potential synergies might be achieved, for example, by charging batteries during off-peak demand and discharging during peak; energy cost may decrease (because energy is bought cheap and sold expensive); energy losses ($I^2R$) can be reduced (less power in transmission lines during on-peak demand); pollution may be reduced (because in general cleaner power plants are used for the supply of baseload demand), and T&D deferral or life extension of the utility can be fulfilled because it mainly depends on the level of the peak demand. Two typical use cases are illustrated in **Figure 2**, where (a) represents the use of energy storage in order to reduce the peak demand. In this case, the power plant responsible for the baseload generation will increase its production in order to charge the BESS (in general the cost and the pollution related to this plant are the lowest compared to the other plants that are used to meet the peak demand). During peak demand, the energy comes from the BESS which replaces costly and high-pollutant power plants. Case (b) represents a typical power production from a solar photovoltaic (PV) plant during a sunny day which is not correlated with the demand profile. The BESS is charging when there is a surplus of energy in order to ensure the stability of the grid (unintentional injection of renewable power is not allowed), and it is discharging when the cost of energy is high (i.e., flattening the energy peak demand in the morning and in late afternoon).

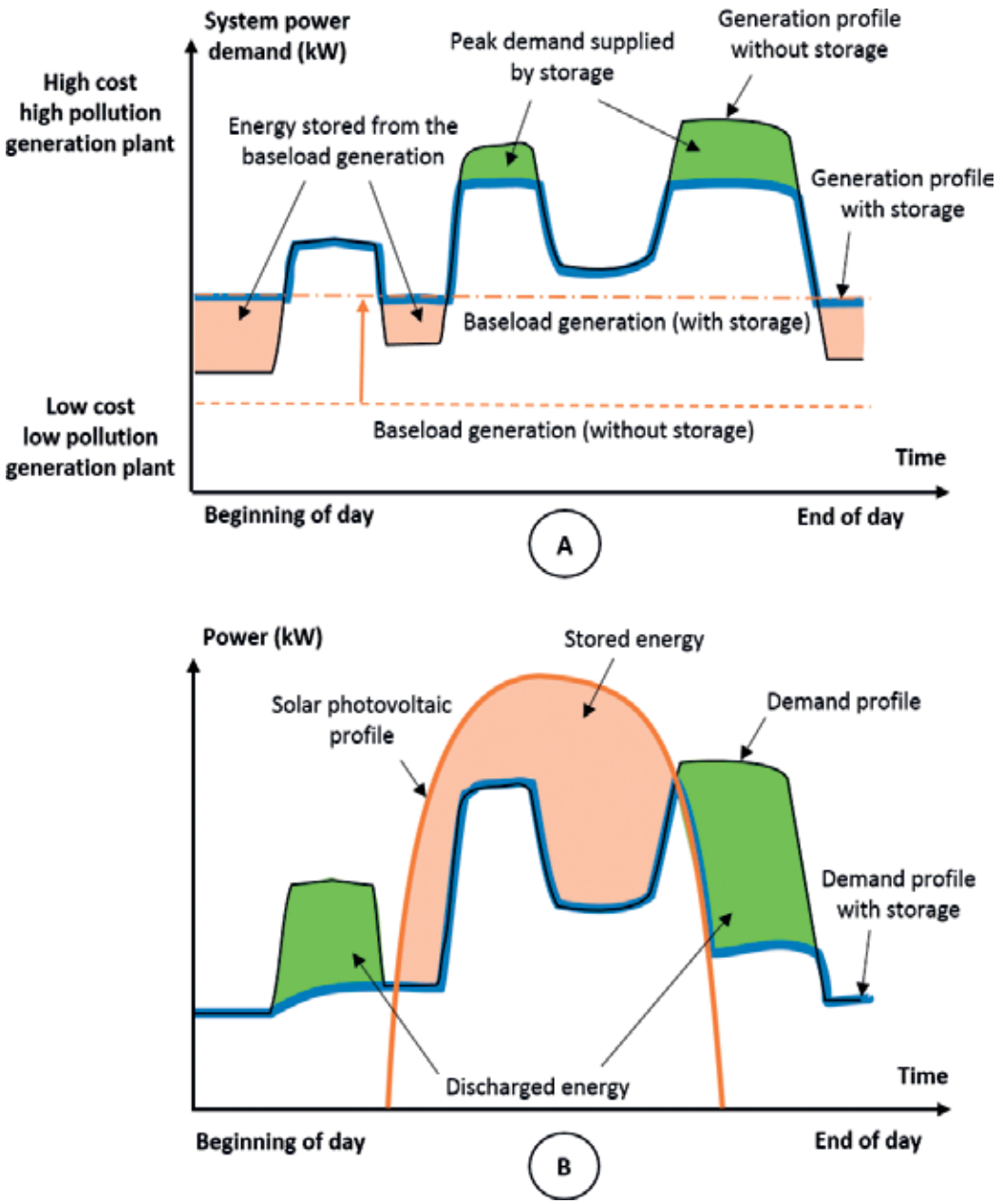


**Figure 2.** Typical use cases of a BESS, (A) peak shaving and load leveling and (B) integration of renewable sources.

### 2.3. Criteria

The following criteria help to quantify the benefits brought by a BESS associated to renewable sources such as solar PV panels and wind turbines (WT).

First of all, the reliability of the distribution system can be assessed by Eqs. (1) and (2):

- Loss of power supply probability (LPSP) is defined as the ratio of energy deficit to the load demand for a given period [13]:

$$\mathrm{LPSP}(t) = \frac{\int_{t_0}^{t} E_{deficit}(t)\,dt}{\int_{t_0}^{t} E_{load}(t)\,dt} \tag{1}$$

- Level of autonomy (LA) is derived from the ratio of the hours that exhibit a loss of load ($H_{LOL}$) to the total hours of operation ($H_{TOT}$) [13]:

$$\mathrm{LA} = 1 - \frac{H_{LOL}}{H_{TOT}} \tag{2}$$

Concerning the economic issue, the BESS can be analyzed by calculating the annualized cost of system (ACS). The formulation (3) is derived from [14, 15] in which the annual cost of a renewable plant (PV or WT) with batteries is calculated. In these studies a replacement cost is added in the calculation of ACS because the duration of the project is often based on the lifetime expectancy of renewable sources which is longer than battery lifetime:

$$\mathrm{ACS} = C_{cap} \times CRF + C_{O\&M} \tag{3}$$

where $C_{cap}$ is the initial capital cost of the BESS (€), $CRF$ is the capital recovery factor defined in Eq. (4) to calculate annual equal payments over the lifetime of the BESS based on the initial capital cost, and $C_{O\&M}$ is the annual cost of operation and maintenance (€):

$$\mathrm{CRF} = \frac{i_r(1+i_r)^n}{(1+i_r)^n - 1} \tag{4}$$

where $i_r$ is the interest rate (between 5% and 10% for such projects [16]) and $n$ is the BESS lifetime (years).

Another popular metric used in renewable plants is the levelized cost of energy (LCOE) which indicates the total cost of energy (generally per kilowatt-hour) by taking into account the cost of all equipment involved in energy production over their entire lifetime. It can be adapted to BESS by using the annualized discharged energy $E_{dis}$, as proposed in Eq. (5):

$$\mathrm{LCOE} = \frac{ACS}{E_{dis}} \tag{5}$$

A good criterion to take into account the environmental aspect is the PV self-consumption Eq. (6) that can be highly improved by the integration of a BESS. A high PV self-consumption implies a good use of the PV source and a local use of produced energy (transmission losses are reduced). In case of grid-connected system, some energy is exchanged with the grid, $E_{DU}$ is the energy directly used from the PV installation to the load, $E_{BC}$ is the PV energy used to charge the BESS, and $E_{PV}$ is the total energy produced by the PV installation:

$$s = \frac{E_{DU} + E_{BC}}{E_{PV}} \tag{6}$$

Other criteria can be taken into account such as the life cycle analysis (LCA) which aims at assessing the environmental impact of a device by taking into account four life stages that are manufacturing, transportation, use, and end of life. A life cycle inventory (LCI) analysis, only focused on the manufacturing of different batteries, is presented in Ref. [9]. In such studies, some data are difficult to obtain and are often estimated (especially those concerning the manufacturing processes which are fast evolving due to improvements of technologies).

### 2.4. Optimization techniques

Several optimization techniques are available for the sizing and the planning of renewable energy-based systems [17]. Some popular software tools such as Hybrid Optimization Model for Electric Renewables (HOMER) and Hybrid Power System Simulation Model (HYBRID2) both developed by the National Renewable Energy Laboratory (NREL), United States, and Hybrid Optimization using Genetic Algorithm (HOGA) developed in the University of Zaragoza, Spain, are presented in Ref. [17] to simulate and optimize any microgrid configuration. Nevertheless, in order to have the highest flexibility in terms of modeling and optimization, other classical tools are commonly used such as MATLAB and General Algebraic Modeling System (GAMS).

In optimization problem, the objective function can be mono-objective (e.g., cost of the entire installation during 20 years) or multi-objective (e.g., a combination of reliability, cost, and environmental impact). Very often, the cost function of a multi-objective problem is defined as a weighted sum of multiple criteria that can be expressed in different quantities. In this case, some arbitrary weighting coefficients are necessarily introduced, and the difficulty is to determine their right value. For example, if the cost function, expressed in euros per year, evaluates the yearly cost of a BESS in a microgrid, what equivalent cost (in euros per kilogram) should be associated to the greenhouse gas (GHG) emissions induced by the production, use, and end of life of batteries? This cost depends on environmental and social impacts that are not globally standardized and are fluctuating from a year to another, whereas the mass of GHG emissions is a fixed value. In this sense, the Pareto representation is very practical because each objective is expressed in the most appropriate quantity and defines its own axis.

In Ref. [18], a robust mixed-integer linear programming (RMILP) is proposed to minimize the cost of the system. In order to take into account uncertainties such as renewable production, load demand, or costs, a stochastic simulation can be achieved through the generation of multiple Monte Carlo scenarios. Heuristic and meta-heuristic optimization techniques are very popular to find the optimal solution among a large number of solutions while using the least computational resources. Two multi-objective problems combining genetic algorithms and Pareto representation are presented in [19, 20]. This method is very promising because a large number of feasible solutions are analyzed and a set of optimal solutions, best trade-off between all criteria, are obtained.

## 3. Modeling of a BESS

In order to simulate the system, a model of BESS has to be defined. In the literature, BESS models developed for the sizing and the scheduling are simple with a few parameters (e.g., nominal capacity, cycle efficiency, maximum number of cycles, etc.) in order to limit the complexity of the problem.

### 3.1. Instantaneous characteristics

The state of charge (*SOC*) of the BESS is the parameter related to the number of charges stored in the battery (a *SOC* of 100% means that the BESS is fully charged, whereas it is considered to be empty at 0%). In [21–23], the online estimation of *SOC* named "coulomb counting" is proposed. This method is based on the measurement of current and takes into account the coulombic efficiency (ampere-hour efficiency):

$$SOC(t) = SOC(t-1) + \eta_{Ch}\frac{I_{Ch}(t)\cdot \mathrm{D}t}{C_n(t)} - \frac{I_{Dis}(t)\cdot \mathrm{D}t}{\eta_{Dis}\cdot C_n(t)} \tag{7}$$

where $\eta_{Ch}$ and $\eta_{Dis}$ are, respectively, the charge and discharge coulombic efficiencies of the BESS (in Ref. [21], the coulombic efficiency is considered equal to 1 during the discharge and smaller than 1 during the charge, due to unwanted side reactions). $I_{Ch}(t)$ and $I_{Dis}(t)$ are the current level at the charge and discharge, respectively. $C_n(t)$ is the nominal capacity of the BESS. It is to notice that the nominal capacity of the BESS is decreasing all along the lifetime of the BESS; this point will be explained in the next section.

Another variable widely used in the literature is the depth of discharge (*DOD*) which describes the emptiness of battery (complement of the *SOC*). Battery manufacturers often provide the maximum number of cycles that a battery can perform for different *DODs*, as depicted in **Figure 3**:

$$DOD(t) = 1 - SOC(t) \tag{8}$$

In order to model the effect of other operating conditions (e.g., C-rate and temperature) on the BESS behavior, the *SOC* can be formulated by introducing the concept of equivalent current. Three technologies of batteries have been tested in Ref. [24], exhibiting both the effect of the C-rate and the temperature on the available discharged capacity. Indeed, it has been empirically formulated by Peukert for lead-acid batteries at the end of the nineteenth century that the discharged capacity is related to the C-rate. The main issue is that this relation is given for a constant level of current during all the discharge conditions (not representative of real conditions). In [25], an improved method is proposed for management of lithium-ion batteries, but the model is difficult to parameterize because it needs a lot of experimental tests to be adapted to the BESS. Usually, a BESS operates at low C-rate in renewable power plants, and the temperature can be assumed to be constant. This is why the state of health (SOH) is the main parameter taken into account in sizing and planning studies.

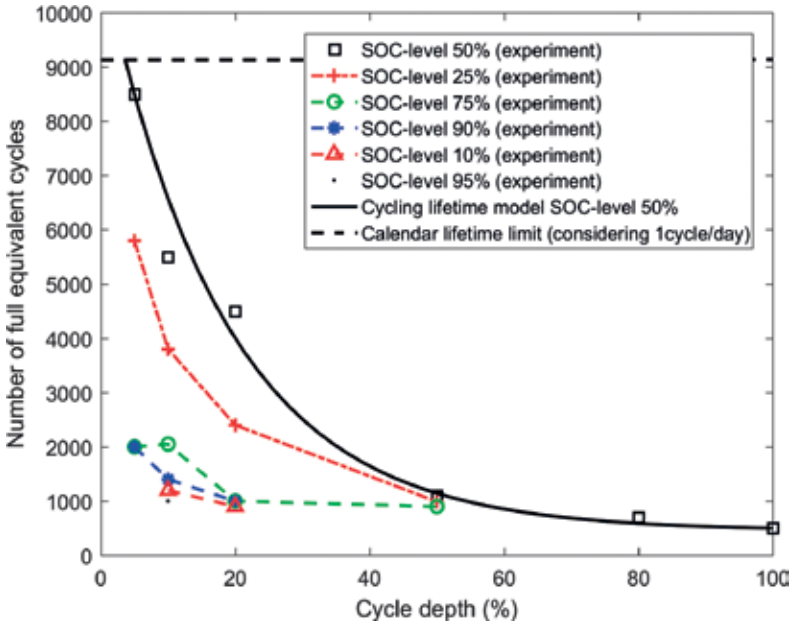


**Figure 3.** Calendar and cycling lifetime model of the BESS derived from [27].

### 3.2. Lifetime analysis

Due to irreversible reactions, the active material is decreasing, and the electrode interfaces are deteriorated. Thus, the capacity decreases, and the internal resistance increases (power capability fade). In order to know when to replace a BESS, a common criterion is to consider the end of life (EOL) of a battery when its capacity drops to less than 20% of the initial nominal capacity [26]. This limit of 20% has been initially set because of the behavior of lead-acid batteries: the capacity fade is quite linear until 20%, and then there was a sudden drop of capacity. Of course all the batteries do not exhibit this large decrease of capacity; this is why some projects such as the second life of batteries have been created (old batteries that do not fulfill the automotive requirements are reused in stationary projects).

Usually, the aging of batteries is monitored by measuring the nominal capacity and comparing it to the initial nominal capacity $C_n(t_0)$. In this case, the battery reaches its EOL when the state of health (SOH) goes below 80%:

$$SOH(t) = \frac{C_n(t)}{C_n(t_0)} \tag{9}$$

The lifetime of batteries is related to calendar aging (shelf life) and cycle aging. In renewable microgrids, a BESS is subjected to variable cycling conditions. The lifetime of a BESS depends on the cycle depth and the *SOC* level (mean of *SOC* during the cycle). As shown in Ref. [27], the degradation of the nominal capacity can be considered linear for both calendar

and cycling lifetime. As presented in **Figure 3**, experimental studies performed on lithium-ion batteries [27] revealed that the maximum number of cycles performed by the BESS is higher for low cycle depths and medium *SOC* levels (close to 50%). Assuming that the BESS will perform at least 1 cycle per day, a limit can be set on the maximum number of cycles that is defined by the calendar aging.

Two main methods are used to estimate the aging of a BESS. In Ref. [28], a simple method called "ampere hour throughput" is based on the assumption that the exchangeable energy of a battery is fixed (because nearly constant) whatever the cycle depth performed by the BESS. In this case, the maximum energy that can be exchanged is calculated as follows:

$$E_{max} = 2\, N_{max}(DOD) \times DOD \times C_n(t_0) \tag{10}$$

in which the initial nominal capacity is expressed in Wh. Another method is called the rainflow counting. A very popular algorithm of rainflow counting has been presented by Downing and Socie [29]. Initially developed to estimate the effect of mechanical stress in automotive and building industries, the rainflow counting is often employed to describe the aging of batteries, as in Ref. [30]. Given a battery *SOC* time series, it is possible to extract the number of cycles with their associated cycle depth and *SOC* level and then update the value of nominal capacity.

## 4. BESS power/energy management schemes

For optimal operation of an energy system equipped with BESSs in different working modes (i.e., grid-connected or islanded), it is crucial to properly design and implement energy management systems (EMSs). These system optimizers normally determine the best possible operating scheme at supply and demand sides in terms of optimized set points for controllable units such as energy storage devices and send them as the control signals into the dedicated control system of interfacing converters. Generally, there are two types of energy/power management strategies used in energy system applications. These are named as interactive schemes based on information sharing mechanisms and passive schemes based on self-autonomy [31].

### 4.1. Interactive power/energy management strategies

In a given interactive power/energy management system (IP/EMS), local and global system information (such as line currents, nodal voltages, frequency, and powers) is communicated in the system and exchanged between corresponding nodes in order to determine operation point of each controllable ESS or distributed generation (DG) unit. These strategies also benefit from a sort of intelligence in the integration of the computing and communications technologies which help them to define and develop the communication structure based on the computation burden of each node and other related system's objectives and constraints [32]. In this regard, three different communication schemes can be realized for an IP/EMS: centralized, decentralized, and hybrid. In each of the mentioned schemes, different communication technologies such as microwave (μW), power line carrier (PLC), fiber optics, infrared, and/or

wireless radio networks (such as global system for mobile (GSM) communications and code division multiple access (CDMA)) can be effectively used and integrated into the existing infrastructures [33, 34].

*4.1.1. Centralized P/EMS*

In a centralized P/EMS, also known as a supervisory scheme, there is a centralized entity or a control center that monitors the system's behavior, collects information from different parts of the network, makes decisions based on the observations, and accordingly updates set points for the controllable units in supply/demand sides [35–37]. In other words, a centralized P/EMS acts as a master unit, while other local controllers within the system are treated as slaves to follow the reference signals coming from the master unit as shown in **Figure 4**. To improve the effectiveness of a P/EMS, it is also very important to clearly define system's objectives and constraints. These objectives (such as operating cost minimization, emission mitigation, power loss reduction, *SOC* equalization, etc.) together with the constraints might be conflicting in some cases which in turn make the optimal decision-making process a difficult or even an impossible task. Different examples of centralized P/EMS for microgrids can be found in the literature [38–40]. The advantages of a centralized scheme mainly lie within the simplicity of implementation and globality of optimal solution; however, it brings two disadvantages: single point of failure which implies that a centralized P/EMS has to be securely designed

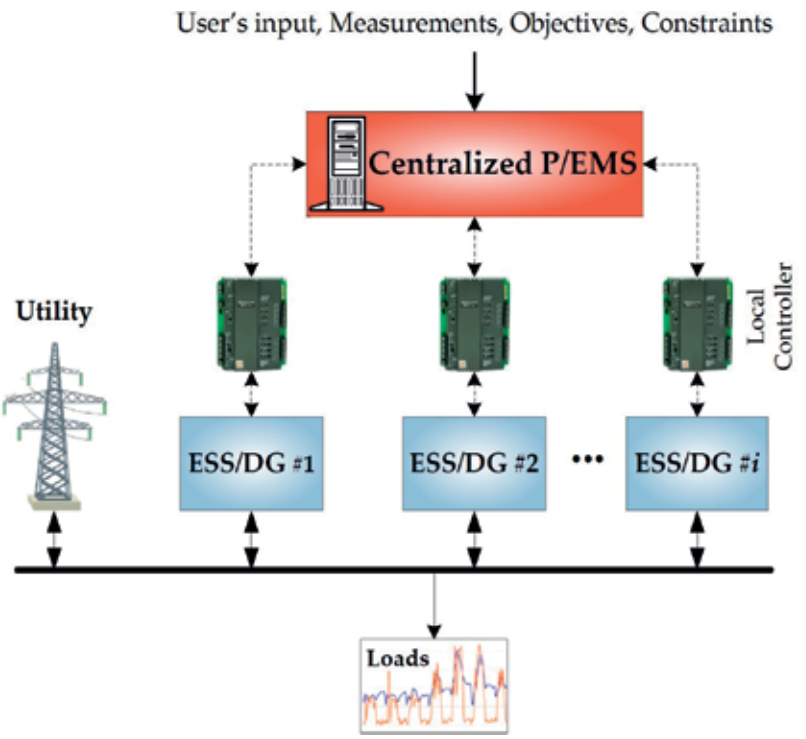


**Figure 4.** Block diagram of a centralized P/EMS.

with appropriate built-in redundancy and massive communication expenditure. The latter is not a challenging problem in small-scale networks, but it could be problematic for larger systems as the complexity of the centralized optimization grows exponentially with the number of units (control variables) in the system.

### *4.1.2. Distributed P/EMS*

Distributed P/EMS is the second interactive scheme for management of a given system in which there is no central supervisory unit, but all the local controllers are connected and communicate with each other through a communication bus [41]. In this sense, each controller not only captures local measurements but also receives information from neighboring nodes which helps in decision-making process according to different optimization objectives [42–43]. In this scheme, intelligent algorithms are often used for better exploration/exploitation of the environment in order to find optimal operation point. **Figure 5** shows the block diagram of a decentralized P/EMS. A distributed scheme has some advantages over a centralized one. First, it supports a scalable structure with Plug-and-Play (PnP) feature for newly added/removed energy sources or load blocks. Second, computation burden of each local controller is mitigated which in turn reduces the required communication bandwidth. Finally, a distributed P/EMS could improve the redundancy and modularity of the system where it is needed. However, there is still a problem if a communication link fails in the system. This failure would not end to a total system collapse, but the performance of the system would not be optimal any longer. Also, a distributed P/EMS suffers from degradation of performance on small/medium networks, increased use of database space, and complex use and administration. Multi-agent system (MAS) is one of the best illustrations for a distributed scheme [44].

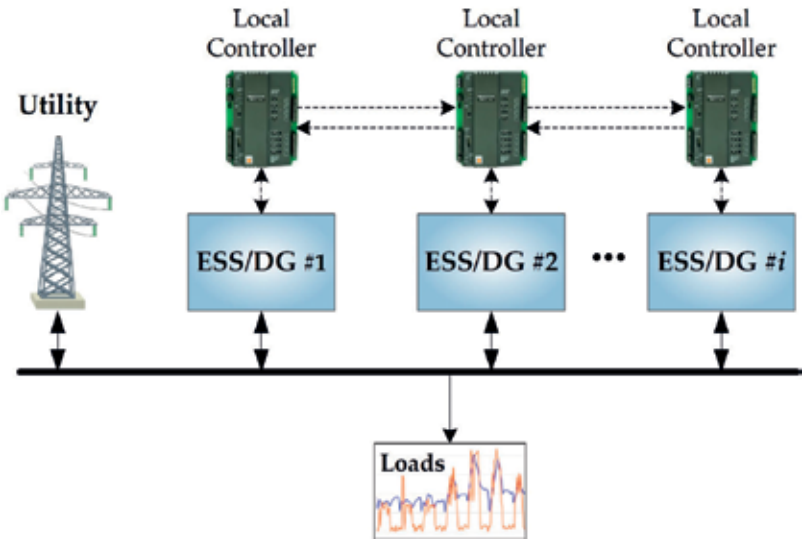


**Figure 5.** Block diagram of a decentralized P/EMS.

### *4.1.3. Hybrid P/EMS*

Hybrid scheme for power/energy management can be realized as another interactive structure that is mainly based on a combination of centralized and distributed schemes. In a hybrid structure, local controllers which are used for operation management of different energy sources are divided into groups [45]. Within each group, a centralized scheme is used to control and optimize the performance of local controllers. On a higher level, a distributed scheme is utilized to coordinate the operation of centralized controllers in different clusters for global optimization. Such a hybrid strategy can be seen in **Figure 6**.

It is notable that a hybrid P/EMS scheme is normally implemented for large-scale networks such as interconnected energy systems or microgrids, where the optimal operation of the entire system depends on cooperation and coordination of different control layers over time. By doing this hybridization, it is very possible to improve the system reliability and resiliency for long-run operations due to the unique features that inherently exist in centralized/decentralized schemes [46].

## 4.2. Passive power/energy management strategies

Self-autonomy of operation for a local controller without having information from neighboring nodes is the main idea of a passive power/energy management scheme (PP/EMS). In this structure, it is assumed that making an information sharing mechanism is too costly or not viable; thus, independent operation of energy sources is required. Moreover, it is needed to clearly define the control objective of each energy source to assure reliable operation of the system. Block diagram for such a power/energy management scheme is shown in **Figure 7**.

Among the existing methods for PP/EMS, droop-based control strategy is regarded as a dominant method [47–49]. This control methodology adopts the behavior of synchronous machines

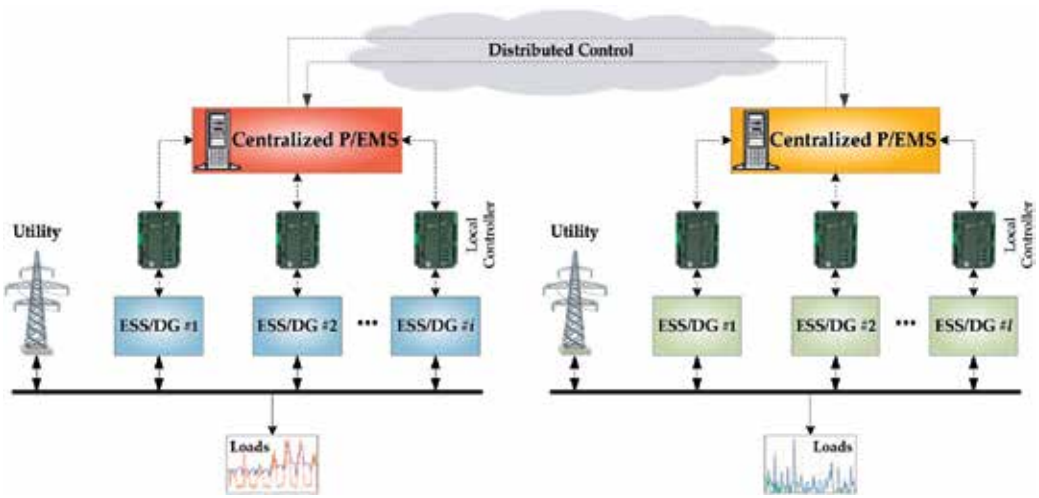


**Figure 6.** Block diagram of a hybrid P/EMS.

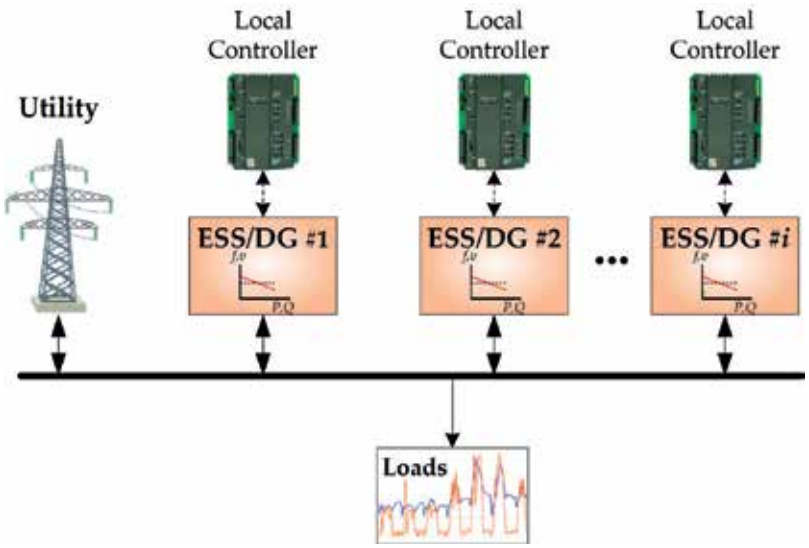


**Figure 7.** Block diagram of a PP/EMS.

in responding to the changes in voltage and frequency and applies similar rules in operation management of converters in ac/dc sides. The droop-based control strategy works based on the assumption that the output impedance of a controllable unit (such as a micro-source) is mainly inductive, and it utilizes droop characteristics of voltage amplitude and frequency of each controllable unit to control its output. In case of a dc microgrid, bus voltages and in case of an ac microgrid the system voltage and frequency are the information sensed by each local droop controller and used subsequently to adjust output active (and/or reactive) power of a BESS or a generation unit. **Figure 8** shows such control strategy for a given dc microgrid. As can be seen in the same figure, either output power or output current can be selected as the feedback signal in droop control. For dc microgrids with power-type load, output power can be used as droop feedback, as shown in Eq. (11).

On the other hand, when current signal is used, as shown in Eq. (12), droop coefficient $m_c$ can be regarded as a virtual internal resistance. In that case, the implementation and design of the parallel converter system in a dc microgrid can be simplified to some extent as the control law is linear:

$$v^*_{DCi} = v^*_{DC} - m_p \,.\, P_{oi} \tag{11}$$

$$v^*_{DCi} = v^*_{DC} - m_c \,.\, i_{oi} \tag{12}$$

where $v^*_{\mathrm{DCi}}$ is the output of the droop controller, i.e., the reference value of dc output voltage of converter #*i*; $v^*_{\mathrm{DC}}$ is the rated value of dc voltage; and $m_p$ and $m_c$ are the droop coefficients in power-based and current-based droop controllers, while $P_{oi}$ and $i_{oi}$ are the output power and current of converter #*i*, respectively. Since there is no communication requirement to fulfill the

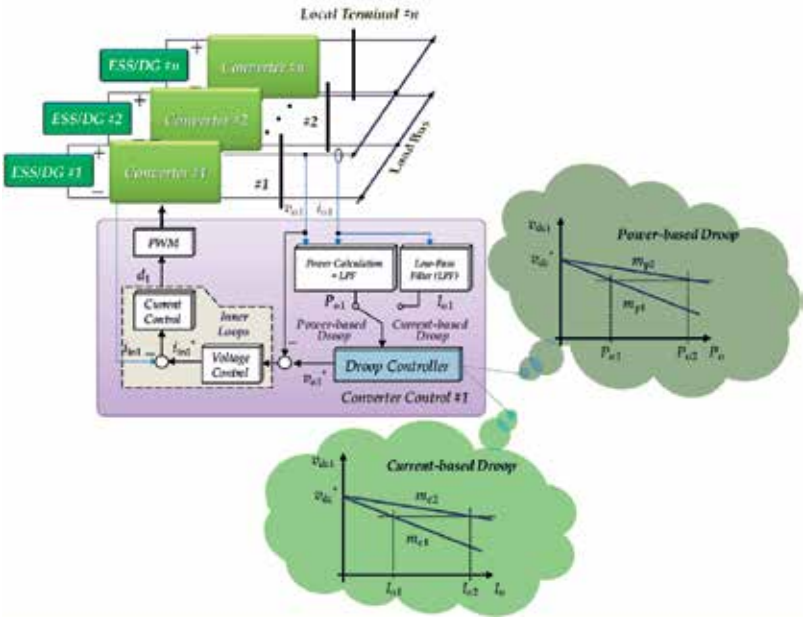


**Figure 8.** Droop control for dc microgrids.

control objectives, this control strategy is highly reliable. Moreover, this control structure could be easily extended to different energy sources while enabling true PnP features. Apart from the benefits, there are several issues in such power/energy management strategy. First, low-voltage regulation and proportional current sharing cannot be addressed directly by this method. Instead, nonlinear and adaptive droop techniques are proposed as key solutions for achieving acceptable voltage regulation at full load and ensuring proportional current sharing. Second, low X/R line impedance ratio may result in active and reactive power coupling and instability issues in low-voltage microgrid systems and cause power sharing errors for generation units [50]. Recently, several works have been done to improve the performance of a conventional droop-based control method by implementing the droop in virtual frames [51], adding virtual impedance in control loops [52], or adjusting the output voltage bandwidth [50]. However, without a coordinating unit such as a central controller or a system optimizer, it would be a challenging task to optimally manage the operation of a microgrid system with PP/EMS.

As another type of PP/EMS, maximum power point tracking (MPPT) control methodology is also applied in microgrids to maximize power extraction from RESs (mainly WTs and PVs) under all conditions [53]. In such power management technique, unit's voltage and current are sampled frequently, and the duty ratio of the interfaced converter is adjusted accordingly. However, it should be noted that in islanded renewable-based microgrids which are controlled based on MPPT principles, ESSs must also be dispatched to provide voltage and frequency regulation services [54]. Considering the drawbacks of IP/EMS and PP/EMS, it seems that a combined P/EMS structure (e.g., a consensus-based droop framework [55] or a droop-based distributed cooperative control [56]) could not only address reliability issues but also enhance control performance of the system both in grid-connected and stand-alone modes.

## Author details

Amjad Anvari-Moghaddam[1]*, Jeremy Dulout[2], Corinne Alonso[2], Bruno Jammes[2] and Josep M. Guerrero[1]

*Address all correspondence to: aam@et.aau.dk

1 Department of Energy Technology, Aalborg University, Denmark

2 LAAS-CNRS, Université de Toulouse, CNRS, UPS, France

## References

[1] Malashenk E, Lee R, Villarreal C, Howard T, Gupta A. Energy storage framework staff proposal. California Public Utility Commission Energy Storage Proceeding, April 3; 2012

[2] Anvari Moghaddam A, Mokhtari G, Guerrero JM. Coordinated demand response and distributed generation management in residential smart microgrids. In: L Mihet editor, Energy Management of Distributed Generation Systems; InTech; 2016. ISBN: 978-953-51-4708-4

[3] Sharifi R, Anvari-Moghaddam A, Fathi SH, Guerrero JM, Vahidinasab V. An economic demand response model in liberalized electricity markets with respect to flexibility of consumers. IET Gener. Trans. Dist., to appear; 2017

[4] Linden D, Reddy TB, editors. Handbook of Batteries. 3rd ed. New York: McGraw-Hill; 2002 ISBN: 978-0-07-135978-8

[5] Broussely M, Pistoia G. Industrial Applications of Batteries - from Cars to Aerospace and Energy Storage. Elsevier; 2007. ISBN: 978-0-444-52160-6

[6] Bagotsky VS, Skundin AM, Volfkovich YM. Electrochemical Power Sources - Batteries, Fuel Cells, and Supercapacitors. Wiley, Hoboken, New Jersey; 2015. ISBN: 978-1-118-46023-8

[7] Pillot C. The rechargeable battery market and main trends 2014-2025. In 32th Annual International Battery Seminar & Exhibit; 2015

[8] Armand M, Tarascon J-M. Building better batteries. Nature. 2008;**451**(7179):652-657

[9] Sullivan JL, Gaines L. Status of life cycle inventories for batteries. Energy Conversion and Management. 2012;**58**:134-148

[10] Sandia Corporation. DOE Global Energy Storage Database. 2017, energystorageexchange.org, [Accessed: 06 Jun 2017]

[11] Electric Power Research Institute (EPRI). Electricity Energy Storage Technology Options - White Paper Primer on Applications, Costs, and Benefits. Electric Power Research Institute. Palo Alto, CA, 1020676; 2010

[12] Eyer J, Corey G. Energy Storage for the Electricity Grid: Benefits and Market Potential Assessment Guide - a Study for the DOE Energy Storage Systems Program, Sandia Report, SAND2010-0815. 2010

[13] Luna-Rubio R, Trejo-Perea M, Vargas-Vázquez D, Ríos-Moreno GJ. Optimal sizing of renewable hybrids energy systems: A review of methodologies. Solar Energy. Apr. 2012;**86**(4):1077-1088

[14] Poonpun P, Jewell WT. Analysis of the cost per kilowatt hour to store electricity. IEEE Transactions on Energy Conversion. Jun. 2008;**23**(2):529-534

[15] Yang H, Wei Z, Chengzhi L. Optimal design and techno-economic analysis of a hybrid solar–wind power generation system. Applied Energy. Feb. 2009;**86**(2):163-169

[16] Rathgeber C, Lävemann E, Hauer A. Economic top–down evaluation of the costs of energy storages—A simple economic truth in two equations. Journal of Energy Storage. Aug. 2015;**2**:43-46

[17] Sinha S, Chandel SS. Review of recent trends in optimization techniques for solar photovoltaic–wind based hybrid energy systems. Renewable and Sustainable Energy Reviews. Oct. 2015;**50**:755-769

[18] Dragicevic T, Pandzic H, Skrlec D, Kuzle I, Guerrero JM, Kirschen DS. Capacity optimization of renewable energy sources and battery storage in an autonomous telecommunication facility. IEEE Transactions on Sustainable Energy. Oct. 2014;**5**(4):1367-1378

[19] Dufo-López R, et al. Multi-objective optimization minimizing cost and life cycle emissions of stand-alone PV–wind–diesel systems with batteries storage. Applied Energy. Nov. 2011;**88**(11):4033-4041

[20] Katsigiannis YA, Georgilakis PS, Karapidakis ES. Multiobjective genetic algorithm solution to the optimum economic and environmental performance problem of small autonomous hybrid power systems with renewables. IET Renewable Power Generation. 2010;**4**(5):404

[21] Lu L, Han X, Li J, Hua J, Ouyang M. A review on the key issues for lithium-ion battery management in electric vehicles. Journal of Power Sources. Mar. 2013;**226**:272-288

[22] Chang WY. The state of charge estimating methods for battery: A review. ISRN Applied Mathematics. 2013;**2013**:1-7

[23] Gholami A, Shekari T, Aminifar F, Shahidehpour M. Microgrid scheduling with uncertainty: The quest for resilience. IEEE Transactions on Smart Grid. Nov. 2016;**7**(6):2849-2858

[24] Stan AI, Swierczynski M, Stroe DI, Teodorescu R, Juhl Andreasen S, Moth K. A comparative study of lithium ion to lead acid batteries for use in UPS applications. In: Telecommunications Energy Conference (INTELEC), 2014 IEEE 36th International. 2014. p. 1-8

[25] Omar N, Bossche P, Coosemans T, Mierlo J. Peukert revisited-critical appraisal and need for modification for lithium-ion batteries. Energies. Oct. 2013;**6**(11):5625-5641

[26] IEEE Power & Energy Society and Stationary Batteries Committee. IEEE Recommended Practice for Sizing Lead-Acid Batteries for Stationary Applications - IEEE Std 485TM-2010. New York: Institute of Electrical and Electronics Engineers; 2011

[27] Ecker M, et al. Calendar and cycle life study of li(NiMnCo)O2-based 18650 lithium-ion batteries. Journal of Power Sources. Feb. 2014;**248**:839-851

[28] Bindner H, Cronin T, Lundsager P, Risø National Lab, Roskilde (DK). Wind Energy Department, Lifetime Modelling of Lead Acid Batteries. Risø National Laboratory, Roskilde, Denmark; 2005. ISBN: 978-87-550-3441-9

[29] Downing SD, Socie DF. Simple rainflow counting algorithms. International Journal of Fatigue. 1982;**4**(1):31-40

[30] Beltran H, Swierczynski M, Aparicio N, Belenguer E, Teodorescu R, Rodriguez P. Lithium ion batteries ageing analysis when used in a PV power plant. In: Industrial Electronics (ISIE), 2012 IEEE International Symposium on. 2012. p. 1604-1609

[31] Li Y, Nejabatkhah F. Overview of control, integration and energy management of microgrids. Journal of Modern Power Systems and Clean Energy. Aug. 2014;**2**(3):212-222

[32] Ghasemkhani A, Anvari-Moghaddam A, Guerrero JM, Bak-Jensen B. An efficient multi-objective approach for designing of communication interfaces in smart grids. In: IEEE PES Innovative Smart Grid Technologies (ISGT 2016). 2016. p. 1-6

[33] Islam SZ, Mariun N, Hizam H, Othman ML, Radzi MAM, Hanif M, Abidin IZ. Communication for distributed renewable generations (DRGs): A review on the penetration to smart grids (SGs). In: PECon 2012 - 2012 IEEE Int. Conf. Power Energy, no. December. 2012. p. 870-875

[34] Liyanage KM, Manaz MAM, Yokoyama A, Ota Y, Taniguchi H, Nakajima T. Impact of communication over a TCP/IP network on the performance of a coordinated control scheme to reduce power fluctuation due to distributed renewable energy generation. In: 2011 6th Int. Conf. Ind. Inf. Syst. ICIIS 2011 - Conf. Proc. 2011. p. 198-203

[35] Anvari-Moghaddam A, Mokhtari G, Guerrero JM. Coordinated demand response and distributed generation Management in Residential Smart Microgrids. In: Mihet L, editor. Energy Management of Distributed Generation Systems. 1st ed. InTech; 2016. p. 27-57

[36] Nejabatkhah F, Li YW. Overview of power management strategies of hybrid AC/DC microgrid. IEEE Transactions on Power Electronics. 2015;**30**(12):7072-7089

[37] Olivares DE, Member S, Cañizares CA. A centralized energy management system for isolated microgrids. IEEE Transactions on Smart Grid. 2014;**5**(4):1864-1875

[38] Anvari-Moghaddam A, Monsef H, Rahimi-Kian A. Cost-effective and comfort-aware residential energy management under different pricing schemes and weather conditions. Energy and Buildings. 2015;**86**:782-793

[39] Modes S, Jiang Q, Xue M, Geng G, Member S. "Energy Management of Microgrid", 2013;**28**(3):3389-2013

[40] Becker DJ, Sonnenberg BJ. DC microgrids in buildings and data centers. In: Telecommunications Energy Conference (INTELEC), 2011 IEEE 33rd International. 2011. p. 1-7

[41] Wang Z, Chen B, Wang J, Kim J. Decentralized energy management system for networked microgrids in grid-connected and islanded modes. IEEE Transactions on Smart Grid. 2016;**7**(2):1097-1105

[42] Anvari-Moghaddam A, Guerrero JJM, Rahimi-Kian A, Mirian MS. Optimal real-time dispatch for integrated energy systems: An ontology-based multi-agent approach. In: 7th International Symposium on Power Electronics for Distributed Generation Systems (PEDG'16). 2016. p. 1-7

[43] Mokhtari G, Anvari-Moghaddam A, Nourbakhsh G. Distributed control and management of renewable electric energy resources for future grid requirements. In: Mihet L, editor. Energy Management of Distributed Generation Systems. 1st, July; InTech ed. Janeza Trdine, Rijeka, Croatia. 2016. p. 1-24

[44] Anvari-Moghaddam A, Rahimi-Kian A, Mirian MS, Guerrero JM. A multi-agent based energy management solution for integrated buildings and microgrid system. Applied Energy. 2017;**203**:41-56

[45] Dou CX, Duan ZS, Liu B. Two-level hierarchical hybrid control for smart power system. IEEE Transactions on Automation Science and Engineering. 2013;**10**(4):1037-1049

[46] Lu T, Wang Z, Ai Q, Lee W-J. Interactive model for energy Management of Clustered Microgrids. IEEE Transactions on Industry Applications. 2017;**9994**(c):1-1

[47] Rodriguez E, Vasquez JC, Josep M, Rodriguez-diaz E, Anvari-moghaddam A, Vasquez JC, Guerrero JM. Multi - Level Energy Management and Optimal Control of a Residential DC Microgrid. IEEE International Conference on Consumer Electronics (ICCE), Las Vegas, NV, 2017, pp. 312-313. DOI: 10.1109/ICCE.2017.7889333

[48] Anvari-moghadam A, Shafiee Q, Vasquez JC, Guerrero JM. Optimal adaptive droop control for effective load sharing in AC microgrids. IECON-42nd Annual Conference of the IEEE Industrial Electronics Society, Florence, Italy, 2016, pp. 3872-3877. DOI: 10.1109/IECON.2016.7793515

[49] Tah A, Das D. An enhanced droop control method for accurate load sharing and voltage improvement of isolated and interconnected DC microgrids. IEEE Transactions on Sustainable Energy. 2016;**7**(3):1194-1204

[50] Li Y, Li YW. Power management of inverter interfaced autonomous microgrid based on virtual frequency-voltage frame. IEEE Transactions on Smart Grid. 2011;**2**(1):18-28

[51] Guan Y, Guerrero JM, Zhao X, Vasquez JC, Guo X. A new way of controlling parallel-connected inverters by using synchronous-reference-frame virtual impedance loop - part I: Control principle. IEEE Transactions on Power Electronics. 2016;**31**(6):4576-4593

[52] Zhang Y, Wei Li Y. Energy management strategy for Supercapacitor virtual impedance. IEEE Transactions on Power Electronics. 2017;**32**(4):2704-2716

[53] Tank I. Renewable Based DC Microgrid with Energy Management System, IEEE International Conference on Signal Processing, Informatics, Communication and Energy Systems (SPICES), Kozhikode, 2015, pp. 1-5. DOI: 10.1109/SPICES.2015.7091542

[54] Anvari-Moghaddam A, Dragicevic T, Vasquez JC, Guerrero JM. Optimal utilization of microgrids supplemented with battery energy storage systems in grid support applications. IEEE First International Conference on DC Microgrids (ICDCM). 2015;**2015**:57-61

[55] Lu L, Chu C. Consensus-based distributed droop control of Synchronverters for isolated micro-grids. IEEE Transactions on Power Apparatus and Systems. 2015;**30**(5):914-917

[56] Lai J, Zhou H, Lu X, Yu X, Hu W. Droop-based distributed cooperative control for microgrids with time-varying delays. IEEE Transactions on Smart Grid. 2016;**7**(4): 1775-1789

Chapter 8

# Fabrication and Characterization of Supercapacitors toward Self-Powered System

Ananthakumar Ramadoss,
Balasubramaniam Saravanakumar and
Sang-Jae Kim

Additional information is available at the end of the chapter

http://dx.doi.org/10.5772/intechopen.73647

**Abstract**

Ever increasing energy demand urges to impelled extensive research in the development of new eco-friendly energy harvesting and storage technologies. Energy harvesting technology exploiting renewable energy sources is an auspicious method for sustainable, autonomous, and everlasting operation of a variety of electronic devices. A new concept of an integrated self-powered system by combining an energy harvesting device with an energy storage device has been established to harvest renewable energy and simultaneously store it for sustainable operation of electronic devices. In this chapter, describes the fabrication of a self-powered system by integrating the supercapacitor with energy harvesting devices such as nanogenerator and solar cells to power portable electronic devices. Initially synthesis and electrochemical characterization of various electroactive materials for supercapacitors and further, fabrication of supercapacitor device were discussed. In conclusion, this chapter demonstrates self-powered system by the integration of energy harvesting, energy storage module with portable electronic devices. The various result validates the feasibility of using supercapacitors as efficient energy storage components in self-powered devices. The proposed self-powered technology based on energy conversion of renewable energy to electrical energy which stored in energy storage device and it will be used to operate several electronic devices as a self-powered device.

**Keywords:** energy harvesting, energy storage, supercapacitors, self-powered system, portable electronics

## 1. Introduction

Recently, a massive demand on the highly reliable energy sources with higher energy density and longer life to operate advanced electronic and optoelectronic devices, which have impelled extensive research in the development of new eco-friendly energy harvesting and storage technologies [1–5]. The advancement of portable electronics, enormous demand for electric vehicles, integration, and development of internet of things (IoT) was highly demanding the high-performance energy storage device with added functionalities like flexibility, light-weight, cost-effective, renewable, and eco-friendly features [6, 7]. At the same time, the ultimatum of our society is also looking for an advanced version of multifunctional electronic devices, which are swelling day by day towards the trend of being a portable, flexible, light-weight, wearable and self-powered devices.

In fact, there is a increasing interest in the energy generation from environment for powering the micro/nano-systems, because it is available everywhere and abundant. However, limited by time, location, weather and other factors [8, 9]. For example, solar and wind energies are intermittent energy but renewable. But, we will not get sunshine during the night time and as well as wind on our demand, which results instability or unsustainable power supply to electronic devices [10, 11]. In order to alleviate these problems, renewable energy converters like solar and vibrational harvesters would be better choice to integrate with energy storage device, to achieve sustainable operation by storing the generated electric energy from energy harvesting devices. The nanogenerator is a device which can efficiently convert mechanical energy into electrical energy through piezoelectric and triboelectrification processes from our living/working environment. However, these mechanical energy sources are uncontrollable fluctuation which reflects in output power [11–13]. Therefore, it cannot be used directly to power electronic devices. In this circumstance, an intermediate efficient energy storage system required to store this irregular renewable energy to achieve independent power source (stable and durable output). The development of self-powered micro/nano-device by integrating energy harvesting device with electrochemical energy storage devices such as supercapacitor and battery is a promising solution for the limitation of both energy harvesting and storage devices. Among them, supercapacitors are superior than lithium-ion batteries because of its higher power capacity, more extended cyclic stability, and fast charging/discharging capability, environmental benignancy, etc. [10, 14–16].

Recently, researchers have been attempted to develop a new hybrid system by integrating the energy harvesting device (solar cell and nanogenerator) along with a storage device (lithium-ion battery and supercapacitor) to perform a self-powered operation [8, 17–23]. However, the obtained results are not up to real-world application level due to low energy conversion and storage efficiency of the devices as well as power management circuit, and further research is required to improve the output performance. The performance of self-powered systems will be substantially improved with a better power management circuit and a rational design of energy harvesting and storage devices. In recent years, significant endeavors have been dedicated to building an integrated sustainable self-power system for the smart electronics with the improved architecture of energy harvesting and storage devices.

This chapter describes the fabrication and electrochemical performance of the supercapacitor device with various electrode materials and integration of supercapacitor device with

different energy harvesters such as solar, vibration for self-powered device applications. Briefly, (i) fabrication and integration of supercapacitor device with vibrational energy harvesters such as piezoelectric and triboelectric nanogenerator and (ii) fabrication and integration of supercapacitor device with solar energy harvesters such as a dye-sensitized solar cell (DSSC).

## 2. Fabrication and testing of self-powered systems

### 2.1. Fabrication and integration of supercapacitor device with vibrational energy harvesters

Recently, a higher attention has been given to the development of two dimensional (2D) materials for various application such as electronic, catalytic, energy conversion and storage application due to their exceptional property like electrical, optical and chemical properties. Among the other 2D materials, graphene offered higher electrical conductivity, surface area (2600 $m^2 g^{-1}$), and excellent mechanical flexibility due to their excellent physio-chemical properties by honeycomb structured carbon atom with atomic thick [24–28]. Because of higher surface area and good conductivity of graphene attracts to energy storage application. However, the specific capacitance, energy and power density of the graphene supercapacitors are lower than the expected values, which varies with synthesis methods. Until now, a various method has been adapted for synthesis of graphene in different forms like pristine graphene, graphene, reduced graphene oxide (rGO), and graphitic oxides by micromechanical exfoliation from graphite, chemical vapor deposition, chemical reduction methods [29–34]. Herein, a flexible graphene-coated fabric electrodes were fabricated by using a simple-cost effective dip-coating technique followed by thermal reduction at 170°C in Ar for 2 h. This fabrication method allows making binder-free, highly flexible, lightweight supercapacitor device and fabrication process is very simple, cost-effective and possible to extend large scale fabrication. A thin, binder-free coating of graphene allows higher electrical conductivity, surface area, and electrochemical activity.

#### *2.1.1. Fabrication and characterization of the thermally reduced graphene oxide (TRGO)-coated fabric electrode*

The fabrication of thermally reduced graphene oxide nanosheets electrode is schematically represented in **Figure 1a**. Briefly, the graphene oxide (GO) was prepared from graphite by modified hummer's method [35]. The prepared GO solution was used to coat on conducting fabric by repeated dip-coating. After each coating, the GO-coated fabric was dried at 60°C for 30 min; this process was repeated for five times. The GO-coated fabric was reduced to a graphene-coated fabric by thermal treatment at 170°C for 2 h in Ar. The surface morphology of the as-prepared film was characterized through Field emission scanning electron microscopy (FE-SEM) analysis, and results are indicating that the uniform deposition of TRGO on the fabric surface which is noted in **Figure 1b–c**. Further, the chemical reduction of GO deposited fabrics was confirmed through Raman, Fourier transforms infrared (FT-IR), and X-ray photoelectron spectroscopy (XPS) analysis and results are presented in **Figure 2**. From Raman spectra (**Figure 2a**), two characteristic peaks were observed at 1602 (G-band) and 1354 $cm^{-1}$

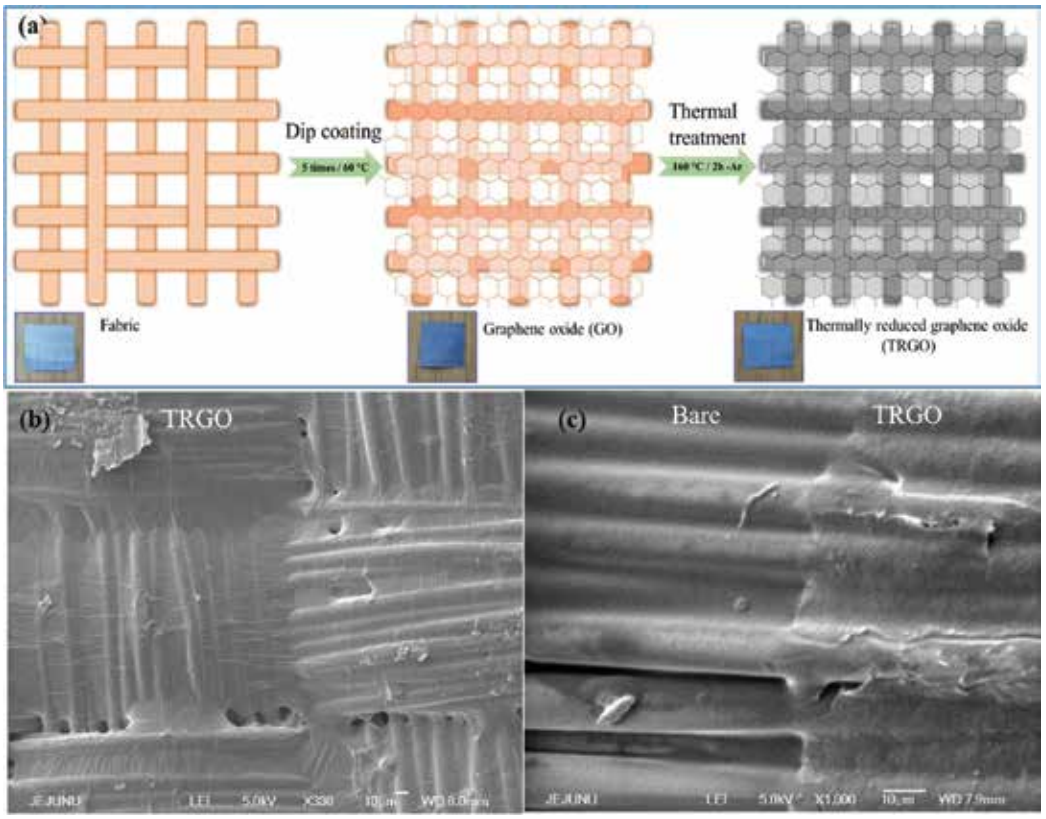


**Figure 1.** (a) Schematic diagram of the formation of thermally reduced graphene oxide nanosheets. (b-c) FE-SEM images of TRGO on the fabric surface. Figures are reproduced with permission from Ref. [19]. Copyright of Elsevier.

(D-band) of graphitic carbon in both GO and TRGO and corresponds to the defects and disorder in the hexagonal graphitic layers and optical $E_{2g}$ mode in-plane vibration phonon at the Brillouin zone center, respectively [26, 36, 37]. Moreover, the chemical reduction of GO into TRGO by characteristics peak shift toward lower wave number and a slight increase in $I_D/I_G$ ratio from 0.95 to 0.97, it is due to structural disorder (defects) generated during thermal reduction process [33]. The FT-IR spectra (**Figure 2b**.) also clearly indicating the reduction of GO into TRGO through the observation of reduced intensities of the absorption bands at 3340 (O—H stretching vibration), 1728 (C = O stretching vibration), 1623 (skeletal vibration of un-oxidized graphitic domains), 1386 (O—H deformation of C—OH groups), 1233 (C—OH stretching vibration), and 1057 $cm^{-1}$ (C—O stretching vibration) [38]. In XPS spectra, three peaks were observed at 284.6, 286.4, and 288.6 eV, which correspond to C = C/C—C (aromatic rings), C—O (hydroxyl and epoxy), and C = O (carbonyl) groups, respectively [26, 36]. The peak intensities of the oxygen-containing groups in the TRGO was lower than GO due to thermal reduction (**Figure 2c–d**). From, these results concluded that the GO was reduced to TRGO after thermal treatment in Ar environment. Moreover, thermal treatment allowed to transform $sp^3$ to $sp^2$ hybridization by reduction of the oxygenating functional group [39].

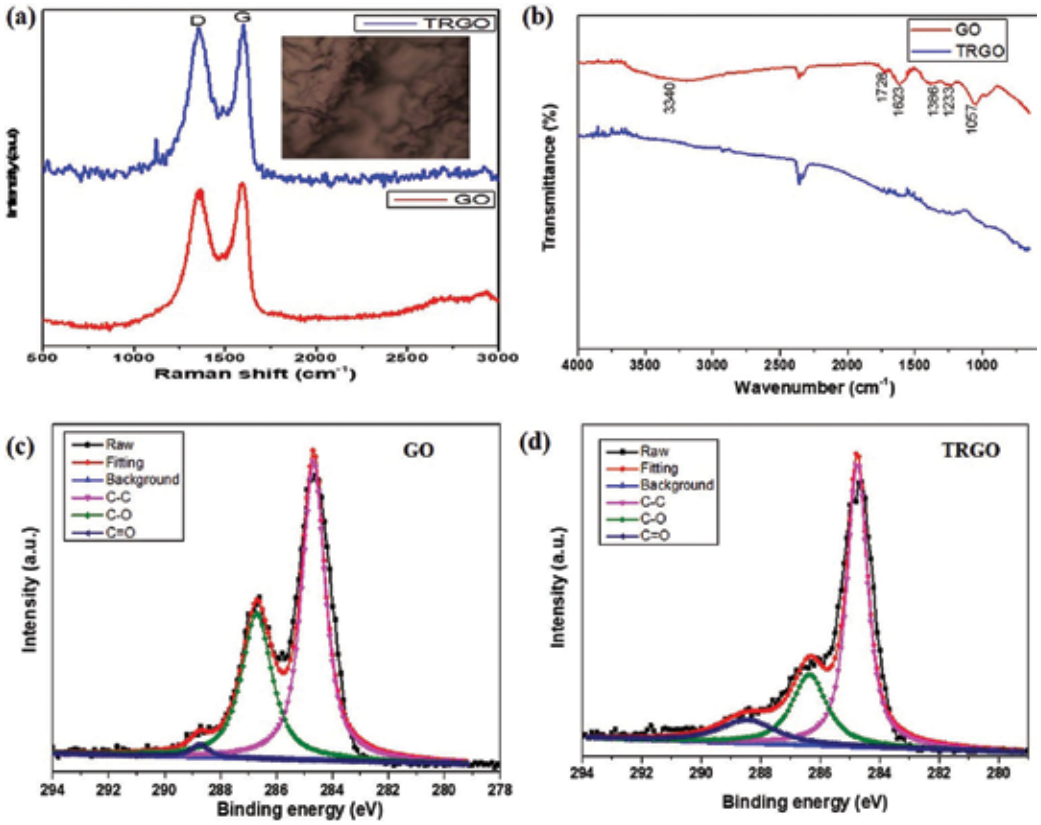


**Figure 2.** (a) Raman, (b) FT-IR and (c-d) C1s XPS spectra of GO and TRGO. Figures are reproduced with permission from Ref. [19]. Copyright of Elsevier.

### *2.1.2. Electrochemical characterization of TRGO-coated fabric electrode*

The electrochemical performance of the as-prepared TRGO-coated fabric electrode was measured in 1 M $H_3PO_4$ electrolyte using the three-electrode system. **Figure 3a** shows the cyclic voltammetry (CV) curves of the TRGO-coated fabric electrode at various sweep rates from 5 to 125 mV $s^{-1}$. The resultant CV curve shows a rectangular-like shape, which indicates the electrochemical double-layer capacitance. Further, the rectangular CV curve accompanied with redox peaks at ~0.32 V of anodic scan and ~0.29 V of the cathodic scan. The co-existence of redox peaks confirmed the Faradic reaction by oxygenated functional groups (carbonyl and quinone groups) in TRGO [36, 40–42], which significantly contributes pseudocapacitance to the system (Inset of **Figure 3a**). The calculated specific capacitance at various scan rates was shown in **Figure 3b**. At a scan rate of 5 mV $s^{-1}$, the higher specific capacitance of 414 F $g^{-1}$ was observed and drops with increasing scan rates [43]. Further, galvanostatic charge-discharge (GCD) was measured at different current densities and results are shown in **Figure 3c**. The resultant GCD curve shows a linear and symmetric shape with a significantly low plateau. The symmetric nature of GCD confirms the double-layer capacitive nature and small plateau

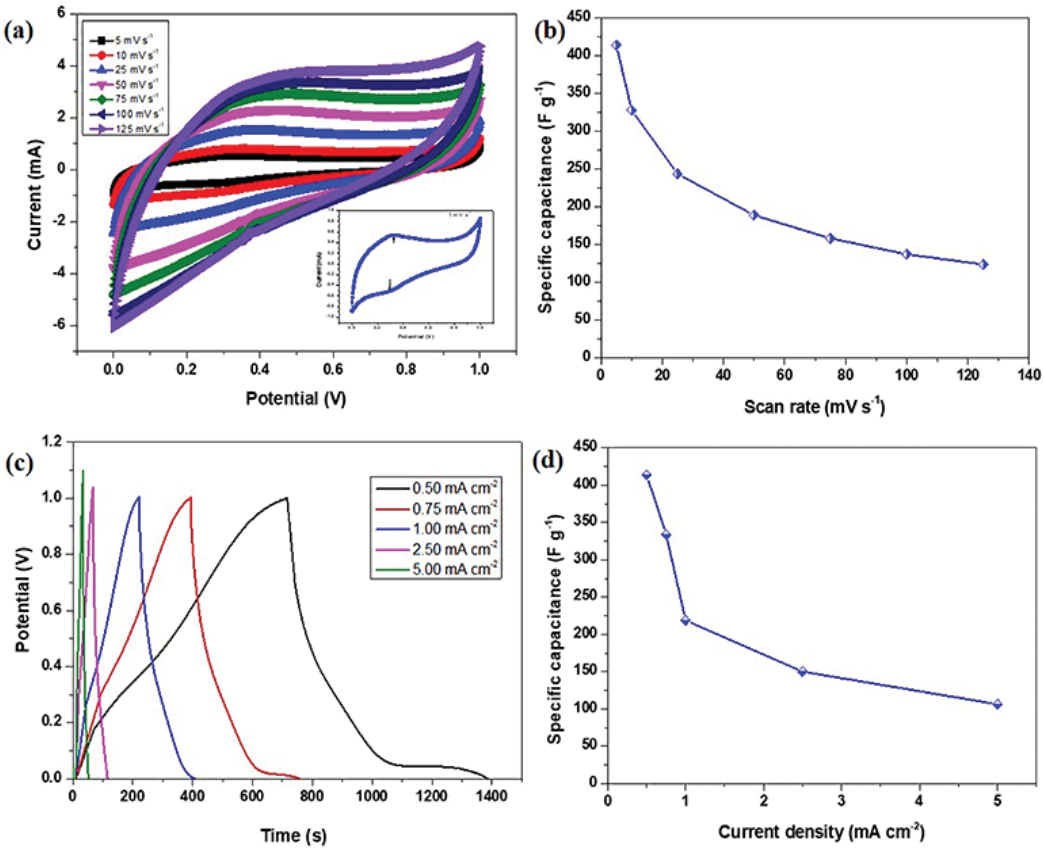


**Figure 3.** (a) CV curves of TRGO-coated fabric electrodes (inset at 5 mV $s^{-1}$). (b) Specific capacitance of TRGO-coated fabrics at different scan rates. (c) GCD curves of TRGO-coated fabric electrodes. (d) Specific capacitance of TRGO-coated fabrics at different current densities. Figures are reproduced with permission from Ref. [19]. Copyright of Elsevier.

appeared due to the faradic reaction. The existence of redox peak in GCD curve well agrees with CV curve. The calculated specific capacitances (**Figure 3d**) were 413, 333, 218, 150, and 106 F $g^{-1}$ at various current densities of 0.5, 0.75, 1, 2.5 and 5 mA $cm^{-2}$, respectively. These values are comparable as well as higher than previously reported values [26, 36, 44–47]. The shorter diffusion path, higher conductivity and higher active surface area of the fabricated TRGO electrode enhances the specific capacitance.

### *2.1.3. Fabrication and electrochemical performance of the flexible solid-state symmetric supercapacitor (SSC) device*

A solid-state SSC was fabricated by sandwiching a $H_3PO_4$/PVA gel electrolyte and filter paper between two pieces of the TRGO-coated fabric electrodes. The electrochemical performance of the solid-state supercapacitor such as CV and GCD was measured at different scan rates and current densities and results shown in **Figure 4**. The CV curve (**Figure 4a**.) of the fabricated supercapacitor device showed rectangular-like shapes even at high scan rates, which is ideal capacitive and fast charge/discharge behavior of the supercapacitor device. The

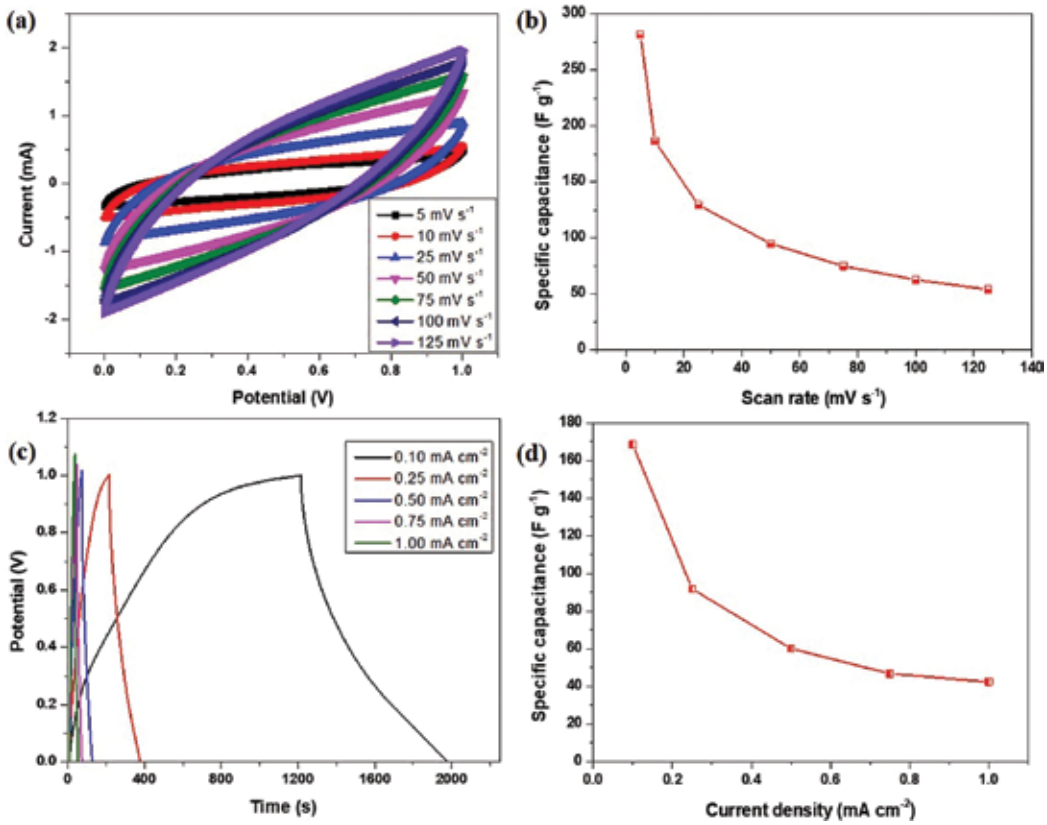


**Figure 4.** (a) CV curves and (b) specific capacitance of fabric SC at different scan rates. (c) GCD profiles and (d) specific capacitance of fabric SC at current densities. Reproduced from Ref. [19] with permission from the Elsevier.

specific capacitance as a function of scan rate is shown in **Figure 4b**. The calculated single electrode specific capacitance decreased from 281 to 54 F $g^{-1}$, when scan rate increased from 5 to 125 mV $s^{-1}$ and it is due to inefficient diffusion of ions at higher scan rates [48, 49]. Further, GCD of solid-state device was measured at various current density, which is shown in **Figure 4c**. The resultant GCD curve shows symmetric nature, which confirms the good capacitive nature of the device. The calculated specific capacitance was shown in **Figure 4d**. The estimated specific capacitance of the cell (flexible supercapacitor) was 70.4 F $g^{-1}$ at 5 mV $s^{-1}$. The highest specific capacitance (single electrode) of 169 F $g^{-1}$ was achieved at a current density of 0.1 mA $cm^{-2}$; this value is comparable to those previously reported results for solid-state supercapacitors [45, 50, 51]. Further, the power and energy densities are two significant parameters to evaluate the performance of the supercapacitor device. The maximum energy and power densities of the solid-state device reached 5.8 W h $kg^{-1}$ at a power density of 27.7 kW $kg^{-1}$ and a power density of 277.6 kW $kg^{-1}$ at an energy density of 1.5 W h $kg^{-1}$. The obtained values are higher and comparable to the previously reported values [44, 50, 52–60]. The excellent electrochemical performance of the solid-state SSC device mainly attributed to the following factors: (1) binder-free deposition of graphene on fabric current collector reduces the conduct resistance, which facilitates faster electrical conduction during electrochemical reaction; (2) the

deposition of thin TRGO nanosheets provides a large accessible surface area which allowed abundant ions access (adsorption/desorption) for electrochemical reaction; (3) direct deposition of electroactive material allows strong adhesion with fabric current collector provide higher mechanical flexibility to device.

*2.1.4. Integration and functional characterization of self-powered UV sensor*

To demonstrate the self-powered application, fabricated SSC device was integrated with piezoelectric nanogenerator and photosensor. Here, piezoelectric nanogenerator used as an energy harvester, which converts the mechanical vibration, environmental noises into electrical energy. The harvested alternate current (AC) electrical signal was stored in the fabricated SSC device with the help of rectifier. The stored energy was used to monitor the ultraviolet (UV) light by integrating the photosensor with this system. The detailed circuit configuration was presented in **Figure 5a**. Here, a commercial piezoelectric nanogenerator was used as the energy source; it generated an average open-circuit voltage and short-circuit current of 8 V and 20 μA, respectively, under continuous finger pressure. The serially connected supercapacitors were charged (0.3 V over 280 s) by piezoelectric nanogenerator under constant finger pressing (**Figure 5b**). To demonstrate a self-powered application, the photodetector was connected to the supercapacitor to monitor UV light (**Figure 5a**) by closing switch S2 and opening switch S1. Here, photodetector was powered by serially connected supercapacitor and photodetector act as a variable load resistance for supercapacitor. The resistance of the photodetector varied linearly with the incident light intensity. The change of load resistance considerably changes the discharge current. The stability of the self-powered device is measured by multiple ON/OFF cycles under a constant illumination intensity of 8 mW $cm^{-2}$ at a wavelength of 365 nm and results showed a stable response during measurement (**Figure 5c**). Additionally, the photoresponse was measured at 0.8 mW $cm^{-2}$ steps for incident light intensity ranging from 0.8 to 8 mW $cm^{-2}$ (**Figure 5d**). The photoresponse current was calculated using the following relation [61]:

$$|I_{PR}| = (I_{OFF} - I_{ON}) \tag{1}$$

where, $I_{PR}$ is the photoresponse current, $I_{OFF}$ is the discharge current at UV light "off" condition, and $I_{ON}$ is the discharge current at UV light "on" condition. The photoresponse current increased linearly with increasing incident intensity (**Figure 5e**). This study suggested that the self-powered device has a massive potential in wearable and portable device applications.

## 2.2. Fabrication and electrochemical characterization of flexible transparent supercapacitor device

First, silver nanowire (AgNW) was spin-coated on polydimethylsiloxane (PDMS) substrate and subsequently dried. Then, PEDOT: PSS/PU nanocomposite was spin-coated over the AgNW/PDMS substrate and film was dried at 150°C for 1 hr. The PEDOT:PSS/PU nanocomposite was prepared by mixing PEDOT:PSS (5–8 wt% dimethyl sulfoxide (DMSO) & 1 wt% zonyl) with 4 wt% polyurethane dispersion (PU). The morphology of the fabricated film was measured through FE-SEM image and result was shown in **Figure 6a**. The resultant FE-SEM

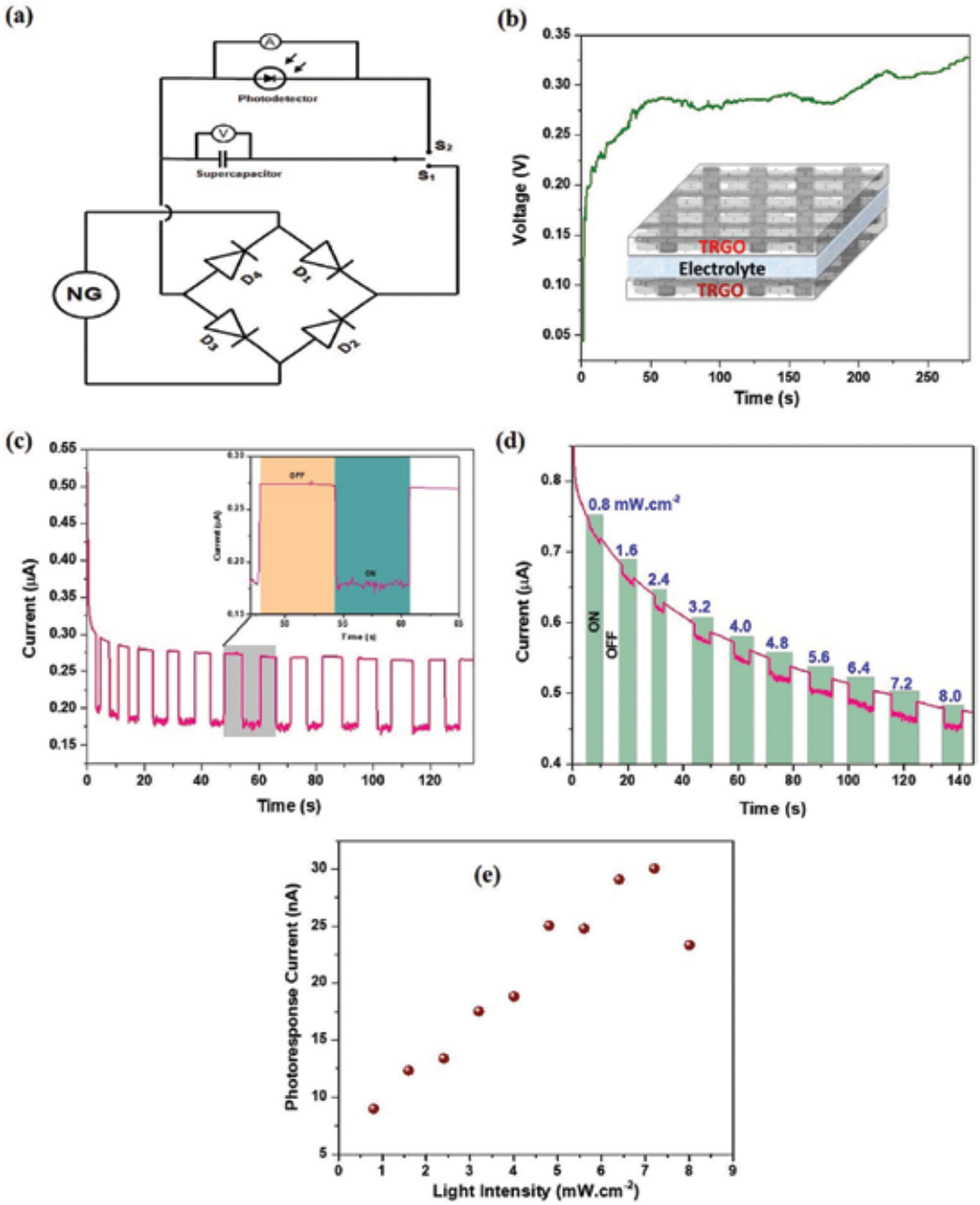


**Figure 5.** (a) Electric circuit diagram of the self-powered photosensor. (b) Charging of F-SCs by piezoelectric nanogenerator; inset is the structure of F-SC. (c) Time-dependent response of multiple ON/OFF cycles at a constant illumination intensity of 8 mW $cm^{-2}$ at $\lambda$ = 365 nm. (d) Time-dependent photoresponse with different illumination intensity. (e) Photoresponse current versus light intensity. Figure is adapted with permission from the Ref. [19]. Copyright of Elsevier.

image is clearly indicating that the deposition of Ag NWs on the flexible PDMS substrate and Ag NWs are randomly oriented on the substrate. Further, spin-coating PEDOT:PSS/PU

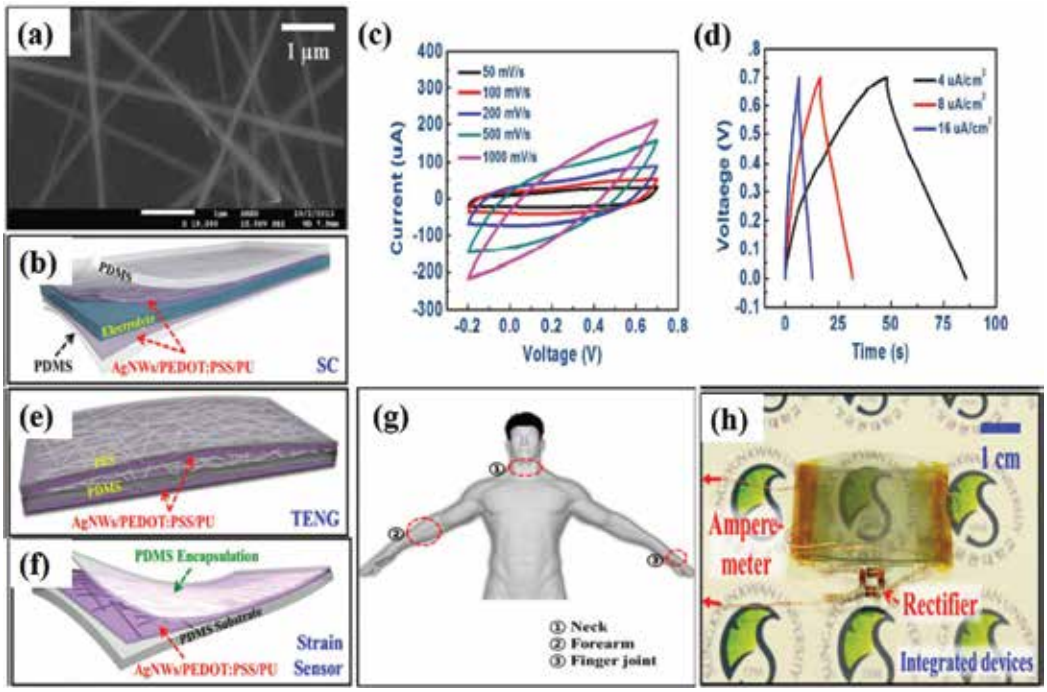


**Figure 6.** (a) FE-SEM image of the AgNW/PEDOT:PSS/PU film on PDMS substrate. (b) Schematic representation, (c) CV and (d) galvanostatic charge-discharge curves of the fabricated transparent flexible supercapacitor device. Schematic illustration of fabricated (e) TENG, (f) transparent strain sensor, and (g) strain sensor on different parts of human body. (h) Digital photograph of the self-powered strain sensor. Figure adapted with permission from the Ref. [23]. Copyright of American Chemical Society.

deposition eliminates the Ag NWs adhesive problems and connect silver nanowires. Moreover, deposition of PEDOT:PSS/PU nanocomposite provides higher flexibility and stretchability to the device by embedding the Ag NW inside polymer matrices. Finally, the flexible supercapacitor device was fabricated by sandwiching poly(vinyl alcohol)/phosphoric acid (PVA/$H_3PO_4$) film between two PDMS/AgNW/PEDOT: PSS/PU substrate [23]. The transparent, stretchable supercapacitor device was schematically illustrated in **Figure 6b**. The performance of the fabricated flexible supercapacitor device was evaluated based on CV and GCD curves at a different scan rate and current densities and results displayed in **Figure 6**c and d. The fabricated PDMS/AgNW/PEDOT:PSS/PU symmetric supercapacitor delivered a maximum areal capacitance of 190 μF $cm^{-2}$ and 396 μF $cm^{-2}$ at a scan rate of 50 mV $s^{-1}$ and a current density of 4 μA $cm^{-2}$, respectively.

### *2.2.1. Fabrication and characterization of transparent, stretchable self-powered patchable sensor*

The arch type triboelectric nanogenerator (TENG) device was fabricated by placing an arch-shaped PES/AgNW/PEDOT:PSS/PU on PDMS/AgNW/PEDOT:PSS/PU and schematic was shown in **Figure 6e**. The fabricated device designed to contact the arch-shaped PES surface with PDMS surface. The transparent, stretchable strain sensor was fabricated same as

http://dx.doi.org/10.5772/intechopen.73647

supercapacitor electrode and additionally, PDMS layer was covered over the electrode to avoid the delamination and increase the stretchable nature. Here, AgNW/PEDOT:PSS/PU coated PDMS substrate was used as an active strain sensor and schematic representation of the fabricated electrode was given in **Figure 6f**. Further, the schematic representation of strain sensor placed on different parts of the human body is shown in **Figure 6g**. To demonstrate the capability of the fabricated strain sensor, it has integrated with supercapacitor device. The original

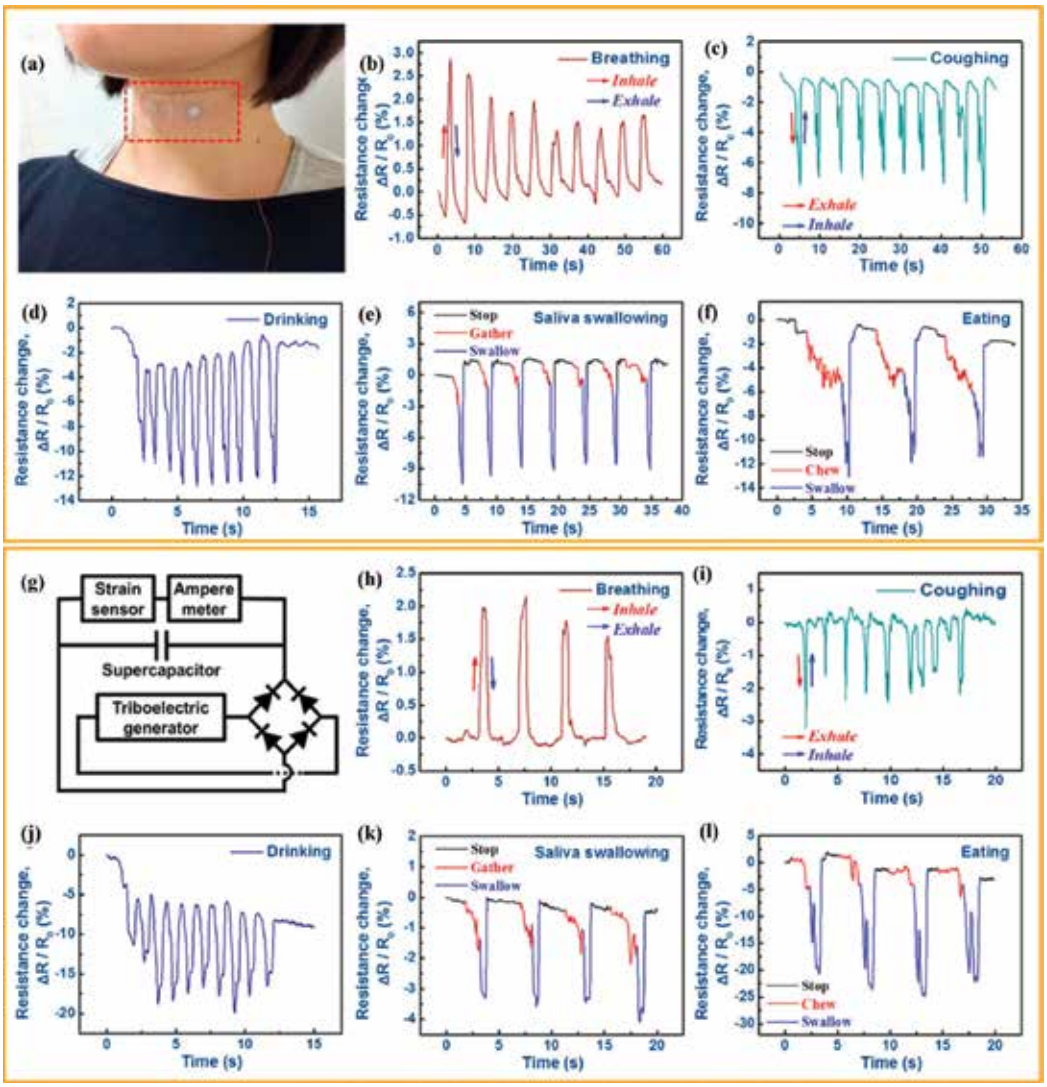


**Figure 7.** Monitoring of strain caused by muscle movement for functions of the trachea and esophagus. (a) Stretchable and transparent strain sensor attached to the neck. Resistance change ($\Delta R/R_0$) of the strain sensor versus time measured by source measurement unit, (b) breathing, (c) coughing, (d) drinking, (e) saliva swallowing, and (f) eating. (g) Circuit diagram of strain according to the sensor with SC charged by TENG. Resistance change ($\Delta R/R_0$) of the strain sensor versus time measured by SC charged by TENG, through (h) breathing, (i) coughing, (j) drinking, (k) saliva swallowing, and (l) eating, respectively. Figures are reproduced with permission from Ref. [23]. Copyright of American Chemical Society.

photocopy of the integrated device was shown in **Figure 6h**. The ability of the fabricated device was calibrated by attaching the device at neck to monitor the muscle movements of the trachea during breathing and coughing and esophagus during drinking, swallowing, and eating. At first, the integrated device was charged by the external power source and used to run the strain sensor. The measured output signal from the embedded device was shown in **Figure 7**, and it is clear that the fabricated device highly sensitive to the muscle movement, well distinguishable between the nature of applied strain. To demonstrate the self-powered operation of the integrated device, the supercapacitor was charge through the triboelectric nanogenerator by mechanical vibration (pushing). The charging performance of the supercapacitor device with integrated TENG was shown in **Figure 8**. The results indicating that the integrated supercapacitor device charge up to 0.9 V at the short period (1500 s) of mechanical vibration.

Further, the self-charged power was used to power the strain sensor to monitor the muscle movement. The output performance of the sensor powered by self-charged supercapacitor device is highly sensitive and almost same type of response observed as like externally charged device. The output performance of the strain sensor was given in **Figure 7h–i**. Similarly, the fabricated device showed higher sensitivity to the various human body activity like twisting, turning the wrist, clenching, etc. This result opens up to use self-powered systems for multiple application in wearable application as well internet of things (IoT).

### 2.3. Fabrication and integration of supercapacitor device with solar energy harvesters

#### *2.3.1. Synthesis and characterization of 3D-$NiCo_2O_4$/Ni fiber electrodes*

The three dimensional (3D) porous nickel (Ni) films on metal fiber substrate were deposited using electrodeposition with a hydrogen bubble template method [62]. Briefly, the 3D porous Ni film was electrodeposited at a constant current of 2.5 A using DC power supply with the electrolyte containing a 0.1 M $NiCl_2$ and 2 M $NH_4Cl$ and then dried at 60°C for 12 h in hot air over. The 3D-$NiCo_2O_4$/Ni nanostructures were prepared by the electrodeposition of

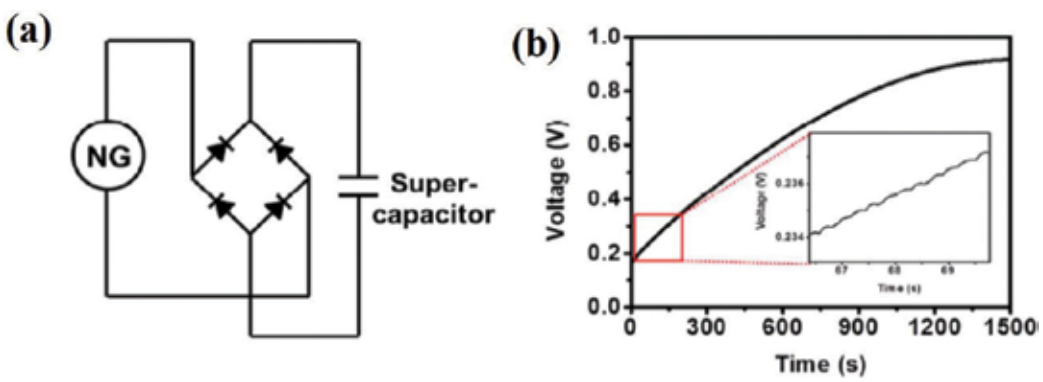


**Figure 8.** Charging property of the transparent and stretchable SC charged by a TENG. (a) Schematic of the rectifying circuit and SC. (b) Charging curve of the SC charged by the power generated by the TENG, and charging steps of the SC (inset). Figure is adapted with permission from the Ref. [23]. Copyright of American Chemical Society.

bimetallic (Ni, Co) hydroxide in a standard three-electrode system in an aqueous solution containing 1:2 molar ratio of 0.02 M nickel nitrate ($Ni(NO_3)_2.6H_2O$) and 0.04 M cobalt nitrate ($Co(NO_3)_2.6H_2O$) at a constant potential of -1 V for 5 min and followed by thermal transformation into spinel $NiCo_2O_4$ at 300°C for 2 h [63]. The construction of 3D architectures electrode would be predictable to exhibit better electrochemical performance in terms of high specific capacitance, high-rate capability, and high energy density. The expectation of enriched performance is mainly due to the enlarged active surface area and open pores which facilitates the diffusion of electrolyte, highly porous interconnected network of nickel metal improves the fast electron transport, the large surface area of electrode contact with the electrolyte as well as lower resistance, better adhesion between the substrate and electroactive material.

The morphology of 3D porous Ni films and 3D-$NiCo_2O_4$/Ni nanostructures were examined by FE-SEM. **Figure 9a–b**. depicts the 3D porous interconnected Ni dendritic walls. The dendritic walls were composed of numerous interlinked nanoparticles and display continuous interspaces. The FE-SEM images of 3D-$NiCo_2O_4$/Ni (**Figure 9c–d**) shows the highly porous flower-like nanostructures over the Ni surface. The elemental composition of the as-prepared 3D-$NiCo_2O_4$/Ni nanostructure film was evaluated by energy-dispersive X-ray spectroscopy and shown in **Figure 9e–f**. The Energy-dispersive X-ray spectroscopy (EDS) spectrum shows the distinctive peaks of Ni, Co and O elements present in the sample, which confirmed the formation of 3D-$NiCo_2O_4$/Ni. Further, the elemental mapping images clearly display the uniform distribution of Ni, Co and O elements within the 3D-$NiCo_2O_4$/Ni structure. Also, XRD spectrum of 3D-$NiCo_2O_4$/Ni exhibited the distinct diffraction peaks at the diffraction angles of 37.1°, 59.1° and 64.9° correspond to the (311), (511) and (440) plane reflections of spinel $NiCo_2O_4$ crystalline structure (JCPDS file no: 20-0781). The electrochemical characterization of as-prepared electrode was analyzed by CV and GCD curves in 2 M KOH electrolyte. **Figure 9g–h** shows the CV and GCD curves of 3D-$NiCo_2O_4$/Ni fiber electrodes. The CV curves of the 3D-$NiCo_2O_4$/Ni electrodes show two pairs of redox peaks during the electrochemical process, which attributed to the reversible faradaic redox processes of $Ni^{2+}/Ni^{3+}$ and $Co^{2+}/Co^{3+}$ transitions [64]. Further, the GCD curves also exhibited a non-linear behavior with voltage plateau indicated the faradaic behavior of the electrodes. The calculated volumetric and gravimetric capacitance of the 3D-$NiCo_2O_4$/Ni fiber electrodes were 29.7 F $cm^{-3}$ and 300 F $g^{-1}$, respectively.

Flexible solid-state fiber supercapacitor based on two 3D-$NiCo_2O_4$/Ni used as a positive and negative electrode, with polyvinyl alcohol- potassium hydroxide (PVA-KOH) gel electrolyte on a polyethylene terephthalate (PET) substrate was fabricated, for real-world applications. The two electrodes were assembled in parallel with separation of 1 mm on the PET substrate using PVA-KOH. The typical CV curves of F-SC at different scan rates as shown in **Figure 10a**, signifying the typical pseudocapacitive behavior. **Figure 10b**. shows the GCD curves of F-SC at different current densities. The GCD curves of F-SC also reveal symmetry and linear in nature, confirms that the device has excellent electrochemical reversibility and capacitive behavior. The calculated gravimetric and volumetric capacitance of the full cell is 18.8 F $g^{-1}$ and 1.86 F $cm^{-3}$, respectively. Further, the F-SC exhibited excellent cyclic stability (**Figure 10c**), even after 5000 cycles, with a capacitance retention of ~ 100%. The key parameter of the F-SC such as energy density and power density was calculated from the GCD curves (**Figure 10d**).

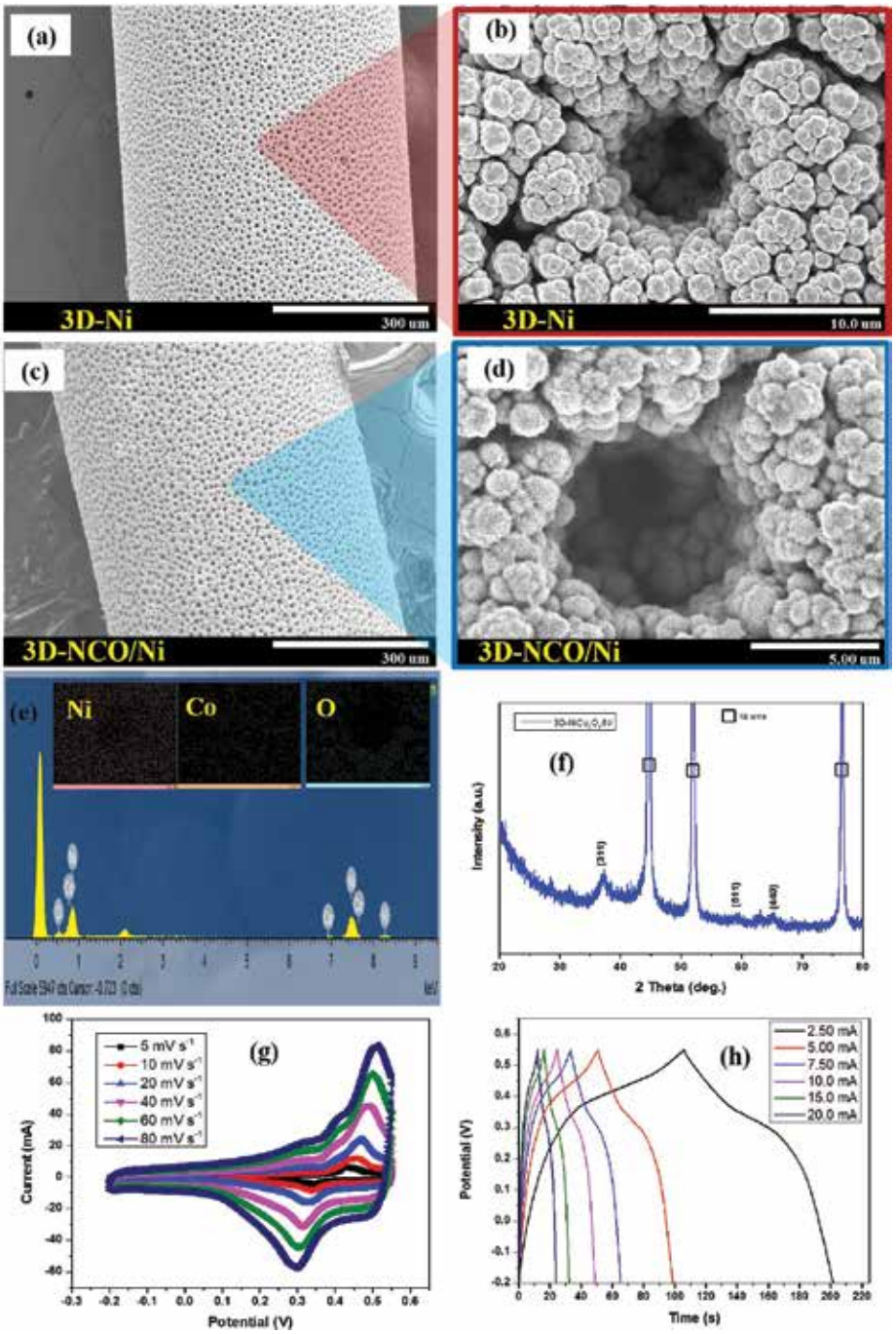


**Figure 9.** FE-SEM images of 3D-Ni (a-b) and 3D-$NiCo_2O_4$/Ni (c-d) nanostructures. (e) EDS and (f) X-ray diffraction (XRD) spectra of 3D-$NiCo_2O_4$/Ni. (g) CV and (h) GCD curves of 3D-$NiCo_2O_4$/Ni. Figure is adapted with permission from the Ref. [7]. Copyright of Royal Society of Chemistry.

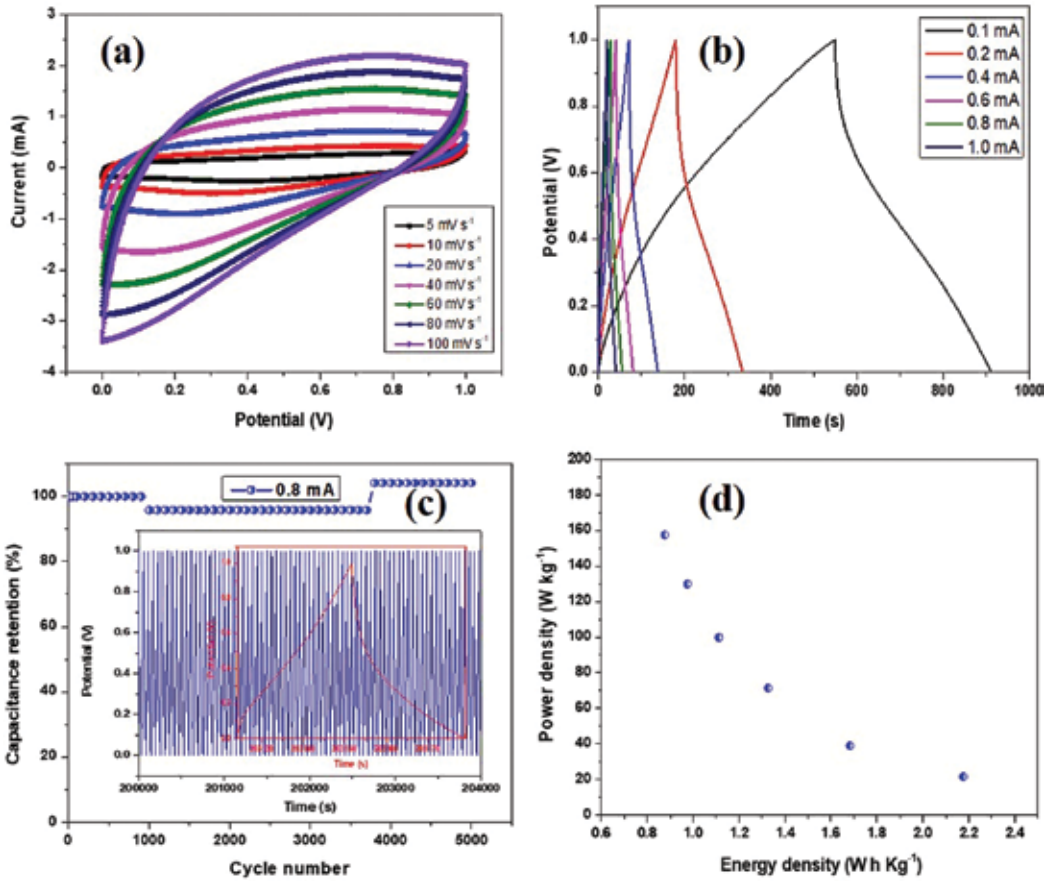


**Figure 10.** (a) Cyclic voltammograms of F-SC at different scan rates. (b) Galvanostatic charge/discharge profiles of F-SC at various currents. (c) the charge/discharge stability of F-SC at 0.8 mA. (d) Ragone plot of the F-SC. Reproduced from Ref. [7] with permission from the Royal Society of Chemistry.

The calculated energy density and power density of the F-SC is 2.18 W h $kg^{-1}$ (0.21 mWh $cm^{-3}$) and 21.6 W $kg^{-1}$ (2.1 mW $cm^{-3}$). The obtained values are higher than or comparable to previously reported F-SCs [20, 65–67].

### *2.3.2. Fabrication and characterization of dye-sensitized solar cells (DSSCs)*

The fabrication and photovoltaic characterization of the DSSC as follows. First, $TiCl_4$ treatment was conducted by immersing the cleaned FTO glass in the 40 mM titanium tetrachloride ($TiCl_4$) solution for 30 min at 70°C. Then, the photoanode $TiO_2$ paste was deposited on the $TiCl_4$ treated FTO glass by doctor blade process followed by calcination at 550°C for 1 h. After that, the dye coating was performed by dipping the as-prepared $TiO_2$ in 0.5 mM of N-719 in tert-butanol/acetonitrile solution (1:1 vol.) for 12 h. The Pt counter electrode (CE) was deposited on the drilled FTO glass by spin-coating (2000 rpm, 2 times) using 30 mM of the $H_2PtCl_6$

solution in isopropyl alcohol (IPA) and annealed at 450 ˚C for 30 min. The working electrode and CE were assembled using 60 μm of Surlyn, and an electrolyte (0.5 M 1-hexyl-2,3-dimethylimidazolium iodide (C-tri), 0.02 M iodine, 0.5 M 4-tert-butylpyridine, and 0.05 M lithium iodide in acetonitrile) was added through a pre-drilled hole.

*2.3.3. Integration and functional characterization of self-powered device*

To demonstrate self-powered application, the fabricated fiber supercapacitor was integrated with DSSC and LED. The schematic illustration of the self-powered device is shown in **Figure 11a**. The self-powered system comprises of four series-connected DSSCs and three series F-SC and light emitting diode (LED). Here, DSSC served as an energy source to harvest the energy from sunlight and then to charge the supercapacitor. After that stored energy was utilized to drive LED without disruption. Initially, the F-SCs was charged with turning the switch S1 is on to connect DSSCs to the circuit. **Figure 11b** shows the current density-voltage curve of the serially-wound DSSCs. The open-circuit voltage, short-circuit current, and power conversion efficiency of the serially-wound DSSCs was 3.08 V, 3.94 mA $cm^{-2}$, and 6.96%, respectively. The inset of **Figure 11b** shows the digital photograph of serially-wound DSSCs. The F-SC charged from 0 to 3.2 V about 60s signifying the stable output of DSSCs as shown in **Figure 11c**. Afterwards, to demonstrate the self-powered operation, by turning the switch S2 is on, while switch S1 is off to illuminate the commercial green LED (**Figure 11c**) using charged supercapacitors. This study validated that fiber supercapacitors could store solar energy harvested from DSSCs, which suggests their massive application potential in diverse electronic devices.

## 2.4. Fabrication and integration of supercapacitor device with hybrid (solar and vibrational) energy harvesters

In this work, hybridized self-charging power textile system was developed by Wen et al., [68] to simultaneously collect outdoor/indoor sunlight and casual body movement energies and stored in an energy storage device for sustainable operation of wearable electronics. **Figure 12** shows the schematic illustration of hybridized self-charging power textile. The self-charging power textile system consists of fiber-shaped dye-sensitized solar cells (F-DSSC, top layer),

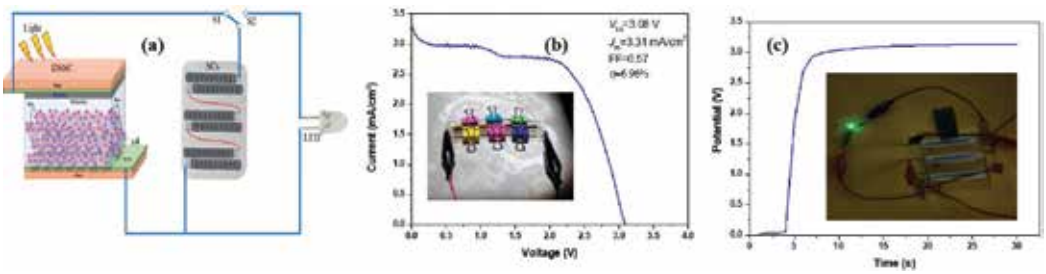


**Figure 11.** (a) Schematic diagram of the integration of F-SCs with DSSCs and LED. (b) J-V curve of the DSSCs connected in series under 1 sun irradiation. Inset is the digital image of four DSSCs assembled in series. (c) Charging curve of F-SCs module by DSSCs module in series; the inset is the digital photograph of green LED driven by F-SCs charged using DSSCs. Figure is adapted with permission from the Ref. [7]. Copyright of Royal Society of Chemistry.

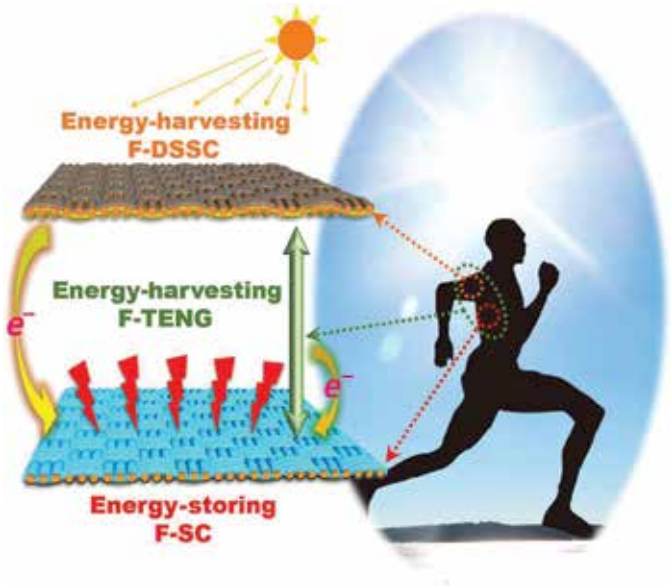


**Figure 12.** Schematic representation of the self-charging power textile. Reproduced from Ref. [68] with permission from the American Association for the Advancement of Science.

fiber-shaped triboelectric nanogenerator (F-TENG, middle layer) and fiber-shaped supercapacitors (F-SC, bottom layer). In this architecture, each solar cell and supercapacitor unit is coupled to one another, making a single triboelectric nanogenerator unit is assembled to scavenge body motion energy simultaneously. Both of the harvested energies could be effortlessly converted into electricity by using several solar cell units (for solar energy) and TENG (for random body motion energy) and then stored as chemical energy in supercapacitor modules for the operation of wearable electronics.

### *2.4.1. Fabrication and characterization of fiber-shaped supercapacitors*

The binder-free $RuO_2{\cdot}xH_2O$ on carbon fiber electrode was synthesized using a vapor-phase hydrothermal technique [69]. Briefly, a Ruthenium(III) chloride ($RuCl_3$) slurry prepared from 0.1 g of $RuCl_3$ and 4 ml of EtOH was coated onto the carbon fibers and dried at 60°C. Then the $RuCl_3$ coated carbon fibers were placed in a 50-ml Teflon-lined stainless steel autoclave with 0.1 M NaOH solution in an oven at 190°C for 5 h to get $RuO_2{\bullet}xH_2O$-coated carbon fibers. Then, two fiber electrodes were closely assembled into the PDMS-covered Cu-coated tube and separated by a paper septum to form an all-solid-state flexible fiber-shaped supercapacitor. Before assembling, the fiber electrodes were immersed in a PVA/$H_3PO_4$ gel electrolyte for 10 min. **Figure 13a** shows the schematic representation of $RuO_2{\cdot}xH_2O$ F-SC. The structural and morphological properties of the as-prepared electrodes were confirmed through SEM and XRD analysis. The SEM image (**Figure 13b–d**) of as-prepared fiber electrode shows the cracked mud morphology and the diameter of the fiber are ~10 mm. The XRD pattern of $RuO_2{\bullet}xH_2O$ coated carbon fiber electrodes revealed an amorphous with partly rutile crystalline structure [70]. The electrochemical performance of F-SC was evaluated by CV and GCD techniques. **Figure 13e**

shows the CV curves of F-SC at different scan rates. It can be observed that the CV curves are maintained their initial shape even at higher scan rates, revealed their good capacitive behavior and better rate capability. The GCD curves of F-SC at various current densities were shown in **Figure 13f**. The GCD curves displayed the symmetric and triangle in shape under various current densities, confirmed the good capacitive behavior. The calculated energy specific capacitance and energy density of F-SC is 1.9 mF $cm^{-1}$ and 1.37 mJ $cm^{-1}$, respectively. Further, the F-SC better cycling stability even after 5000 cycles with no obvious capacitance change as well as excellent mechanical stability under various bending conditions (from 0° to 180°).

*2.4.2. Fabrication and functional characterization of fiber-shaped hybrid energy harvester using dye-sensitized solar cells and triboelectric nanogenerator*

Firstly, a photoanode ($TiO_2$ nanotube) was prepared on Ti wire surface by anodization techniques in a solution containing 0.3 wt % $NH_4F$/EG and 8 wt % $H_2O$ at 60 V for 6 h using a two-electrode cell with Pt wire as a counter electrode [71]. After that, the anodized Ti wire was annealed at 500°C for 1 h and then immersed in 40 mM $TiCl_4$ solution at 70°C for 30 min. Afterwards, the as-prepared samples were annealed again at 450°C for 30 min. Secondly, the

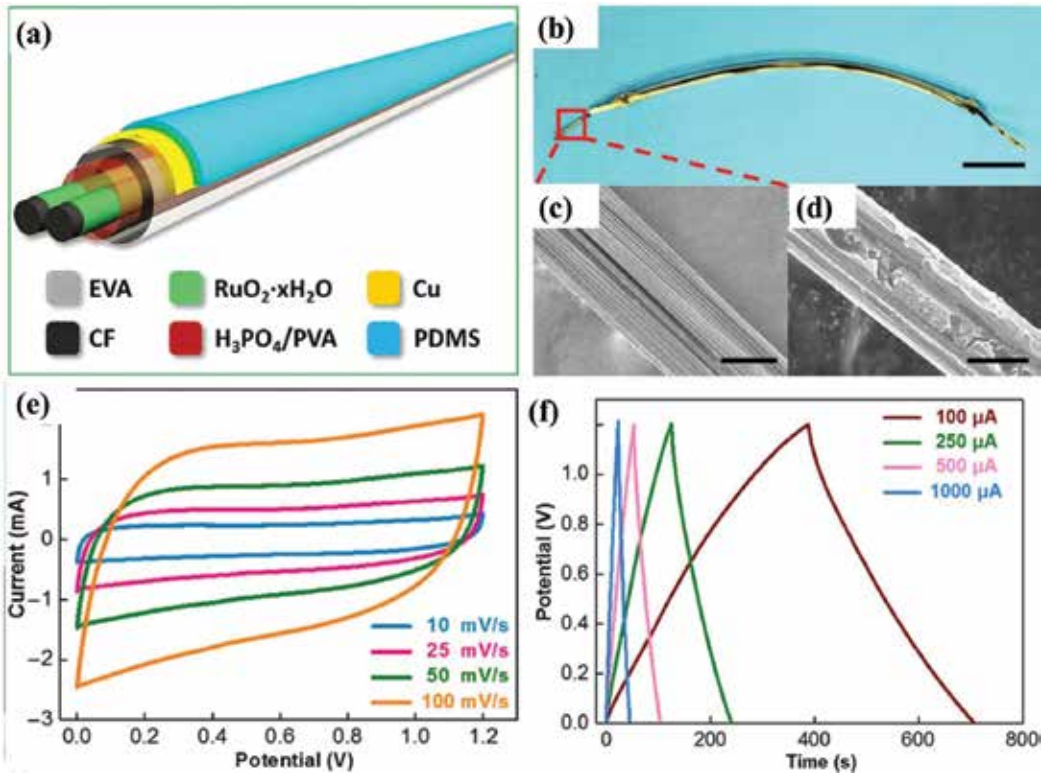


**Figure 13.** (a) Schematic diagram and (b) photograph of F-SC. (c-d) SEM images of $RuO_2{\cdot}xH_2O$-coated carbon fiber electrode. (e) CV and (f) GCD curves of F-SC at various scan rates and current densities. Figure is adapted with permission from the Ref. [68]. Copyright of American Association for the Advancement of Science.

prepared photoanode was immersed in a 3 × $10^{-4}$ M of N719 dye solution in ACN and tBA (v/v = 1/1) at room temperature for 24 h. Thirdly, the platinum counter electrode was fabricated by soaking carbon fiber in an $H_2PtCl_6 \bullet 6H_2O$ aqueous solution (5 mg/ml) for 5 min followed by thermal treatment at 400°C for 30 min. Finally, F-DSSC was fabricated by inserting a Pt-coated carbon fiber and a dye-sensitized Ti photo anode into the Cu-coated ethylene vinyl acetate (EVA) tube in parallel and then injected an electrolyte into the tubing (0.1 M LiI, 0.05 M I2, 0.6 M DMPII, and 0.5 M tBP in MPN). Finally, the pipe was sealed with sealing glue to prevent the electrolyte leakage. The schematic illustration and digital photograph of F-DSSC are shown in **Figure 14a**. Vertically oriented arrays of $TiO_2$ nanotubes with a diameter of ~50 nm on Ti wires surface were confirmed through SEM images (**Figure 14b–d**). The current density-voltage (J-V) characteristic of F-DSSC was assessed under standard illumination (100 mW cm − 2; AM1.5). The short-circuit current density, open-circuit voltage, fill factor, and power conversion efficiency of the F-DSSC is 11.92 mA $cm^{-2}$, 0.74 V, 0.64, and 5.64%, respectively.

A fiber-shaped triboelectric nanogenerator (F-TENG) was fabricated by connecting a Cu-coated EVA tube as a triboelectric electrode and the PDMS-covered Cu-coated EVA tube as another electrode. The copper (Cu) electrode with 1 mm thickness was deposited onto the EVA tubing surface by physical vapor deposition at 100 W in Ar atmosphere for 40 min. Then, the PDMS-covered Cu-coated EVA tubing was deposited by dip-coating process [72, 73] and dried at room temperature for 12 h. **Figure 14e–f** displays the schematic diagram and a digital photograph of F-TENG. The output performance of the fabricated F-TENG was studied through the periodic contact and separation under different frequencies. The open-circuit voltage (~12.6 V) and charge of the device are almost constant (~4.5 nC,) when the frequencies vary from 1 to 5 Hz, but the short-circuit current (ISC) increased from ~0.06 to ~0.15 μA. These result confirmed that the fabricated device could harvest the renewable energy efficiently.

### *2.4.3. Fabrication and testing of the hybridized self-charging power textile*

The hybridized self-charging power textile was fabricated by intertwined several solar cells and supercapacitors into the fabric to form a textile structure with serial/parallel connection (tune the output voltage and capacitance of devices to drive real wearable electronics). The textile-based F-TENG system was constructed by assembling the intertwined F-DSSC textile

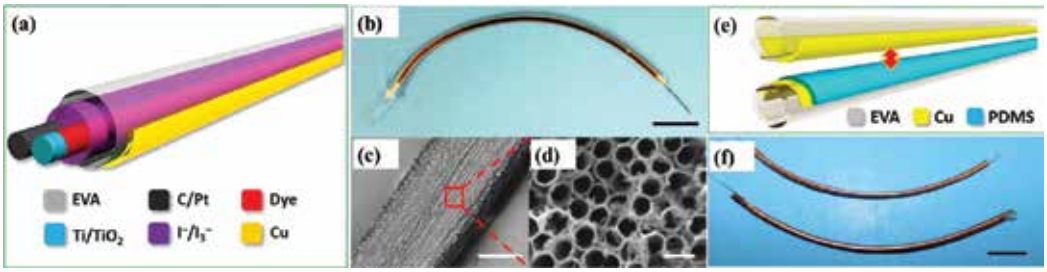


**Figure 14.** (a) Schematic diagram and (b) photograph of F-DSSC. (c-d) SEM images of $TiO_2$ nanotube arrays. (e) Schematic illustration and (f) digital photograph of F-TENG. Figure is adapted with permission from the Ref. [68]. Copyright of American Association for the Advancement of Science.

fabric as the top layer to harvest solar energy, and the bottom layer of intertwined F-SC textile was used to store harvested energies. Meanwhile, both woven textiles instantaneously engage in recreation as triboelectric layers to collect mechanical energies from human body motion, which were also stored in F-SC after rectification.

To check the real-time applications, the fabricated textile device was attached with a T-Shirt (**Figure 15**) and harvests both sunlight as well as body motion in outdoor and indoor activities, respectively. The whole device consists of three F-DSSC and 6 F-SC units in serial and then intertwined separately in a 3 × 3 network. The demonstration of self-charging power textile under outdoor and indoor activities is shown in **Figure 15a–c**. **Figure 15d** shows the equivalent circuit of hybridized self-charging power textile. Herein, an AC generated from F-TENG was converted into DC by a bridge rectifier, and it stored in F-SC. Moreover, a diode in the circuit blocks the inflow current through an F-DSSC. The self-charging characteristic was achieved by harvesting solar and mechanical energies from human motion through the as-fabricated hybrid device and is presented in **Figure 15e**. Initially, the F-SC was charged through a turn on the switch S0 and S1, which connect F-DSSC to F-SC, while the S2 switch is in off. The stable F-DSSCs output charge the F-SC to 1.8 V from 0 at 69 s. The F-SCs charging voltage persists at 1.8 V, due to the low output voltage of the F-DSSCs, which limits their reliability and practicability and it indicated by light blue-shaded area in **Figure 15e**. Further, the F-SCs can be charged continuously to a higher voltage as highlighted (light red-shaded area)

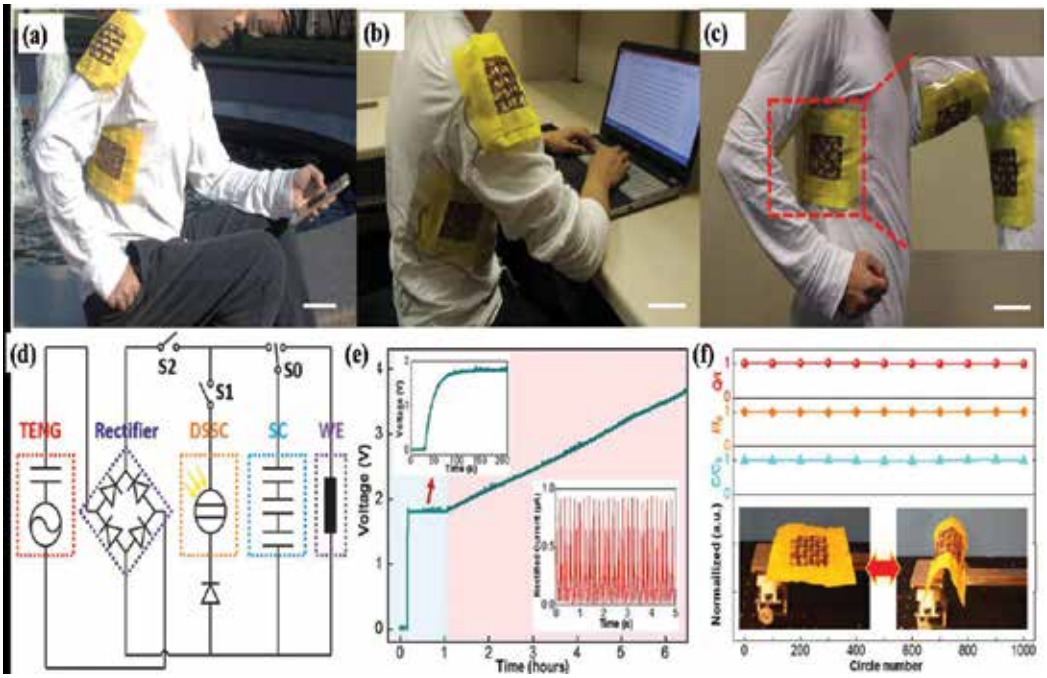


**Figure 15.** Demonstration of the self-charging powered textile. Digital photograph of the hybrid device under outdoor (a), indoor (b), and movement (c) environments. (d) the equivalent circuit of the self-charging powered textile for portable electronics. (e) the self-charging curve of the F-DSSC and F-TENG hybrid. (f) Durability studies of the fabricated devices for 1000 cycles. Insets show the photographs of bending status between 0° and 180°. Reproduced from Ref. [68] with permission from the American Association for the Advancement of Science.

in charging curves through F-TENGs by turn on the S2 switch. Then the charged F-SCs can power the portable electronic devices including LEDs, smart watches, sensors, etc. Moreover, the charging efficiency can be improved through impedance matching of DSSCs, TENGs, and SCs. Finally, the stability of the fabricated device was tested under continuous bending motion for 1000 cycles using the linear motor, as shown in **Figure 15f**. The advancement in the present efforts provides a new path for self-powered systems in wearable technology.

## 3. Conclusion

In summary, a self-powered system was successfully demonstrated by charging the supercapacitor using an energy harvester and powered a photosensor as well as portable devices. The various results showed the feasibility of using a supercapacitor as an efficient energy storage components and their application in self-powered devices due its high power density (uptake pulses) leads to the high energy conversion and storage efficiency. This work offers a welcome advancement in the supercapacitor toward the self-powered system application in flexible/wearable technology, which will pledge promising developments in self-powered flexible displays, infrastructure, and environmental monitoring, internet of things, defense technologies and wearable electronics (artificial electronic skin, smart textiles/watch straps), among others.

## Acknowledgements

This work was supported by 2018 Jeju Sea Grant College Program funded by the Ministry of Oceans and Fisheries (MOF) and by the National Research Foundation of Korea (NRF) funded by the Korea Government GRANT (2016R1A2B2013831).

## Author details

Ananthakumar Ramadoss[1,2], Balasubramaniam Saravanakumar[1,3,4] and Sang-Jae Kim[1*]

*Address all correspondence to: kimsangj@jejunu.ac.kr

1 Nanomaterials and System Lab, Department of Mechatronics Engineering, Jeju National University, Jeju, Republic of Korea

2 Laboratory for Advanced Research in Polymeric Materials, Central Institute of Plastic Engineering and Technology, Bhubaneswar, India

3 School of Chemistry and Environment, South China Normal University, Guangzhou, China

4 Engineering Research Center of MTEES (Ministry of Education), Research Center of BMET (Guangdong Province), Engineering Laboratory of OFMHEB (Guangdong Province), Key Laboratory of ETESPG (GHEI) and Innovative Platform for ITBMD (Guangzhou Municipality), South China Normal University, Guangzhou, China

## References


[1] Nykvist B, Nilsson M. Rapidly falling costs of battery packs for electric vehicles. Nature Climate Change. 2015;**5**:329-332

[2] Yu G, Gao J, Hummelen JC, Wudl F, Heeger AJ. Polymer photovoltaic cells: Enhanced efficiencies via a network of internal donor-acceptor heterojunctions. Science. 1995;**270**:1789

[3] Ma W, Yang C, Gong X, Lee K, Heeger AJ. Thermally stable, efficient polymer solar cells with nanoscale control of the interpenetrating network morphology. Advanced Functional Materials. 2005;**15**:1617-1622

[4] Kim J, Lee SM, Hwang YH, Lee S, Park B, Jang JH, et al. A highly efficient self-power pack system integrating supercapacitors and photovoltaics with an area-saving monolithic architecture. Journal of Materials Chemistry A. 2017;**5**:1906-1912

[5] Chu S, Majumdar A. Opportunities and challenges for a sustainable energy future. Nature. 2012;**488**:294-303

[6] Ramadoss A, Yoon KY, Kwak MJ, Kim SI, Ryu ST, Jang JH. Fully flexible, lightweight, high performance all-solid-state supercapacitor based on 3-dimensional-graphene/graphite-paper. Journal of Power Sources. 2017;**337**:159-165

[7] Ramadoss A, Kang KN, Ahn HJ, Kim SI, Ryu ST, Jang JH. Realization of high performance flexible wire supercapacitors based on 3-dimensional $NiCo_2O_4$/Ni fibers. Journal of Materials Chemistry A. 2016;**4**:4718-4727

[8] Xu X, Li S, Zhang H, Shen Y, Zakeeruddin SM, Graetzel M. A power pack based on organometallic perovskite solar cell and supercapacitor. ACS Nano. 2015;**9**:1782-1787

[9] Saito Y, Ogawa A, Uchida S, Kubo T, Segawa H. Energy-storable dye-sensitized solar cells with interdigitated nafion/polypyrrole-Pt comb-like electrodes. Chemistry Letters. 2010;**39**:488-489

[10] Simon P, Gogotsi Y. Materials for electrochemical capacitors. Nature Materials. 2008;**7**:845-854

[11] Wang J, Li X, Zi Y, Wang S, Li Z, Zheng L, et al. A flexible fiber-based supercapacitor-triboelectric-nanogenerator power system for wearable electronics. Advanced Materials. 2015;**27**:4830-4836

[12] Wang ZL, Song J. Piezoelectric nanogenerators based on zinc oxide nanowire arrays. Science. 2016;**312**:242

[13] Gao PX, Song J, Liu J, Wang ZL. Nanowire piezoelectric nanogenerators on plastic substrates as flexible power sources for Nanodevices. Advanced Materials. 2007;**19**:67-72

[14] Miller JR, Simon P. Electrochemical capacitors for energy management. Science. 2008;**321**:651

[15] Kötz R, Carlen M. Principles and applications of electrochemical capacitors. Electrochimica Acta. 2000;**45**:2483-2498

[16] Wang G, Zhang L, Zhang JA. Review of electrode materials for electrochemical supercapacitors. Chemical Society Reviews. 2012;**41**:797-828

[17] Guo W, Xue X, Wang S, Lin C, Wang ZL. An integrated power pack of dye-sensitized solar cell and li battery based on double-sided $TiO_2$ nanotube arrays. Nano Letters. 2012;**12**: 2520-2523

[18] Wang X, Liu B, Liu R, Wang Q, Hou H, Chen D, et al. Fiber-based flexible all-solid-state asymmetric supercapacitors for integrated photodetecting system. Angewandte Chemie, International Edition. 2014;**53**:1849-1853

[19] Ramadoss A, Saravanakumar B, Kim SJ. Thermally reduced graphene oxide-coated fabrics for flexible supercapacitors and self-powered systems. Nano Energy. 2015;**15**:587-597

[20] Xiao X, Li T, Yang P, Gao Y, Jin H, Ni W, et al. Fiber-based all-solid-state flexible supercapacitors for self-powered systems. ACS Nano. 2012;**6**:9200-9206

[21] Yang P, Xiao X, Li Y, Ding Y, Qiang P, Tan X, et al. Hydrogenated ZnO core-shell nanocables for flexible supercapacitors and self-powered systems. ACS Nano. 2013;**7**:2617-2626

[22] Jung S, Lee J, Hyeon T, Lee M, Kim DH. Fabric-based integrated energy devices for wearable activity monitors. Advanced Materials. 2014;**26**:6329-6334

[23] Hwang BU, Lee JH, Trung TQ, Roh E, Kim DI, Kim SW, et al. Transparent stretchable self-powered patchable sensor platform with ultrasensitive recognition of human activities. ACS Nano. 2015;**9**:8801-8810

[24] Li D, Kaner RB. Graphene-based materials. Science. 2008;**320**:1170

[25] Stankovich S, Dikin DA, Dommett GHB, Kohlhaas KM, Zimney EJ, Stach EA, et al. Graphene-based composite materials. Nature. 2006;**442**:282-286

[26] Sun D, Yan X, Lang J, Xue Q. High performance supercapacitor electrode based on graphene paper via flame-induced reduction of graphene oxide paper. Journal of Power Sources. 2013;**222**:52-58

[27] Tan YB, Lee JM. Graphene for supercapacitor applications. Journal of Materials Chemistry A. 2013;**1**:14814-14843

[28] Xu C, Xu B, Gu Y, Xiong Z, Sun J, Zhao XS. Graphene-based electrodes for electrochemical energy storage. Energy & Environmental Science. 2013;**6**:1388-1414

[29] Kim KS, Zhao Y, Jang H, Lee SY, Kim JM, Kim KS, et al. Large-scale pattern growth of graphene films for stretchable transparent electrodes. Nature. 2009;**457**:706-710

[30] Xuekun L, Minfeng Y, Hui H, Rodney SR. Tailoring graphite with the goal of achieving single sheets. Nanotechnology. 1999;**10**:269

[31] Berger C, Song Z, Li X, Wu X, Brown N, Naud C, et al. Electronic confinement and coherence in patterned epitaxial graphene. Science. 2006;**312**:1191

[32] Choucair M, Thordarson P, Stride JA. Gram-scale production of graphene based on solvothermal synthesis and sonication. Nature Nanotechnology. 2009;**4**:30-33

[33] Stankovich S, Dikin DA, Piner RD, Kohlhaas KA, Kleinhammes A, Jia Y. Synthesis of graphene-based nanosheets via chemical reduction of exfoliated graphite oxide. Carbon. 2007;**45**:1558-1565

[34] Park S, Ruoff RS. Chemical methods for the production of graphenes. Nature Nanotechnology. 2009;**4**:217-224

[35] Saravanakumar B, Mohan R, Kim SJ. Facile synthesis of graphene/ZnO nanocomposites by low temperature hydrothermal method. Materials Research Bulletin. 2013;**48**:878-883

[36] Zhang D, Zhang X, Chen Y, Wang C, Ma Y. An environment-friendly route to synthesize reduced graphene oxide as a supercapacitor electrode material. Electrochimica Acta. 2012;**69**:364-370

[37] Tuinstra F, Koenig JL. Raman spectrum of graphite. The Journal of Chemical Physics. 1970;**53**:1126-1130

[38] Chen C, Long M, Xia M, Zhang C, Cai W. Reduction of graphene oxide by an in-situ photoelectrochemical method in a dye-sensitized solar cell assembly. Nanoscale Research Letters. 2012;**7**:101

[39] Eda G, Chhowalla M. Chemically derived graphene oxide: Towards large-area thin-film electronics and optoelectronics. Advanced Materials. 2010;**22**:2392-2415

[40] Chen Y, Zhang X, Zhang D, Yu P, Ma Y. High performance supercapacitors based on reduced graphene oxide in aqueous and ionic liquid electrolytes. Carbon. 2011;**49**:573-580

[41] Xu B, Yue S, Sui Z, Zhang X, Hou S, Cao G, et al. What is the choice for supercapacitors: Graphene or graphene oxide? Energy & Environmental Science. 2011;**4**:2826-2830

[42] Lin Z, Liu Y, Yao Y, Hildreth OJ, Li Z, Moon K, et al. Superior capacitance of functionalized graphene. The Journal of Physical Chemistry C. 2011;**115**:7120-7125

[43] Ramadoss A, Kim SJ. Improved activity of a graphene–$TiO_2$ hybrid electrode in an electrochemical supercapacitor. Carbon. 2013;**63**:434-445

[44] Kaempgen M, Chan CK, Ma J, Cui Y, Gruner G. Printable thin film supercapacitors using single-walled carbon nanotubes. Nano Letters. 2009;**9**:1872-1876

[45] Li Y, van Zijll M, Chiang S, Pan N. KOH modified graphene nanosheets for supercapacitor electrodes. Journal of Power Sources. 2011;**196**:6003-6006

[46] Liu C, Yu Z, Neff D, Zhamu A, Jang BZ. Graphene-based supercapacitor with an ultra-high energy density. Nano Letters. 2010;**10**:4863-4868

[47] Zhu Y, Murali S, Stoller MD, Velamakanni A, Piner RD, Ruoff RS. Microwave assisted exfoliation and reduction of graphite oxide for ultracapacitors. Carbon. 2010;**48**:2118-2122

[48] Ramadoss A, Kim GS, Kim SJ. Fabrication of reduced graphene oxide/$TiO_2$ nanorod/reduced graphene oxide hybrid nanostructures as electrode materials for supercapacitor applications. CrystEngComm. 2013;**15**:10222-10229

[49] Lee M, Balasingam SK, Jeong HY, Hong WG, Lee HBR, Kim BH, et al. One-step hydrothermal synthesis of graphene decorated $V_2O_5$ nanobelts for enhanced electrochemical energy storage. Scientific Reports. 2015;**5**:8151

[50] Xu Y, Lin Z, Huang X, Liu Y, Huang Y, Duan X. Flexible solid-state supercapacitors based on three-dimensional graphene hydrogel films. ACS Nano. 2013;**7**:4042-4049

[51] Yu A, Roes I, Davies A, Chen Z. Ultrathin, transparent, and flexible graphene films for supercapacitor application. Applied Physics Letters. 2010;**96**:253105

[52] Choi BG, Chang SJ, Kang HW, Park CP, Kim HJ, Hong WH, et al. High performance of a solid-state flexible asymmetric supercapacitor based on graphene films. Nanoscale. 2012;**4**:4983-4988

[53] El-Kady MF, Strong V, Dubin S, Kaner RB. Laser scribing of high-performance and flexible graphene-based electrochemical capacitors. Science. 2012;**335**:1326

[54] Weng Z, Su Y, Wang DW, Li F, Du J, Cheng HM. Graphene-cellulose paper flexible supercapacitors. Advanced Energy Materials. 2011;**1**:917-922

[55] Choi BG, Hong J, Hong WH, Hammond PT, Park H. Facilitated ion transport in all-solid-state flexible supercapacitors. ACS Nano. 2011;**5**:7205-7213

[56] Kang YJ, Chun SJ, Lee SS, Kim BY, Kim JH, Chung H, et al. All-solid-state flexible supercapacitors fabricated with bacterial Nanocellulose papers, carbon nanotubes, and triblock-copolymer ion gels. ACS Nano. 2012;**6**:6400-6406

[57] Meng C, Liu C, Chen L, Hu C, Fan S. Highly flexible and all-solid-state paperlike polymer supercapacitors. Nano Letters. 2010;**10**:4025-4031

[58] Yu Jin K, Haegeun C, Chi-Hwan H, Woong K. All-solid-state flexible supercapacitors based on papers coated with carbon nanotubes and ionic-liquid-based gel electrolytes. Nanotechnology. 2012;**23**:065401

[59] Hu S, Rajamani R, Yu X. Flexible solid-state paper based carbon nanotube supercapacitor. Applied Physics Letters. 2012;**100**:104103

[60] Meng C, Liu C, Fan S. Flexible carbon nanotube/polyaniline paper-like films and their enhanced electrochemical properties. Electrochemistry Communications. 2009;**11**:186-189

[61] Yang Q, Guo X, Wang W, Zhang Y, Xu S, Lien DH, et al. Enhancing sensitivity of a single ZnO micro-/nanowire photodetector by piezo-phototronic effect. ACS Nano. 2010;**4**:6285-6291

[62] Xia XH, Tu JP, Zhang YQ, Mai YJ, Wang XL, Gu CD, et al. Three-dimentional porous Nano-Ni/co$(OH)_2$ Nanoflake composite film: A pseudocapacitive material with superior performance. The Journal of Physical Chemistry C. 2011;**115**:22662-22668

[63] Yuan C, Li J, Hou L, Zhang X, Shen L, Lou XW. Ultrathin mesoporous $NiCo_2O_4$ nanosheets supported on Ni foam as advanced electrodes for supercapacitors. Advanced Functional Materials. 2012;**22**:4592-4597

[64] Gupta V, Gupta S, Miura N. Electrochemically synthesized nanocrystalline spinel thin film for high performance supercapacitor. Journal of Power Sources. 2010;**195**:3757-3760

[65] Wang Q, Wang X, Xu J, Ouyang X, Hou X, Chen D, et al. Flexible coaxial-type fiber supercapacitor based on $NiCo_2O_4$ nanosheets electrodes. Nano Energy. 2014;**8**:44-51

[66] Gu S, Lou Z, Ma X, Shen G. $CuCo_2O_4$ nanowires grown on a Ni wire for high-performance, flexible fiber supercapacitors. ChemElectroChem. 2015;**2**:1042-1047

[67] Wu H, Lou Z, Yang H, Shen G. A flexible spiral-type supercapacitor based on $ZnCo_2O_4$ nanorod electrodes. Nanoscale. 2015;**7**:1921-1926

[68] Wen Z, Yeh MH, Guo H, Wang J, Zi Y, Xu W, et al. Self-powered textile for wearable electronics by hybridizing fiber-shaped nanogenerators, solar cells, and supercapacitors. Science Advances. 2016;**2**

[69] Park J, Lee JW, Ye BU, Chun SH, Joo SH, Park H, et al. Structural evolution of chemically-driven $RuO_2$ nanowires and 3-dimensional design for photo-catalytic applications. Scientific Reports. 2015;**5**:11933

[70] Wu ZS, Wang DW, Ren W, Zhao J, Zhou G, Li F, et al. Anchoring hydrous $RuO_2$ on graphene sheets for high-performance electrochemical capacitors. Advanced Functional Materials. 2010;**20**:3595-3602

[71] Yang Z, Deng J, Sun X, Li H, Peng H. Stretchable, wearable dye-sensitized solar cells. Advanced Materials. 2014;**26**:2643-2647

[72] Zhong J, Zhang Y, Zhong Q, Hu Q, Hu B, Wang ZL, et al. Fiber-based generator for wearable electronics and mobile medication. ACS Nano. 2014;**8**:6273-6280

[73] Zhong J, Zhong Q, Hu Q, Wu N, Li W, Wang B. Stretchable self-powered fiber-based strain sensor. Advanced Functional Materials. 2015;**25**:1798-1803

*Edited by Xiangping Chen and Wenping Cao*

Energy storage technologies play an important role in terms of high-efficient energy utilisation and stable energy flow in the system. This book provides a glimpse of some latest advancements in energy storage technologies, management and control, innovative energy conversion, energy efficiency and system integration. It is aimed at providing a guideline for developing similar storage systems and for the readers who are interested in energy storage-related technologies, wind energy, solar energy, smart grid and smart buildings.

Published in London, UK


IntechOpen

ISBN 978-1-83881-346-8
9 781838 813468